

NEWCASTLE UNIVERSITY

DOCTORAL THESIS

**The Accuracy of Electron Density
from Theory: Calculating Electric
Field Gradients and X-ray
Scattering for Molecules and
Solutions**

Author:

Josh LITTLEFAIR

Supervisor:

Dr. Thomas PENFOLD

*A thesis submitted in fulfilment of the requirements
for the degree of Doctor of Philosophy*

in the

Penfold Group

School of Natural and Environmental Sciences


November 8, 2021

Declaration of Authorship

I, Josh LITTLEFAIR, declare that this thesis titled, “The Accuracy of Electron Density from Theory: Calculating Electric Field Gradients and X-ray Scattering for Molecules and Solutions” and the work presented in it are my own. I confirm that:

- This work was done wholly or mainly while in candidature for a research degree at this University.
- Where any part of this thesis has previously been submitted for a degree or any other qualification at this University or any other institution, this has been clearly stated.
- Where I have consulted the published work of others, this is always clearly attributed.
- Where I have quoted from the work of others, the source is always given. With the exception of such quotations, this thesis is entirely my own work.
- I have acknowledged all main sources of help.
- Where the thesis is based on work done by myself jointly with others, I have made clear exactly what was done by others and what I have contributed myself.

Signed:

A handwritten signature in cursive script that reads "J. Littlefair". The signature is written in black ink on a light green rectangular background.

Date: 9/1/2020

Newcastle University

Abstract

Chemistry

School of Natural and Environmental Sciences

Doctor of Philosophy

**The Accuracy of Electron Density from Theory: Calculating Electric Field
Gradients and X-ray Scattering for Molecules and Solutions**

by Josh LITTLEFAIR

Electron density is the principle determinant of the characteristic properties of molecules, their structure and dynamics. For this reason it is vital to ascertain accurate densities. One method of predicting electron densities is density functional theory (DFT). It is derived from the Hohenberg-Kohn theorem which states that an exact ground-state energy should yield an exact electron density and vice versa. In reality the exact solution is not fully known as exchange and correlation have to be estimated. Were it known, accurate densities and energies could be calculated at a fraction of *ab initio* computational cost. However, it is noted that functional methods have deviated from the path to the exact functional due to energetic overfitting. This study used the electric field gradient (EFG) as an electron-density probe to facilitate comparison both to *ab initio* calculation (CCSD(T)) and microwave spectroscopy for simple transition metal complexes and halogenated aromatic compounds. EFGs improved with increased Hartree-Fock (HF) exchange fraction encountered for higher rungs of Jacob's Ladder due to self-interaction error (SIE) reduction. SIE cancellation was uneven between transition metals, halogens and aromatic rings, causing functional-dependent electronegativity. Electron density can also be inferred from X-ray scattering. X-ray free-electron lasers (XFELs) are used to probe molecular structure and dynamics on ultrafast time scales. Solutions contains additional scattering signals other than the desired solute from the solvent and solute-solvent. The solvent term can be extracted experimentally or via molecular dynamics (MD) trajectories. Theory is also the only method of predicting the solute-solvent term independently. The solvent force-field parameters can be derived from experiment or theoretically from DFT calculation. The impact of the chosen force field on the the predicted scattering profiles was evaluated herein, Quantum Bespoke Kit (QUBE) and all-atom Optimised Potentials for Liquid Simulations (OPLS-AA) force-fields were used to assess theoretically- and experimentally-derived parameters respectively for common solvents for the same test solute (I_2). Force-field dependence is elucidated for both terms due to differences in non-bonded parameters. There also remains further investigation to better approximate experimental solvent terms. Solute-solvent scattering occurs on comparable scales to the solute scattering. XFELs have also been applied recently to improve understanding metal-to-ligand charge transfer (MLCT) in transition metal complexes and the influence of polar solvents in their structures. QUBE was

used to investigate the ground and excited states of $[\text{Cu}(\text{phen})_2]^+$ and compared to recent classical MD and quantum-mechanical/molecular mechanical (QM/MM) simulations. It performed particularly well in regards to identifying Cu-N bond asymmetry and solvent influence in the ligand-ligand dihedral in the triplet state which were not identified in previous theoretical investigation but in agreement with recent experimental understanding. This improvement was attributed to its use of high-rung DFT in parameterisation ($\omega\text{B97X-D}$). Overall this investigation evaluate thoroughly the current state of theory in reproducing accurate electron densities, highlighting the importance of reducing DFT SIE to improve density accuracy, which in turn impacts force-field parameter quality, indicating that DFT improvement impacts all branches of theoretical chemistry.

Acknowledgements

I'd like to take this opportunity to thank the many people who have helped me through the last four years and three months. I would like to extend my thanks to my supervisor, Dr Tom Penfold, for giving me the opportunity to pursue this PhD, to have an experience of life as an academic and providing immeasurable support at every step. I would also like to acknowledge my secondary supervisor, Dr Daniel Cole, for his great help when I have called upon him, particularly in all things regarding force fields. I am grateful for the support and friendship of many within the Penfold group and throughout the students and staff of the Bedson Building, who have made this experience unforgettable. I would especially like to thank Dr Stuart Thompson, Emanuele Falbo and Yang Cao for their friendship and support during these years. And finally, I would like to thank my family, for supporting me every step of the way in my PhD journey.

Contents

Declaration of Authorship	iii
Acknowledgements	ix
1 Introduction	1
2 Theory and Methodology	7
2.1 Introduction	7
2.2 The Schrödinger Equation	7
2.3 The Born-Oppenheimer Approximation	11
2.4 Hartree-Fock Theory	13
2.5 Coupled-Cluster Theory	18
2.6 Density Functional Theory	19
2.7 Electric Field Gradient	24
2.8 X-ray Scattering	26
2.9 Force-Field Methods	31
2.10 Molecular Dynamics	36
3 Assessing Functional Errors using Atomisation Energies and Electric Field Gradients	41
3.1 Introduction	41
3.2 Theory and Computational Details	43
3.3 Results	46
3.3.1 CuCl	46
3.3.2 Ar \cdots CuCl	49
3.3.3 OC \cdots CuCl	51
3.4 Discussion and Conclusions	52
4 Extending the Understanding of Density and Energetic Error for Silver Complexes and Halogenated Aromatic Compounds	57
4.1 Introduction	57
4.2 Theory and Computational Details	58
4.3 Silver Complexes	59

4.4	Halogenated Aromatic Compounds	66
4.5	Discussion and Conclusions	73
5	Analysis of Forcefield Methods to Predict Solvent-Term Ultrafast X-ray Scattering Relative to Experimental Metrics	77
5.1	Introduction	77
5.2	Theory and Computational Details	79
5.3	Results	80
5.4	Discussion and Conclusions	86
6	Analysis of Forcefield Methods to Predict Solute-Solvent Ultrafast X-ray Scattering	89
6.1	Introduction	89
6.2	Theory and Computational Details	90
6.3	Results	91
6.4	Discussion and Conclusions	101
7	Analysis of Cu(I)-Phenanthroline Excited-State Properties using QM-Derived Forcefield Parameters	105
7.1	Introduction	105
7.2	Theoretical and Computational Details	107
7.3	Results	109
7.4	Discussion and Conclusions	113
8	Conclusion	115
A	Assessing Functional Errors using Atomisation Energies and Electric Field Gradients	121
A.1	Atomisation - EFG Characteristic by Functional Group	121
A.2	ω B97X Tuning via Koopmans' Theorem	123
A.3	Core Polarisation Contribution to Cu Electric Field Gradient	124
B	Extending the Understanding of Density and Energetic Error for Silver Complexes and Halogenated Aromatic Compounds	135
B.1	Silver Complexes	136
B.1.1	Atomisation - EFG Characteristic by Functional Group	136
B.1.2	ω B97X Tuning via Koopmans' Theorem	141
B.2	Halogenated Aromatic Compounds	146
B.2.1	Atomisation - EFG Characteristic by Functional Group	146
B.2.2	ω B97X Tuning via Koopmans' Theorem	151

B.3	Core Polarisation Contribution to Ag Electric Field Gradient . . .	155
C	Analysis of Forcefield Methods to Predict Solvent-Term Ultrafast X-ray Scattering Relative to Experimental Metrics	161
C.1	Temperature-Dependent and Density-Dependent Solvent Scattering Term	162
C.2	Comparison of Temperature-Dependent Solvent Scattering Terms	164
C.3	Radial Distribution Functions of Atom Combinations with Large Contributions to scattering	167
D	Analysis of Forcefield Methods to Predict Solute-Solvent Ultrafast X-ray Scattering	169
D.1	Temperature-Dependent Solute-Solvent Scattering Term	170
D.2	Comparison of Temperature-Dependent Solute-Solvent Scattering Terms	171
D.3	Radial Distribution Functions with Large Contributions to Solute-Solvent Scattering	174
D.4	Temperature-Dependent Solute Scattering Terms	177
D.5	Comparison of Temperature-Dependent Solute Scattering Terms	178
D.6	I-I Radial Distribution Functions for Solute Scattering	182

List of Figures

3.3.1 Plot of the CuCl atomisation energy as a function of Cu (a) and Cl (b) electric field gradient in the complex by functional group. GGA, hGGA, dhGGA and rshGGA are represented in blue, grey, red and light purple respectively. CCSD(T) is denoted in green, while the dashed line represents experimental EFG and atomisation.	46
3.3.2 Plot of the change in atomisation and a) Cu b) Cl EFG of ω B97X for CuCl as the value of ω is adjusted from 0.05 to 0.8. Optimal ω (green) and CCSD(T) (blue) are also indicated	48
3.3.3 Plot of the Ar \cdots CuCl atomisation energy as a function of a) Cu b) Cl electric field gradient in the complex by functional group. GGA, hGGA, dhGGA and rshGGA are represented in blue, grey, red and light purple respectively. CCSD(T) is denoted in green, while the dashed line represents experimental EFG.	49
3.3.4 Plot of the change in atomisation and copper EFG of ω B97X for CuCl as the value of ω is adjusted from 0.05 to 0.8. Optimal ω (green) and CCSD(T) (blue) are also indicated	50
3.3.5 Plot of the OC \cdots CuCl atomisation energy as a function of a) Cu b) Cl electric field gradient in the complex by functional group. GGA, hGGA, dhGGA and rshGGA are represented in blue, grey, red and light purple respectively. CCSD(T) is denoted in green, while the dashed line represents experimental EFG	52
3.3.6 Plot of the change in atomisation and copper EFG of ω B97X for CuCl as the value of ω is adjusted from 0.05 to 0.8. Optimal ω (green) and CCSD(T) (blue) are also indicated	53

4.3.1 AgCl Atomisation-EFG characteristic for a) silver and b) chlorine. GGA, hGGA, dhGGA and rshGGA are represented in blue, grey, red and light purple respectively. CCSD(T) is denoted in green, while the dashed line represents experimental EFG.	60
(a)	60
(b)	60
4.3.2 AgI Atomisation-EFG characteristic for a) silver and b) iodine. GGA, hGGA, dhGGA and rshGGA are represented in blue, grey, red and light purple respectively. CCSD(T) is denoted in green, while the dashed line represents experimental EFG. . .	61
(a)	61
(b)	61
4.3.3 AgCl ω B97X change in atomisation and EFG for a) silver and b) chlorine for $\omega=0.05-1$. Optimal $\omega=0.45$ is denoted in green, with CCSD(T) in cyan. Step-wise atomisation energies for high- ω functionals is on account of rounding to the maximum number of significant figures possible in this system.	64
(a)	64
(b)	64
4.3.4 AgI ω B97X change in atomisation and EFG for a) silver and b) chlorine for $\omega=0.05-1$. Optimal ω is not contained within the given range. CCSD(T) denoted in cyan. Experimental EFG is denoted by the dashed line. Step-wise atomisation energies for high- ω functionals is on account of rounding to the maximum number of significant figures possible in this system. . .	65
(a)	65
(b)	65
4.4.1 Halogenated aromatic compounds used in this investigation with halogen atom position denoted in red, the position of bromine or iodine. Carbon (grey), hydrogen (white), sulfur (yellow) and nitrogen (blue) are also show in the diagrams of a) 2-halothiophene b) 3-halothiophene c) 2-halopyrimidine and d) 2-halopyridine e) 3-halopyridine f) 4-halopyridine g) p-halotoluene h) 4-halopyrazole i) halobenzene. Images from <i>PubChem</i>	67
(a)	67
(b)	67

(c)	67
(d)	67
(e)	67
(f)	67
(g)	67
(h)	67
(i)	67
4.4.2	Atomisation-halogen EFG characteristic for a) 2-bromothiophene b) 3-bromothiophene c) 2-iodothiophene and d) 3-iodothiophene. GGA, hGGA, dhGGA and rshGGA are represented in blue, grey, red and light purple respectively. CCSD(T) is denoted in green, while the dashed line represents experimental EFG. . .	68
(a)	68
(b)	68
(c)	68
(d)	68
4.4.3	ω B97X change in atomisation and EFG for a) 2-bromothiophene b) 3-bromothiophene c) 2-iodothiophene and d) 3-iodothiophene over range $\omega=0.05-1$. Optimal $\omega=0.25$ for all halothiophene isomers and is denoted in green, with CCSD(T) in cyan. Ex- perimental EFG is denoted by the dashed line	72
(a)	72
(b)	72
(c)	72
(d)	72
5.2.1	Solvents used in this investigation for a) acetonitrile b) chloro- form c) dichloromethane and d) ethanol	80
(a)	80
(b)	80
(c)	80
(d)	80
5.3.1	$\frac{\partial S}{\partial T}$ per solvent molecule characteristic calculated from 1K sol- vent differences from OPLS-AA (blue) and QUBE (red), com- pared with experimental calculations (black) [1] for a) acetoni- trile b) chloroform c) dichloromethane and d) ethanol	80
(a)	80
(b)	80

(c)	80
(d)	80
5.3.2 $\frac{\partial S}{\partial T}$ per solvent molecule characteristic of acetonitrile calculated from 1K (red) and 5K (green) solvent differences for a) QUBE and b) OPLS-AA, compared with experimental calculations (black) [1]	82
(a)	82
(b)	82
5.3.3 $\Delta g(r)$ contributions of dominant scattering atom combinations calculated from 1K solvent differences from OPLS-AA (blue) and QUBE (red), a) acetonitrile (N-N) b) chloroform (Cl-Cl) c) dichloromethane (Cl-Cl) and d) ethanol (O-O). Constituent atoms are labelled by colour, including carbon (grey), hydrogen (white), nitrogen (blue), chlorine (green) and oxygen (red). Image from <i>PubChem</i>	84
(a)	84
(b)	84
(c)	84
(d)	84
5.3.4 $g(r)$ contributions of dominant scattering atom combinations at ground temperature (298.15K) from OPLS-AA (blue) and QUBE (red), a) acetonitrile (N-N) b) chloroform (Cl-Cl) c) dichloromethane (Cl-Cl) and d) ethanol (O-O)	85
(a)	85
(b)	85
(c)	85
(d)	85
6.3.1 $\frac{\partial S}{\partial T}$ per solvent molecule characteristic of the I ₂ solute calculated from 1K solution differences from OPLS-AA (blue) and QUBE (red) for a) acetonitrile b) chloroform c) dichloromethane and d) ethanol	91
(a)	91
(b)	91
(c)	91
(d)	91

6.3.2	$\frac{\partial S}{\partial T}$ per solvent molecule characteristic for the cross-term contribution of acetonitrile calculated from 1K (red) and 5K (green) solvent differences for a) QUBE and b) OPLS-AA	93
	(a)	93
	(b)	93
6.3.3	$\Delta g(r)$ contributions of dominant scattering atom combinations calculated from 1K solvent differences from OPLS-AA (blue) and QUBE (red), a) acetonitrile (I-N) b) chloroform (I-Cl) c) dichloromethane (I-Cl) and d) ethanol (I-O)	95
	(a)	95
	(b)	95
	(c)	95
	(d)	95
6.3.4	$g(r)$ contributions of dominant scattering atom combinations at ground temperature (298.15K) from OPLS-AA (blue) and QUBE (red), a) acetonitrile (N-N) b) chloroform (Cl-Cl) c) dichloromethane (Cl-Cl) and d) ethanol (O-O)	96
	(a)	96
	(b)	96
	(c)	96
	(d)	96
6.3.5	$\frac{\partial S}{\partial T}$ per solvent molecule characteristic calculated from 1K solution differences from OPLS-AA (blue) and QUBE (red) for a) acetonitrile b) chloroform c) dichloromethane and d) ethanol	97
	(a)	97
	(b)	97
	(c)	97
	(d)	97
6.3.6	$\frac{\partial S}{\partial T}$ per solvent molecule characteristic for the solute-term contribution of molecular iodine solvated in acetonitrile calculated from 1K (red) and 5K (green) solvent differences for a) QUBE and b) OPLS-AA	98
	(a)	98
	(b)	98
6.3.7	$\Delta g(r)$ contributions of the I-I solute atoms calculated from 1K solvent differences from OPLS-AA (blue) and QUBE (red), a) acetonitrile b) chloroform c) dichloromethane and d) ethanol	100
	(a)	100

(b)	100
(c)	100
(d)	100
6.3.8 $g(r)$ contributions of the I-I solute atoms at ground temperature (298.15K) from OPLS-AA (blue) and QUBE (red), a) acetonitrile b) chloroform c) dichloromethane and d) ethanol . .		101
(a)	101
(b)	101
(c)	101
(d)	101
7.2.1 $[\text{Cu}(\text{phen})_2]^+$ structure in a) ground S_0 and b) excited T_1 states. This illustrates the change in dihedral angle (DHA) between the planes of the phenanthroline ligands due to the pseudo Jahn-Teller effect		107
(a)	107
(b)	107
7.3.1 Radial distribution function $g(r)$ of Cu-solvent atom combinations of solvated $[\text{Cu}(\text{phen})_2]^+$ in ground and excited states (GS and ES respectively). Combinations illustrated are a) GS Cu- N_{MeCN} b) GS Cu- Cl_{DCM} c) ES Cu- N_{MeCN} d) ES Cu- Cl_{DCM} . QUBE and AMBER denoted in red and blue respectively. . . .		111
(a)	111
(b)	111
(c)	111
(d)	111
A.1.1 Plot of the $\text{H}_2\text{O} \cdots \text{CuCl}$ atomisation energy as a function of Cu (a) and Cl (b) electric field gradient in the complex by functional group. GGA, hGGA, dhGGA and rshGGA are represented in blue, grey, red and light purple respectively. CCSD(T) is denoted in green, while the dashed line represents experimental EFG.		121
A.1.2 Plot of the $\text{H}_2\text{S} \cdots \text{CuCl}$ atomisation energy as a function of Cu (a) and Cl (b) electric field gradient in the complex by functional group. GGA, hGGA, dhGGA and rshGGA are represented in blue, grey, red and light purple respectively. CCSD(T) is denoted in green, while the dashed line represents experimental EFG.		122

A.2.1	Plot of the change in atomisation and Cu (a) and Cl (b) EFG of ω B97X for $\text{H}_2\text{O} \cdots \text{CuCl}$ as ω is adjusted from 0.05 to 0.8. Optimal ω (green) and CCSD(T) (blue) are also indicated . . .	123
A.2.2	Plot of the change in atomisation and Cu (a) and Cl (b) EFG of ω B97X for $\text{H}_2\text{S} \cdots \text{CuCl}$ as ω is adjusted from 0.05 to 0.8. Optimal ω (green) and CCSD(T) (blue) are also indicated . . .	124
B.1.1	$\text{H}_2\text{O} \cdots \text{AgCl}$ Atomisation-EFG characteristic for a) silver and b) chlorine. GGA, hGGA, dhGGA and rshGGA are represented in blue, grey, red and light purple respectively. CCSD(T) is denoted in green, while the dashed line represents experimental EFG.	136
	(a)	136
	(b)	136
B.1.2	$\text{H}_2\text{S} \cdots \text{AgCl}$ Atomisation-EFG characteristic for a) silver and b) chlorine. GGA, hGGA, dhGGA and rshGGA are represented in blue, grey, red and light purple respectively. CCSD(T) is denoted in green, while the dashed line represents experimental EFG.	137
	(a)	137
	(b)	137
B.1.3	$\text{H}_2\text{O} \cdots \text{AgI}$ Atomisation-EFG characteristic for a) silver and b) iodine. GGA, hGGA, dhGGA and rshGGA are represented in blue, grey, red and light purple respectively. CCSD(T) is denoted in green, while the dashed line represents experimental EFG.	138
	(a)	138
	(b)	138
B.1.4	$\text{H}_2\text{S} \cdots \text{AgI}$ Atomisation-EFG characteristic for a) silver and b) iodine. GGA, hGGA, dhGGA and rshGGA are represented in blue, grey, red and light purple respectively. CCSD(T) is denoted in green, while the dashed line represents experimental EFG.	139
	(a)	139
	(b)	139

B.1.5 $\text{H}_3\text{N} \cdots \text{AgI}$ Atomisation-EFG characteristic for a) silver and b) iodine. GGA, hGGA, dhGGA and rshGGA are represented in blue, grey, red and light purple respectively. CCSD(T) is denoted in green, while the dashed line represents experimental EFG.	140
(a)	140
(b)	140
B.1.6 $\text{H}_2\text{O} \cdots \text{AgCl}$ ωB97X change in atomisation and EFG for a) silver and b) chlorine for $\omega=0.05-1$. Optimal $\omega=0.4$ is denoted in green, with CCSD(T) in cyan	141
(a)	141
(b)	141
B.1.7 $\text{H}_2\text{S} \cdots \text{AgCl}$ ωB97X change in atomisation and EFG for a) silver and b) chlorine for $\omega=0.05-1$. Optimal $\omega=0.3$ is denoted in green, with CCSD(T) in cyan	142
(a)	142
(b)	142
B.1.8 $\text{H}_2\text{O} \cdots \text{AgI}$ ωB97X change in atomisation and EFG for a) silver and b) iodine for $\omega=0.05-1$. Optimal $\omega > 1$ and therefore beyond the current range, with CCSD(T) in cyan	143
(a)	143
(b)	143
B.1.9 $\text{H}_2\text{S} \cdots \text{AgI}$ ωB97X change in atomisation and EFG for a) silver and b) iodine for $\omega=0.05-1$. Optimal $\omega=0.3$ is denoted in green, with CCSD(T) in cyan	144
(a)	144
(b)	144
B.1.10 $\text{H}_3\text{N} \cdots \text{AgI}$ ωB97X change in atomisation and EFG for a) silver and b) iodine for $\omega=0.05-1$. Optimal $\omega=0.3$ is denoted in green, with CCSD(T) in cyan	145
(a)	145
(b)	145
B.2.1 Atomisation-halogen EFG characteristic for a) bromopyrazole and b) iodopyrazole. GGA, hGGA, dhGGA and rshGGA are represented in blue, grey, red and light purple respectively. CCSD(T) is denoted in green, while the dashed line represents experimental EFG.	146
(a)	146

(b)	146
B.2.2 Atomisation-halogen EFG characteristic for a) bromobenzene and b) iodobenzene. GGA, hGGA, dhGGA and rshGGA are represented in blue, grey, red and light purple respectively. The dashed line denotes experimental EFG.	147
(a)	147
(b)	147
B.2.3 Atomisation-halogen EFG characteristic for a) 2-bromopyrimidine and b) 2-iodopyrimidine. GGA, hGGA, dhGGA and rshGGA are represented in blue, grey, red and light purple respectively. CCSD(T) is denoted in green (2-bromopyrimidine only), while the dashed line represents experimental EFG (2-bromopyrimidine only).	148
(a)	148
(b)	148
B.2.4 Atomisation-halogen EFG characteristic for a) p-bromotoluene and b) p-iodotoluene. GGA, hGGA, dhGGA and rshGGA are represented in blue, grey, red and light purple respectively. The dashed line denotes experimental EFG.	149
(a)	149
(b)	149
B.2.5 Atomisation-halogen EFG characteristic for a) 2-bromopyridine b) 2-iodopyridine c) 3-bromopyridine d) 3-iodopyridine e) 4-bromopyridine f) 4-iodopyridine . GGA, hGGA, dhGGA and rshGGA are represented in blue, grey, red and light purple respectively. The dashed line denotes experimental EFG.	150
(a)	150
(b)	150
(c)	150
(d)	150
(e)	150
(f)	150
B.2.6 ω B97X change in atomisation and EFG for a) bromopyrazole and b) iodopyrazole over range $\omega=0.05-1$. Optimal $\omega=0.25$ and is denoted in green, with CCSD(T) in cyan. Experimental EFG is denoted by the dashed line	151
(a)	151
(b)	151

B.2.7 ω B97X change in atomisation and EFG for a) bromobenzene and b) iodobenzene over range $\omega=0.05-1$. Optimal $\omega=0.25$ and is denoted in green. Experimental EFG is denoted by the dashed line	152
(a)	152
(b)	152
B.2.8 ω B97X change in atomisation and EFG for a) 2-bromopyrimidine and b) 2-iodopyrimidine over range $\omega=0.05-1$. Optimal $\omega=0.3$ and 0.35 respectively and is denoted in green, with CCSD(T) in cyan (2-bromopyrimidine only). Experimental EFG is denoted by the dashed line (2-bromopyrimidine only)	153
(a)	153
(b)	153
B.2.9 ω B97X change in atomisation and EFG for a) p-bromotoluene and b) p-iodotoluene over range $\omega=0.05-1$. Optimal $\omega=0.25$ and is denoted in green. Experimental EFG is denoted by the dashed line	154
(a)	154
(b)	154
B.2.10 ω B97X change in atomisation and EFG for a) 2-bromopyridine b) 2-iodopyridine c) 3-bromopyridine d) 3-iodopyridine e) 4-bromopyridine f) 4-iodopyridine over range $\omega=0.05-1$. Optimal $\omega=0.25$ and is denoted in green. Experimental EFG is denoted by the dashed line	155
(a)	155
(b)	155
(c)	155
(d)	155
(e)	155
(f)	155
C.1.1 $\frac{\partial S}{\partial T}$ per solvent molecule characteristic calculated from 5K solvent differences from OPLS-AA (blue) and QUBE (red), compared with experimental calculations (black) [1] for a) acetonitrile b) chloroform c) dichloromethane and d) ethanol	162
(a)	162
(b)	162
(c)	162

(d)	162
C.1.2 $\frac{\partial S}{\partial \rho}$ per solvent molecule characteristic calculated from 0.05 bar and 0.20bar solvent pressure differences from OPLS-AA (blue) and QUBE (red), compared with experimental calculations (black) [1] for acetonitrile. Density change for this change in pressure is simply too low to yield meaningful accurate results, hence the predicted scattering change is simply too large. This exact rationale for this erroneous prediction requires further investigation.	163
(a)	163
(b)	163
C.2.1 $\frac{\partial S}{\partial T}$ per solvent molecule characteristic of chloroform calculated from 1K (red) and 5K (green) solvent differences for a) QUBE and b) OPLS-AA, compared with experimental calculations (black) [1].	164
(a)	164
(b)	164
C.2.2 $\frac{\partial S}{\partial T}$ per solvent molecule characteristic of dichloromethane calculated from 1K (red) and 5K (green) solvent differences for a) QUBE and b) OPLS-AA, compared with experimental calculations (black) [1].	165
(a)	165
(b)	165
C.2.3 $\frac{\partial S}{\partial T}$ per solvent molecule characteristic of ethanol calculated from 1K (red) and 5K (green) solvent differences for a) QUBE and b) OPLS-AA, compared with experimental calculations (black) [1].	166
(a)	166
(b)	166
C.3.1 $g(r)$ contributions of dominant scattering atom combinations at 299.15K (1K above ground temperature) from OPLS-AA (blue) and QUBE (red), a) acetonitrile (N-N) b) chloroform (Cl-Cl) c) dichloromethane (Cl-Cl) and d) ethanol (O-O)	167
(a)	167
(b)	167
(c)	167
(d)	167

C.3.2	$g(r)$ contributions of dominant scattering atom combinations at 303.15K (5K above ground temperature) from OPLS-AA (blue) and QUBE (red), a) acetonitrile (N-N) b) chloroform (Cl-Cl) c) dichloromethane (Cl-Cl) and d) ethanol (O-O)	168
(a)	168
(b)	168
(c)	168
(d)	168
D.1.1	$\frac{\partial S}{\partial T}$ per solvent molecule characteristic calculated from 5K solution differences from OPLS-AA (blue) and QUBE (red) for a) acetonitrile b) chloroform c) dichloromethane and d) ethanol	170
(a)	170
(b)	170
(c)	170
(d)	170
D.2.1	$\frac{\partial S}{\partial T}$ per solvent molecule characteristic for the cross-term contribution of chlorine calculated from 1K (red) and 5K (green) solvent differences for a) QUBE and b) OPLS-AA	171
(a)	171
(b)	171
D.2.2	$\frac{\partial S}{\partial T}$ per solvent molecule characteristic for the cross-term contribution of dichloromethane calculated from 1K (red) and 5K (green) solvent differences for a) QUBE and b) OPLS-AA	172
(a)	172
(b)	172
D.2.3	$\frac{\partial S}{\partial T}$ per solvent molecule characteristic for the cross-term contribution of ethanol calculated from 1K (red) and 5K (green) solvent differences for a) QUBE and b) OPLS-AA	173
(a)	173
(b)	173
D.3.1	$\Delta g(r)$ contributions of dominant scattering atom combinations calculated from 5K solvent differences from OPLS-AA (blue) and QUBE (red), a) acetonitrile (I-N) b) chloroform (I-Cl) c) dichloromethane (I-Cl) and d) ethanol (I-O)	174
(a)	174
(b)	174
(c)	174

(d)	174
D.3.2 $g(r)$ contributions of dominant scattering atom combinations at 299.15K (1K above ground temperature) from OPLS-AA (blue) and QUBE (red), a) acetonitrile (I-N) b) chloroform (I-Cl) c) dichloromethane (I-Cl) and d) ethanol (I-O)	175
(a)	175
(b)	175
(c)	175
(d)	175
D.3.3 $g(r)$ contributions of dominant scattering atom combinations at 303.15K (5K above ground temperature) from OPLS-AA (blue) and QUBE (red), a) acetonitrile (I-N) b) chloroform (I-Cl) c) dichloromethane (I-Cl) and d) ethanol (I-O)	176
(a)	176
(b)	176
(c)	176
(d)	176
D.4.1 $\frac{\partial S}{\partial T}$ per solvent molecule characteristic if the I ₂ solute calculated from 5K solution differences from OPLS-AA (blue) and QUBE (red) for a) acetonitrile b) chloroform c) dichloromethane and d) ethanol	177
(a)	177
(b)	177
(c)	177
(d)	177
D.5.1 $\frac{\partial S}{\partial T}$ per solvent molecule characteristic for the solute-term contribution of molecular iodine solvated in acetonitrile calculated from 1K (red) and 5K (green) solvent differences for a) QUBE and b) OPLS-AA	178
(a)	178
(b)	178
D.5.2 $\frac{\partial S}{\partial T}$ per solvent molecule characteristic for the solute-term contribution of molecular iodine solvated in chloroform calculated from 1K (red) and 5K (green) solvent differences for a) QUBE and b) OPLS-AA	179
(a)	179
(b)	179

D.5.3 $\frac{\partial S}{\partial T}$ per solvent molecule characteristic for the solute-term contribution of molecular iodine solvated in dichloromethane calculated from 1K (red) and 5K (green) solvent differences for a) QUBE and b) OPLS-AA	180
(a)	180
(b)	180
D.5.4 $\frac{\partial S}{\partial T}$ per solvent molecule characteristic for the solute-term contribution of molecular iodine solvated in ethanol calculated from 1K (red) and 5K (green) solvent differences for a) QUBE and b) OPLS-AA	181
(a)	181
(b)	181
D.6.1 $\Delta g(r)$ contributions of the I-I solute atoms calculated from 5K solvent differences from OPLS-AA (blue) and QUBE (red), a) acetonitrile b) chloroform c) dichloromethane and d) ethanol	182
(a)	182
(b)	182
(c)	182
(d)	182
D.6.2 $g(r)$ contributions of the I-I solute atoms at 1K above ground temperature (299.15K) from OPLS-AA (blue) and QUBE (red), a) acetonitrile b) chloroform c) dichloromethane and d) ethanol	183
(a)	183
(b)	183
(c)	183
(d)	183
D.6.3 $g(r)$ contributions of the I-I solute atoms at 5K above ground temperature (303.15K) from OPLS-AA (blue) and QUBE (red), a) acetonitrile b) chloroform c) dichloromethane and d) ethanol	184
(a)	184
(b)	184
(c)	184
(d)	184

List of Tables

2.9.1 Table of assorted constants associated with the parameterisation of a force field	34
3.2.1 The functionals, including type and reference used within this work.	45
7.2.1 Non-bonded parameters of the Cu and N atoms, partial charge (q) and the Lennard-Jones (L-J) parameters (ϵ and σ). See section 7.3 for data concerning the internal structure of the Cu-N bonds. *L-J parameters taken from previous model of Jahn-Teller effect [2]. ** There is an asymmetry in the triplet state partial charge of the nitrogen atoms between the two ligands, with corresponding adjustments made in QUBE for the L-J parameters	108
7.3.1 Mean Cu-N bond length, NCuN_{intra} angle formed between copper and nitrogens of the same phenanthroline ligand and dihedral angle (DHA) formed by the two ligand planes (figure 7.2.1), along with standard deviations (σ) for ground and $^3\text{MLCT}$ states. Classical MD (CMD)-simulation-derived geometries utilising the QUBE parameters herein are compared with CMD and QM/MM AMBER calculations from Capano <i>et al</i> [3]	109
A.3.1 Core polarisation contribution to copper electric field gradient of CuCl of default functionals and CCSD(T)	125
A.3.2 Core polarisation contribution to copper electric field gradient of CuCl of ωB97X functionals with ω altered from 0.05 through 1.5	126
A.3.3 Core polarisation contribution to copper electric field gradient of $\text{Ar}\cdots\text{CuCl}$ of default functionals and CCSD(T)	127

A.3.4	Core polarisation contribution to copper electric field gradient of Ar...CuCl of ω B97X functionals with ω altered from 0.05 through 1.5	128
A.3.5	Core polarisation contribution to copper electric field gradient of OC...CuCl of default functionals and CCSD(T)	129
A.3.6	Core polarisation contribution to copper electric field gradient of OC...CuCl of ω B97X functionals with ω altered from 0.05 through 1.5	130
A.3.7	Core polarisation contribution to copper electric field gradient of H ₂ O...CuCl of default functionals and CCSD(T)	131
A.3.8	Core polarisation contribution to copper electric field gradient of H ₂ O...CuCl of ω B97X functionals with ω altered from 0.05 through 1.5	132
A.3.9	Core polarisation contribution to copper electric field gradient of H ₂ S...CuCl of default functionals and CCSD(T)	133
A.3.10	Core polarisation contribution to copper electric field gradient of H ₂ S...CuCl of ω B97X functionals with ω altered from 0.05 through 1.5	134
B.3.1	Core polarisation contribution to silver electric field gradient of AgCl of default functionals and CCSD(T)	156
B.3.2	Core polarisation contribution to silver electric field gradient of AgCl of ω B97X functionals with ω altered from 0.05 through 1.00	157
B.3.3	Core polarisation contribution to silver electric field gradient of AgI of default functionals and CCSD(T)	158
B.3.4	Core polarisation contribution to silver electric field gradient of AgI of ω B97X functionals with ω altered from 0.05 through 1.00	159

Chapter 1

Introduction

Theoretical chemistry spans a large range of modern scientific research, from prediction of X-ray scattering, study of biological systems, organic light-emitting diode (OLED) emission properties and force-field parameterisation [1–5]. Much of this work is directly or indirectly assisted by density functional calculations. Density functional theory (DFT) represents a cornerstone of modern science, its versatility shown through the use of DFT calculations in over >30,000 journal papers every year [6]. Its advantage over *ab initio* theory is found in its premise, as set out in the Hohenberg-Kohn theorems [7], that the total energy of electrons moving under the influence of an external potential is a unique functional of the electron density. Thus the density that minimises total energy is the ground-state density. This accelerates electronic structure calculations significantly relative to orbital-based gold-standard post-Hartree-Fock methods such as CCSD(T) (Coupled Cluster theory with Singlet, Doublet and perturbatively-corrected Triplet correction) [8,9]. This permits calculation on systems simply too large for *ab initio* calculation within reasonable time frames [10]. The Hohenberg-Kohn theorems predict the existence of an exact ground-state functional which would yield an exact density [7,11]. This exact density could then be cast into theoretical non-interacting Kohn-Sham (KS) orbitals which exactly reproduce it, which would be an accurate reproduction of the real *ab initio* Hamiltonian, without the computational expense of the latter. The success of DFT rests on creating an exact effective external potential, which includes the effect of electron-electron repulsion, such that the non-interacting system successfully replicates the real system [11]. This is entirely feasible for mean-field Coulomb repulsion, but this still neglects exchange (Fermi repulsion) and Coulomb correlation, combined into an exchange-correlation (XC) potential (V_{xc}), which comprises 1% of the total repulsion. Exchange comprises the electron-electron repulsion that occurs between electrons of parallel spin and

in of itself is a form of correlation. Coulomb correlation deals with electron-electron repulsions which are not resultant from the mean-field Coulomb interaction between an electron and the surrounding electron cloud. Both are seen visibly as a probability hole, where electron probability density is lower than that expected via mean-field interaction alone. Earlier approaches to accounting for the XC term involved adapting the exact exchange of the orbital-free Thomas-Fermi model [12, 13], a precursor to modern DFT, to KS DFT. These approaches assume a homogeneous electron gas, and are collectively referred to as the Local Density Approximation (LDA) and Local Spin Density Approximation (LSDA) where densities are individualised in terms of their respective spin [14]. The assumption of uniform electron gas has been observed to underestimate exchange and overestimate correlation, which often offset each other to some degree [15]. Thereon correction for first- and second-order electron density change have formed the Generalised Gradient Approximation (GGA) [16–18] and meta-Generalised Gradient Approximation (mGGA) [16] respectively. Collectively LDA, LSDA, GGA and mGGA constitute "pure" DFT functionals, without XC correction contribution from other methods. From observation of pure DFT XC functionals, it is seen that XC often undergoes sudden drop-offs as distance increases, such that long-range exchange is poorly described [19, 20]. For this reason, Becke introduced the hybrid approach (hGGA) [21]. Therein a fraction of total exchange is calculated using Hartree-Fock exchange applied to the KS orbitals. Such an approach improves long-range exchange, however the use of KS orbitals in such an *ab initio* approach means that full cancellation of self-interaction error is unlikely to be achieved. Double hybrid functionals (dhGGA) incorporate HF exchange fractions and second-order Møller-Plesset perturbation theory (MP2) fractions to describe correlation [22–24]. Like HF exchange, applying MP2's ability to exactly describe correlation is limited by the use of KS orbitals. Recently, approaches have been made to apply DFT and HF exchange in the short- and long-range domains where they are most useful, with factors included to increase HF exchange as inter-electron distance increases up to a given fraction or all exchange, termed collectively range-separated functionals (rshGGA) [25, 26]. Together these methods are organised into rungs of Jacob's Ladder, with each higher rung a step closer to the "heaven of chemical accuracy" [10, 27].

It was originally assumed that given the premise of the Hohenberg-Kohn theorems, improving DFT agreement with known energetic data would in

turn improve electron density accuracy and help ascertain a universal functional, however recent papers have called for reconsideration of this approach, highlighting large density errors relative to those predicted by *ab initio* calculation [19,27,28]. Dipole studies also highlight limitations to success in replicating experimental metrics linked to electron density [29]. There are therefore growing concerns that density functional theory is "straying from the path to the exact functional" [27], though other studies contest that assessment of the current state of functional development [30–32]. However, it is clear that there needs to be closer integration of electron density accuracy in the development and assessment of density functional methods. Furthermore, there remain "difficult cases" that DFT struggles to replicate, in particular transition metal diatomics and complexes, which has been associated with incomplete cancellation of self-interaction error (SIE) [33]. Self-interaction error cancellation has been shown to be functional dependent and particularly sensitive to the fraction of Hartree-Fock exchange, as illustrated in dipole studies [34]. Srebro *et al* have demonstrated promising results with one well-known challenging case, CuCl [33]. Tuning range-separated hybrid functionals' ionisation potentials via Koopmans' theorem, it illustrated agreement with *ab initio* and experimental copper electric field gradients (EFGs). The EFG is a direct probe of the polarisation of the valence electron density of an atom as measured from its nucleus, and can be calculated from nuclear quadrupole coupling constants (NQCCs) obtained from microwave spectroscopy [35]. Therewith one has a versatile metric with which comparisons with *ab initio* theory and experiment can be made, while equally allowing direct insight into the arrangement of valence density. Using Srebro's study as a starting point, an initial study was set up to assess the performance of 26 functionals taken from across Jacob's Ladder [21,22,25,36–56], and the performance of a default range-separated functional (ω B97X) tuned via Koopman's theorem for CuCl and CuCl complexed with simple ligands (Ar, CO, H₂O, H₂S) which have available experimentally-derived EFGs [57–59]. CCSD(T) provides benchmark *ab initio* EFGs. Atomisation energy was provided as an energetic metric to compare to EFG and analyse whether there is a breakdown in energetic vs. electron density accuracy. Thereon in chapter 4 the investigation was expanded to include other molecules of interest to microwave spectroscopy: silver diatomics (AgCl, AgI) with simple complexing molecules (H₂O, H₂S and H₃N (for AgI only))

[58–62], and included brominated and iodinated aromatic compounds (4-halopyrazoles [63]; 2- and 3-halothiophenes; 2- [64, 65], 3- [66, 67] and 4-halopyridines [64, 65]; 2-halopyrimidine (bromine only) [68]; halobenzene [69, 70] and *p*-halotoluene [71]).

X-ray scattering presents another experimental method of inferring electron density [72]. It has widespread application from solid-state physics [73] to biology [74–76] as an experimental way of elucidating molecular structure and dynamics. The recent development of X-ray Free-Electron Lasers (XFELs) has expanded the application of scattering to observation of chemical reactions and dynamics on ultrafast time scales [72, 77–83]. Successful imaging of the solute depends on the ability to extract solvent and solvent-solute scattering signals [1] from the total signal. Solvent terms can be extracted experimentally [84–87] or theoretically using radial distribution functions (RDFs) from molecular dynamics (MD) trajectories [86–91]. However, independent determination of the cross term is only possible theoretically [92, 93]. Despite the potential utility of MD, particularly with its potential to extract the cross term independently, there has been little investigation of the relative impact of force-field choice on theoretical scattering or assessment of relative accuracy. Recently, the Cole group have developed Quantum Bespoke Kit (QUBE) [4, 5], which utilises DFT calculation to derive force-field parameters, such that a bespoke force field could be created for any desired molecule without the need for experimental data. Moreover, QUBE is designed to use ω B97X-D [25] functionals. Four common solvents are studied (MeCN, DCM, EtOH, CHCl₃) to ascertain the solvent term (chapter 5) and cross term with a molecular iodine (I₂) solute (chapter 6) (I₂ parameterisation is kept the same for QUBE and all-atom Optimised Potentials for Liquid Simulations (OPLS-AA) solvents). MD trajectories were used to create the conditions before and after the hydrodynamic rearrangement of a pump-event. Solvent terms were also assessed relative to experimental solvent terms [1].

Recently many XFEL scattering studies have exploited the ultrafast visualisation provided to observe the excited-state dynamics of transition metal complexes undergoing metal-to-ligand charge transfer (MLCT) [82, 83, 94]. They have been subject of extensive research interest due to their luminescence following photonic or electronic excitation, which raises the possibility of using such compounds as OLEDs [3]. Of particular interest has been Cu(I) ions complexed with phenanthroline ligands, [Cu(phen)₂]⁺ [95–97], due to the relative abundance and lower cost of Cu relative to other transition metals. Experimental [98–104] and theoretical [3, 101, 104–109] approaches have

been taken to better understand the photophysics of copper phenanthroline. Excitation of the $[\text{Cu}(\text{phen})_2]^+$ leads to metal-to-ligand charge transfer to the S_1 state. The d^9 configuration of Cu(II) disfavours the tetrahedral ground-state geometry, and undergoes intersystem crossing (ISC) to the lowest-energy triplet excited state (T_1) via the pseudo Jahn-Teller effect, adopting near square-planar geometry. Emission lifetime is reduced by donating solvents such as MeCN [3, 110], illustrated visually by greater flattening of the dihedral angle between the phenanthroline ligands, indicating a smaller excited-ground energy gap. The Cu(II) is stabilised by the donating solvent, favouring non-radiative decay to the ground state. It is proposed that the solvent forms an exciplex with the Cu(II) ion [110] to stabilise it but there is currently insufficient consensus to explain the exact nature of the solute [3].

Chapter 2

Theory and Methodology

2.1 Introduction

This chapter introduces the key theoretical concepts underpinning the four investigations carried out in this work. Firstly it will focus on key quantum concepts, beginning with the Schrödinger equation [111] upon which fundamental quantum concepts are founded. This allows treatment of solving the Schrödinger equation in molecular systems, and the transition from Hartree-Fock (HF) to post-Hartree-Fock methods. Hartree-Fock will be treated first, with a logical progression into post-Hartree-Fock methods, in particular focusing upon the coupled-cluster (CC) method that forms the theoretical gold standard [8,9] in investigations pertaining to the electric field gradient (EFG) carried out in this work. However, the CC method is computationally expensive and unviable for large systems [14]. Then the alternative approach of calculation of ground-state energy via functionals of the electron density will be expanded upon. In particular the development of density functional theory (DFT). Furthermore theoretical scattering calculation from radial distributions is outlined, along with the methods of force-field derivation and molecular dynamics theory wherefrom they are calculated.

2.2 The Schrödinger Equation

The most fundamental equation in quantum mechanics is the equation of motion, the Schrödinger equation. It is analogous to the Newtonian equation of motion in classical mechanics [112]

$$\vec{F} = m\vec{a} = \frac{\partial \vec{V}}{\partial \vec{r}} \quad (2.2.1)$$

Here \vec{V} is the potential; \vec{r} the displacement; m represents mass with \vec{a} as acceleration and \vec{F} the resultant force. The theory was reformulated by Hamilton into a form purely considering the energetic contributions to the system:

$$H = T + V \quad (2.2.2)$$

With H representing the total energy of the system. T is the kinetic energy, as is often written as [112, 113]

$$T = \frac{\vec{p}^2}{2m} \quad (2.2.3)$$

And V is the potential energy contained within the system. However, unlike classical systems, the particle in a quantum system is considered to be a wave, with its wave function Ψ written as:

$$\Psi(r, t) = A \exp^{i(kr - \omega t)} \quad (2.2.4)$$

Here the A is a constant of wave amplitude, while ω and k are the wave angular frequency and wavenumber respectively. Ψ is a function of r and time, t . ω represents the increase in wave energy, E as governed by the Planck rule:

$$E = \hbar\omega \quad (2.2.5)$$

The Planck reduced constant for angular frequency, \hbar is the constant of proportionality. The wavenumber is defined as in terms of the inverse of the wavelength, λ :

$$k = \frac{2\pi}{\lambda} \quad (2.2.6)$$

It can be related to the momentum of any object with a wavelength via the de Broglie relation :

$$p = \hbar k \quad (2.2.7)$$

It is now possible to rewrite the term for T as:

$$T = \frac{\hbar^2 k^2}{2m} \quad (2.2.8)$$

Utilising the Hamiltonian, and multiplying through with the wavefunction yields:

$$H\Psi = T\Psi + V\Psi \quad (2.2.9)$$

Using the de Broglie equation and the wave equation:

$$T\Psi = \frac{\hbar^2 k^2}{2m}\Psi = \frac{-\hbar^2}{2m} \frac{\partial^2 \Psi(r, t)}{\partial r^2} \quad (2.2.10)$$

And in the same manner, combining the wave equation and Plack's equation one can write the general time-dependent Schrödinger equation (TDSE) [111–113]

$$H\Psi = \hbar\omega\Psi = i\hbar \frac{\partial \Psi(r, t)}{\partial t} \quad (2.2.11)$$

Thus combining to create an expression for the Schrödinger equation in position basis:

$$i\hbar \frac{\partial \Psi(r, t)}{\partial t} = \frac{-\hbar^2}{2m} \frac{\partial^2 \Psi(r, t)}{\partial r^2} + V(r, t)\Psi(r, t) \quad (2.2.12)$$

The probability $P(\vec{r}, t)$ of an electron's being in a specific region of space or time is yielded as the square of the wave function $\Psi(\vec{r}, t)$:

$$P(\vec{r}, t) = \Psi^* \Psi = \Psi^2(\vec{r}, t) \quad (2.2.13)$$

Where Ψ^* is the complex conjugate of the wavefunction. This can be considered analogous to the intensity of a wave at a given point. In the quantum realm, this lack of certainty about the exact state will lead to fundamental reformulation of how properties are calculated. The discretised states are reformulated into a n-dimensional vector in Hilbert space [113], represented as a ket in Dirac notation [14], $|\Psi\rangle$:

$$|\Psi\rangle = \begin{bmatrix} \Psi_1 \\ \Psi_2 \\ \vdots \\ \Psi_n \end{bmatrix} \quad (2.2.14)$$

With each component of the vector corresponding to a distinct state across the system. Each n^{th} -state of Ψ corresponds to:

$$|\Psi_n\rangle = c_n |\phi_n\rangle \quad (2.2.15)$$

Here c_n forms the probability density and ϕ_n the corresponding eigenstate. It is written such that $|c_n|^2$ corresponds to the probability of observing state ϕ_n . A bra serves as the complex conjugate in Dirac notation such that:

$$\langle \Psi | = \left[\Psi_1^* \quad \Psi_2^* \quad \dots \quad \Psi_n^* \right] \quad (2.2.16)$$

It is now that the notation for particular molecular properties, such as the energy must change. Instead of linear functions, operators must now be introduced. Operators are matrices which serve to transform the vector of discretised states such that normalisation yield an expectation value for the quantity that the operator represents, i.e. for a hypothetical quantity, A :

$$\langle \Psi | \hat{A} | \Psi \rangle = \langle A \rangle \quad (2.2.17)$$

The operator \hat{A} transforms the ket $|\Psi\rangle$ and then undergoes normalisation across all space, thus yielding the expectation value $\langle A \rangle$. Operators are the analogue of classical properties and it is therefore possible to rewrite the Hamiltonian as:

$$\hat{H} = \hat{T} + \hat{V} \quad (2.2.18)$$

As stated above the operators are matrices, they can only act in conjunction with the vector of discretised states. It is therefore useful to multiply through the equation using a ket of the wave function:

$$\hat{H} |\Psi\rangle = \hat{T} |\Psi\rangle + \hat{V} |\Psi\rangle \quad (2.2.19)$$

One can combine the Hamiltonian written in Dirac notation with the TDSE written in position basis to give:

$$i\hbar \frac{\partial}{\partial t} |\Psi\rangle = \frac{-\hbar^2}{2m} \frac{\partial^2}{\partial r^2} |\Psi\rangle + V(r, t) |\Psi\rangle \quad (2.2.20)$$

The operator for kinetic energy is thereby extracted as:

$$\hat{T} = \frac{-\hbar^2}{2m} \frac{\partial^2}{\partial r^2} \quad (2.2.21)$$

And in turn the momentum operator is:

$$\hat{p} = -i\hbar \frac{\partial}{\partial r} \quad (2.2.22)$$

Standing waves that have no time-dependent component of the wave function can also be considered, the crucial change being in the time-independent formulation of the Schrödinger equation (TISE):

$$\hat{H} |\Psi\rangle = E |\Psi\rangle \quad (2.2.23)$$

With E remaining constant with time. In turn:

$$\frac{-\hbar^2}{2m} \frac{\partial^2}{\partial r^2} |\Psi\rangle + V(r) |\Psi\rangle = E |\Psi\rangle \quad (2.2.24)$$

Indeed, the time-independent equation is useful for solving time-dependent systems, where the potential of a bound system remains constant, such that the TDSE can be rewritten:

$$\hat{H}(r)\Psi(r, t) = E(r)\Psi(r, t) = i\frac{\partial\Psi(r, t)}{\partial t} \quad (2.2.25)$$

And therefore the time-dependent element of Ψ is resolved as:

$$\Psi(r, t) = \Psi(r) \exp^{-iEt} \quad (2.2.26)$$

2.3 The Born-Oppenheimer Approximation

Now the focus shifts to account for the different contributions to the potential. The total Hamiltonian in a typical atom or molecule is composed as:

$$H = T_e + T_n + V_{ne} + V_{ee} + V_{nn} \quad (2.3.1)$$

Where V_{ne} is the nuclear-electronic interaction, V_{ee} the electron-electron interaction and V_{nn} the nuclear-nuclear interaction, and T_e and T_n the electronic and nuclear kinetic energies. The TDSE can now be recast to include the contribution of the nucleus:

$$\hat{H}(r, R)\Psi(r, R, t) = i\hbar\frac{\partial\Psi(r, R, t)}{\partial t} \quad (2.3.2)$$

Where R is the position vector of the nuclei. Note that the Hamiltonian assumes time-independent energy. The molecular Hamiltonian can be expressed as:

$$\hat{H}(r, R) = -\sum_i^N \frac{\hbar^2}{2M_{tot}} \nabla_i + \hat{H}_e(r, R) \quad (2.3.3)$$

M_{tot} is the total mass of the nuclei, and N the number of nuclei in the molecule. Indeed ∇ is simply:

$$\nabla = \left(\frac{\partial}{\partial x}, \frac{\partial}{\partial y}, \frac{\partial}{\partial z} \right) = \frac{\partial}{\partial r} \quad (2.3.4)$$

In cartesian coordinates. Note that \hat{H}_e is the electronic Hamiltonian, given as:

$$\hat{H}_e = T_e + V_{ee} + V_{ne} + V_{nn} = - \sum_k \frac{\hbar^2}{2} \nabla_k^2 + \sum_{k < l} \frac{1}{|r_k - r_l|} - \sum_{i,k} \frac{Z_i}{|R_i - r_k|} + \sum_{i < j} \frac{Z_i Z_j}{|R_i - R_j|} \quad (2.3.5)$$

The electronic Hamiltonian shows a parametric dependence on the nuclear coordinates but not nuclear momentum. The Born-Huang ansatz recasts the total wavefunction as [114,115]

$$\Psi_{tot}(r, R, t) = \sum_k \Omega_k(R, t) \Phi_k(r, R) \quad (2.3.6)$$

Here the total wavefunction of the atom/molecule is expanded in the complete set of electronic eigenfunctions, \hat{H}_e [115]. The expansion coefficients, $\Omega_i(R, t)$ are functions of the nuclear coordinates and time-dependent [115]. This is an exact solution for the total wave function. Reintroducing the Born-Huang ansatz into the TDSE and multiplying by the complex conjugate, Φ^* and integrating over over r :

$$i\hbar \frac{\partial}{\partial t} \Omega_k(R, t) = [- \sum_i \frac{\hbar^2}{2M_i} \nabla_i^2 + E_k^{el}(R)] \Omega_k(R, t) + \sum_i F_{kl}(R) \Omega_k(R, t) \quad (2.3.7)$$

The "off-diagonal" function F comprises the elements of the non-adiabatic coupling matrix [115,116]. The terms contained within it induce non-adiabatic coupling between different electronic states due to nuclear motion [115,116]. It is usually smaller than E_k^{el} by a factor comparable with the nuclear-electronic mass ratio [14]. It is this fact that allows the Born-Oppenheimer approximation to neglect all F terms [117,118], leaving the electronic energy to play the role of the potential energy [14]:

$$i\hbar \frac{\partial}{\partial t} \Omega_k(R, t) = [- \sum_i \frac{\hbar^2}{2M_i} \nabla_i^2 + E_k^{el}(R)] \Omega_k(R, t) \quad (2.3.8)$$

In the Born-Oppenheimer model, the nuclei move on a potential energy surface (PES) which is a solution to the electronic SE [115,116]. Solving for the nuclear wave function leads to discretised energy levels for molecular vibration and rotation, which have many uses, particularly in spectroscopy [14,119].

2.4 Hartree-Fock Theory

Having reduced the problem to consider the electronic potential only via the Born-Oppenheimer approximation, methods must be encountered to solve the electronic SE. Clearly, the SE can only be solved exactly for one-electron systems, so approximate methods will have to be introduced as a means to obtain physically-accurate answers [14]. Furthermore, spin will now have to be included as a quantum effect for many-electron systems [120]. Electron spins can take two states, $\frac{1}{2}$ and $-\frac{1}{2}$ corresponding to "spin-up" and "spin-down". They are respectively denoted as α and β , and follow the orthonormality associated with quantum states such that [113]

$$\langle \alpha | \alpha \rangle = \langle \beta | \beta \rangle = 1 \quad (2.4.1)$$

$$\langle \alpha | \beta \rangle = \langle \beta | \alpha \rangle = 0 \quad (2.4.2)$$

The variational principle states that any approximate wave function has energy above or equal to the exact energy. Clearly, the equality only holds if the wave function it is compared to is the exact function. By constructing a trial wave function using certain parameters, one can minimise the energy to generate a best-approximation of the actual wave function, following the variational principle's equality. The energy of an approximate wave function can be calculated as [14]

$$E_e = \frac{\langle \Psi | H_e | \Psi \rangle}{\langle \Psi | \Psi \rangle} \quad (2.4.3)$$

Where the numerator is the expectation value. For normalised wave functions, the expression simply becomes [121]

$$E_e = \langle \Psi | H_e | \Psi \rangle \quad (2.4.4)$$

The total electron wave function must be antisymmetric with respect to the interchange of any two electron coordinates such that for the total wave function of two particles x_1 and x_2 to reflect the Pauli exclusion principle for spin [120]:

$$\Psi(x_1, x_2) = -\Psi(x_2, x_1) \quad (2.4.5)$$

Simply multiplying the wave functions, otherwise known as the Hartree ansatz [121, 122], for the two wave functions does not satisfy this condition [123, 124]. This is overcome by taking a linear combination of Hartree

products [121]:

$$\Psi(x_1, x_2) = \frac{1}{\sqrt{2}}[x_1(x_1)x_2(x_2) - x_1(x_2)x_2(x_1)] \quad (2.4.6)$$

which can be rewritten as a Slater determinant [123]

$$\Psi(x_1, x_2) = \frac{1}{\sqrt{2}} \begin{vmatrix} x_1(x_1) & x_2(x_1) \\ x_1(x_2) & x_2(x_2) \end{vmatrix} \quad (2.4.7)$$

Generalising the Slater determinant for a N-particle system [121]

$$\Psi(x_1, x_2, \dots, x_N) = \frac{1}{\sqrt{N!}} \begin{vmatrix} x_1(x_1) & x_2(x_1) & \cdots & x_N(x_1) \\ x_1(x_2) & x_2(x_2) & \cdots & x_N(x_2) \\ \vdots & \vdots & \ddots & \vdots \\ x_1(x_N) & x_2(x_N) & \cdots & x_N(x_N) \end{vmatrix} \quad (2.4.8)$$

The Slater determinant thereby provides a candidate formalism to represent a many-particle wave function representing an atom or molecule. Now attention turns to writing an expression for the energy for such a system and determine its energy, in terms of the Slater determinant. The Hamiltonian can now be written as the following [14]:

$$\hat{H}_{el} = \sum_i \hat{h}_i + \sum_{i < j} \hat{v}(i, j) + \hat{V}_{nn} \quad (2.4.9)$$

The one-electron Hamiltonian is only dependent on one electron coordinate, i , and is defined as [121]:

$$\hat{h}_i = -\frac{1}{2}\nabla_i^2 - \sum_A^{N_{nuclei}} \frac{Z_A}{|R_A - r_i|} \quad (2.4.10)$$

Representing the electron kinetic energy and the potential from the nucleus. Z_A and R_A represent nuclear charge and position respectively. The two-electron potential is dependent on two electron coordinates and represents the electron-electron repulsion [121]

$$\hat{v}_{ij} = \frac{1}{|r_i - r_j|} \quad (2.4.11)$$

The nuclear repulsion operator, V_{nn} , is a constant [14, 121] owing to the Born-Oppenheimer approximation i.e.:

$$\langle \Psi | V_{nn} | \Psi \rangle = V_{nn} \langle \Psi | | \Psi \rangle = V_{nn} \quad (2.4.12)$$

That is, it can change the magnitude of the eigenvalues but plays no role in the eigenfunctions calculated. For the one-electron operator there is no electron-electron coupling so the operator is successfully diagonalised [14] such that:

$$\langle x_1(x_1) | \hat{h}_i | x_1(x_1) \rangle = h_i \quad (2.4.13)$$

Only the identity operator therefore contributes. However, the two-electron potential has two contributions, the first being from the identity operator:

$$\langle x_i(x_i)x_j(x_j) | v_{ij} | x_i(x_i)x_j(x_j) \rangle = J_{ij} \quad (2.4.14)$$

Here the matrix element J_{ij} represents the Coulomb repulsion created by the charge distributions described by the wave functions $x_i(x_i)$ and $x_j(x_j)$. However, the off-diagonal term must also be considered, written as:

$$\langle x_i(x_i)x_j(x_j) | v_{ij} | x_j(x_i)x_i(x_j) \rangle = K_{ij} \quad (2.4.15)$$

The term K_{ij} is the exchange term and falls out of the Pauli exclusion principle and is non-zero where two spin-orbitals have like spin, i.e. both spin-up ($+\frac{1}{2}$) or spin-down ($-\frac{1}{2}$). The total energy for a system can therefore be written:

$$E = \sum_i^{N_{elec}} h_i + \frac{1}{2} \sum_i^{N_{elec}} \sum_j^{N_{elec}} (J_{ij} - K_{ij}) + V_{nn} \quad (2.4.16)$$

It is multiplied by a factor $\frac{1}{2}$ to allow a double sum to run over all the electrons (clearly, electrons of unlike spin do not feel the exchange effect) as the self-interaction error of the Coulomb term, J_{ii} is cancelled out exactly by the corresponding exchange term, K_{ii} [125]. Under the variational principle, one must seek a minimum point in the energy of the theoretical system in order to approximate better the real system [112] however under the strict condition that all the orbitals remain orthogonal [14]. The variation of the energy,

δE , is given as [14, 121]

$$\begin{aligned} \delta E = & \sum_i^{N_{elec}} \langle \delta x_i | \hat{h}_i | x_i \rangle + \langle x_i | \hat{h}_i | \delta x_i \rangle \\ & + \frac{1}{2} \sum_{ij}^{N_{elec}} \langle \delta x_i | \hat{J}_j - \hat{K}_j | x_i \rangle + \langle x_i | \hat{J}_j - \hat{K}_j | \delta x_i \rangle + \langle \delta x_j | \hat{J}_i - \hat{K}_i | x_j \rangle + \langle x_j | \hat{J}_i - \hat{K}_i | \delta x_j \rangle \end{aligned} \quad (2.4.17)$$

Collecting terms, it is seen that the summations over i and j are the same such that identical terms can be collected and the problem reformulated in terms of i^{th} orbitals and j^{th} orbitals, with the factor of $\frac{1}{2}$ simply doubled to account for the replaced terms [14]

$$\delta E = \sum_i^{N_{elec}} \langle \delta x_i | \hat{h}_i | x_i \rangle + \langle x_i | \hat{h}_i | \delta x_i \rangle + \sum_{ij}^{N_{elec}} \langle \delta x_i | \hat{J}_j - \hat{K}_j | x_i \rangle + \langle x_i | \hat{J}_j - \hat{K}_j | \delta x_i \rangle \quad (2.4.18)$$

Defining the variation in terms of the Fock operator, \hat{F}_i :

$$\delta E = \sum_i^{N_{elec}} \langle \delta x_i | \hat{F}_i | x_i \rangle + \langle x_i | \hat{F}_i | \delta x_i \rangle \quad (2.4.19)$$

One can extract an expression for the Fock operator as:

$$\hat{F}_i = \hat{h}_i + \sum_j^{N_{elec}} (\hat{J}_j - \hat{K}_j) \quad (2.4.20)$$

Thereby the operator represents the electron's kinetic energy and nuclear attraction, and the repulsion caused by all other electrons on that particular electron [14]. Lagrangian multipliers, λ_{ij} , can be used to minimise the variation such that the Lagrangian [121], L is written:

$$\delta L = \delta E - \sum_{ij}^{N_{elec}} \lambda_{ij} (\langle \delta x_i | x_j \rangle - \langle x_i | \delta x_j \rangle) = 0 \quad (2.4.21)$$

Combining this relation with the definition for the Fock matrix yields:

$$\delta L = \sum_i^{N_{elec}} \langle \delta x_i | \hat{F}_i | x_i \rangle + \langle x_i | \hat{F}_i | \delta x_i \rangle - \sum_{ij}^{N_{elec}} \lambda_{ij} (\langle \delta x_i | x_j \rangle - \langle x_i | \delta x_j \rangle) \quad (2.4.22)$$

Using complex conjugates of the orbitals, this can be reformulated as [14,121]

$$\delta L = \sum_i^{N_{elec}} \langle \delta x_i | \hat{F}_i | x_i \rangle - \sum_{ij}^{N_{elec}} \lambda_{ij} (\langle \delta x_i | x_j \rangle + \sum_i^{N_{elec}} \langle \delta x_i | \hat{F}_i | x_i \rangle^* - \sum_{ij}^{N_{elec}} \lambda_{ij} (\langle \delta x_i | x_j \rangle^* = 0 \quad (2.4.23)$$

Both the original terms and the complex conjugates should cancel to leave zero [14]. Using the complex conjugate of the last two terms:

$$\sum_{ij}^{N_{elec}} (\lambda_{ij} - \lambda_{ji}^*) \langle \delta x_i | x_j \rangle = 0 \quad (2.4.24)$$

The Lagrangian multipliers can therefore be used to calculate elements of the Fock matrix:

$$\hat{F}_i x_i = \sum_j^{N_{elec}} \lambda_{ij} x_j \quad (2.4.25)$$

Which is the formalism of the Hartree-Fock equation. The molecular orbitals can be written as a linear combination of atomic orbitals (LCAO) [126–128]

$$x_i = \sum_{\alpha}^{N_{basis}} c_{\alpha i} \chi_{\alpha} \quad (2.4.26)$$

The coefficients $c_{\alpha i}$ represent the relative contributions of the atomic orbitals χ_{α} to the molecular orbital. In terms of the Fock matrix:

$$F_i \sum_{\alpha}^{N_{basis}} c_{\alpha i} \chi_{\alpha} = \epsilon_i \sum_{\alpha}^{N_{basis}} c_{\alpha i} \chi_{\alpha} \quad (2.4.27)$$

Where ϵ_i is the energy contribution of orbital i . The coefficients can be found by diagonalising the Fock matrix however the Fock matrix can only be known if all the molecular orbitals are known [14]. An initial ansatz of the coefficients is therefore taken, and used to calculate the elements of the Fock matrix, which is in turn diagonalised to calculate a new set of coefficients for the molecular orbitals. This is repeated until the coefficients entering the system equal those calculated by the system (to a given degree of accuracy) and this point of convergence is called a self-consistent field [14].

2.5 Coupled-Cluster Theory

Hartree-Fock captures around 99 percent of all the contributions to the energy of a molecular system but fails to capture the contribution of the electron-electron correlation to the electron-electron repulsion. Given that HF is so close to the full wave function, it is often taken as a starting point for electron correlation methods such that the wave function is written as:

$$\Psi = a_0 x_0 + \sum_{i=1} a_i x_i \quad (2.5.1)$$

Here $a_0 \Psi_0$ is the weighted contribution from the HF method and the sum represents a correlation correction to Hartree-Fock to capture the entire electron energy [14]. The correction takes into account all the possible excitations (relative to the ground-state HF system) present in the molecular system *ad infinitum*. Indeed, such a series, for an infinite basis set, would yield an exact result [14]. This, of course, would be extremely computationally expensive and beyond the capacity of the memory of most computers,. Approximations to the exact solution have to be made, a compromise between accuracy and computational cost, to give the correlation method utility in everyday computational science. Coupled-cluster theory is written such that an excitation operator T generate the excitation contributions out of the HF reference wave function, where the operator is written:

$$T = T_1 + T_2 + T_3 + \dots + T_{all} \quad (2.5.2)$$

T_1 is a singlet excitation operator, T_2 a doublet and so on such that the final term represents the excitation operator for a fully excited wave function, with no electrons remaining in the ground state. The singlet and doublet cluster operators correspond to:

$$T_1 x_0 = \sum_i^{N_o} \sum_a^{N_{vir}} t_i^a x_i^a \quad (2.5.3)$$

N_o is a sum across all occupied molecular orbitals and N_{vir} across all virtual orbitals, t_i^a is the annihilation operator to excite an electron from the i_{th} occupied orbital to the a_{th} unoccupied orbital. A coupled-cluster wave function utilises an exponential function of the cluster operator:

$$\Psi_{CC} = e^T x_0 \quad (2.5.4)$$

The exponential function can be expanded following the Taylor expansion [14]:

$$e^T = 1 + T + \frac{1}{2}T^2 + \frac{1}{6}T^3 + \dots + \sum_{k=0}^{\infty} \frac{1}{k!}T^k \quad (2.5.5)$$

Expanding in terms of component excitations of the T operator [14]:

$$e^T = 1 + T_1 + (T_2 + \frac{1}{2}T_1^2) + (T_3 + T_2T_1 + \frac{1}{6}T_1^3) + \dots \quad (2.5.6)$$

All the singlet, doublet, triplet excitations and so on have been grouped together for clarity. They fall into the category of "connected" or "true" excitations which are caused by the simultaneously interacting electrons [14] and those which are unconnected, that are produced from a combination of non-interacting excitations (i.e. a triplet created from three singlet excitations or a singlet and a doublet). The Schrödinger equation for Coupled-Cluster is written:

$$\hat{H}e^T x_0 = E_{CC}e^T x_0 \quad (2.5.7)$$

In reality the coupled-cluster formalism must be limited or *truncated* for the sake of computational efficiency. In the case of CCSD(T), the T operator is defined as:

$$T = T_1 + T_2 \quad (2.5.8)$$

It explicitly includes the singlet and doublet contributions. The triplet excitations are calculated as a perturbation added to the CCSD wave function from fourth-order Møller-Plesset (MP4) perturbation theory [129] and a singlet-triplet coupling term from MP5.

2.6 Density Functional Theory

The only issue with methods that add Slater determinants is the computational expense of obtaining meaningful results in realistic timescales. The computational expense of CCSD(T) scales with the number of molecular orbitals in the system to the power of seven. It is therefore necessary to seek other methods of obtaining meaningful information for chemical systems without such expense. The Hohenberg-Kohn (HK) theorems state that the electron energy can be elucidated solely by the electron density of a system, ρ . Wilson reasoned that the HK theorem was true owing to the integral of the density representing the number of electrons, the cusps in that density defining nuclear position, and the height of the cusps defining the nuclear

charge [14]. Such a simplification reduces the number of variables in the system studied from 4 variables per electron (three spatial coordinates and a spin coordinate) to simply four variables for an overall electron density. While the number of coordinates for a wave-function based system increases exponentially with the increase in occupied orbitals, the electron density remains dependent on four-coordinates, representing a huge computational advantage as system size increases [14]. The mathematics of Density Functional Theory (DFT) based on the HK theorems were then formalised by Kohn-Sham theory.

All density functional theories, as stated above, rest on the assumption that the ground-state energy can be calculated as functionals of the density, which in turn is a function of the position vector \vec{r} . It is formalised as:

$$E[\rho] = \langle \Psi[\rho] | \hat{H} | \Psi[\rho] \rangle \quad (2.6.1)$$

The total energy E can be written in terms of its respective contributions:

$$E[\rho] = T[\rho] + V_{ee}[\rho] + \int V_{ne}(\vec{r})\rho(\vec{r})d\vec{r}^3 \quad (2.6.2)$$

The kinetic energy functional, T , and electron-electron potential, V_{ee} , are universal, such that they can be applied to the density of any system. The only potential that changes is the electro-nuclear potential, V_{ne} which is system-specific (as it depends on the nuclear charge). The electron-electron potential is composed of contributions from the Coulomb potential, and exchange and correlation, which is conventionally written as a collective *exchange-correlation* term :

$$V_{ee}[\rho] = \int \int d\vec{r}^3 \frac{\rho(\vec{r})}{|\vec{r} - \vec{r}'|} + V_{xc}[\rho] \quad (2.6.3)$$

The exchange-correlation term is unknown, but if this term is found correctly, it could be applied universally. Kohn and Sham conjectured a theoretical system of non-interacting electrons, that could utilise the density functionals and mimic the properties of a "real" system of interacting electrons, by creating an effective potential, V_s :

$$\left(-\frac{1}{2} \frac{\hbar^2}{m} \nabla^2 + V_s(\vec{r})\right)\phi_i = E_i\phi_i \quad (2.6.4)$$

Here the non-interacting Kohn-Sham orbitals, ϕ_i mimic the behaviour of the

original multi-electron system but are treated as individual one-electron potentials acting under the influence of V_s :

$$V_s(\vec{r}) = \int V_{ne}(\vec{r})\rho(\vec{r})d\vec{r}^3 + \int \int d\vec{r}^3 \frac{\rho(\vec{r}')}{|\vec{r} - \vec{r}'|} + V_{xc}[\rho] \quad (2.6.5)$$

The KS orbitals allow for better representation of the kinetic energy and bonding in the molecule under study, which is why orbitals are reintroduced. Again the electron density is related to the KS orbitals [14]:

$$\rho = \sum_{i=1}^{N_{elec}} |\phi_i|^2 \quad (2.6.6)$$

Of course, bringing in orbitals does create a computational expense of three dimensional coordinates per electron, thus adding in some computational expense [14]. It is now paramount that a suitable approximation for the exchange-correlation functional be made such that density functional theory be brought within a comparable accuracy to post-Hartree-Fock methods. The exchange and correlation both reduce the probability of finding an electron close to another, leading to a *probability hole*. That is that the probabilities are not independent [14]:

$$\rho_j(\vec{r}_i, \vec{r}_j) = \rho_i(\vec{r}_i)\rho_j(\vec{r}_j) + \rho_i(\vec{r}_i)h_{xc}(\vec{r}_i, \vec{r}_j) \quad (2.6.7)$$

Where h is a conditional probability factor, making h the subject of the equation gives:

$$h_{xc}(\vec{r}_i, \vec{r}_j) = \frac{\rho_j(\vec{r}_i, \vec{r}_j)}{\rho_i(\vec{r}_i)} - \rho_j(\vec{r}_j) \quad (2.6.8)$$

This illustrates the nature of the density dependence of the exchange-correlation effects. The exchange and correlation functionals are generalised across the electron density as:

$$E_{xc}[\rho] = \int \rho(\vec{r})\epsilon_x[\rho(\vec{r})]d\vec{r} + \int \rho(\vec{r})\epsilon_c[\rho(\vec{r})]d\vec{r} \quad (2.6.9)$$

ϵ_x and ϵ_c are the exchange and correlation energy densities respectively. The local density approximation (LDA) is the first attempt at approximating the E_{xc} functional and assumes a slowly-varying density that can be considered locally uniform [14]. The exchange is given by the Dirac formula for uniform electron gases :

$$E_x^{LDA}[\rho] = -C_x \int \rho^{\frac{4}{3}}(\vec{r})d\vec{r} \quad (2.6.10)$$

The correlation energy for uniform electron gases can be expressed explicitly in the high- and low-density regimes [14]. The formulations can take interpolation factors to express correlation in intermediate-density spaces, with different formulations proposed, such as Vosko-Wilk-Nusair (ϵ_C^{VWN}) [130] and Perdew-Wang (ϵ_C^{PW}) [131].

Indeed, most systems will not have completely invariant density. It is therefore beneficial for the exchange-correlation to include terms that depend on the change in density. This brings about the next rung of Jacob's Ladder, the Generalised Gradient Approximation (GGA) [16–18]. The most widespread exchange GGA functional is Becke's 1988 exchange correction. Its formalism is expressed as [132]:

$$\epsilon_x^{B88} = \epsilon_x^{LDA} + \Delta\epsilon_x^{B88} \quad (2.6.11)$$

The $\Delta\epsilon_x^{B88}$ correction is defined as:

$$\Delta\epsilon_x^{B88} = \beta\rho^{\frac{1}{3}} \frac{x^2}{1 + 6\beta x \sinh^{-1}x} \quad (2.6.12)$$

The factor, x , is an enhancement factor:

$$x = \frac{\nabla\rho}{\rho^{\frac{4}{3}}} \quad (2.6.13)$$

This is characteristic of GGA functionals to include enhancement factors and other terms dependent on the spatial derivative of the density. Correlation terms also include enhancement factors, such as the Lee-Yang-Parr (LYP) correction [41]. All GGA exchange-correlation functionals can be surmised as:

$$\epsilon_{xc}^{GGA} = \epsilon_{xc}[\rho, \nabla\rho] \quad (2.6.14)$$

The next logical step is to create functionals with enhancement factors depending on higher-order derivatives of the density. The second-order derivative is included in the third rung of Jacob's Ladder, meta-GGA (mGGA) [16]. An alternative approach is to indirectly depend on the second-order density derivatives via the KS-orbital kinetic energy [16]. Both methods carry the same information, and are related via the relation for kinetic energy density τ [14]:

$$\tau(\vec{r}) = \frac{1}{2} \sum_i \epsilon_i |\Psi_i(\vec{r})|^2 - V_{eff}(\vec{r})\rho(\vec{r}) + \frac{1}{2} \nabla^2 \rho(\vec{r}) \quad (2.6.15)$$

This allows flexibility with the applied variable. Indeed it is often more numerically stable to calculate the orbital kinetic energy density as opposed as the second-order density derivative, such that the kinetic energy density is often the chosen variable [14]. Meta-GGA functionals can be surmised as:

$$\epsilon_{xc}^{mGGA} = \epsilon_{xc}[\rho, \nabla^2 \rho] \quad (2.6.16)$$

$$\epsilon_{xc}^{mGGA} = \epsilon_{xc}[\rho, \tau] \quad (2.6.17)$$

Examples of well-known meta-GGA functionals include the Tao-Perdew-Staroverov-Scuseria (TPSS) family [55] and Minnesota 2006 family [47–49].

In order to further the accuracy of the density functionals, attention turns to taking advantage of other methods to determine improved exchange-correlation functionals, in combination with GGA or mGGA methods. The fourth rung of Jacob's Ladder incorporates HF exchange with that of DFT methodology, creating *hybrid* functionals (hGGA). Indeed, if it were HF orbitals that were used, the exchange would be exact [14]. With respect to KS orbitals, this cannot be guaranteed. The approach is to weight the respective exchange contributions calculated from HF and DFT methods. A popular example of hGGA functionals is B3LYP [21, 39]:

$$E_{xc}^{B3LYP} = (1 - a)E_x^{LSDA} + aE_x^{HF} + \Delta E_x^{B88} + (1 - c)E_c^{LSDA} + cE_c^{LYP} \quad (2.6.18)$$

Which includes Becke's 1988 exchange correction and LYP correlation. The constants a, b and c are calculated via fitting to established experimental data. Indeed, both exchange and correlation are balanced between two different methods. Other hybrid methods add further contributions from other DFT methods and weight them accordingly, such as B97 [40]. These are calculated across the occupied KS orbitals.

The next logical step is to include calculation across the non-occupied KS orbitals, and bring in a orbital-based method for the correlation energy, in this case second-order Møller-Plesset perturbation theory (MP2) as Hartree-Fock cannot calculate correlation. As both exchange and correlation are taking meaningful contributions from the wave-function-based methods, this method is named *double hybrids* (dhGGA). A typical formulation is given as [22–24]:

$$E_{xc}^{dhGGA} = (1 - a)E_x^{DFT} + aE_x^{HF} + (1 - b)E_c^{DFT} + bE_c^{MP2} \quad (2.6.19)$$

The MP2 term would predict correlation for "real" systems [14] but like HF,

cannot be guaranteed to do so in theoretical KS orbitals. However, MP2 entails computational cost that scales with the number of KS orbitals to the power of 5. Indeed, more expensive computational methods (MP3, MP4, CCSD(T)) have yielded little improvement, making MP2 the established staple [24].

The next rung, considered highest in Jacob’s Ladder, is range-separated hybrids (rshGGA). This interpolates between the DFT-derived and Hartree-Fock-derived exchange in the short- and long-range \vec{r} [25,26]:

$$\frac{1}{|\vec{r}_1 - \vec{r}_2|} = \frac{1 - \text{erf}(\omega r_{12})}{r_{12}} + \frac{\text{erf}(\omega r_{12})}{r_{12}} \quad (2.6.20)$$

ω determines the rate of interpolation between DFT-defined and HF-defined exchange regions [26]. The advantage of such a bespoke control over the fraction of HF exchange is that it can be used to minimise the self-interaction error that arises from incomplete cancellation of exchange and Coulomb interaction from the density of a single electron that plagues DFT-derived exchange terms, which adversely affects loosely-bound, valent electrons that undergo interaction with other electrons in the long-range domain [133]. In the worst case this can lead to the valence electron’s self-interaction error exceeding the binding energy within the atom/molecule, thus incorrectly predicting an unbound electron [133]. Using HF in the long-range domain reduces DFT overdelocalization of charge and thus improves the excitation energies for charge-transfer states [134]. This makes it useful for time-dependent DFT (TDDFT) as well. This thereby completes the rungs of Jacob’s Ladder as of current research.

2.7 Electric Field Gradient

The theoretical methods, be they *ab initio* or DFT, are aimed at capturing the electron density present around an atom or molecule. However, the theoretical densities can only be compared to each other. Indeed, the electron density is usually measured against computationally-expensive methods such as CCSD or CCSD(T) [27, 28, 30]. Other metrics such as bond lengths [135] and energetic properties such as ionisation or atomisation [30] also compare predominantly with CCSD(T). A means to compare the density with experimental results is via the electric field gradient (EFG) [35]. It is defined as the rate of change of electric field strength relative to the nucleus. The field

gradient q of field E can be defined as [136]:

$$q = \nabla E = \nabla^2 V \quad (2.7.1)$$

Such that the EFG is the Laplacian of the electrostatic potential, V . The EFG can be observed if it interacts with a nuclear quadrupole that has formed [35]. Such disparities in the charge distribution can only be the result of combinations of atomic orbitals with orbital angular momentum components that do not possess spherical symmetry, such as p-orbitals and d-orbitals. Furthermore, the uneven charge distribution can only occur if a p- or d-shell is incomplete, such that the charge imbalance caused by the occupied orbitals is not offset by imbalances in other directions to make a net field change of zero. Given that such phenomena in the ground state only occur for valence electron shells, this makes the EFG an excellent probe of chemically-relevant electron density. The electric field gradient can be measured using a variety of experimental spectroscopic methods, including nuclear magnetic resonance (NMR), electron paramagnetic resonance (EPR), nuclear quadrupole resonance (NQR), Mössbauer spectroscopy and rotational microwave spectroscopy. Such a variety of techniques provides a basis to compare the relative success of theoretical methods in capturing the chemically-relevant electron density relative to experimental metrics, which forms the basis of chapters 3 and 4. The experimental technique used in this investigation is microwave spectroscopy. This technique is used to elucidate the nuclear quadrupole moment (NQM), Q . [35]. Its advantage over NQR and Mössbauer spectroscopy is its ability to be used in the gas phase instead of restriction to the solid state, and requires less energy to perform than EPR. In rotational microwave spectroscopy, the nuclear spin couples with rotational angular momentum, which is observed as hyperfine splitting of the rotational energy levels on the microwave spectra. The energies of the resultant sub-levels are proportional to the magnitude of the NQM. The NQM can in turn be converted to the EFG via the nuclear quadrupole coupling constant (NQCC) C_q :

$$q = \frac{C_q \hbar}{e^2 Q} \quad (2.7.2)$$

It is possible to use established nuclear quadrupole moments [137] and nuclear quadrupole coupling constants calculated from microwave spectroscopy [57–59, 63, 138–140] to calculate experimental EFGs to compare to those calculated theoretically from the electron density distribution via DFT or wavefunction-based methods.

2.8 X-ray Scattering

The EFG is one way of experimentally elucidating the electron density experimentally, such that theoretical comparison can be made. Another method that can be used to infer electron density is X-ray scattering. Indeed, the predominant usage of X-ray scattering is to determine the structure of molecules and observe chemical dynamics [72,141]. The scattering intensity, S , is a function of the scattering vector, \vec{q} , which is defined as:

$$\vec{q} = \vec{k} - \vec{k}_0 \quad (2.8.1)$$

That is, the difference between the incident wave vector \vec{k}_0 and the scattered wave vector, \vec{k} . It is particularly useful in defining the momentum transfer resulting from the scattering event, i.e.:

$$\Delta\vec{p} = \hbar\vec{k} - \hbar\vec{k}_0 = \hbar\vec{q} \quad (2.8.2)$$

The magnitude of the scattering vector in an idealised elastic scattering system (no energy transfer, no change in momentum magnitude) is given as [72,142]

$$q = \frac{4\pi}{\lambda} \sin\theta \quad (2.8.3)$$

θ is half the scattering angle and λ the wavelength of the x-rays. Indeed, in a system with no change in wavelength, \vec{q} is simply proportional to the sin of the angle of deflection. The wave, ψ , scattered in the direction of \vec{r} , is defined as [142]

$$\psi = \psi_0 F(\lambda, \theta) \frac{e^{ikr}}{r} \quad (2.8.4)$$

Here f is the scattering factor [72,142,143] that determines the probability of deflection through angle 2θ at wavelength λ . This is an effective dependency on q . The molecular form factor is determined as a Fourier transform of the electron density ρ_e [143] about:

$$F(\vec{r}, \vec{q}) = \int_V \rho_e(\vec{r}; \vec{R}) e^{i\vec{q}\cdot\vec{r}} d\vec{r} \quad (2.8.5)$$

Here R is the nuclear coordinates that the electron density is centered upon. Recent studies have indicated that the electron density in the chemical bonding plays little role in scattering [77]. This allows the molecular form factor to be decomposed into individual atomic contributions (f_j), otherwise known

as the independent atom model (IAM):

$$F(\vec{R}, \vec{q}) = F_{IAM}(\vec{R}, \vec{q}) = \sum_j^N f_j(q) e^{i\vec{q} \cdot \vec{r}} \quad (2.8.6)$$

The scattered wave amplitude A can be expressed as [72]

$$A(\vec{q}) = \int \rho_e(r; R) e^{-i\vec{q} \cdot \vec{r}} d\vec{r} \quad (2.8.7)$$

However, only the scattered intensity S is detectable experimentally [72,143]. where:

$$S(\vec{q}) = |A(\vec{q})|^2 = \left| \int \rho_e(r; R) e^{-i\vec{q} \cdot \vec{r}} d\vec{r} \right|^2 \quad (2.8.8)$$

It is more convenient to parameterise in terms of atomic coordinates, creating a superposition of electron densities localised about the atomic centres [72]

$$\rho_e(\vec{r}) = \sum_j p_j(\vec{r} - \vec{R}_j) \quad (2.8.9)$$

Such that the scattering amplitude can be rewritten [72]:

$$A(\vec{q}) = \sum_j f_j(\vec{q}) e^{-i\vec{q} \cdot \vec{R}_j} \quad (2.8.10)$$

In turn, S is written for an N-atom system as [72,143]:

$$S(\vec{q}) = \int_{V^N} \rho_N(\vec{R}) \sum_j \sum_k f_j(q) f_k(q) e^{-i\vec{q} \cdot (\vec{R}_j - \vec{R}_k)} d^N \vec{R} \quad (2.8.11)$$

Where ρ_N is the average nuclear probability distribution. Taking the cases where $j=k$ and $j \neq k$ [143]

$$S(\vec{q}) = \int_{V^N} \rho_N(\vec{R}) \left(\sum_j f_j(q)^2 + \sum_j \sum_{k \neq j} f_j(q) f_k(q) e^{-i\vec{q} \cdot (\vec{R}_j - \vec{R}_k)} \right) d^N \vec{R} \quad (2.8.12)$$

Integrating out all other dependencies other \vec{R}_j and \vec{R}_k and defining new variables $\vec{R}_{jk} = \vec{R}_j - \vec{R}_k$ and $\vec{R}'_{jk} = \frac{\vec{R}_j + \vec{R}_k}{2}$ [143], and also noting that integrating the first part $\sum_j f_j(q)^2$ is simply equal to $\sum_j f_j(q)^2$:

$$\begin{aligned} S(\vec{q}) &= \sum_j f_j(q)^2 + \sum_j \sum_{k \neq j} f_j(q) f_k(q) \int_{V^2} \rho_{jk}(\vec{R}_{jk}, \vec{R}'_{jk}) e^{-i\vec{q} \cdot \vec{R}_{jk}} d\vec{R}_{jk} d\vec{R}'_{jk} \\ &= \sum_j f_j(q)^2 + \sum_j \sum_{k \neq j} f_j(q) f_k(q) \int_V \rho_{jk}(\vec{R}_{jk}) e^{-i\vec{q} \cdot \vec{R}_{jk}} d\vec{R}_{jk} \end{aligned} \quad (2.8.13)$$

To further the calculation, it is now assumed that:

$$\rho_{jk}(\vec{R}_{jk}) = \rho_{jk}(R_{jk}) \quad (2.8.14)$$

This is the isotropic assumption, such that there is equal probability of finding the molecule in any orientation [143]. Applying the isotropic assumption to the exponential [72] such that $S(\vec{q})$ is averaged into $S(q)$ [72, 143]:

$$S(q) = \sum_j f_j(q)^2 + \sum_j \sum_{k \neq j} f_j(q) f_k(q) 4\pi \times \int_0^{R_{max}} \rho_{jk}(R_{jk}) \frac{\sin(qR_{jk})}{qR_{jk}} R_{jk}^2 dR_{jk} \quad (2.8.15)$$

Here j and k run across all atom pairs in the system. However, this leaves a risk of double-counting atom pairs [143]. Furthermore, it is useful to distinguish atoms into respective types, as they will share the same form factor in the IAM. Taking hypothetical atom types l and m , with N atoms of each respective type, they are related via [143]:

$$\rho_{lm}(R_{jk}) = \frac{1}{N_l(N_m - \delta_{lm})} \sum_{j \in l} \sum_{k \in m} \rho_{jk}(R_{jk}) \quad (2.8.16)$$

Rearranging and substituting back into the equation for S [143]:

$$S(q) = \sum_l N_l f_l(q) + \sum_{l,m} f_l(q) f_m(q) N_l(N_m - \delta_{l,m}) 4\pi \times \int_0^{R_{max}} \rho_{lm}(R_{jk}) \frac{\sin(qR_{jk})}{qR_{jk}} R_{jk}^2 dR_{jk} \quad (2.8.17)$$

In order to make use of theory, it is useful to bring in the pairwise radial distribution function, g_{lm} that can be extracted from MM simulation boxes [72, 143]. Defining $g_{l,m}$ via the probability density ratio:

$$g_{lm}(R_{jk}) = \frac{\rho_{lm}(R_{jk})}{\rho_{0,lm}} \quad (2.8.18)$$

With the $\rho_{0,lm}$ serving as the isotropic probability density:

$$\rho_{0,lm} = \frac{1}{V} \quad (2.8.19)$$

Hence for RDFs containing solvent atom types, as $R_{jk} \rightarrow \infty$, $g_{lm}(R_{jk}) \rightarrow 1$. That is, the distribution tends towards isotropy as R_{jk} increases. The only exceptions are RDFs involving exclusively solute molecules, in such case as $R_{jk} \rightarrow \infty$, $g_{lm}(R_{jk}) \rightarrow 0$. Rearranging the above relations and rewriting S in terms of $g_{lm}(R_{jk})$:

$$S(q) = \sum_l N_l f_l(q)^2 + \sum_{l,m} f_l(q) f_m(q) \frac{N_l(N_m - \delta_{lm})}{V} 4\pi \times \int_0^{R_{max}} R_{jk}^2 g_{lm}(R_{jk}) \frac{\sin(qR_{jk})}{qR_{jk}} R_{jk}^2 dR_{jk} \quad (2.8.20)$$

For mathematical convenience, the RDF is redefined as:

$$g_{lm}(R_{jk}) = g_{lm}(R_{jk}) - g_{0,lm} + g_{0,lm} \quad (2.8.21)$$

Here, $g_{0,lm}$ is the long-distance, constant radial distribution [143]. Inserting into the equation for S :

$$\begin{aligned} S(q) &= \sum_l N_l f_l(q)^2 \\ &+ \sum_{l,m} f_l(q) f_m(q) \frac{N_l(N_m - \delta_{lm})}{V} 4\pi \times \left(\int_0^{R_{max}} R_{jk}^2 (g_{lm} - g_{0,lm})(R_{jk}) \frac{\sin(qR_{jk})}{qR_{jk}} R_{jk}^2 dR_{jk} \right. \\ &+ \left. g_{0,lm} \int_0^{R_{max}} R_{jk}^2 \frac{\sin(qR_{jk})}{qR_{jk}} R_{jk}^2 dR_{jk} \right) \end{aligned} \quad (2.8.22)$$

The last integral is assumed to only contribute as $q \rightarrow 0$ [143] and is therefore excluded in most instances. This leaves:

$$\begin{aligned} S(q) &= \sum_l N_l f_l(q)^2 \\ &+ \sum_{l,m} f_l(q) f_m(q) \frac{N_l(N_m - \delta_{lm})}{V} 4\pi \times \int_0^{R_{max}} R_{jk}^2 (g_{lm} - g_{0,lm})(R_{jk}) \frac{\sin(qR_{jk})}{qR_{jk}} R_{jk}^2 dR_{jk} \end{aligned} \quad (2.8.23)$$

As stated above, for for RDFs containing solvent atom types, as $R_{jk} \rightarrow \infty$, $g_{lm}(R_{jk}) \rightarrow 1$ such that $g_{0,lm}$ can be rewritten as 1 [72, 143]:

$$S_{solvent}(q) = \sum_l N_l f_l(q)^2 + \sum_{l,m} f_l(q) f_m(q) \frac{N_l(N_m - \delta_{lm})}{V} 4\pi \times \int_0^{R_{max}} R_{jk}^2 (g_{lm} - 1)(R_{jk}) \frac{\sin(qR_{jk})}{qR_{jk}} R_{jk}^2 dR_{jk} \quad (2.8.24)$$

$$S_{cross}(q) = \sum_l N_l f_l(q)^2 + \sum_{l,m} f_l(q) f_m(q) \frac{N_l(N_m - \delta_{lm})}{V} 4\pi \times \int_0^{R_{max}} R_{jk}^2 (g_{lm} - 1)(R_{jk}) \frac{\sin(qR_{jk})}{qR_{jk}} R_{jk}^2 dR_{jk} \quad (2.8.25)$$

Here $S_{solvent}(q)$ and $S_{cross}(q)$ are the contributions from solvent scattering and solvent-solute interface to the scattering signal respectively. Likewise for solute-exclusive atom pairs, $g_{lm}(R_{jk}) \rightarrow 0$ so this term simply vanishes [143]:

$$S_{solute}(q) = \sum_l N_l f_l(q)^2 + \sum_{l,m} f_l(q) f_m(q) \frac{N_l(N_m - \delta_{lm})}{V} 4\pi \times \int_0^{R_{max}} R_{jk}^2 g_{lm}(R_{jk}) \frac{\sin(qR_{jk})}{qR_{jk}} R_{jk}^2 dR_{jk} \quad (2.8.26)$$

$S_{solute}(q)$ is the contribution from the solute to the scattering signal. Of course, most experimental X-ray scattering involves a pump laser pulse which provides the initial energy to initiate the dynamics of a solution, in particular with regard to photoinduction of chemical reactions [1, 72, 143]. The scattering change between the 'pumped' sample and the initial 'unpumped' sample is taken to identify the change in molecular structure observed in the solution [1, 72, 143], defined as:

$$\Delta S(q) = S_{on}(q) - S_{off}(q) \quad (2.8.27)$$

Here "on" and "off" correspond to the pumped and unpumped sample [143]. Likewise, the change in the RDF due to the solution rearrangement is written [143]:

$$\Delta g_{lm}(R_{jk}) = g_{lm,on}(R_{jk}) - g_{lm,off}(R_{jk}) \quad (2.8.28)$$

Such that the change in signal can be signal can be rewritten [143]:

$$\begin{aligned} \Delta S(q) = & \sum_l N_l f_l(q)^2 \\ & + \sum_{l,m} f_l(q) f_m(q) \frac{N_l(N_m - \delta_{lm})}{V} 4\pi \times \int_0^{R_{max}} R_{jk}^2 \Delta g_{lm}(R_{jk}) \frac{\sin(qR_{jk})}{qR_{jk}} R_{jk}^2 dR_{jk} \end{aligned} \quad (2.8.29)$$

Which can apply individually to all three contributions to the scattering. This allows the use of simulation boxes to capture the change in scattering via the change in rdf due to a change in hydrodynamic parameters i.e. temperature or pressure increase [1, 143]. Such simulation boxes can be created and their dynamics simulated via molecular mechanics (MM) software, in this case using ultrafast timescales to simulate ultrafast X-ray scattering events.

2.9 Force-Field Methods

In order to create realistic simulations of the molecular mechanics of solutions on ultrafast timescales, it is crucial to have accurate force-field parameterisation. Indeed, it is the impact of different force-field parameterisation methods on predicting X-ray scattering that is at the centre of the scattering-centric chapters of this work. All force fields seek to describe the intramolecular and intermolecular potentials a molecule possesses, to explain its conformation and intermolecular interactions respectively. The force-field energy, E_{FF} , can be written as composed of the following components [14]:

$$E_{FF} = E_{str} + E_{bend} + E_{tors} + E_{cross} + E_{el} + E_{vdw} \quad (2.9.1)$$

E_{str} is the energy to stretch a bond, E_{bend} is energy to bend a bond angle formed by three atoms, E_{tors} the torsional energy to rotate around a bond, and E_{cross} the coupling between the stretch, bending and torsional energies [14]. The other two represent the non-bonded parameters, E_{el} represents the electrostatic potential caused by the uneven distribution of charge around the molecule (forming a dipole moment or areas of partial charge) [14]. E_{vdw} represents the Van der Waals forces, which takes into account all other intermolecular forces, such as polarisation (from the induction of dipoles from permanent dipoles) and dispersion (interaction of instantaneous dipoles) [144].

The stretch energy is approximated as a simple harmonic motion (SHM) about an equilibrium length R_0 [14]:

$$E_{Str}(R - R_0) = k_{str}(R - R_0)^2 = k_{str}(\Delta R)^2 \quad (2.9.2)$$

k_{str} is the constant analogous to a spring constant. Similarly the bending energy can be defined about an equilibrium angle Θ_0 :

$$E_{bend}(\Theta - \Theta_0) = k_{bend}(\Theta - \Theta_0)^2 = k_{bend}(\Delta\Theta)^2 \quad (2.9.3)$$

However, torsion does not mimic the SHM-like form of the other terms. It is formed by a combination of four atoms A-B-C-D. The angle is defined by that subtended by the planes A-B-C and B-C-D [14]. Torsion terms are written in a Fourier series of weighted contributions [14]:

$$E_{tors}(\omega) = \sum_n V_n \cos(n\omega) \quad (2.9.4)$$

Which encompasses potential barriers V_n associated with varying periodicity [14]. The torsion is further distinguished from the stretch and bend energy as the potential barrier to rotation is influenced by the non-bonded contributions to the force field.

Cross terms illustrate the interrelated nature of the bonded terms. For example, compression or widening of the equilibrium angle in turn changes the equilibrium length of the bonds. Indeed the stretch/bend term tends to be the most significant cross term, which for atom combination A-B-C is written:

$$E_{str/bend} = k_{str/bend}^{ABC} (\Theta^{ABC} - \Theta_0^{ABC}) [(R^{AB} - R_0^{AB}) - (R^{BC} - R_0^{BC})] \quad (2.9.5)$$

$k_{str/bend}$ is the coupling constant between the stretch and bend parameters. Likewise similar coupling constants can be used to express the relationship between stretch/torsion and bend/torsion:

$$\begin{aligned} E_{str/tors} &= k_{str/tors}^{ABCD} (R^{AB} - R_0^{AB}) \cos(n\omega^{ABCD}) \\ E_{bend/tors} &= k_{str/tors}^{ABCD} (\Theta^{ABC} - \Theta_0^{ABC}) \cos(n\omega^{ABCD}) \end{aligned} \quad (2.9.6)$$

Coupling constants can also be used to express the influence of a bond stretch on another, i.e. the influence of bond A-B on the bond B-C and in the same manner the influence of one bond angle bend or torsion on another. An

example of a stretch/stretch coupling is written:

$$E_{str/str} = k_{str/str}^{ABC} (R^{AB} - R_0^{AB})(R^{BC} - R_0^{BC}) \quad (2.9.7)$$

With bend/bend and torsion/torsion couplings following analogous forms. It is also possible to have three-way couplings, for example stretch/torsion/bend or bend/torsion/bend.

The Van der Waals interaction takes into account multiple forms of interaction between charge distributions. It is repulsive at short distance owing to electron cloud overlap, leading to both classical and Fermi repulsion [14], which has a proportionality of R^{-12} . However, at intermediate distances it is (slightly) attractive owing to instantaneous formation of dipoles as the electrons move around the nucleus, which in turn can polarise other molecules, leading to interaction [14]. The induced interaction is proportional to R^{-6} , where R is the interatomic/intermolecular distance [14]. Dispersion takes into account multipole interactions, which can be proportional to increased negative powers of R , such as R^{-8} , R^{-10} etc. [14]. The Lennard-Jones potential is often used to model the Van der Waals forces [4, 14, 145]:

$$E_{LJ}(R) = 4\epsilon \left[\left(\frac{\sigma}{R} \right)^{12} - \left(\frac{\sigma}{R} \right)^6 \right] \quad (2.9.8)$$

σ and ϵ are constants to be determined for the elements involved in the simulation, and are specified as non-bonded parameters.

Now attention turns to E_{el} . This encompasses the interaction of dipoles in the system under consideration [4, 14]. The permanent dipoles are caused by an uneven distribution of electronic charge across the molecule and are called "partial charges" q [4]. Their behaviour is governed by electrostatics:

$$E_{el}(R) = \frac{q_1 q_2}{\epsilon R} \quad (2.9.9)$$

Here ϵ represents the dielectric constant in the space between the two partial charges. After collecting the bonded and non-bonded terms, it is seen that there are several constants that need to be determined. One of the most long-standing force fields is the Optimised Potentials for Liquid Simulations (OPLS) force field developed by the Jorgensen group [146]. Its bonded parameters largely follow those laid out for a standard force field. The only

Force-Field Term	Constants
E_{str}	k_{str}, R_0
E_{bend}	k_{bend}, Θ_0
E_{tors}	V_n
E_{cross}	$k_{str/bend}, k_{str/tors}, k_{bend/tors} + \text{various coupling constants}$
E_{vdw}	ϵ, σ
E_{el}	q

Table 2.9.1: Table of assorted constants associated with the parameterisation of a force field

slight exception being the torsional energy, which is written:

$$E_{tors} = \sum \left(\frac{V_1}{2} [1 + \cos(\phi - \phi_1)] + \frac{V_2}{2} [1 - \cos(2\phi - \phi_2)] + \frac{V_3}{2} [1 + \cos(3\phi - \phi_3)] + \frac{V_4}{2} [1 - \cos(4\phi - \phi_4)] \right) \quad (2.9.10)$$

The other distinct quality is the consideration of the nonbonded parameters [147]. For atoms i and j , it combines E_{el} and E_{vdw} into:

$$E_{non-bonded} = \sum_{i>j} f_{ij} \left(4\epsilon \left[\left(\frac{\sigma_{ij}}{R_{ij}} \right)^{12} - \left(\frac{\sigma_{ij}}{R_{ij}} \right)^6 \right] + \frac{q_i q_j}{\epsilon R_{ij}} \right) \quad (2.9.11)$$

The factor f_{ij} is the "fudge factor", which only plays a role for atoms three or more bonds apart, where it changes from a nominal value of 1 to 0.5 [147]. The version of OPLS used here is OPLS-AA, denoting that all atoms are explicitly parameterised, as opposed to the OPLS-UA (united atom) force field, where hydrogen atoms are included implicitly as corrections to the carbon parameters [148]. OPLS is distinguished as a system that utilises liquid experimental data, such as densities and heat of vapourisation, for parameterisation [148].

However, other parameterisation methods seek to utilise theoretical methodology to parameterise. The Quantum Mechanical Bespoke force field, better known as QUBE, is oriented at calculating parameters (via QUBEKit) from a theoretical standpoint and reducing dependency on finding experimental parameters [5]. It ties together multiple forms of theoretical software to derive parameters. With respect to the bonded parameters, they are derived from the Seminario method [5, 149]. It maps the forces felt by an atom due to the displacement of a neighboring one onto their mutual bond vector to calculate bonded constants [5, 149]. The method is vulnerable to double-counting of angle parameter in larger molecules [5, 150]. This is due to the angle formed by one particular set of atoms changing the angle for another

set with atoms in common. This can be modified to compensate for the chemical environment and rescale the angle spring constant to make sure it isn't artificially too stiff [150].

QUBE also has theoretical treatment for non-bonded parameters. It utilises atoms-in-molecule (AIM) analysis to calculate partial charge for the constituent atoms of a molecule [4,5]. The total electron density from QM calculation, $n(\vec{r})$, is partitioned into atomic densities, $n_i(\vec{r})$ [4,5]:

$$n_i(\vec{r}) = \frac{w_i(\vec{r})}{\sum_k w_k(\vec{r})} n(\vec{r}) \quad (2.9.12)$$

$w_i(\vec{r})$ functions as a weighting factor determines density allocation and is dependent on the partitioning method used [5]. QUBE utilises density-derived electrostatic and chemical partitioning (DDEC) [151,152]. Its weighing factor is optimised iteratively to create a spherical average of $n_i(\vec{r})$ and an ion of the same atomic species [5,151,152]. It uses a mixture of iterative Hirschfeld and iterative Stockholder atoms to construct the charge distribution [4,5]. The partial charge q on atom i is then calculated as:

$$q_i = z_i - \int n_i(\vec{r}) d^3\vec{r} \quad (2.9.13)$$

z_i is the nuclear charge associated with atom i and the integration of the electron density across all space is subtracted from it. What is left is the partial charge.

QUBE also has treatment for the Lennard-Jones parameters to encapsulate the VdW forces. Again, atom-in-molecule partitioning methods are used to capture the LJ characteristic of the atom within the molecule. The electron density of a free atom can be scaled to fit the AIM atom, and likewise the LJ parameters can be calculated in this way [153]. Defining the LJ parameters in terms of A and B , where:

$$A = 4\epsilon\sigma^{12}; B = 4\epsilon\sigma^6 \quad (2.9.14)$$

Such that the LJ potential be rewritten:

$$E_{LJ}(R) = \frac{A_{ij}}{R_{ij}^{12}} - \frac{B_{ij}}{R_{ij}^6} \quad (2.9.15)$$

The dispersion coefficient B_{ij} is scaled up as [5]

$$B_{ij} = \left(\frac{V_i^{AIM}}{V_i^{free}} \right)^2 B_{ij}^{free} \quad (2.9.16)$$

Here V_i is the atomic volume for an atom-in-molecule partitioned atom and a free atom. The AIM atomic volume is calculated as:

$$V_i^{AIM} = \int r^3 n_i(\vec{r}) d^3 \vec{r} \quad (2.9.17)$$

The B_{ij}^{free} constant is calculated using time-dependent DFT (TDDFT) and V_i^{free} using MP4 [5, 154]. To ensure that the LJ potential reach a minimum at the Van der Waals radius, A_{ij} is taken:

$$A_{ij} = \frac{1}{2} B_{ij} (2R_{i,vdw}^{AIM})^6 \quad (2.9.18)$$

Again, the Van der Waals radii are scaled via reference free atoms [5, 153]:

$$R_{i,vdw}^{AIM} = \frac{V_i^{AIM}}{V_i^{free}} R_{i,vdw}^{free} \quad (2.9.19)$$

The AIM approach has provided competitive heats of vapourisation, free energies of hydration and liquid densities to force fields designed to align with experimental data. The advantage of applying AIM partitioning to LJ parameters has been best demonstrated in the calculation of the binding free energies of proteins and free energies of hydration, which AIM electrostatic charges with unadjusted LJ parameters cannot reproduce well [4].

2.10 Molecular Dynamics

In order to compare the relative performance of force-field methods, and to generate the RDFs for theoretical X-ray scattering, the solution must be allowed interact on ultrafast timescales. The motion is governed by Newtonian mechanics. Written in terms of the potential of the system, V :

$$- \frac{dV}{d\vec{r}} = m \frac{d^2 \vec{r}}{dt^2} \quad (2.10.1)$$

\vec{r} represents the atomic positions in the simulation box. To propagate the simulation box forwards in time by an incremental time step Δt , such that

atomic positions \vec{r}_i progress to r_{i+1} [14]:

$$r_{i+1}^{\vec{}} = \vec{r}_i + \vec{v}_i(\Delta t) + \frac{1}{2}\vec{a}_i(\Delta t)^2 + \dots \quad (2.10.2)$$

\vec{v}_i and \vec{a}_i are the velocity and acceleration of the particles at point \vec{r}_i . To regress back in time by a time step Δt to atomic positions r_{i-1} :

$$r_{i-1}^{\vec{}} = \vec{r}_i - \vec{v}_i(\Delta t) + \frac{1}{2}\vec{a}_i(\Delta t)^2 + \dots \quad (2.10.3)$$

Adding together the terms for the anterior and subsequent time steps, an equation can be derived for the subsequent time step in terms of the previous and current time steps [155]:

$$r_{i+1}^{\vec{}} = (2\vec{r}_i - r_{i-1}^{\vec{}}) + \vec{a}_i(\Delta t)^2 \quad (2.10.4)$$

This is the Verlet algorithm [14, 155]. This can be used to solve Newtonian motion numerically. Recalling the equation for potential V , the acceleration is defined as [14, 155]

$$\vec{a}_i = \frac{\vec{F}_i}{m_i} = -\frac{1}{m_i} \frac{dV}{d\vec{r}_i} \quad (2.10.5)$$

Indeed, the initial positions r_0 have no previous time step, which is estimated via [14]:

$$r_{-1}^{\vec{}} = \vec{r}_0 - \vec{v}_0(\Delta t) \quad (2.10.6)$$

The acceleration is evaluated from the net force at each time step, in turn allowing the atomic positions to be propagated in time and generating a trajectory [14, 155]. The smaller the time step, the more accurate the trajectory is to a real-life trajectory for the given initial atomic positions, though the computational expense is increased for the total trajectory time. There is a limit to the numerical accuracy of the calculation (as time steps cannot be infinitesimally small) so there will be inevitably some cumulative error. The only issue with the Verlet algorithm is that the velocity is not explicitly written into the equation, such that it is difficult to maintain a consistent velocity distribution, which in turn makes it hard to maintain an ensemble of constant temperature [14]. In order to facilitate maintaining a constant temperature, the velocity can be explicitly written in the velocity Verlet algorithm [14, 156]:

$$v_{i+1}^{\vec{}} = \vec{v}_i + \frac{1}{2}(\vec{a}_i + a_{i+1}^{\vec{}})\Delta t \quad (2.10.7)$$

In the particular case of the systems under study here, they are designed

to mimic the rearrangement caused by an X-ray pulse event on ultrafast timescales. It assesses the impact on scattering of temperature change and pressure change, taking the impact of each parameter individually. With this in mind the ensemble is an NPT ensemble, that is, the number of molecules, the pressure and the temperature are to be maintained as closely as possible for each solution box, with the change in RDF between solution boxes representing the scattering change. The volume is allowed to vary in order to maintain constant temperature and pressure. The MD simulation would automatically be set for a NVE (number of particles, volume, energy) simulation box and the temperature would fluctuate. In order to correct for this and maintain a steady temperature, the velocity distribution must be scaled down to reflect the average kinetic energy corresponding to the desired temperature. Given that the average kinetic energy of a system is given as [14]

$$\overline{E_{kin}} = \frac{3}{2}NkT = \frac{1}{2} \sum_i^N m_i \vec{v}_i^2 \quad (2.10.8)$$

The proportionality between the temperature and average velocity is therefore given as:

$$\bar{v} \propto T^{\frac{1}{2}} \quad (2.10.9)$$

In order to stabilise the temperature around that which be desired in the system, the velocity distribution \vec{v}_i must be scaled accordingly at each time step by $(\frac{T_{desired}}{T_{actual}})^{\frac{1}{2}}$ [14]. However, such "instantaneous correction" can vastly alter the dynamics and introduce periodicity into the system over time, both highly unrealistic and undesirable [14]. In order to alleviate these problems, a less instantaneous method can be employed, in which the temperature would be scaled towards the desired value over a time interval τ such that [14, 157]:

$$\frac{dT}{dt} = \frac{T_{desired} - T_{actual}}{\tau} \quad (2.10.10)$$

This makes the heat transfer gradual and is the theoretical analogue to coupling the system to a heat bath. With the gradual approach to temperature consistency factored in, the velocity scale factor is recalculated as [157]:

$$\left(\frac{T_{actual} + \delta t \frac{dT}{dt}}{T_{actual}}\right)^{\frac{1}{2}} = \sqrt{1 + \frac{\delta t}{\tau} \left(\frac{T_{desired}}{T_{actual}} - 1\right)} \quad (2.10.11)$$

This method of regulating temperature is called a thermostat. It must be noted that this improves considerably the average temperatures but the fluctuations in temperature are still not statistically canonical. This is improved

by assigning the heat bath fictitious dynamic variables that are allowed to play out and interact with the system, creating more realistic fluctuations, and thereby produce more accurate ensembles that can be proven statistically canonical [14, 158, 159]. Such methods are collectively called *Nosé-Hoover* methods. Similarly, the pressure can be controlled via a pressure bath. Here the influence is not upon scaling the velocity but the coordinates of the constituent molecules, allowing the volume to change in order to maintain constant pressure. Again, correction to the desired pressure is staged across a time interval τ :

$$\frac{dP}{dt} = \frac{P_{desired} - P_{actual}}{\tau} \quad (2.10.12)$$

In turn the coordinate scale factor is written:

$$\sqrt[3]{1 + \kappa \frac{\delta t}{\tau} (P_{desired} - P_{actual})} \quad (2.10.13)$$

κ is the compressability of the system. This method, analogous to the thermostat, is called the barostat. Again, to make the system canonical with statistically acceptable pressure fluctuation, the *Nosé-Hoover* methods are applied to the system, with the pressure bath given dynamic variables permitted to evolve and interact with the system [14, 158, 159].

Chapter 3

Assessing Functional Errors using Atomisation Energies and Electric Field Gradients

3.1 Introduction

Density Functional Theory (DFT) is by far the most popular quantum chemistry methods with over >30,000 papers containing DFT calculations published each year [6]. It can be applied in a broad range of scenarios including both fundamental as well as applied research fields and consequently has become critical in contemporary research fields such as high-throughput material design and accelerated drug development.

At the heart of DFT are the Hohenberg-Kohn theorems [7], which demonstrate that for any system consisting of electrons moving under the influence of an external potential $v_{ext}(\mathbf{r})$ (e.g. attractions to the nuclei) that the this external potential and consequently, the total energy, is a unique functional, $F[n]$, of the electron density $n(\mathbf{r})$. In addition, they demonstrated that the ground state energy of this density can be obtained variationally. The density which minimises the total energy is the exact ground state density:

$$E = \min_n \left\{ F[n] + \int d^3r n(\mathbf{r}) v_{ext}(\mathbf{r}) \right\} \quad (3.1.1)$$

Here $v_{ext}(\mathbf{r})$ is the one-body potential of the systems, $F[n]$ is the functional of the one electron density, $n(\mathbf{r})$. The most common approach of density functional calculations is the Kohn-Sham scheme [11]. This casts the system into a fictitious set of noninteracting electrons with the same ground-state density as the real Hamiltonian. This is solved self-consistently as:

$$[-\nabla^2/2 + v_{eff}(\mathbf{r})] \phi_i(\mathbf{r}) = \epsilon_i \phi_i(\mathbf{r}) \quad (3.1.2)$$

where $\phi_i(\mathbf{r})$ is KS orbital i with eigenvalue ϵ_i . Here the density of the orbitals is defined to match the true density and the energy can be found from:

$$F[n] = T_s[n] + U[n] + E_{xc}[n] \quad (3.1.3)$$

where T_s is the Kohn-Sham kinetic energy, U is the orbitals Hartree energy and the effective potential is defined as:

$$v_s(\mathbf{r}) = v_{ext}(\mathbf{r}) + \int d\mathbf{r}'^3 \frac{n(\mathbf{r}')}{|\mathbf{r} - \mathbf{r}'|} + v_{xc}(\mathbf{r}) \quad (3.1.4)$$

and

$$v_{xc}(\mathbf{r}) = \frac{\delta E_{xc}}{\delta n(\mathbf{r})} \quad (3.1.5)$$

In all practical calculations, $F[n]$ is approximated $\tilde{F}[n]$. In turn, minimising the approximate functional will yield an approximate density, $\tilde{n}(\mathbf{r})$. The use of approximate energy functionals means that errors appear in the density via the exchange-correlation potential. The exchange-correlation potential decays too rapidly with inter-electron distance in many standard approximations such as the local density approximation (LDA) and the generalised gradient approximation (GGA) [19, 20]. This causes a upward shift of ϵ_i by several eV. Although, as the effect on v_{xc} is usually a uniform upshift of the potential, it often has a limited effect on the occupied orbital shapes and on the bulk electron density. [20, 160]

In this regime, the total energetic error of any self-consistent KS DFT calculation may be split into a functional and density errors [19]:

$$\Delta E = \Delta E_F + \Delta E_D \quad (3.1.6)$$

The functional error, $\Delta E_F = \tilde{F}[n] - F[n]$, is the energetic error arising from the approximate exchange-correlation functional for any given density, even if it is the exact density. The density error, corresponds to the energetic error arising from the use of an approximate density, $\tilde{n}(\mathbf{r})$. As mentioned above, in many cases KS-DFT calculations calculate excellent densities, and consequently it is the functional error which dominates [19, 31, 32]. Importantly, the two errors are interrelated in the standard KS scheme: A poor exchange-correlation functional leads to a poor energy, while its functional derivative yields to a poor potential which yields a poor density. Hence, energy and density are related by virtue of the KS potential: (equation 3.1.5). The dominance of functional errors means that, with the notable exception of

the HCTH (Hemprecht-Cohen-Tozer-Handy) series of functionals [161–163], the development of new functionals have focused upon improving energy, and not the density the calculations produce. The accuracy of a functional is typically assessed by the errors in energies derived from transformations of the type, $\Delta E = E_2[\rho_2] - E_1[\rho_1]$ where ΔE represents a chemical conversion. However, in this case errors will contain both density and functional errors and therefore modifying functionals to improve energetic results may result in improve energies arising from the cancellation of errors, especially for highly parameterised functionals. Indeed, Medevdev et al. [27] recently proposed that modern density functionals are contravening the Hohenberg-Kohn theorems because although energy is improving the proposed density is actually getting worse following their study of the energy and density of ions, suggesting that this was due to a over parametrisation of modern density functionals. However, there has been significant discussion about the relevance of these results, much of which has focused upon the significance and/or chemical relevance of density errors arising from the model systems chosen [19,28,31,32]. Using a two different approaches for characterising the density and functionals errors, Kepp [31] and Sim *et al.* [32] have both concluded that the density error of such cations used by Medevdev et al. [27] is energy-wise insignificant and therefore does not provide proof of contravention of the Hohenberg-Kohn theorems.

Given these discussions, it is clearly timely to consider approaches that are able to simultaneously assess the accuracy of the density alongside functional errors. While density differences calculated from the accurate *ab initio* approach and a more approximate density functional is conceptually appealing, the values obtained are very sensitive to the exact details of the calculations, e.g. sampling points. [19,28,32]. An alternative way of assessing the accuracy of density is through electric field gradients (EFG), for which highly accurate values can be derived from microwave spectroscopy [63]. Consequently, in the present work, we use EFG's as a probe of the electron density and probe the correlation between energy and density for a range of density functionals approximations for 5 molecular complexes.

3.2 Theory and Computational Details

We calculate the atomisation energy, the energy required to disassociate a molecule into its constituent atoms, and electric field gradients (EFG) for; CuCl, H₂O···CuCl [58], Ar···CuCl [57], OC···CuCl and H₂S···CuCl [58,

59]. The EFG's for these complexes have been determined from experimentally determined nuclear quadrupole coupling constants (NQCCs) from microwave spectroscopy:

$$Q(x) = \frac{v_Q(x)}{234.9647q(x)} \implies q(x) = \frac{v_Q(x)}{234.9647Q(x)} \quad (3.2.1)$$

in which $Q(x)$, $v_Q(x)$, and $q(x)$ are the nuclear quadrupole moment (NQM) (in barns), the NQCC (in MHz), and the EFG (in a.u.) of a nucleus x respectively. The EFG measures the change in electric field strength from the nucleus as a result of the distribution of charge [35]. Localised increases in charge density yield positive gradients (the electric field strength increases) while localised decreases in charge density (decreasing electric field strength) lead to negative gradients. Gradients taken in three dimensions therefore provide indicators of the electron density mapping across the atom. Changes in density distribution caused by covalent bonding are therefore captured by the EFG.

All density functionals (see Table 3.2.1) and CCSD(T) calculations were performed using the ORCA quantum chemistry package [164] at the CCSD(T) optimised geometries. All calculations were performed using an aug-cc-pVQZ-DK [165–169] and a fine integration grid (Grid 7). Relativistic effects were included using a Douglas-Kroll-Hess Hamiltonian up to second order. For the range-separated functionals, the interpolation between the short-range DFT and long-range Hartree Fock is determined by the ω parameter:

$$\frac{1}{r_{1,2}} = \frac{1 - \text{erf}(\omega r)}{r_{1,2}} + \frac{\text{erf}(\omega r)}{r_{1,2}} \quad (3.2.2)$$

where $r_{1,2}$ is the inter-electron separation. The optimal tuning approach applied was achieved by minimising the objective [170]:

$$J(\omega) = |\epsilon_{HOMO} + \epsilon_{IP}| \quad (3.2.3)$$

Here ϵ_{HOMO} is the energy of the highest occupied molecular orbital (HOMO) of a neutral system and ϵ_{IP} is the first ionisation potential of the system, as determined by the difference in ground state energies between a neutral and positively-charged system. The optimal value of ω is achieved when J is minimised.

Functional	Type	Ref.
B2GP-PLYP	dhGGA	[36]
B2PLYP-D3	dhGGA	[37]
B2PLYP	dhGGA	[38]
B3LYP	hGGA	[21, 39]
B97-D3	GGA	[37]
B97	hGGA	[40]
BLYP	GGA	[41]
BP86	GGA	[42]
CAM-B3LYP	rshGGA	[43]
DSD-BLYP-D3	dhGGA	[44, 45]
LC-BLYP	rshGGA	[171]
M062X	hmGGA	[48]
M06L	mGGA	[47, 49]
M06	hmGGA	[47, 48]
mPW2PLYP	dhGGA	[50]
O3LYP	hGGA	[51]
PBE0	hGGA	[52]
PBE	GGA	[53]
PW6B95	hGGA	[54]
PWPB95	dhGGA	[22]
TPSS0	hmGGA	[55]
TPSSh	hmGGA	[55]
TPSS	mGGA	[55]
ω B97	rshGGA	[25]
ω B97X	rshGGA	[25]
ω B97X-D3	rshGGA	[56]

Table 3.2.1: The functionals, including type and reference used within this work.

3.3 Results

3.3.1 CuCl

Figure 3.3.1 shows a plot of the CuCl atomisation energy against electric field gradient for Cu (a) and Cl (b). In both cases there is no trend between the energy and EFG for the functionals studied herein. All of the atomisation energy falling within a range of 13 kcal mol^{-1} , with the majority functional achieving an atomisation energy between 0.135-0.140 a.u. On the EFG axis, the values begin to approach both the coupled cluster and experimental results as Jacob's ladder is climbed, with pure (GGA or mGGA), followed by hybrid functionals, range separated functionals and finally double hybrid functionals.

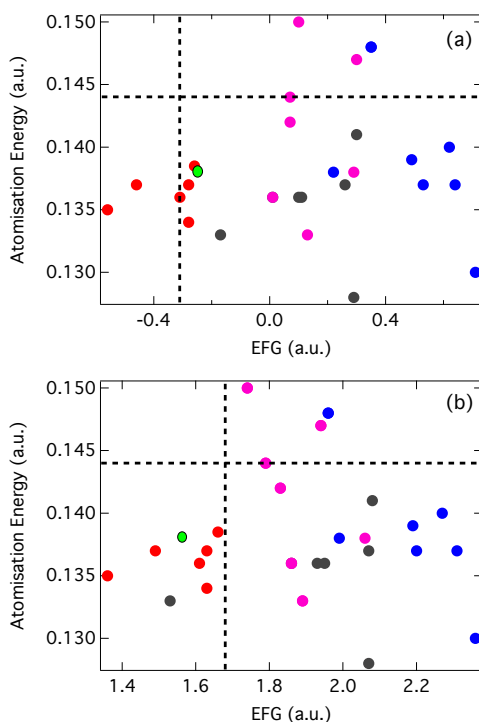


Figure 3.3.1: Plot of the CuCl atomisation energy as a function of Cu (a) and Cl (b) electric field gradient in the complex by functional group. GGA, hGGA, dhGGA and rshGGA are represented in blue, grey, red and light purple respectively. CCSD(T) is denoted in green, while the dashed line represents experimental EFG and atomisation.

This reflects the importance of Hartree-Fock exchange for describing the EFG. Indeed, while the double hybrid functionals provide excellent agreement this is not a result of the inclusion MP2 correlation, but that these

functionals contain a large fraction of Hartree-Fock exchange. Increasing Hartree-Fock exchange fraction corresponds to an increase in electronegativity of chlorine relative to copper leading to increased charge transfer into Cl $3p_z$, making the EFG less positive as the imbalance of charge favouring polarisation in the x-y plane reduces. The Cu EFG becomes more negative as more charge that remains on the Cu transfers from Cu $4s$ into Cu $4p_z$ and d-orbitals with alignment with the bond, in particular $4d_{z^2}$, increasing polarisation in the bond even as the total charge on Cu actually decreases. The role of Hartree-Fock exchange in describing transition metal systems in DFT was highlighted by Yanagisawa *et al.* [172] for the first-row transition metal dimers and has been observed throughout d-block transition metals [172–175]. They demonstrated that pure DFT tends to favour configurations containing a higher fraction of higher angular momentum orbitals, while HF exchange strongly favours orbitals with low angular momenta. They cast this in terms of the 3d-4s inter-configurational energy (i.e. $4s^23d^{n-2}$ to $4s^13d^{n-1}$) and the ionisation potentials of the 4s and 3d orbitals, which were found to be closely related. The Cu ionisation potentials therefore increase with Jacob’s Ladder with a preferred 4s occupation. This indicates an increased Mulliken electronegativity of Cu with increased HF exchange. However, the increase in Cl electronegativity is greater, such its electron density increase at the expense of the Cu density. The remaining valence Cu $4s$ becomes degenerate with the previously-unoccupied $4p_z$ orbitals aligned with the bond. This is however not the only driver of EFG change across Jacob’s Ladder on the Cu atom. As evidenced in table A.3.1, the core polarisation contribution is very significant and of comparable magnitude to the valence contribution. This is unsurprising given the proximity of the core and valence electrons. The higher HF-exchange functionals are more z-polarised in the valence region. The long-range nature of the HF exchange then mediates the increased repulsion, both Coulomb and Fermi, to z-polarised core orbitals, increasing the negativity of the core contribution to the EFG. When the breakdown of the EFG contributions are considered with respect to CCSD(T) it is noteworthy that many of the dhGGA functionals that align with the CCSD(T) Cu EFG have a more z-polarised valence contribution but less polarised core contribution. That is that their valence region polarisation overcompensates for the lack of core polarisation. The purely HF exchange contribution of CCSD(T) allows for more long-range Fermi repulsion to induce polarity in the core region, which DFT functionals cannot do without eliminating important local effects of pure-DFT exchange.

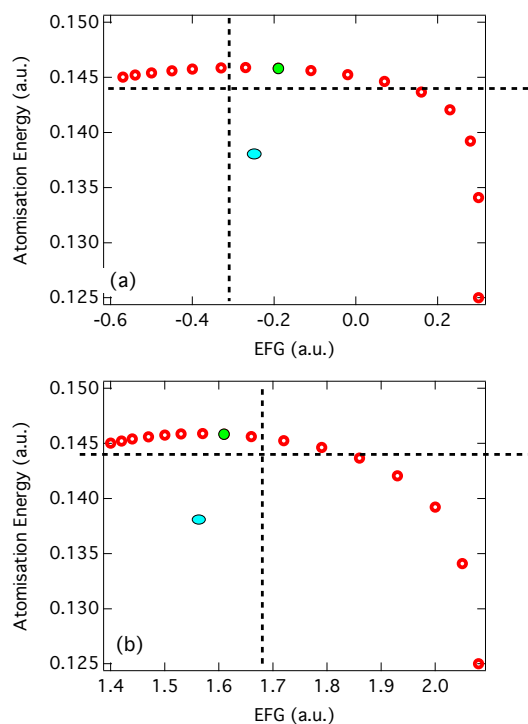


Figure 3.3.2: Plot of the change in atomisation and a) Cu b) Cl EFG of ω B97X for CuCl as the value of ω is adjusted from 0.05 to 0.8. Optimal ω (green) and CCSD(T) (blue) are also indicated

Figure 3.3.2 shows a plot of the CuCl atomisation energy against electric field gradient for Cu (a) and Cl (b) for the long-range corrected functional ω B97X for which the range separation parameters ω (equation 3.2.2) has been tuned between 0.05-0.8. This shows improvement in energy and density (through the EFG) which are largely independent. An initial increase in the accuracy of the atomisation energy compared to experiment is observed until $\omega=0.45 \text{ a}_0^{-1}$, in close agreement with the default value of $\omega=0.30 \text{ a}_0^{-1}$ for ω B97X. This is followed by a decrease in the EFG for larger ω consistent with the importance of Hartree-Fock exchange. However, in this region, the change in the atomisation energy is minimal. The green filled circle in figure 3.3.2 shows the point in which the value of ω minimises the objective shown in equation 3.2.3, and therefore corresponds to the optimal tuned value of ω [170]. While, previous work by Srebro *et al.* [33] showed that the optimal tuning approach was able to improve the description of the EFG for CuCl, this shows that this improvement is not achieved at the sacrifice of energy.

The lack of apparent correlation between energy and density shown in figure 3.3.1 arises due to their respective sources of error. Indeed, the error in the EFG derives solely from the error in the approximate density obtained

from the KS optimisation. In contrast, the energetic error originates from combination of the the functional and density error (Equation 6). In many cases the functional error is expected to dominate [176], but this is not always the case.

3.3.2 Ar···CuCl

Figure 3.3.3 shows the atomisation energy plotted against the EFG for copper (a) and chlorine (b) for the Ar···CuCl complex. This is chosen because the Ar binds very weakly to the CuCl, as demonstrated by the small difference in the calculated atomisation energy compared to CuCl. Consequently it could be expected to provide minimal perturbation from the results obtained for CuCl.

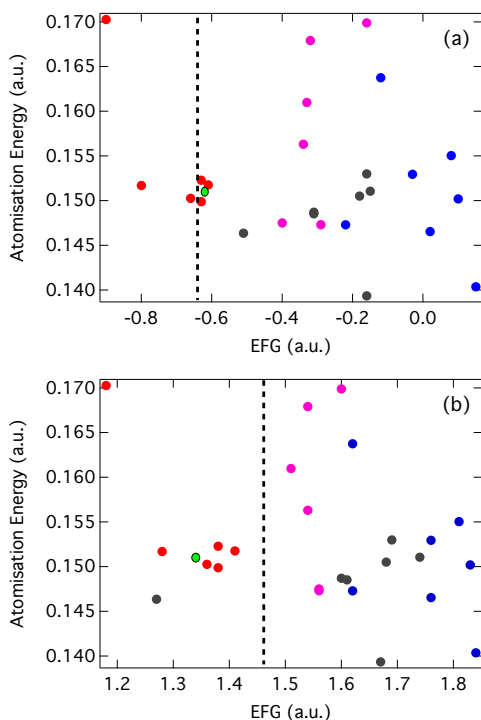


Figure 3.3.3: Plot of the Ar···CuCl atomisation energy as a function of a) Cu b) Cl electric field gradient in the complex by functional group. GGA, hGGA, dhGGA and rshGGA are represented in blue, grey, red and light purple respectively. CCSD(T) is denoted in green, while the dashed line represents experimental EFG.

Despite this, a sizeable shift in the EFGs are observed and the principal-axis EFGs of both the copper and the chlorine are shifted to lower values, with the bulk of calculated copper EFGs now negative and chlorine EFGs now slightly less positive. This shift occurs due to an an increase in Cu $4p_z\sigma$

and $4d_{z^2}\sigma$, and Cl $4p_z\sigma$ orbital populations at the expense of the Ar $3s\sigma$ population. Increased Cu electronegativity relative to Ar at higher rungs of Jacob's Ladder, and increased shift of charge from Cu $4s\sigma$ to $4p_z\sigma$ and $4d_{z^2}\sigma$ further contributes to the EFG negativity, along with a small drop in π -bonding in the x-y plane..

As observed for CuCl, there is no clear trend involving both atomisation energy and EFG which as previously identified is due to dual contribution of density and functional error in the atomisation energy with only the density error contributing to EFG. The best agreement between the experimental and CCSD(T) for the Cu EFG is again achieved for functionals containing a large fraction of Hartree-Fock exchange, such as double hybrids and M06-2X. Again, the importance of core polarisation contributing to the Cu EFG is highlighted (table A.3.3), with overall alignment of CCSD(T) EFG with large-fraction HF functionals the result of overcompensation of valence EFG polarisation for lack of core polarisation relative to CCSD(T). However, in contrast to CuCl, the agreement with the EFG of Cl is described equally well with long-range corrected functionals.

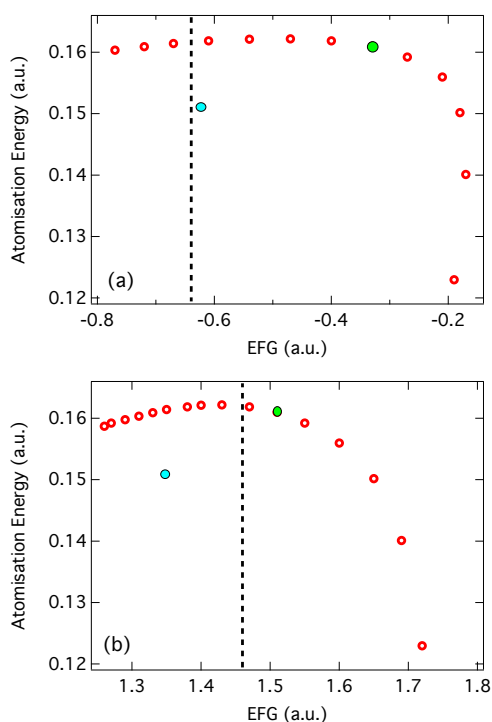


Figure 3.3.4: Plot of the change in atomisation and copper EFG of ω B97X for CuCl as the value of ω is adjusted from 0.05 to 0.8. Optimal ω (green) and CCSD(T) (blue) are also indicated

Figure 3.3.4 shows the results of tuning the range-separation parameters

in ω B97X. A similar trend is observed with a sizeable increase in the atomisation energy for small values of ω and a subsequent increase in the EFG towards the experimental value, for which the change in the atomisation energy is minimal. This again highlights the almost independent improvement in energy and EFG as a function of ω . Interestingly, while the optimal value of ω provides a very good agreement for the EFG of chlorine, it provides much poorer agreement for Cu. This is because for CuCl, the 3d-4s inter-configurational energy which was important for achieving the correct description of the EFG is closely linked to the ionisation potential of the Cu 3d orbitals [172]. This is tuned during the optimal tuning approach. However, for Ar...CuCl this is not true because the highest occupied orbitals contain orbital overlap between the Cu 3d σ and the Ar 3p σ orbitals, such that the HOMO-IP agreement shifts away from a value suitable for transition metals and towards a lower value ideal for halogens and noble gases, in effect reverting to the default ω .

3.3.3 OC...CuCl

In the previous section we studied the effect of a weak interaction between Ar on CuCl. Here we study the effect of the strong interaction which arises between CuCl...CO [177]. Previous calculations have shown that the Cu-C interaction is formed by σ -bonding from the carbon to copper with only a small contribution to d π^* -back-donation from Cu to C [177]. This strong interaction further distorts the electron density of CuCl and results in a further negative shift of both the Cu and Cl EFGs.

Figure 3.3.5 shows the atomisation energy plotted against the EFG for copper (a) and chlorine (b) for OC...CuCl. The results are consistent with observations for the other systems, with no particular trend between the accuracy of the energy and the EFG. However, while the accuracy of the EFG for Cu is still strongly modulated by the fraction of Hartree-Fock exchange, this effect is significantly weaker for Cl, for which only the EFG of double hybrid functionals being significantly separated along the x -axis than the other functionals.

Figure 3.3.6 shows the atomisation energy and EFG for the ω B97X. Interestingly, as observed for CuCl, the optimal value of ω yields very good agreement for the Cu EFG, although the agreement is not as good as for chlorine. Indeed for the 5 systems studied, the results show that there is no guarantee that a good EFG on one atom will translate to an equally good one

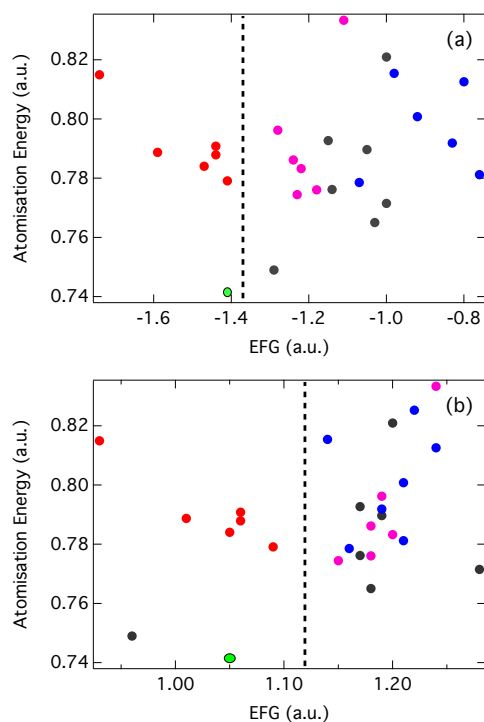


Figure 3.3.5: Plot of the $\text{OC}\cdots\text{CuCl}$ atomisation energy as a function of a) Cu b) Cl electric field gradient in the complex by functional group. GGA, hGGA, dhGGA and rshGGA are represented in blue, grey, red and light purple respectively. CCSD(T) is denoted in green, while the dashed line represents experimental EFG

on the other atom. This is due to the amount of the HOMO that is concentrated on the transition metal and the amount of the Cl and added ligand. The more on the transition metal, the greater the importance of a larger pure HF-exchange region over inter-electron distance in HOMO-IP agreement. If it reduces, however, the default ω becomes more favourable as this describes better the ionisation in the Cl and the ligands.

3.4 Discussion and Conclusions

Herein we have calculated and analysed the EFG and atomisation energies of CuCl , $\text{Ar}\cdots\text{CuCl}$ and $\text{OC}\cdots\text{CuCl}$. Calculations of two additional complexes, $\text{H}_2\text{O}\cdots\text{CuCl}$ and $\text{H}_2\text{S}\cdots\text{CuCl}$ are shown in the supporting information (see appendix A) and their results are consistent with those presented in the main text. As previously reported, the copper EFG in CuCl molecule represents a particularly challenging case for density functional theory and

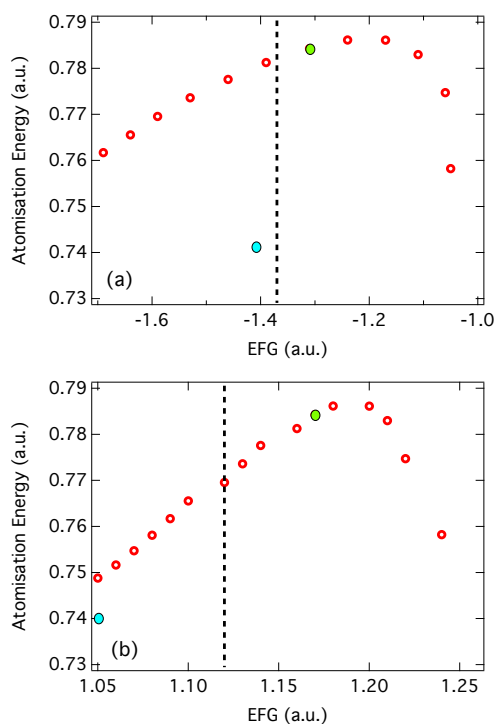


Figure 3.3.6: Plot of the change in atomisation and copper EFG of ω B97X for CuCl as the value of ω is adjusted from 0.05 to 0.8. Optimal ω (green) and CCSD(T) (blue) are also indicated

most popular functionals even fail reproduce the its sign, let alone its magnitude. This failure has been linked to the exchange part of the functional [33, 178, 179].

Ar, CO, H₂O and H₂S were chosen because they provide varying bonding strengths to the CuCl, resulting in distorted binding energies and EFGs. For Ar a weak interaction is formed by overlap between Cu 3d σ and the Ar 3p σ orbitals, for CO a much strong interaction is formed arising from σ -bonding from the carbon to copper with only a small contribution to d π^* -back-donation from Cu to C. For both H₂O \cdots CuCl and H₂S \cdots CuCl, bonding occurs through the non-bonding pairs on sulphur and oxygen which align to the CuCl axis [58, 59] similar to that expected for hydrogen-and halogen-bonded complexes. Although as noted in ref [59]. It is further significant to note that the metal-containing complexes are significantly more strongly bound than their hydrogen- and halogen-bonded analogues.

Importantly, despite the EFG having an r^{-3} dependency [35] and the large number of core-orbitals relative to valence orbitals, it provides a excellent measure of the valence electron density. This is because the EFG is only non-zero for orbitals which exhibit a deviation from cubic symmetry. Its ability to provide a measure of valence electron density makes it appropriate

to provide insight into the chemically relevant density accuracy, which has recently received significant attention [19,27,28,31,32]. However, it is important to note the role of core polarisation in the Cu EFG. Here it is of similar magnitude to the valence EFG. Furthermore, the alignment of CCSD(T) and dhGGA functionals supports recent theoretical dipole studies into DFT accuracy [29, 180]. This agreement is the result of the latter's higher valence EFG compensating its lower core polarisation relative to the former. This highlights the importance of HF exchange in mediating the valence polarisation effect to the core orbitals, which gives CCSD(T), which contains pure HF exchange, a distinct advantage.

Across the 26 functionals and 5 systems studied in the present work, our results show that the accuracy of the EFG is a reflection of the amount of HF exchange included in the functional. This is because pure DFT tends to favour configurations containing a higher fraction of higher angular momentum orbitals, i.e. the 3d orbitals. However in contrast the inclusion of HF exchange favours orbitals with low angular momenta. This as a result of the 3d-4s interchange energy [172]. In turn with this shift in arrangement of the valence orbitals, the relative electronegativity of Cu to Cl decreases as one ascends Jacob's Ladder, leading to an increase in charge polarised in the principal axis on the Cl and therefore a less negative EFG. As the Cl exerts more attraction on the electron density in the bond, more charge that is retained on Cu shifts from Cu 4s into orbitals aligned with the principal axis, in particular Cu 4p_z and Cu 3d_{z²}. This drives increased Cu EFG negativity at higher rungs of Jacob's Ladder as more charge polarises in the principal axis, as opposed to remaining in the non-contributing 4s orbital.

In agreement with previous work of Srebro *et al.* [33], we observe that optimally tuned range separated functionals can provide a route to provide a simultaneously good agreement with the electron density and the energy in the case of CuCl, as well as attributing the challenging nature of capturing its EFG to the self-interaction error. However, this is not general and breaks down for complexes with Ar, H₂O and H₂S, which while providing good EFGs are not as good as in the case of CuCl. This is as a result of these added ligands shifting the HOMO such that less is located on the Cu, such that the tuning favours an ω that suits better Cl and the ligand atoms, which tends it towards its default ω .

Finally, identifying the accuracy of approximate functionals in terms of energy and density is going challenging for real molecule systems. The present case is limited to CuCl containing systems, for the reason that as

previously demonstrated this provides a challenging case for EFG. The next chapter will be focused upon establishing how broadly this applies, both for challenging transition metals but also in unrelated systems.

Chapter 4

Extending the Understanding of Density and Energetic Error for Silver Complexes and Halogenated Aromatic Compounds

4.1 Introduction

The previous chapter explored the notion of evaluating the relationship between energy and electron density performance of DFT functionals via the atomisation and EFG respectively. Utilising theoretical benchmarking via CCSD(T) and experimental benchmarking from spectroscopic data, the performance of CuCl and its associated complexes, known for providing a notoriously difficult transition-metal EFG to capture theoretically, was evaluated under this method. This established the potential of EFG as a metric for functional assessment, indicating dhGGA to perform best relative to both experiment and CCSD(T). Furthermore, the breakdown of the EFG by core and valence contribution indicated that the struggle to capture the EFG of copper was the result of the functional difficulty in reproducing the core polarisation, with functionals often aligning with the CCSD(T) EFG through overcompensation in the valence contribution. This highlighted issues in electron exchange in particular, with increased HF exchange of dhGGA functionals being responsible for improved core polarisation, while suffering limitations as to the improvements that can be made through the use of HF-exchange for Kohn-Sham orbitals.

However, it is imperative that the conclusions of the previous study, as well as the EFG metric as a measure of density performance, be tested with

an increasing number of systems, both transition-metal systems and otherwise for which there be available data. To this end, this study presents 25 relevant candidate molecular systems which have sufficient experimental data as an expansion of the initial study with 5 candidates in the previous chapter. In order to determine the validity of the previous chapter for transition metals, AgCl and AgI are included, along with their monohydrated metal-aquo complexes, hydrogen sulfide complexes and ammonia complex (AgI only), utilising the nuclear quadrupole coupling constants (NQCCs) from rotational spectroscopic investigations of these molecules to calculate experimental EFGs [58–62]. These studies provide the EFGs for the halogens, comprising chlorine and iodine within these systems. These are supplemented with experimental NQCCs for bromine and iodine from halogenated aromatic compounds used extensively within medicinal chemistry as precursors: 4-halopyrazoles [63]; 2- and 3-halothiophenes; 2- [64, 65], 3- [66, 67] and 4-halopyridines [64, 65]; 2-halopyrimidine (bromine only) [68]; halobenzene [69, 70] and *p*-halotoluene [71]. Halogenation of drug candidate molecules is a common method for improving their effectiveness [181]. This provides sufficient variety of system type to assess the conclusions of the previous study while maintaining a useful point of comparison through the use of halogens in both systems.

4.2 Theory and Computational Details

Here the methodology is very similar to that established in chapter 3, with the experimental electric-field gradients calculated from the rotational spectroscopic data via:

$$Q(x) = \frac{v_Q(x)}{234.9647q(x)} \implies q(x) = \frac{v_Q(x)}{234.9647Q(x)} \quad (4.2.1)$$

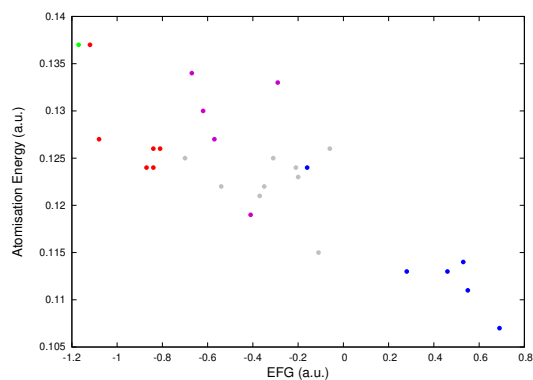
in which $Q(x)$, $v_Q(x)$, and $q(x)$ are the nuclear quadrupole moment (NQM) (in barns), the NQCC (in MHz), and the EFG (in a.u.) of a nucleus x , respectively. The same density functionals are used as those in the previous study, and along with CCSD(T), all calculations are performed using the Neese group's ORCA quantum chemistry software [164]. However, due to the high computational cost, some halogenated aromatic compounds' CCSD(T) were still ongoing at time of writing (all halopyridine isomers, halobenzenes, *p*-halotoluenes and 2-iodopyrimidine), such that only experimental comparison is currently possible (2-iodopyrimidine is compared with its brominated

analogue). Geometry optimisation was done with the B3LYP functional. All the calculations used aug-cc-pVQZ-DK [165–169] though due to the incompatibility of this basis set with larger atoms, TZVP [182] was assigned to silver, iodine and bromine. Bromine was treated the same way as iodine to facilitate comparison for the halogenated aromatic compounds. All calculations used a fine integration grid. Relativistic correction was utilised via 2nd-order Douglas-Kroll-Hess Hamiltonians, and a finite nucleus was used [183]. Optimal tuning of the ω parameter was again achieved through minimisation of the J -parameter [170].

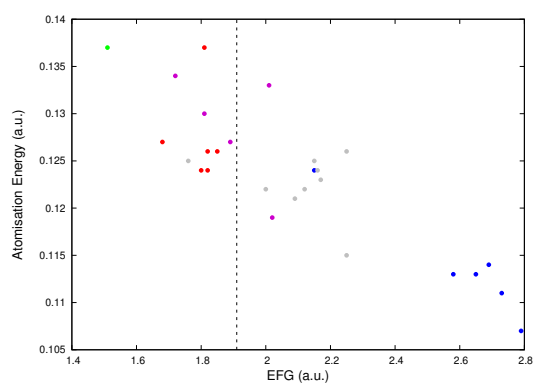
4.3 Silver Complexes

This section focuses upon the relationship between atomisation and electric field gradient for silver complexes AgCl and AgI, both isolated as diatomic heteronuclear compounds and with added complexing agents H₂O (to form a metal-aquo complex), H₂S and H₃N (for AgI only). AgCl and its associated complexes allow for comparison of atomisation to Ag and Cl EFG, with the same analysis possible with AgI, albeit with I EFG in place of Cl EFG. This allows for observation of how atomisation and EFG change with added complexing agents, as well as differences caused by the choice of halogen in the diatomic for the same added ligand.

From figures 4.3.1 and 4.3.2, atomisation energy is greater for AgCl than AgI, reflecting the relative strength of the two bonds, with AgCl the more stable structure by ~ 0.03 a.u. This is carried forward as the bulk of the atomisation energy difference between AgCl and AgI complexes for the same added ligand (see B.1.1). The atomisation energy increases as atoms are added to the complex (figures B.1.1-B.1.5), and H₂O complexes exhibit greater atomisation energy than H₂S complexes, due to the increased bond stability with the addition of the O atom due to its increased electronegativity relative to sulfur. H₃N is even more stable, owing to its strong polar covalent bonds. Studying the relative performance of functionals of various rungs of Jacob's Ladder, it is apparent that there is no discernible correlation between atomisation energy and Jacob's Ladder, and that in virtually all cases they lie close to the theoretical-gold-standard-predicted atomisation energy. The only notable outlying behaviour was the Minnesota hmGGA functional M06-2X, which predicted extremely-high atomisation energies for hydrogen-containing complexes, due to predicting a lower potential for the ground state of atomised hydrogen.

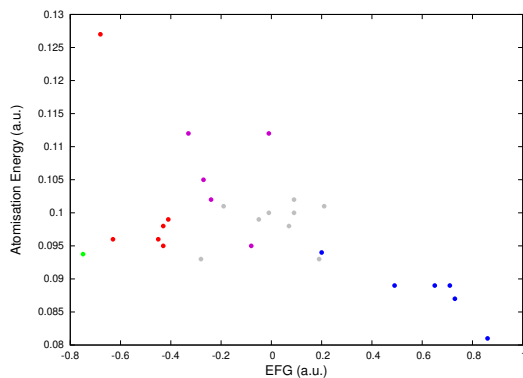


(a)

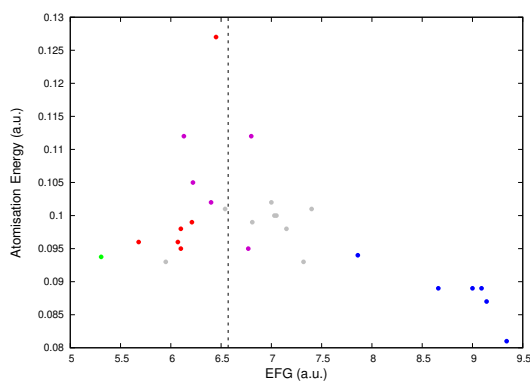


(b)

Figure 4.3.1: AgCl Atomisation-EFG characteristic for a) silver and b) chlorine. GGA, hGGA, dhGGA and rshGGA are represented in blue, grey, red and light purple respectively. CCSD(T) is denoted in green, while the dashed line represents experimental EFG.



(a)



(b)

Figure 4.3.2: AgI Atomisation-EFG characteristic for a) silver and b) iodine. GGA, hGGA, dhGGA and rshGGA are represented in blue, grey, red and light purple respectively. CCSD(T) is denoted in green, while the dashed line represents experimental EFG.

Electric-field-gradient variation is observed between AgCl and AgI when taken in isolation, and between different added ligands. Ag reports a more negative EFG in the AgCl diatomic over the AgI. Both are negative and oriented in the z-direction because of charge transfer from the halogens' valence s-orbitals (Cl 3s and I 5s) into the previously-unoccupied Ag 5p_z orbital via σ_{sp} -bonding exceeding that transferred into the Ag 5p_x and 5p_y orbitals via π -bonding with the halogens' xy-polarised valence p-orbitals. However, the relative difference between z-polarised and xy-polarised charge is greater for Ag in AgCl than AgI, despite more charge transferring overall to Ag in the AgI system. Hence AgCl reports a more negative EFG. Both Cl and I report positive EFGs in their respective diatomics, however, the magnitude of their positive EFG somewhat differs, with I being around three times larger. This is predominantly due to the iodine's increased nuclear charge, which exceeds the impact of the radial distance change of its valence electrons, such

that field gradient increases relative to chlorine. There is also increased difference in charge between polarisations contributing to and offsetting the EFG. This occurs on the iodine to increased transfer of z-polarised charge to the Ag atom. Shifting attention to the impact of ligand addition, it is perhaps unsurprising that the Ag atom, which is in close proximity to the added ligand, experiences a larger change in EFG than the halogen EFGs. The metal-aquo-complexes lead to an increased charge transfer from the O 2s and 2p_z into the Ag 5p_z orbital, with some Ag 4dz² charge transferred back into O 2p_z. There is also small amount of π -bonding reducing the charge in the x-y plane in Ag into the O 2p_x and 2p_y on AgCl, while the charge transfer occurs in reverse for AgI. The overall impact is an increase in the magnitude of the negative Ag EFG polarised in the z-direction. H₂S complexes result in increased charge transfer to the Ag, due to sulfur's reduced electronegativity relative to oxygen. There is actually some additional transfer via π -bonding into the S 3p_x and 3p_y orbitals from Ag 4d_{xy} and 4d_{x²-y²}, which further increases the z-polarisation of the Ag EFG. H₃N results in a reorientation of the principal axis of the EFG from the z-direction into the xz plane. There is charge transfer between that observed of H₂O and H₂S, with σ -bonding through N 2p_x and 2p_y bonds, with some charge transfer back through Ag 4d_{xz}.

Once these influences on the EFG have been accounted for, attention turns to the influence of Jacob's Ladder. It is quickly apparent, across all rungs of Jacob's Ladder, that dhGGA functionals are the group that ascertains the most accurate EFGs of Ag, Cl and I across all systems relative to theoretical gold standards, followed by rshGGA, hGGA and GGA. The experimental halogen benchmarks are more positive than the theoretical benchmarks, but still strongly align with dhGGA and rshGGA for AgCl and its associated ligands, while rshGGA and hGGA align better for systems containing AgI. Differences between experimental and theoretical benchmarks can either be resultant of experimental error in ascertaining NQCCs or limitations on theory, such as not having an unlimited basis set. Across all systems, the most important driver of Cl and I EFG is the polarisation of the valence density due to its bond with the Ag atom. As one descends Jacob's Ladder, the relative electronegativity of chlorine and iodine relative to silver falls, such that less charge is transferred to them in the σ_{sp} bond with Ag 5s, resulting in a more positive EFG in the z-direction. Likewise, more charge is transferred from their valence orbitals to the Ag 5p orbitals. However, much of this transfer to Ag is manifested as π -bonding to xy-oriented

orbitals, which increases positivity of the Ag EFG. The Ag 5s orbital is more hybridised with the 5p_z and 4d_{z²} orbitals as Jacob's Ladder is ascended, such that z-polarised EFG increases, even while more charge is lost to the halogens overall. The combination of these effects leads to the Ag EFG becoming more negative higher up Jacob's Ladder. Increased Ag electronegativity relative to sulfur and oxygen as one descends Jacob's Ladder negates this effect somewhat as one considers the added H₂O and H₂S ligands, such that the concentration of Ag 5p_z at the highest and lowest rungs of Jacob's Ladder are very similar. However, valence density alone cannot explain the big disparity in Ag EFG. If valence density solely determined the Ag EFG, all the EFGs would be negative, and those with added ligands would be more or less identical across Jacob's Ladder. Indeed, many would be more z-polarised than CCSD(T). However, lower rungs report positive Ag EFGs in the diatomic AgCl and AgI systems, and despite similar valence EFGs, there is still a big disparity between lower-rung EFGs and higher-rung EFGs in the ligand systems. Referring to tables B.3.1-B.3.4, this is due to the core polarisation, which is z-polarised for higher-rung functionals, making the overall EFG more negative, while lower-rung EFGs are xy-polarised, negating the z-polarised valence EFG. The orbitals responsible are in the Ag 4p shell, where the 4p_z EFG outweighs those of 4p_y and 4p_x for higher-rung functionals. This owes to the bigger energy difference between the orbitals corresponding to a relative increase in x- and y-polarised contributions relative to z-polarised, such that they outweigh the latter. Less energetic change for higher-rung orbitals yields that the z-polarised orbital yields the largest EFG of the three. It also underscores an important point; that often the agreement with CCSD(T) Ag EFG benchmarks are not due to valence EFG agreement, but rather an overestimate of valence EFG which offsets a less z-polarised core polarisation relative to CCSD(T).

Figures 4.3.3 and 4.3.4 show the outcome of ω B97X tuning for AgCl and AgI respectively. Silver complex tuning is shown in B.1.2. The ω B97X tuning was carried out for $\omega=0.05-1.0$ in steps of 0.05 for all systems. The functional was optimally tuned via Koopmans' theorem, where the difference between the highest-occupied molecular orbital (HOMO) potential and the first ionisation potential (IP), the J-parameter, was minimised. It is found that the atomisation initially increases rapidly before plateauing above $\omega=0.2$, reflecting that the bond has reached a peak stability. These peak atomisation energies are overall comparable to the CCSD(T) atomisation benchmarks. In all cases this plateau occurs before the optimal HOMO-IP agreement. Indeed,

relative to the default $\omega=0.3$ for a standard ω B97X functional, the results for HOMO-IP agreement between the silver diatomics and silver complexes differs significantly. Comparing the diatomics, AgCl favours $\omega=0.45$ while AgI has no distinct point of agreement, though it is clear that optimal $\omega > 1.0$ and lies outside of our scale, with the closest functional $\omega=1.0$. The monohydrated metal-aquo complexes exhibit similar behaviour for HOMO-IP agreement, with $\omega=0.4$ and $\omega > 1.0$ for $\text{H}_2\text{O} \cdots \text{AgCl}$ and $\text{H}_2\text{O} \cdots \text{AgI}$ respectively. However, they fall into agreement for the H_2S and H_3N ligands respectively, with $\omega=0.3$ for both silver diatomics, in line with the default ω for the ω B97X functional. This corresponds to the diatomics and metal-aquo complexes having similar quantities of Ag and I contributing to the first ionisation potential, while H_2O and H_3N ligands favour a first ionisation potential more concentrated on the halogen, such that ω converges to a lower value.

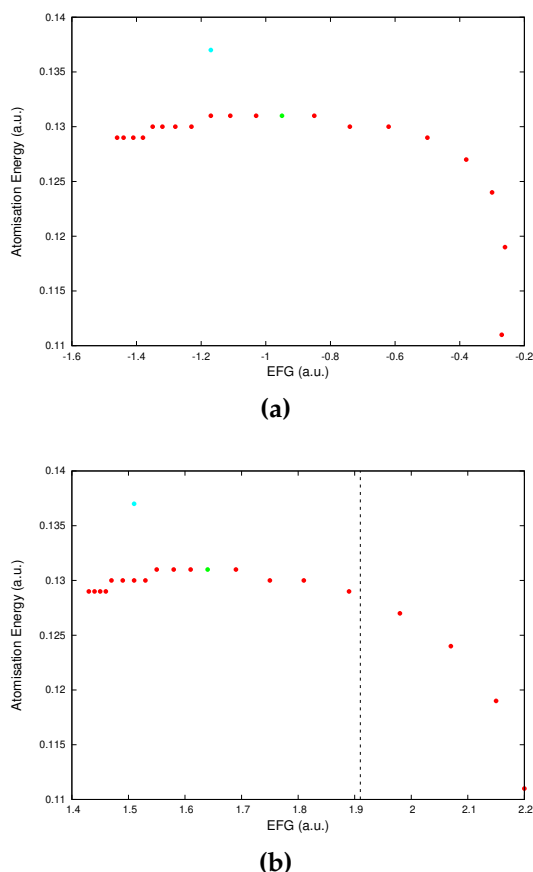
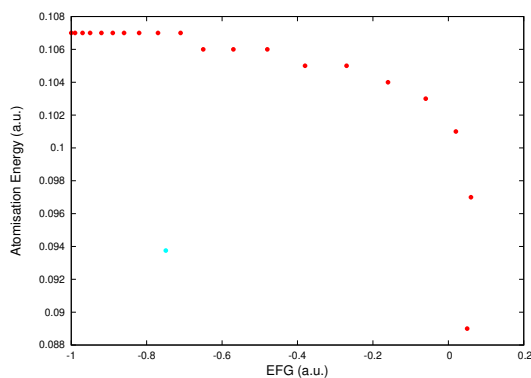
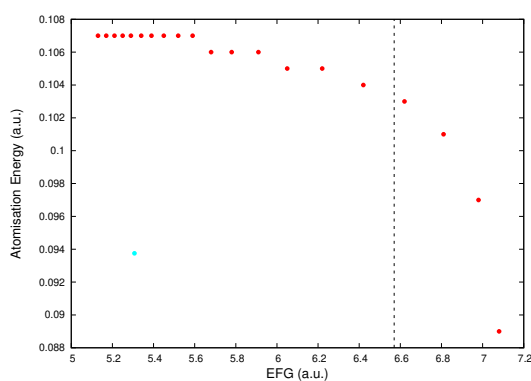


Figure 4.3.3: AgCl ω B97X change in atomisation and EFG for a) silver and b) chlorine for $\omega=0.05-1$. Optimal $\omega=0.45$ is denoted in green, with CCSD(T) in cyan. Step-wise atomisation energies for high- ω functionals is on account of rounding to the maximum number of significant figures possible in this system.



(a)



(b)

Figure 4.3.4: AgI ω B97X change in atomisation and EFG for a) silver and b) chlorine for $\omega=0.05-1$. Optimal ω is not contained within the given range. CCSD(T) denoted in cyan. Experimental EFG is denoted by the dashed line. Step-wise atomisation energies for high- ω functionals is on account of rounding to the maximum number of significant figures possible in this system.

This is similar optimal- ω to those calculated for halogens for the halogenated aromatic complexes in the subsequent section. The overall trend is that there is an initial rapid negative change in EFG for both Ag and the halogens across all systems, which then slows beyond $\omega=0.3-0.4$. This mirrors relative electronegativity increase, of the halogens relative to silver, as mirrored by the respective atomic valence orbital potentials. This leads to halogen EFG rapidly becoming less positive, and increased degeneracy of the Ag 5s orbital with the Ag 5p_z orbital through the σ -bond with the respective halogens, leading to increased negativity of the Ag EFG. After this initial rapid increase, silver atomic valence orbital potential ceases to increase and plateaus, while the halogen atomic valence orbital potential continues to increase, but at a slower rate, such that the rate of charge transfer to the halogen decreases. The plateauing of the Ag atomic valence orbital also prevents further polarisation of the Ag 5s with Ag 5p_z, such that any further increase

in EFG corresponds to a fall in $5p_x$ and $5p_y$ occupancy as more charge is transferred via π -bonding to the halogen. This slowdown in charge transfer results in a slowdown in EFG change on both the Ag and the halogens. When the ligands are added, there are two competing effects which effect the Ag $5p_z$ occupancy, the hybridisation that increases $5p_z$ occupancy as ω increases up to the previously-observed, and the increase in oxygen, sulfur and nitrogen electronegativity as ω increases relative to silver, which reduces the charge transfer via the σ_{sp} -bond to the silver atom as ω increases. This leads to peak increase in Ag EFG negativity with intermediate ω , while the halogen EFG change with increased ω retains the ever-slowing negative change in EFG with increased ω as seen for the isolated diatomics. When compared with theoretical and experimental benchmarks, it is observed that best theoretical EFG alignment for silver is achieved at $\omega=0.55-0.6$ while the halogens favour $\omega=0.65-0.75$ and $\omega=0.7-0.8$ for chlorine and iodine respectively. Experimental alignment for the halogens would favour $\omega=0.25-0.3$ and $\omega=0.05-0.2$ for chlorine and iodine respectively. Given CCSD(T)'s tendency to predict more charge transfer to the halogens and favour a higher charge in Ag $5p_z$, it is within what is expected that intermediate ω aligns better with Ag and high ω with the halogens. The experimental halogen EFGs are very positive, suggesting a smaller z-polarised halogen charge, such that less charge is drawn from Ag, favouring the very low ω .

4.4 Halogenated Aromatic Compounds

This section focuses upon the relationship between the atomisation and the electric field gradient of the halogens bromine and iodine when added to aromatic compounds (figure 4.4.1). Those considered here are the brominated and iodinated versions of the following organic compounds: halobenzene, 2-halopyrimidine, 2-halopyridine, 3-halopyridine, 4-halopyridine, 2-halothiophene, 3-halothiophene, halopyrazole and p-halotoluene. The broad range of aromatic organic compounds yields ample opportunity to contrast the EFGs of brominated and iodinated compounds, as well as variation caused by the composition of the compounds themselves and structural isomers thereof.

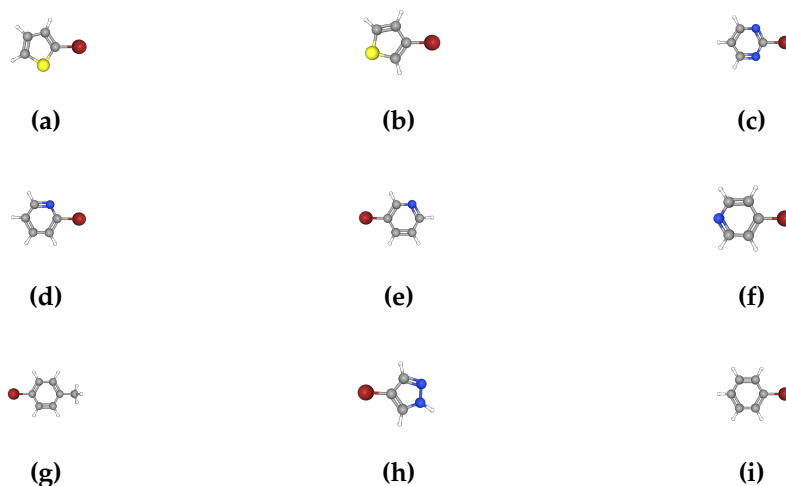


Figure 4.4.1: Halogenated aromatic compounds used in this investigation with halogen atom position denoted in red, the position of bromine or iodine. Carbon (grey), hydrogen (white), sulfur (yellow) and nitrogen (blue) are also show in the diagrams of a) 2-halothiophene b) 3-halothiophene c) 2-halopyrimidine and d) 2-halopyridine e) 3-halopyridine f) 4-halopyridine g) p-halotoluene h) 4-halopyrazole i) halobenzene. Images from *PubChem*

Figure 4.4.2 shows the atomisation-EFG characteristic for both isomers of halothiophene considered here, with the rest in B.2.1. Atomisations between brominated and iodinated compounds are relatively comparable, with the brominated compounds consistently displaying a slightly higher atomisation, reflecting that its bond with the aromatic compounds is slightly stronger, unsurprising given that bromine is a more reactive, electronegative halogen compared with iodine. Furthermore, there is variation in the atomisation of each compound. The halothiophenes possess the lowest atomisation, followed by halopyrazoles, 2-halopyrimidines, halopyridines, halobenzenes and p-halotoluenes. Indeed, it is quickly apparent that the structures with more double bonds (in particular between carbons) are the most stable structures, such as the halobenzenes, p-halotoluenes and halopyridines, and therefore they have the highest atomisations. The double bonds consist of hybridised sp^2 σ bond in the x-y plane, and a π bond between parallel p_z orbitals perpendicular to the x-y plane. The increased electronegativity of nitrogen relative to sulfur provides stronger bonding for halopyridines and halopyrazoles relative to halothiophenes. Within pyridine isomers, 2-halopyridine proves to be the most stable, with the nitrogen closer to the halogen, while thiophene is more stable with the sulfur further away from the halogen. Overall, Jacob's Ladder does not show any distinct relationship

between rung and atomisation energy for the halogenated aromatic compounds, in a similar manner to the transition metal complexes previously explored.

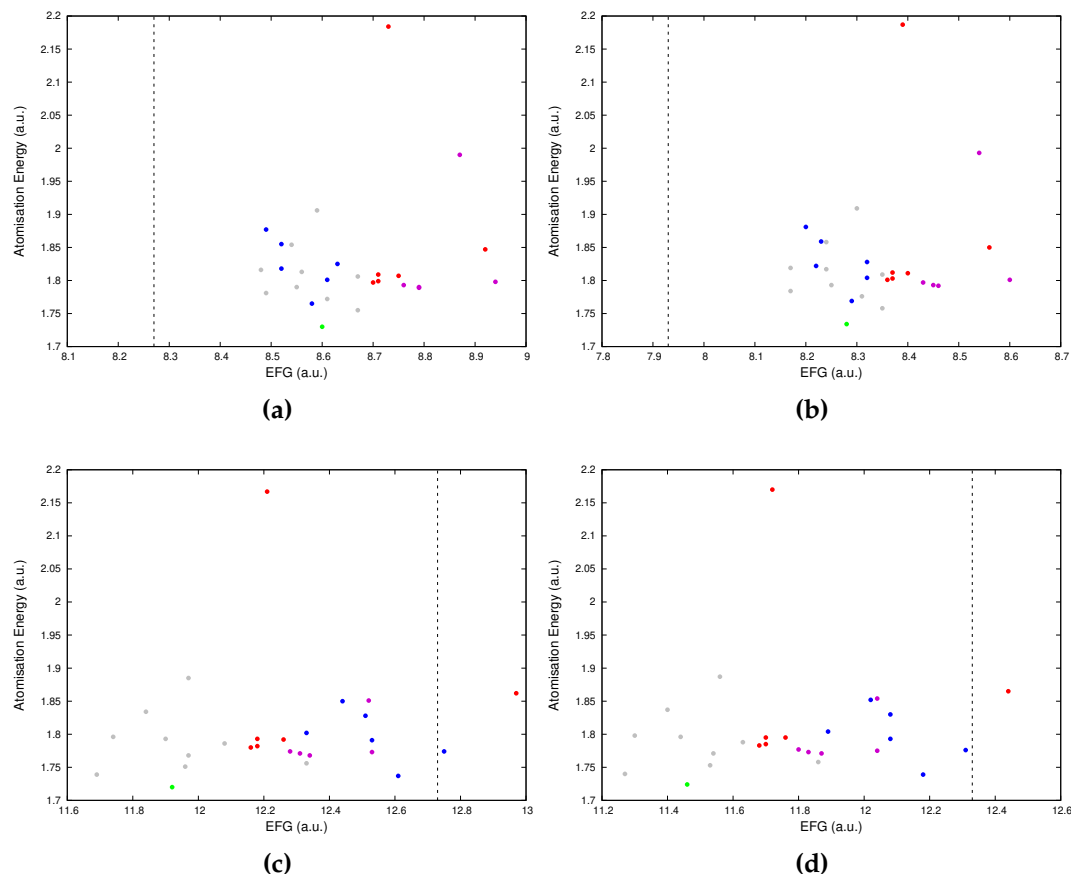


Figure 4.4.2: Atomisation-halogen EFG characteristic for a) 2-bromothiophene b) 3-bromothiophene c) 2-iodothiophene and d) 3-iodothiophene. GGA, hGGA, dhGGA and rshGGA are represented in blue, grey, red and light purple respectively. CCSD(T) is denoted in green, while the dashed line represents experimental EFG.

With regards to the electric field gradient, the field gradient of iodine is consistently more positive than that of bromine on all tested compounds. This is on account of its reduced electronegativity, such that more charge transfer to the aromatic ring occur for the iodine, disproportionately through the $5p_x$ orbital, such that the EFG through the x-direction increase significantly, which is the direction that aligns most with the bond the halogen has with the carbon that attaches it to the aromatic ring. Comparing the compounds, all of them are positive, due to the valent p_x orbitals on the halogen possessing less charge than p_y and p_z orbitals. The most-positive EFG is 2-halothiophene, followed by halopyrazole, 3-halothiophene, 2-halopyrimidine,

3-halopyridine, 4-halopyridine, halobenzene, 2-halopyridine and p-halotoluene is the least positive. From the Löwdin analysis, it is clear that the main driver is the concentration of p_x on the halogen, the more that is retained with this polarisation and not transferred to bonded atoms on the aromatic ring, the lower the EFG. Other important drivers are the changes in the p_y and p_z concentrations relative to $4p_x$. If these contributions increase relative to p_x , then the EFG becomes more positive as the polarisation increases in the z-y plane. In most cases, the p_z , which undergoes π -bonding with the carbon $2p_z$ orbitals, in particular with the carbon directly bonded to the halogen, stays relatively consistent regardless of the aromatic system considered. The concentration of p_y influences the x-direction EFG. A good example of the importance of this effect is the EFGs of 3-halothiophenes and 3-halopyridines. The concentration of halogen p_x actually falls relative to 3-halothiophene on the 3-halopyridine, however, the 3-halothiophene has a higher concentration of p_y localised on the halogen, increasing the polarisation in y relative to that in x, such that the EFG be higher on the 3-halothiophene. Considering the bonding in isomers, it is quickly apparent that the stability of the isomer (with increased atomisation) increases the less positive the EFG becomes. The halothiophenes become more stable as the number of bonds between the sulfur and the halogen increases. The sulfur in 2-halothiophene possesses a larger bond length with the halogen than that the equivalent carbon has in the 3-halothiophene, with the sulfur in 3-halothiophene also giving up more charge in the sp^2 bonds to the rest of the aromatic ring, and via the delocalised nature of aromatic bonding, increases the amount of charge in the carbon-carbon and halogen-carbon bonds overall, including a small increase in the p_x concentration in the halogen itself. thus a slightly less positive EFG. For the halopyridine isomers, a similar pattern between atomisation and lower positive EFG is reported. In this case however, 2-halopyridine is the most stable isomer, with the nitrogen closer to the halogen and in a double bond with the carbon directly bonded to the halogen. Here the nitrogen bond with the halogen is shorter than the equivalent carbon bonds reported in the 3- and 4-halopyridine isomers. The nitrogen reduces the influence of the proximal carbons to withdraw charge x-y polarised charge from the halogen, as it is moved away, this influence is weakened. Indeed, the small reduction in positivity of halogen EFG in 4-halopyridine relative to 3-halopyridine is actually due to a relative decrease in p_z charge concentration to the conjugated π -bond on the ring, due to the increased symmetry in the molecule.

Having established the driving forces behind changes in electric field gradient for the different halogenated aromatic compounds, attention now turns to the relationship between Jacob's Ladder and EFG. Indeed, it is noteworthy that in virtually all cases, the theoretically-predicted CCSD(T) EFG contains a larger positive core polarisation than all rungs of Jacob's Ladder, while the valence contribution is more positive on the DFT methods than the theoretical gold-standard. Furthermore, this trend continues as the HF fraction decreases down the rungs of Jacob's Ladder, with a reduction in the core polarisation for pure-DFT orbitals, while valence polarisation in the z-y plane increases. What is most interesting is that further study of the valence density reveals that pure-DFT methods contain a higher occupancy of valent p_x orbitals on the halogen, and lower quantities of p_z and p_y relative to higher-rung methods. By this measure alone, the halogen valence polarisation should be lower than that of methods containing a higher HF fraction, but in practice is not the case. Closer inspection of the orbital contributions to the halogen EFG reveals that the individualised contributions to the EFG are larger than those for B2GP-PLYP, even where the occupation is identical. This signifies that for smaller occupancy disparities between polarised orbitals, a larger EFG will result, as the field gradient generated per unit polarised charge is greater than for higher-level rungs of Jacob's Ladder. By inspection of atomic first ionisation potentials, it is clear that the halogens are predicted to be slightly more electronegative relative to carbon for lower rungs of Jacob's Ladder, and sp^2 -hybridised carbon in the aromatic ring is known to have electronegativity comparable, if slightly higher, to a generic non-hybridised carbon [184]. This explains why less xy-polarised charge is lost to the aromatic ring from the halogen, with the losses occurring more through the conjugated π -bond instead. The larger electric field gradients on lower rungs Jacob's Ladder are proportional to a larger virial ratio than those of hybrid functionals - a higher potential relative to kinetic energy. This ensures that the molecular orbitals are more concentrated closer to the nucleus, hence the larger EFG contributions per unit polarised charge. The larger core polarisation on the higher-rung functionals corresponds to a slightly higher angular momentum of polarised orbitals relative to lower-rung methods. This yields a larger relative increase in polarisation between core orbitals aligned with the EFG and those perpendicular thereto. The two counteracting drivers of halogen polarisation yield interesting results less clear than the silver complexes for DFT performance relative to theoretical and experimental benchmarks. For iodine, the valence

polarisation effect dominates more than on bromine, such that GGA functionals go from the least polarised functionals to the most, exhibiting large positive EFGs. hGGA and dhGGA groups are more stable and exhibit consistently less and more positive EFGs respectively, irrespective of the halogen concerned. rshGGA tends to be largely in line with dhGGA, or slightly more positive. Following experimental benchmarks, GGA tends to follow the experimental EFG, with experimental iodine EFGs largely in line with GGA, and to a lesser degree with dhGGA and rshGGA. For bromine, the experimental EFGs are usually less positive than those predicted theoretically, with GGA and hGGA representing the closest theoretical methods. When theoretical benchmarks are considered, it is observed that hGGA performs best for iodine EFGs, while GGA and hGGA perform best for bromine EFGs, though there are exceptions when dhGGA and rshGGA perform better, such as 2-bromopyrimidine. These results contrast greatly with those of silver complexes and indeed those observed in the CuCl complexes in the previous chapter, where dhGGA was the undisputed best-performing functional group, and favour pure-DFT functionals or those with a smaller HF-fraction.

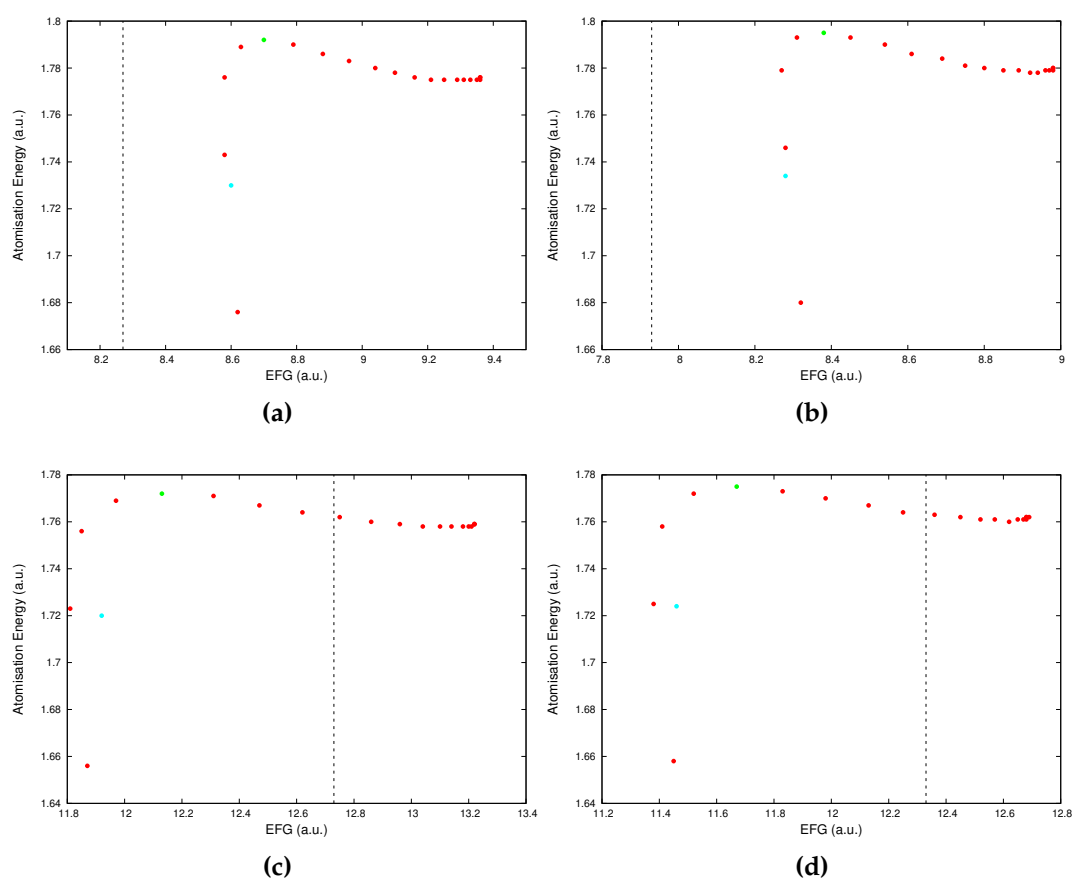


Figure 4.4.3: ω B97X change in atomisation and EFG for a) 2-bromothiophene b) 3-bromothiophene c) 2-iodothiophene and d) 3-iodothiophene over range $\omega=0.05-1$. Optimal $\omega=0.25$ for all halothiophene isomers and is denoted in green, with CCSD(T) in cyan. Experimental EFG is denoted by the dashed line

Figure 4.4.3 demonstrates ω B97X tuning for halothiophene isomers, the rest are shown in appendix section B.2.2. The ω B97X tuning study offers further evidence for the importance of the role of the HF-fraction in halogenated aromatic compounds. Save 2-halopyrimidines, that favour $\omega=0.3$, the default ω -fraction of ω B97X, the vast majority of aromatic compounds favour $\omega=0.25$ for best HOMO-IP agreement, a slightly more gradual rate of HF-fraction increase over inter-electron distance. For both halogens, increase in ω initially leads to very small increase in EFG positivity, with the rate of EFG increase with ω increasing just after the optimal- ω functional. When this is broken down into EFG contributions, it is apparent that the predominant driver of the EFG change is the valence density contribution. The valence density positive EFG increase at high- ω is driven by the halogens' becoming less electronegative relative to the sp^2 -hybridised carbon, such that more π -polarised charge be lost to the aromatic ring, with the concentration of charge

increasing in the conjugated π -bond, increasing z-polarised charge, with the overall effect of increasing the x-oriented positive EFG.

4.5 Discussion and Conclusions

Overall, this study has elucidated some key points of interest in regards to the performance of DFT functionals relative to theoretical and experimental benchmarks, and been further confirmed through the tuning of ω B97X functionals, in particular with regard to the impact of HF fraction in all of these systems. There is a key impact of increasing HF fraction consistently through all these systems, namely an increase in the HOMO potential. This is seen as HF fraction is increased as Jacob's Ladder is ascended, and also observed as the domain of high-fraction HF is increased in the tuning tests. This increased HOMO potential is indicative of increased electronegativity of all atoms studied, silver and the three halogens Cl, Br and I. This fits with the improvements HF exchange makes in cancelling self-interaction error and balancing the abrupt exponential dropoff of DFT exchange as inter-electronic distance increases, increasing the potential in which the occupied electron orbitals are held, including valence orbitals, thus increasing ionisation potential, and in turn electronegativity. However, it is the relative difference in electronegativities that is important for determining the polar covalent bonding that dominates the different systems studied herein. Crucially, the electronegativities do not increase by the same amount as one rises through Jacob's Ladder. Silver's electronegativity plateaus as HF-fraction is increased, seen both in Jacob's Ladder and in the Koopmans' tuning investigation of ω B97X, while electronegativity of halogens continues to increase, albeit at a slower rate. This relative increase favours increased polarity in the bonds with the halogens, with the halogen's negative charge increasing. This is offset by increased occupancy of Ag $5p_z$ which aligns with the σ -bond with the halogen at the expense of the Ag $5s$ orbital and the increased z-polarised core polarisation, which leads to Ag following a similar EFG change to the halogens despite charge loss. The core polarisation is a direct consequence of valence-electron rearrangement, and relies on long-range exchange mediate its effect to core electrons. Increasing polarisation of valence charge leads to increased repulsion of core charge in the line of valence polarisation, via Coulomb repulsion but also crucially via Fermi repulsion, which concentrates z-polarised core charge closer to the nucleus relative to that polarised in the x-y plane. This increases the principal-axis polarisation and in

turn the EFG in the line of the valence polarisation. However, the less the HF-fraction in the exchange, the less polarisation can be mediated back to the core electrons. Likewise these functionals have less z-polarised valence charge, such that there is less charge to mediate core polarisation. This behaviour is largely comparable to the characteristics observed of copper in the previous chapter and indicates the sensitivity of transition metal core polarisation to small perturbations in the valence density, and the favouring of a larger HF-exchange fraction over a larger inter-electron separation domain in the ω B97X tuning investigation for both transition metals relative to the halogens to which they are bonded. The ω -parameter only falls in systems where the HOMO becomes more localised on the halogen.

Likewise in the aromatic systems, higher HF-fraction leads to halogens becoming less electronegative relative to sp^2 -hybridised carbon, so that more charge is localised in the ring in the polar-covalent bonds formed with the halogen, leading to halogen EFG increase. However, it is crucial not to overlook all contributing factors to the EFG. Iodine EFG actually increases without any HF-fraction, with the GGA functionals obtaining the largest positive EFGs. This is explained by a quick glance at the GGA virial ratio, the high potential relative to kinetic energy yields higher EFG contributions from polarised orbitals due to the slightly shorter radii of electrons from the nucleus, such that in imbalance in polarised valence orbitals smaller than that of dhGGA actually yields a larger net EFG. However, it is clear that the functional groups with HF-fraction follow largely the same pattern be they bromine or iodine. ω B97X tuning further confirms this pattern, with increased HF-exchange over more of the inter-electron separation domain favouring a more electronegative ring relative to the halogen.

It is noteworthy that in all systems studied herein, the CCSD(T) valence EFG is often lower than the corresponding DFT functionals, but core polarisation is higher. This is especially prevalent for the silver EFGs in the silver complexes, and halogens in the aromatic systems (halogen EFG is also lower in the silver complexes, owing to their electronegativity in these systems being higher than silver for CCSD(T), leading to more principal-axis-polarised charge on the halogen thereby reducing the overall x-y polarisation and making the EFG less positive). In these systems, the atoms are less electronegative relative to those around them (though electronegativity increases overall due to exact self-interaction cancellation for non-Kohn-Sham orbitals) and therefore lose charge to the atom/ring with which they are bonded, though compensating with more of the remaining valence charge

occupying previously-unoccupied z-polarised orbitals in a similar manner to high HF-fraction DFT functionals. However, the valence polarisation is more able to polarise the core orbitals, due to pure HF exchange.

What is seen in the overall investigation throughout chapters 3 and 4 is the direct impact of HF-exchange in the systems studied. Firstly, the impact of HF-exchange in reducing the electron self-interaction error. The reported link between electronegativity error and self-interaction error has been reported in previous dipole and ionisation potential studies [29, 34, 185–187]. However, the extent to which this can correct self-interaction, while also losing some of the more local DFT exchange, leads to disparities in electronegativity change between different atomic species. Halogens become more electronegative relative to transition metals, but less relative to carbon or oxygen. This accounts for the change in EFG of the halogens in both the silver-complex and aromatic environments. The ability to polarise the core electron density is contingent on the ability to execute non-local exchange, hence the dramatic change in core polarisation on the silver atom, in particular in the diatomics AgCl and AgI without the added ligands as HF-exchange fraction increases. However, the disparities between the DFT and CCSD(T) valence and core contributions are striking, particularly in the silver EFG. Even where there is alignment, it is often that the DFT functional has predicted a higher valence polarisation relative to CCSD(T) to compensate for its lower core polarisation. It is indicative of a flaw still inherent to DFT - it is limited in its ability to capture core polarisation by the amount of HF exchange present. However, HF exchange is no silver bullet in DFT. Its effect to limit self-interaction of Kohn-Sham orbitals cannot match the *ab initio*-derived orbitals of CCSD(T), limited further by the loss of local DFT exchange, and the extent to which it is effective varies from atom to atom. Hence, relative to experimental and CCSD(T) benchmarks, the functionals sometimes predict a larger bond polarity than CCSD(T) predicts. The range-separated functional group is designed to effectively capture the advantages of both DFT and HF exchange, but from investigation of ω B97X tuning, it is clear that the transition metals perform better at different ω relative to the halogens, and that HOMO-IP agreement moves around depending on which atom the HOMO is majoritarily concentrated for the silver complexes. Indeed, many of the hGGA, rshGGA and dhGGA functionals are parameterised to perform well for properties dependent on valence properties - ionisation potentials, electron affinity, atomisations. Hence, despite the disparities with

the EFGs, there was no notable change in atomisation relative to theoretical benchmarks. This, however, fails to probe sufficiently the core density, which as it is proven here, does have a role to play in capturing the EFG of transition metals in particular.

This reflects the actuality of DFT research, some hybrid functionals here are guilty of obtaining the right answer for the EFGs but for the wrong reasons - predicting greater valence density polarisation which offsets errors in core density. In order to yield further improvement in the future in particularly difficult systems such as transition metal complexes, it is perhaps prudent to study further properties associated with the core to improve future functionals, such as photon-induced ionisation from core electrons, or photo-absorption spectra for transition metals. The utility of the EFG is that it is an indicator of density rearrangement that can be compared to experiment as well as theoretical benchmarks. Indeed, as shown by the iodine EFG in the aromatic compounds, theoretical and experimental benchmarks are not always in perfect agreement, and both have their sources of error. But both provide essential indicators of DFT performance, with the additional advantage of CCSD(T) of being able to probe the electron density further, to see how well Kohn-Sham orbitals approximate those obtained via *ab initio* method. The performance of dhGGA functionals for transition metal complexes in both the previous chapter and this one stresses the utility of HF exchange, while the performance of GGA and hGGA for halogens in aromatic compounds relative to the two benchmarks chosen suggests the need to balance this with DFT exchange. It is with this in mind that the utility of the rshGGA functionals - extracting the best of both exchange contributions - could be further explored, but as suggested here, more will be required than simple tuning to valence properties. The high computational cost of CCSD(T), as outlined in section 4.2, illustrates the need for accurate DFT calculation. The EFG provides a useful mechanism to further study DFT performance both theoretically and with regard to experimental reality, and provide deeper understanding of the roles of HF and DFT exchange in future such that more useful and resilient functionals can be developed in future to the advancement of theoretical chemistry.

Chapter 5

Analysis of Forcefield Methods to Predict Solvent-Term Ultrafast X-ray Scattering Relative to Experimental Metrics

5.1 Introduction

X-ray scattering is one of the most common and versatile techniques used to image molecular structure throughout physical science, utilised in all fields from structural biology [72, 74–76] to solid-state physics [73]. Recently, the development of X-ray free-electron lasers (XFELs) has allowed for the observation of chemical reaction dynamics and solvent-solute interaction on ultrafast time scales [72, 77–83], further expanding the utility of this technique in physical science. Pump-probe techniques utilised in scattering experiments lead to scattering signal change under hydrodynamic rearrangement [1, 143]. In order to discern the change in solute structure under such conditions, terms associated with the solvent and the solute-solvent interface must be extracted from the total received signal. Solute-solvent terms are only possible to extract directly via theoretical calculation, and are dealt with in chapter 6. Solvent terms have the option of extraction experimentally [84–87] or through approximation theoretically from molecular dynamics (MD) trajectories [86–91]. Theoretical prediction utilises radial distribution functions (RDFs) from the MD trajectories and utilises the independent-atom-model (IAM) to predict scattering profiles, whereby atomic scattering factors $f(Q)$ are used to predict scattering, without consideration of the influence of bonding in the molecule [72, 143]. Recent studies indicate that the IAM is sufficient, with bonding not significantly changing the predicted profiles [77].

Theoretical IAM scattering change under hydrodynamic rearrangement is directly attributable to the change in radial distribution $\Delta g_{lm}(R_{jk})$ [143]. Recalling from chapter 2:

$$\begin{aligned} \Delta S(Q) = & \sum_l N_l f_l(Q)^2 \\ & + \sum_{l,m} f_l(Q) f_m(Q) \frac{N_l(N_m - \delta_{lm})}{V} 4\pi \times \int_0^{R_{max}} R_{jk}^2 \Delta g_{lm}(R_{jk}) \frac{\sin(QR_{jk})}{QR_{jk}} R_{jk}^2 dR_{jk} \end{aligned} \quad (5.1.1)$$

Indeed, theoretical scattering has the potential to tailor solvent-term extraction to any solvent molecule for any form or hydrodynamic rearrangement to mimic the change in conditions incurred by a pump-probe event. MD trajectories can be configured to ultrafast time scales comparable to XFEL pulses to obtain radial distribution functions reflecting femtosecond time scales. However, there has been little investigation into the significance of force-field selection in determining the solvent scattering or evaluation of overall accuracy. Herein, two force fields utilising different methods of parameterisation are utilised and evaluated relative to experimentally-extracted solvent terms and to each other. OPLS-AA (Optimised Potential for Liquid Simulations-All Atom) is a popular force-field used throughout computational chemistry. It is parameterised to ensure agreement with experimental data of liquid properties, such as heat of vapourisation and density [146, 148] and compares well with other force fields [188]. Recently, the Cole group has developed QUBE, derived from QUBEKit (Quantum Bespoke Kit) software, utilises theory to determine bonded and non-bonded parameters [4, 5] via DFT calculation, thereby having more transferability and versatility than experimentally-derived force fields, which often struggle outside the experimental data for which they were designed [5]. QUBE is designed to use ω B97X-D [25] functionals, part of the rshGGA group which proved the most versatile functional group across all systems studied in minimising self-interaction error through use of large fractions of Hartree-Fock exchange, particularly in long-range Fermi repulsion. This places it ideally to provide high-quality electron densities from which to derive bonded parameters and partial charges. Here both are evaluated as candidate force fields to determine the scattering change of common solvents per unit temperature and pressure change, relative to experimental benchmarks for pump-probe events [1], whereby areas of divergence between force fields are related to their parameterisations.

5.2 Theory and Computational Details

Molecular dynamics simulations were used to calculate radial distribution functions for common organic solvents: acetonitrile (MeCN), chloroform (CHCl_3), dichloromethane (DCM) and ethanol (EtOH). The simulations utilised OpenMM software [189] with femtosecond time intervals. Data was reported every 500fs and the total trajectory was 20ns. The first 100ps was excluded to ensure equilibrium box conditions. The solvent scattering term is designed to mimic the change in conditions caused by a pump-probe event, i.e.:

$$\Delta S(Q) = S_{on}(Q) - S_{off}(Q) \quad (5.2.1)$$

Whereby two simulations are carried out, one corresponding to an unpumped/ground sample (S_{off}), taking as room temperature under standard atmospheric pressure (298.15K, 1.0bar) and another to represent change incurred by a pump event. S_{on} is simulated through the second box, with a perturbation in hydrodynamic conditions. Scattering change per unit temperature is calculated using simulations 1K and 5K above the unpumped sample to recreate initial temperature increase from the sample to the solvent. Pressure changes (0.05bar and 0.20bar) were used to recreate subsequent density rearrangement. Total scattering from a pump-probe event is a summation of these two rearrangements [1]:

$$\Delta S(Q) = \Delta T \frac{\partial S(Q)}{\partial T} + \Delta \rho \frac{\partial S(Q)}{\partial \rho} \quad (5.2.2)$$

Δg_{lm} between the two simulations allows for calculation of scattering change. It is important to note that experimental hydrodynamic rearrangement is a non-equilibrium effect. $\Delta S(q)$ is ascertained from the time-averaged Δg_{lm} via in-house scattering software.



Figure 5.2.1: Solvents used in this investigation for a) acetonitrile b) chloroform c) dichloromethane and d) ethanol

5.3 Results

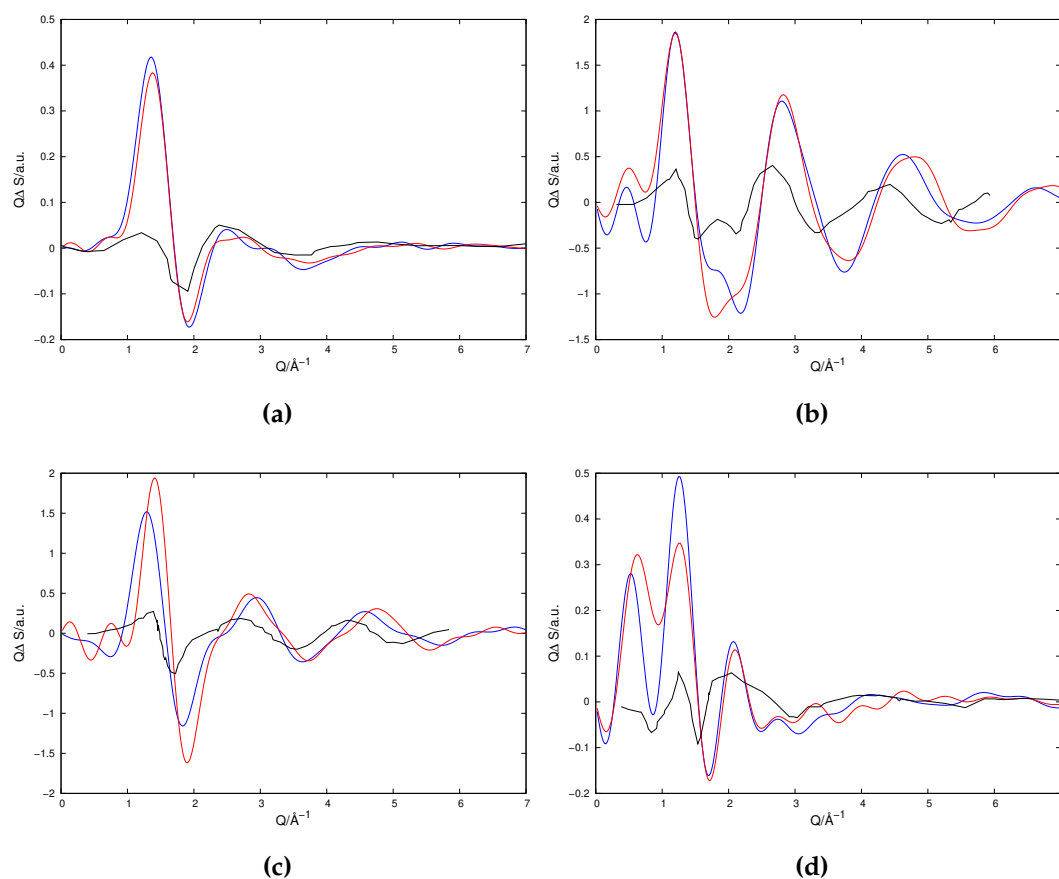


Figure 5.3.1: $\frac{\partial S}{\partial T}$ per solvent molecule characteristic calculated from 1K solvent differences from OPLS-AA (blue) and QUBE (red), compared with experimental calculations (black) [1] for a) acetonitrile b) chloroform c) dichloromethane and d) ethanol

Figure 5.3.1 illustrates the difference between the temperature-dependent solvent scattering characteristic derived theoretically and compared with experiment. Density-dependent solvent scattering was also investigated but density change from pressure increase was too low and therefore predicted incorrect results (see figure C.1.2 as an example for MeCN) so has been discounted from this investigation pending future work. Figure 5.3.2 also shows near concordant results derived from 5K results, with the scalability of the 1K and 5K illustrated for both theoretical methods, the example of acetonitrile is shown therein, with similar results for the other solvents (figures C.2.1-C.2.3). The majority of the scattering change per unit temperature occurs in the low- Q region. Indeed, MeCN and EtOH report virtually no change for $Q > 3$. CHCl_3 and DCM have less drop-off in the high- Q region, though the profiles are still dominated by change in lower scattering magnitudes. Scattering per molecule is also higher for these solvents, with peaks around 4x those of MeCN and EtOH. This is accounted for by the presence of Cl atoms with high scattering amplitude (relative to the other atoms contain within the solvents). The dominance of the Cl atoms is further shown by the near-concordance of the scattering magnitudes for which peaks are observed between these solvents. There is strong agreement between OPLS-AA and QUBE (particularly for MeCN) with concordance between scattering peaks increasing with Q . However there remains small differences in $S(Q)$ for $Q < 2$, particularly in DCM and CHCl_3 , affecting the relative amounts of scattering and scattering magnitudes for which they occur between the QUBE and OPLS-AA profiles. The increase of low scattering magnitudes at the expense of higher magnitudes and relative agreement of $\frac{\partial S}{\partial T}$ regardless of temperature change attests to increase in equilibrium distance between solvent molecules driven by solvent heating. Change in scattering peak heights are associated with changes in the magnitude of $g(r)$ for dominant atom combinations, while shifts in Q at which they occur are driven by change in r at which the RDF peaks (i.e. change in the equilibrium r). Differences between QUBE and OPLS-AA solvents are therefore associated with the non-bonded parameters that govern intermolecular interactions. Interestingly, there is some theoretical-experimental agreement for Q but not the scattered intensity, with theoretical scattering change around 5x that found experimentally. This appears to suggest that changes in the ordering of real solvents are less dramatic than theoretical prediction. Indeed the theoretical solvents represent ideal conditions at equilibrium temperatures, while solvent heating in experiment is a non-equilibrium event [72, 84–87], with heating localised on

the solute and transferring to the solvent over time.

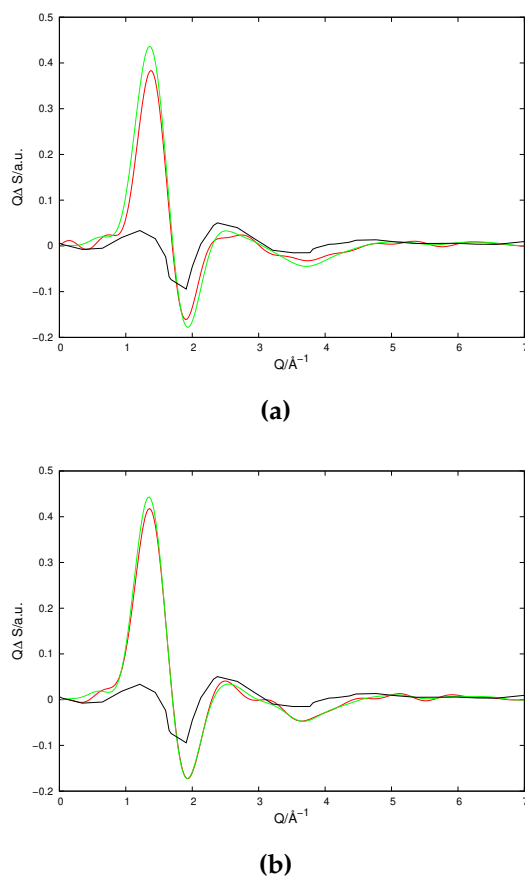


Figure 5.3.2: $\frac{\partial S}{\partial T}$ per solvent molecule characteristic of acetonitrile calculated from 1K (red) and 5K (green) solvent differences for a) QUBE and b) OPLS-AA, compared with experimental calculations (black) [1]

However, it is visible in figures C.2.1-C.2.3 that as the temperature change upon which the scattering change is based reduces down from 5K to 1K, there is some increased fluctuation in the scattering relative to experiment, and indeed between the force fields. This is particularly observable in the case of chlorinated solvents. Within this low temperature change, natural fluctuation in the distribution in the solution comprises a larger part of the radial distribution function, which is then carried forward when via Fourier transform when one converts from the RDFs into scattering magnitudes as a function of the deflected wave vector, leading to a less smooth profile. However, the aforementioned overall success in linear scaling in figure 5.3.2 represents a strongly desired quality if one is to generalise the findings of the force fields to predict scattering change on account of a heating event caused by the X-ray pulse in scattering events.

Having identified the sources of deviation from the experimental results, attention now turns towards the source of deviation between the scattering profiles of the OPLS-AA and QUBE methods. The independent-atom model (IAM) has been assumed throughout this investigation, so the contributing factors to the scattering change observed are the atomic scattering factors for the various constituent atom species themselves and the degree of difference between the radial distribution functions predicted by OPLS-AA and QUBE for pairwise combinations of atomic species. Across the solvents studied herein, atomic scattering factor plays a crucial role in amplifying smaller OPLS-AA-QUBE RDF differences between larger scatterers in the scattering profile, underscored in particular by the dominance of the chlorine scattering amplitudes in figure 5.3.1 for DCM and CHCl_3 . The contributions of the combinations of atomic species with the largest scattering factors is demonstrated in figure 5.3.3 (5K differences are in C.3). Key examples are the chlorine-containing solvents, chloroform and dichloromethane. The differences between OPLS-AA and QUBE Cl-Cl RDFs are amongst the smallest in both solvents, with the Cl-Cl radial distribution function yielding the smallest difference of all atomic species combinations. Indeed, figure 5.3.3 shows this difference to be smaller than those of the dominant combinations in EtOH (O-O). However, the Cl-Cl combination has a combined scattering factor that amplifies its influence in the scattering signal. Small changes in chlorine-containing RDFs lead to strong localised changes in the scattering profile when converted into wave vector space. Indeed, the dominant atomic species combinations responsible for the difference in the chloroform and dichloromethane scattering profiles are Cl-Cl and C-Cl, with a much smaller contribution from C-C (despite its having a similar RDF difference). Similarly, the dominant atomic combinations in acetonitrile contain the atom with the largest scattering factor, nitrogen and oxygen respectively. Indeed, ethanol's O-O combination also corresponds to the largest RDF difference between the two force fields, ensuring its precedence in influencing the scattering profile. The N-N term is also dominant in acetonitrile, though C-N and C-C also make significant contributions. Overall, the larger the scattering factor of the atom, the more significant any divergence between force fields or between the force-field predictions and experiment will be in all of the systems considered here. To the reverse, large differences in hydrogen-containing distributions are effectively masked, due to the low contribution of the hydrogen atoms to the scattering profile.

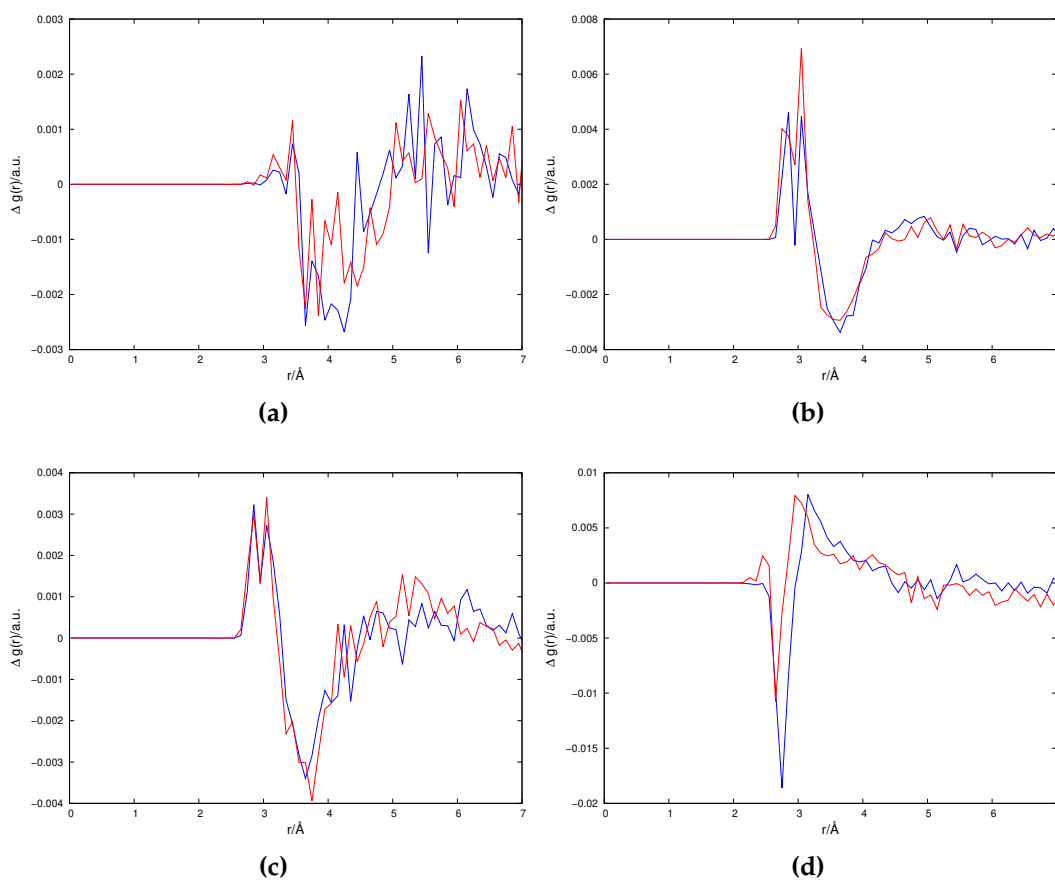


Figure 5.3.3: $\Delta g(r)$ contributions of dominant scattering atom combinations calculated from 1K solvent differences from OPLS-AA (blue) and QUBE (red), a) acetonitrile (N-N) b) chloroform (Cl-Cl) c) dichloromethane (Cl-Cl) and d) ethanol (O-O). Constituent atoms are labelled by colour, including carbon (grey), hydrogen (white), nitrogen (blue), chlorine (green) and oxygen (red). Image from *PubChem*

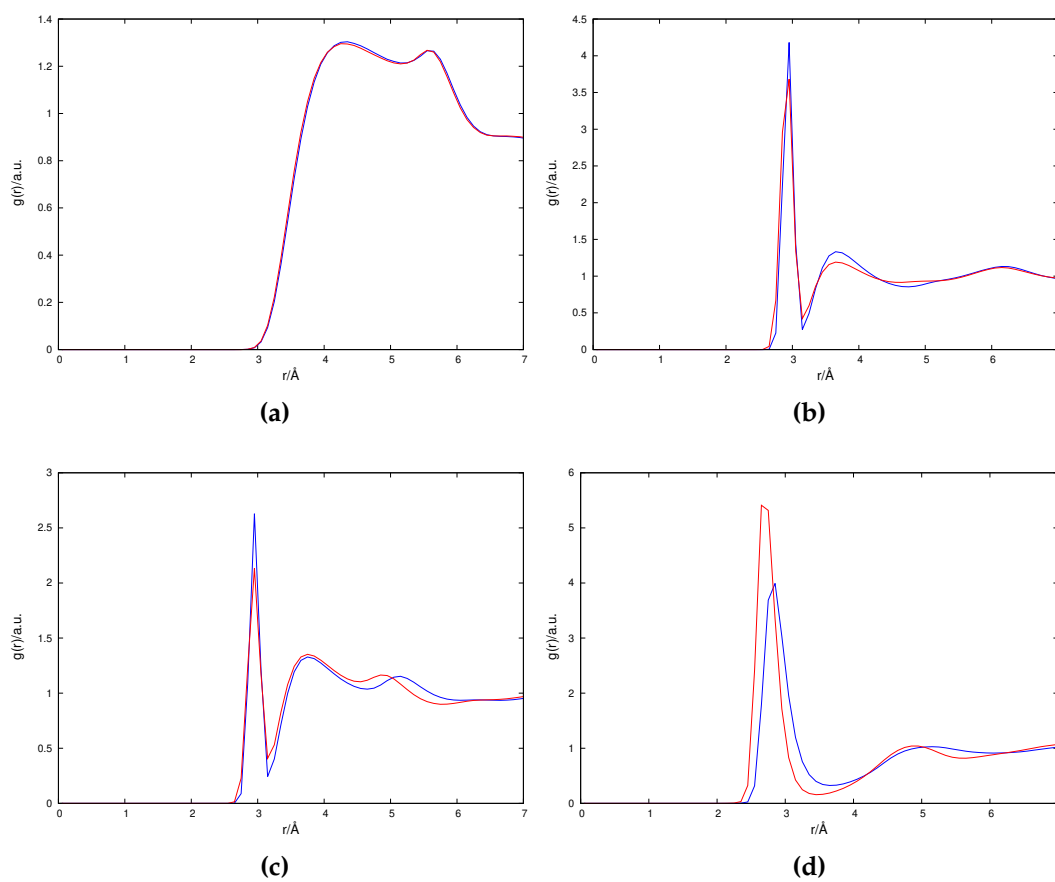


Figure 5.3.4: $g(r)$ contributions of dominant scattering atom combinations at ground temperature (298.15K) from OPLS-AA (blue) and QUBE (red), a) acetonitrile (N-N) b) chloroform (Cl-Cl) c) dichloromethane (Cl-Cl) and d) ethanol (O-O)

The source of the OPLS-AA-QUBE RDF divergences are sourced predominantly from the non-bonded parameters due to the crucial role of intermolecular interaction change in the solvents at different temperatures. The non-bonded term is composed of the partial charge and the Lennard-Jones (LJ) parameters, representing permanent and instantaneously induced dipoles respectively. Given that LJ parameters are often derived from free atom LJ data scaled to the partial charge via the Tkatchenko-Scheffler (TS) method [153], the partial charge difference is primarily responsible for the non-bonded parameter difference. This difference arises as a result of the different methodologies utilised by OPLS-AA and QUBE to determine partial charge, with OPLS-AA basing partial charges on agreement with experimental values for free energy of hydration and QUBE utilising atom-in-molecule (AIM) partitioning. Furthermore, the chloroform and dichloromethane solvents have virtual sites to account for local electron charge asymmetries in

QUBE, but not in OPLS-AA. These differences change the level of inter-molecular repulsion and attraction via dipole-dipole interaction, which in turn change the reported inter-molecular distances. This contributes into all RDFs once beyond the bonded radius. A clear example of this is ethanol - the larger QUBE partial charges indicate larger dipoles, and therefore a smaller intermolecular distance, due to dipole-dipole attraction. It also reduces the effect of external potentials i.e. temperature increase. Hence the RDF change is greatest for OPLS-AA with a larger accompanying shift in r , which leads to a larger reported increase in temperature-dependent increase in low- Q scattering intensity. Figure 5.3.4 illustrates the ground radial distribution functions of all four solvents, which facilitates understanding of the temperature-dependent perturbations in figure 5.3.3 (299.15 and 303.15K radial distribution are provided in figures C.3.1 and C.3.2 respectively). It illustrates the differences in equilibrium distances given by the different parameterisation methods, particularly for the O-O separation in the EtOH. The Cl-Cl RDFs show the presence of Cls on the solvent molecule, which cause the initial high gdrs at 2.9-3.0Å. Here differences arise due to the respective bond angles and force constants of Cl-C-Cl angles, and the C-Cl bond lengths that determine the resultant separation. Small changes in equilibrium conditions due to interaction with the solvent or minority contributions in this range from surrounding chlorine atoms at close range will have the effect of increasing broadening. The small range over which this occurs also leaves it especially sensitive to the RDF integrator step. Beyond 3.2Å the Cl-Cl distributions are governed exclusively by the non-bonded interaction.

5.4 Discussion and Conclusions

This investigation has provided a good overview on the performance of force fields and MD simulation as an alternative to experimental extraction of the solvent scattering, and accounted for difference in scattering prediction between the force fields as a result of RDF differences, arising from differences within the parameterisations of QUBE and OPLS-AA. Furthermore, it has established the relative importance of accurate RDFs, with the sensitivity of the profiles to small perturbations in RDFs containing large scatterers very high, while low scatterers' perturbations are effectively masked from the scattering profile.

From the analysed profiles, the force field profiles are indeed more similar to each other than to experiment, however, it is clear that particularly

in the ranges where most scattering change is observed ($Q < 3\text{\AA}$) that there is a difference in the OPLS-AA and QUBE profiles. The scattering change is driven solely by differences in their radial distributions [143], and can therefore be related to the temperature-dependent increase in intermolecular distance. Though the significance of the difference is also proportional to the magnitude of the atomic scattering factors pertaining to the radial distribution function in question [72, 143]. This leads to the important realisation that the significance of the differences in RDF between OPLS-AA and QUBE are proportional to the magnitude of the scattering of the constituent atoms. Thus very small differences in chlorine-containing RDFs are highly significant in shaping the scattering profile, while large differences in hydrogen-containing RDFs are invisible when the scattering profile is generated. The accuracy of the scattering profile is therefore more important as more electron-rich larger atoms with large scattering profiles are included as the size of the solvent scattered intensity increases relative to observed solute(s). Therefore RDF accuracy becomes increasingly important to prediction of accurate solvent terms as the atomic scattering factor of its constituent atoms increases. The difference with experiment require further investigation. It is unclear whether the differences arise from the limitations of MD trajectories to recreate an event which is in essence non-equilibrium and therefore time dependent, whereby the local atomic ordering suggested by theory would be less pronounced, or whether this results from force-field limitations, which would lead to cumulative error in the resultant trajectories and radial distributions obtained therefrom.

The differences in the RDFs for combinations of these most significant scattering species are sourced predominantly from differences in non-bonded parameters. The non-bonded parameters determine the intermolecular potentials, which in turn govern the equilibrium average distributions and intermolecular distances. These potentials also determine the influence of external potentials (temperature increase as a result of an external heat bath) in changing the radial distributions and their respective equilibrium distances. This is significant in driving the difference in scattering, particularly at smaller Q . As outlined in the results section, determining accurate intermolecular interaction is contingent on accurate determination of the partial charge, which differs between our candidate force fields. From the previous two chapters, the partial charge is directly connected with the relative electronegativities between atomic species, which differs between density functionals due to different rates of self-interaction error cancellation

[29, 34, 185–187]. Given QUBE's use of rshGGA, its accuracy is fully dependent on reduction of DFT error in predicting electron density as a result of HF exchange, particularly for long-range exchange. In essence it represents the most accurate theory possible within realistic time frames for theoretical research, as *ab initio* parameterisation would highly restrict its versatility and utility, particularly when parameterising larger molecules/complexes (see chapters 4 and 7 for limitations of *ab initio* theory in aromatic compound QM calculations and QUBE's parameterisation of transition metal complexes respectively). QUBE utilises the partition of charge throughout molecules to adjust the Lennard-Jones parameters, such that all non-bonded parameters depend on accurate electron density distribution. Its strong performance against a popular force field with charge distribution determined through free-energies of hydration of high chemical accuracy [190] vindicates the validity of theoretical parameterisation methods, and indicates future potential as theory improves.

This investigation provides a clear pathway forwards in developing force-field methods to better approximate theoretical X-ray scattering. Force-field differences indicate the importance of accurate force-field parameters, in particular non-bonded parameters, when simulating hydrodynamic rearrangement as a result of pump-probe events. The non-bonded parameters are all derived from the partial charge, and therefore depend on accurate description of molecular dipole moments. QUBE outlines the possibility of being able to parameterise any molecule without dependency on existent experimental free hydration data. For this method to maximise its parameter accuracy, it is important that the DFT calculations upon which it is based yield greater chemical accuracy than those possible through free energy of hydration data, and that this translates into accurate RDFs in molecular dynamical trajectories. The differences between experimental scattering and theory still remain, and there needs to be further investigation of the origins of such limitations such that theoretical extraction of solvent data continue to improve.

Chapter 6

Analysis of Forcefield Methods to Predict Solute-Solvent Ultrafast X-ray Scattering

6.1 Introduction

In chapter 5, the significance of force-field choice was established and evaluated with respect to experimental benchmarks. It also established that the scattering difference between OPLS-AA and QUBE could be attributed to differences in the radial distribution functions of combinations of elements with large atomic scattering factors. RDF differences arise due to differences in the non-bonded parameters of the solvents, particularly the partial charge. The partial charge alters the molecules' dipoles, and therefore the intermolecular potentials, changing the equilibrium intermolecular distances and thus the effect of solvent heating. This effect is less pronounced in solvents containing atoms with smaller scattering amplitudes, particularly MeCN, where there was virtually no difference between the scattering predicted by QUBE and OPLS-AA radial distributions. Theoretical scattering profiles' distinct advantage is in predicting solute-solvent interface, or "cross" scattering terms, that result from the interaction of the solute and solvent, something which cannot be done experimentally without convolution with either the solvent or solute term [1, 72, 92, 93]. Having now established that differences in parameterisation lead to divergences in scattering profile, it is now paramount to ascertain to what degree the cross-term is affected and the significance of this effect on ascertaining solute structure. This is particularly important given the role of non-bonded terms in driving divergence in the previous chapter, which determine the interaction between the

solute and the solvent. Any resultant change in the radial distribution function leads to in the resultant scattering [143].

In this investigation, the same solvents as those in chapter 5 are used, with solvated molecular iodine (I_2) as the candidate solute, which has received considerable experimental investigation via x-ray scattering methods [79, 191, 192]. Indeed, experimental observation of chemical dynamics of I_2 , in particular recombination from photodissociated I atoms, is noted as challenging due to the solute-solvent scattering, which changes with hydrodynamic rearrangement during pump-probe events [79, 192]. The solute dependence of the bond length of molecular iodine in polar solvents has received considerable investigation [193–197], characterised as undergoing a solvatochromatic shift [198, 199]. Kim *et al* recently studied molecular iodine solvatochromism in MeOH and via QM calculation elucidated the influence of the solvent in polarising the molecular iodine, leading to partial occupation of antibonding σ molecular orbitals and a resultant increase in I-I bond length [192]. The solute-solvent interaction of molecular iodine places it ideally for cross-term study of the force-field dependence of cross-terms, with the cross-scattering and iodine bond length serving as indicators of the interaction of the iodine with the solvent shell. Herein, cross terms are theoretically calculated using OPLS-AA and QUBE, with differences in performance related to change in radial distribution terms between solute and solvent atom species. These differences are evaluated with respect to non-bonded force-field parameter differences, and compared with the performance for solvent terms in chapter 5. The significance of the solvent and cross contributions can then be evaluated for their significance relative to the solute term.

6.2 Theory and Computational Details

This investigation follows the same method as that in section 5.2. The radial distribution terms are restricted to only those containing solute-solvent combinations in order to calculate scattering, with the according alteration made to the in-house scattering software to calculate cross-terms only. The density-dependent scattering problems in chapter 5 oblige that this study be also restricted to temperature-dependent scattering effects to facilitate direct comparison. I_2 required a bespoke parameterisation, DFT (B3LYP [21, 39]) was used to calculate bond length and force constants, Lennard-Jones parameters follow those used by OPLS-AA. It is used for both OPLS-AA and QUBE

solvents. Thus, differences between cross-terms could be directly linked to the solvent parameters. Solvents are those from chapter 5, and represent a scale of polarities. DCM is least polar, followed by CHCl_3 , EtOH and MeCN, the latter is considered a highly-polar solvent.

6.3 Results

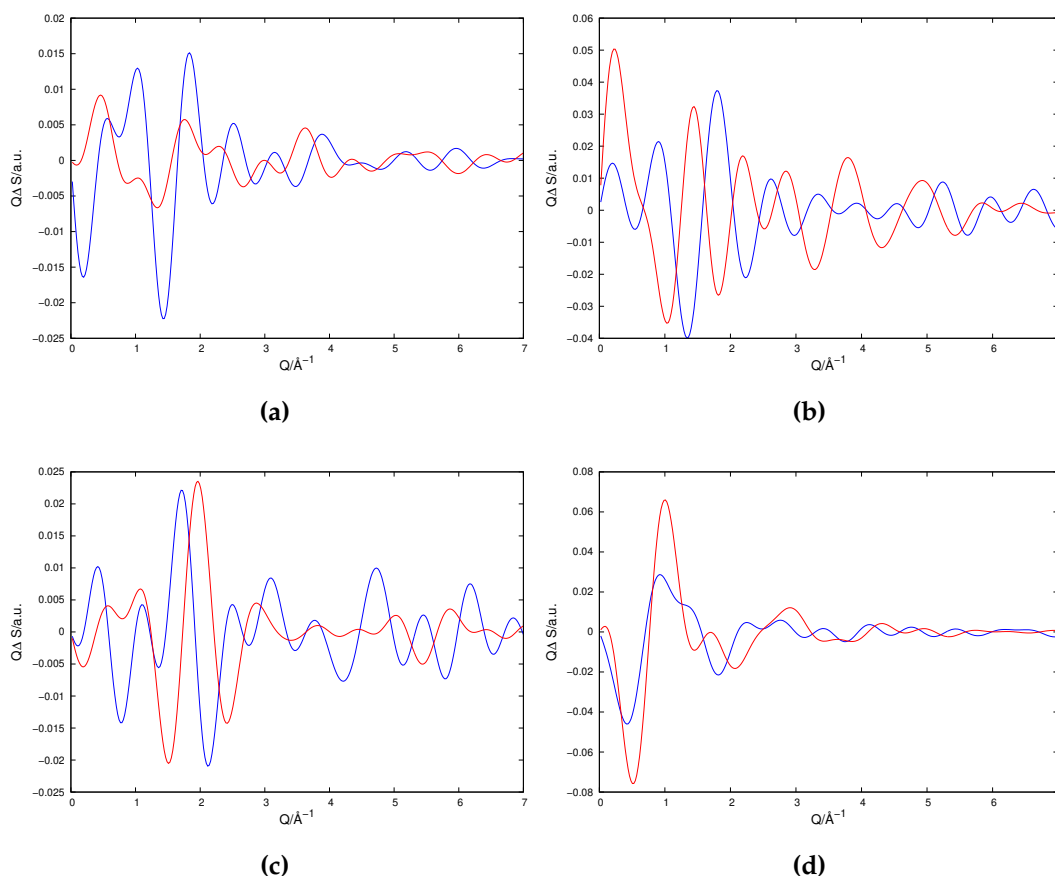
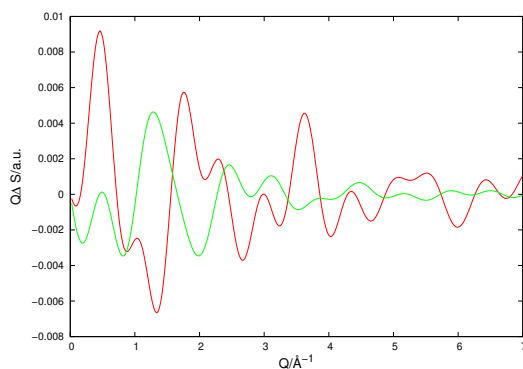


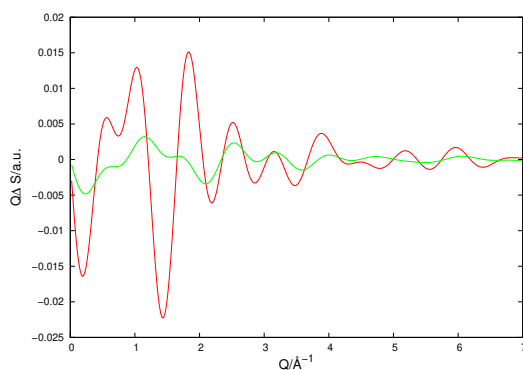
Figure 6.3.1: $\frac{\partial S}{\partial T}$ per solvent molecule characteristic of the I_2 solute calculated from 1K solution differences from OPLS-AA (blue) and QUBE (red) for a) acetonitrile b) chloroform c) dichloromethane and d) ethanol

Figure 6.3.1 illustrates the change in temperature-dependent solute-solvent scattering between the solvated I_2 molecule and the solvents considered herein (for 5K differences see D.1). It is noted that the resultant scattered intensity is considerably smaller than that of the solvent scattering, around 25x smaller than the solvent-term scattering for all four solvents. This is unsurprising, as this contribution is resultant from only the solute-solvent interface. The scattering change occurs predominantly for $Q < 3$, reflecting

that this change is predominantly driven by the intermolecular interaction between solute and solvent. Again, there is increased cross-scattering with the solvents containing Cl atoms, CHCl_3 and DCM, illustrating that atoms with large scattering factors report larger cross terms. The notable difference is in ethanol, with comparable scattering change to that of the chlorine-containing solvents. This is suggestive of a larger change in RDF relative to the larger scatterers. However, the reduction in scattered intensity of all solvents relative to solvent terms does leave the scattering profiles vulnerable to small changes in the radial distribution functions. There is poorer agreement for scaling of the scattering change per unit temperature between 1K and 5K temperature differences, as illustrated for MeCN in figure 6.3.2 (other solvents shown in D.2), with 1K differences accounting for larger reported change per molecule when adjusted for comparison. Importantly, it is observed that within these graphics there is noted divergence between the OPLS-AA- and QUBE-predicted scattering profiles. Given that there are no direct means of experimental cross-term extraction, difference between force fields is therefore significant and requires explanation in order to ascertain the utility of the predicted profiles.



(a)



(b)

Figure 6.3.2: $\frac{\partial S}{\partial T}$ per solvent molecule characteristic for the cross-term contribution of acetonitrile calculated from 1K (red) and 5K (green) solvent differences for a) QUBE and b) OPLS-AA

As identified in the previous solvent-term investigation and above, the application of the independent-atom model in this investigation allows for the identification of the most significant atomic species combinations, such that the significance of RDF divergences between force-field methods can be identified. The solute I_2 possesses a high atomic scattering factor, and therefore the most significant contributing RDFs to the cross scattering profile will be those that also possess large scattering profiles. In particular I-Cl combinations in chloroform and dichloromethane, and I-N and I-O combinations in acetonitrile and ethanol respectively. Cross-factors with small scattering atoms such as hydrogen are so low that they are in effect masked from the cross-scattering profiles, regardless of the size of the contributing RDF. Figure 6.3.3 illustrates these RDF changes. The I-Cl RDF changes are smaller than MeCN, but their larger scattering factors amplify this difference in figure 6.3.1. The larger difference in EtOH is noted, with a region (between 3-4Å) of significant divergence. The other RDFs are characteristic of small

overall increases in distance from the solute with temperature increase, with different initial solvent shell distances from the solute due to the differences of OPLS-AA and QUBE non-bonded parameters reported in chapter 5 and seen visually in the ground-temperature radial distribution functions of the same dominant atom contributions in figure 6.3.4 (for radial distributions 1K and 5K above ground temperature, see figures D.3.2 and D.3.3). Here there are large differences between I-O distributions derived from the respective methods, with OPLS-AA reporting a larger initial $g(r)$ increase relative to QUBE, before entering closer agreement just around 4.9\AA . It is therefore readily seen that the non-bonded parameters differences in partial charge interacting with the Lennard-Jones forces of the I_2 will be most significant in divergences between the profiles of the two force fields. In the case of EtOH, a possible explanation is that the dipole-dipole attractions between solvent molecules are stronger in the QUBE-parameterised EtOH, such that there be less interaction with the solute than for OPLS-AA-parameterised EtOH, while both methods predicting a larger solute-solvent intermolecular distance than the other systems studied herein. Temperature increase appears to more interaction with the solute, increasing probability of interaction with its L-J potential, which may be a potential explanation for the reporting of increased scattering in figure 6.3.1 for $1\text{\AA}^{-1} < Q < 2\text{\AA}^{-1}$ at the expense of scattering around $Q=0.5\text{\AA}^{-1}$, which would be associated with larger solute-solvent separation. This effect is offset overall for 5K as the temperature increase causes intermolecular separation to increase again. However, more research is required of EtOH to ascertain whether this accounts for its scattering change.

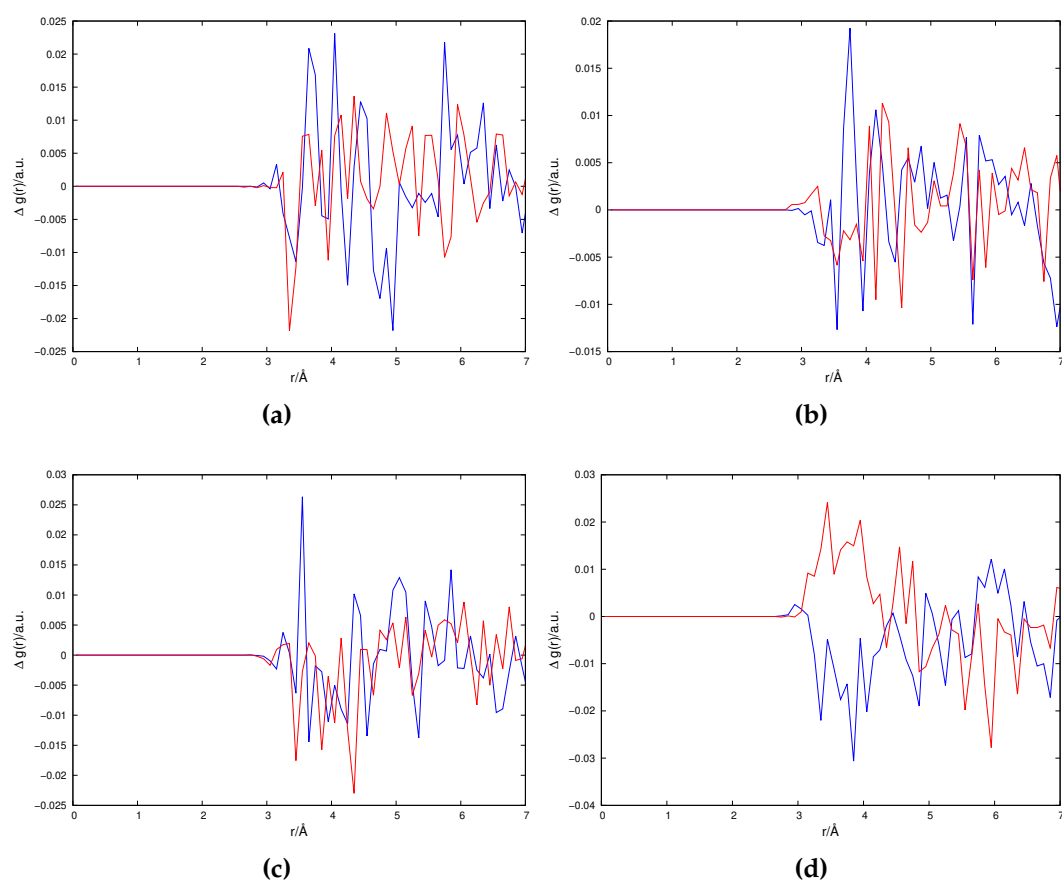


Figure 6.3.3: $\Delta g(r)$ contributions of dominant scattering atom combinations calculated from 1K solvent differences from OPLS-AA (blue) and QUBE (red), a) acetonitrile (I-N) b) chloroform (I-Cl) c) dichloromethane (I-Cl) and d) ethanol (I-O)

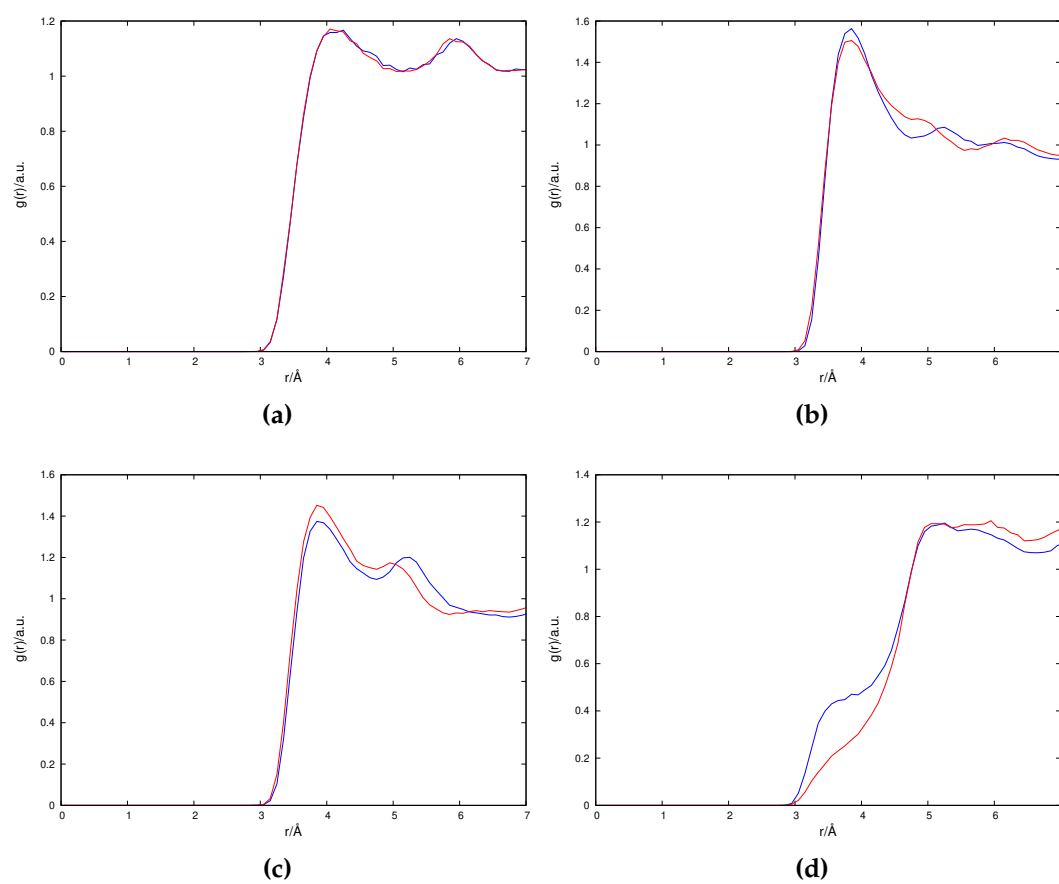


Figure 6.3.4: $g(r)$ contributions of dominant scattering atom combinations at ground temperature (298.15K) from OPLS-AA (blue) and QUBE (red), a) acetonitrile (N-N) b) chloroform (Cl-Cl) c) dichloromethane (Cl-Cl) and d) ethanol (O-O)

Having established the most significant RDFs and localised the solvent non-bonded parameters as the main driver of that difference, it is observed that a key difference between I-Cl RDFs for chloroform and dichloromethane is the inclusion of virtual sites in the QUBE parameterisation of the solvent, along with increased negative partial charge localised upon the Cl overall relative its OPLS-AA homologue. The virtual sites are included in order to better reflect the distribution of charge around an atom, a characteristic lost when the partial charge across an atom is reduced to a point charge. The increased overall negative charge on the chlorine is reflective of increased electronegativity of the chlorine atoms within the bonds. This is reflective of the underlying methodology. OPLS-AA utilises scaled $1.14 \times \text{CM1}$ charges within this investigation [190, 200, 201], which scale Mulliken charges calculated from semi-empirical AM1 quantum-mechanical calculations such that theoretical and experimental free energies of hydration align [202–205]. Other methods of charge derivation are possible, such as Localised Bond-Charge

Corrected (LBCC) CM1A and 1.20*CM5 [206], the latter being an example of advanced restrained electrostatic potential charges (RESP2). QUBE forms an example of the RESP2 approach, and utilises atoms-in-molecule (AIM) partitioning [4,5] to map partial charges on to theoretical charge distributions from DFT, with virtual sites used to simulate more accurate charge distributions where necessary. QUBE's increased electronegativity of halogens aligns well with the results of the previous chapters within this work that measured EFG performance with regard to Jacob's Ladder, and concluded that higher rungs with increased HF exchange fractions led to increased relative electronegativities of halogens through cancellation of self-interaction, with QUBE's parameters themselves ascertained from ω B97X-D calculations.

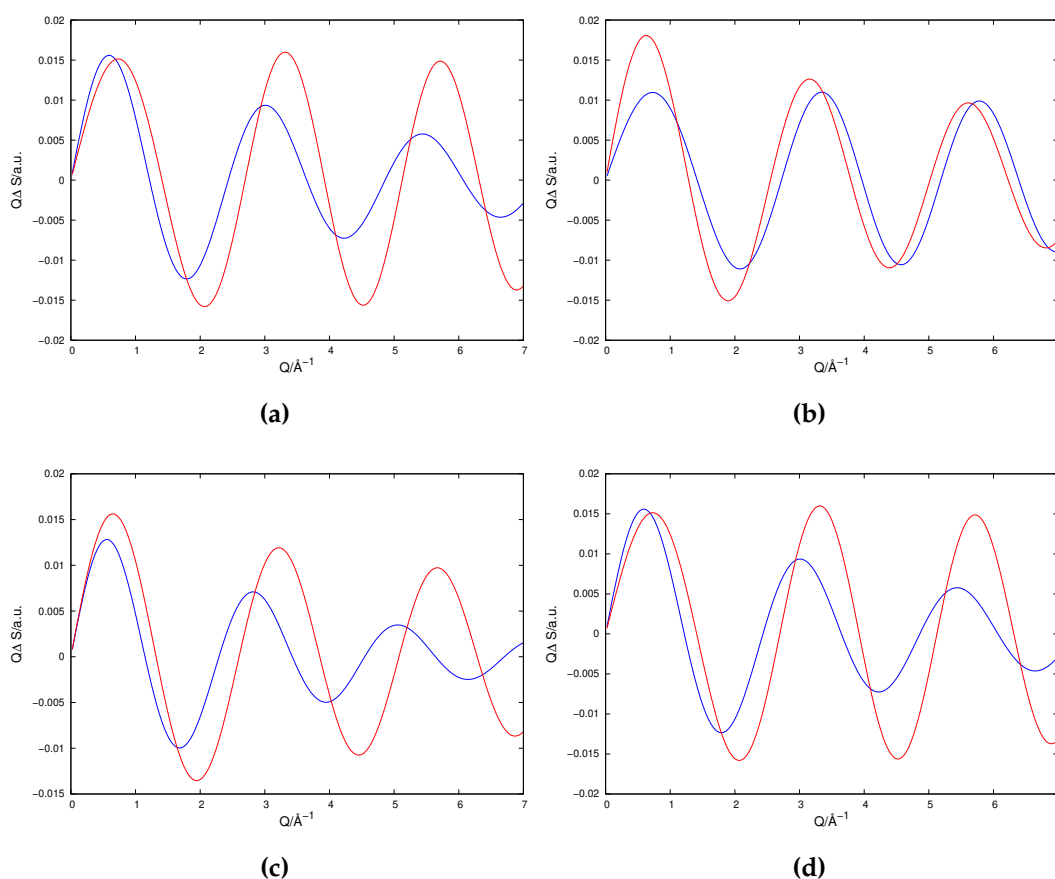
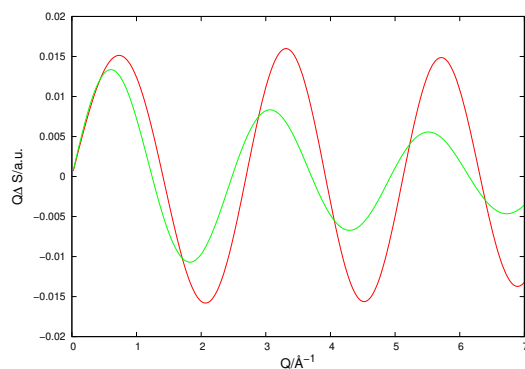
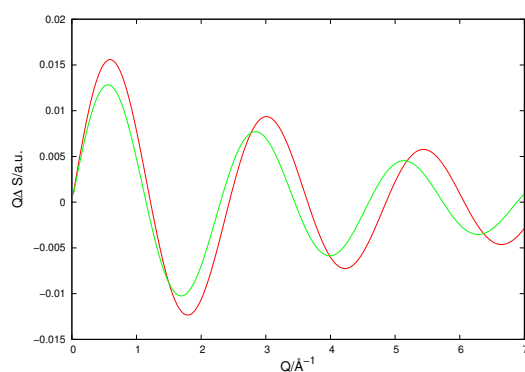


Figure 6.3.5: $\frac{\partial S}{\partial T}$ per solvent molecule characteristic calculated from 1K solution differences from OPLS-AA (blue) and QUBE (red) for a) acetonitrile b) chloroform c) dichloromethane and d) ethanol



(a)



(b)

Figure 6.3.6: $\frac{\partial S}{\partial T}$ per solvent molecule characteristic for the solute-term contribution of molecular iodine solvated in acetonitrile calculated from 1K (red) and 5K (green) solvent differences for a) QUBE and b) OPLS-AA

Figures 6.3.5 and 6.3.6 allow for assessment of the significance of the cross-terms, and evaluate the impact of solute-solvent interaction on the temperature-dependent scattering change of I_2 , given its solvatochromism (5K differences shown in D.4, scaling for other solvents in D.5). It is illustrated that the temperature-dependent solute scattering change is reported on scales comparable to that of cross scattering. The cross-scattering could therefore distort significantly the solute data if not correctly extracted. This is important as the cross-term extraction is fully dependent on the accuracy of the theoretical methods with no experimental alternative. This illustrates the importance of accurate theoretical prediction of the solute-solvent interaction. The figures show in addition that the choice of force field does influence the solute scattering term. Given that the I_2 parameters are the same regardless of the parameterisation of the solvent, this is directly related to the solvent environment with which the molecular iodine interacts. Figures 6.3.7 and 6.3.8 directly relate this to the change in radial distribution

iodine atoms, and compare it with the ground-state iodine-atom separation in solvent respectively (all other solute RDFs section D.6). In this context the change in radial distribution represents a small broadening or contraction of the I-I bond length. The tendency observed for MeCN and CHCl₃ is a small decrease in the iodine bond length, while the reverse occurs in EtOH. DCM illustrates a dependency on solvent parameters - QUBE predicts a small decrease in average I-I bond length, while OPLS-AA predicts a more general broadening, with increase in both shorter and longer bond lengths. Though these changes are small in the context of perturbation from the ground temperature distributions of the I-I bond length, but become significant due to amplification by the strength of the iodine form factors. The EtOH I-I bond length increase is of particular interest as it suggests a small increase in bond weakening as temperature increases, reflecting the bond weakening observed for MeOH in Kim's paper [192]. However, this broadening is not reflected in the ground state or for the other significant polar solvent herein, MeCN. The limitation of the fixed force-field parameters is that they cannot fully reflect the dynamical nature of the solute-solvent interaction and the induction of the partial charge in anti-bonding σ orbitals induced in molecular iodine by polar solvents. The non-polar solvents suggest an overall contraction in I-I bondlength relative to the ground temperature. This suggests less solute-solvent interaction as distance increases - reflecting the changes in solute-solvent observed in figures 6.3.1 and 6.3.3 - such that external potentials affect less the molecular iodine bond length. However this also needs further elucidation.

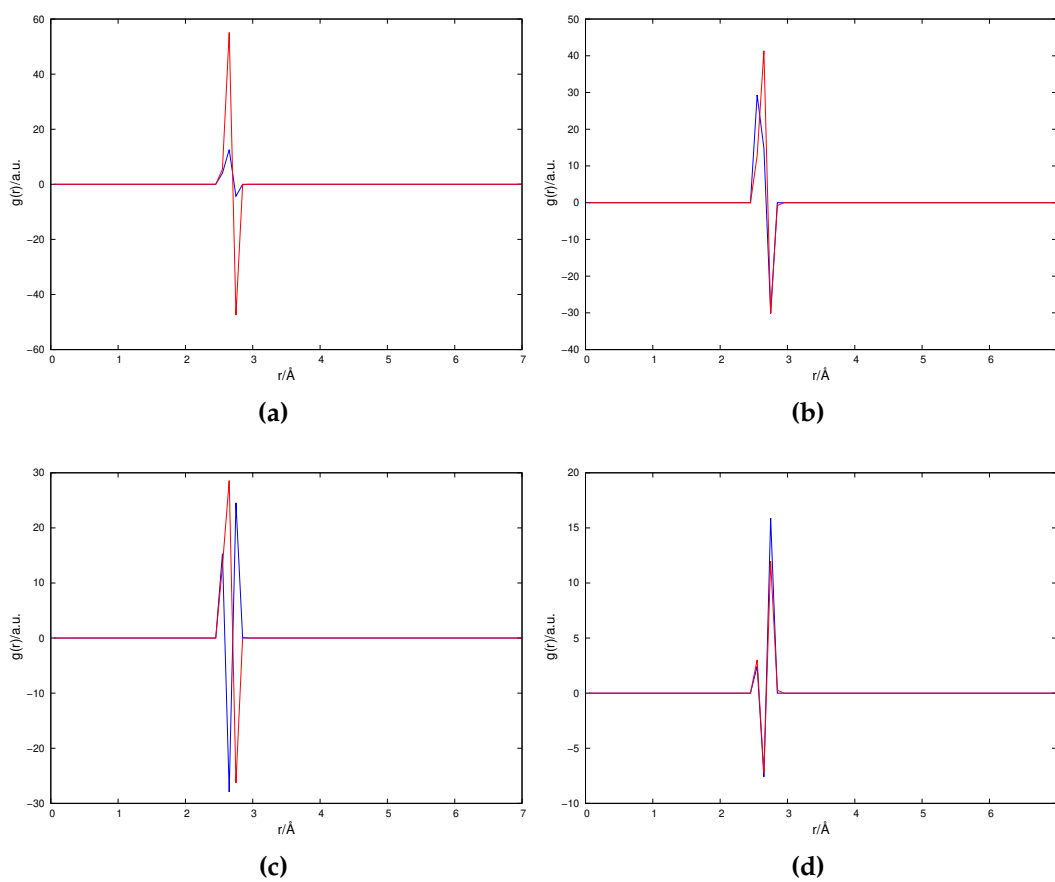


Figure 6.3.7: $\Delta g(r)$ contributions of the I-I solute atoms calculated from 1K solvent differences from OPLS-AA (blue) and QUBE (red), a) acetonitrile b) chloroform c) dichloromethane and d) ethanol

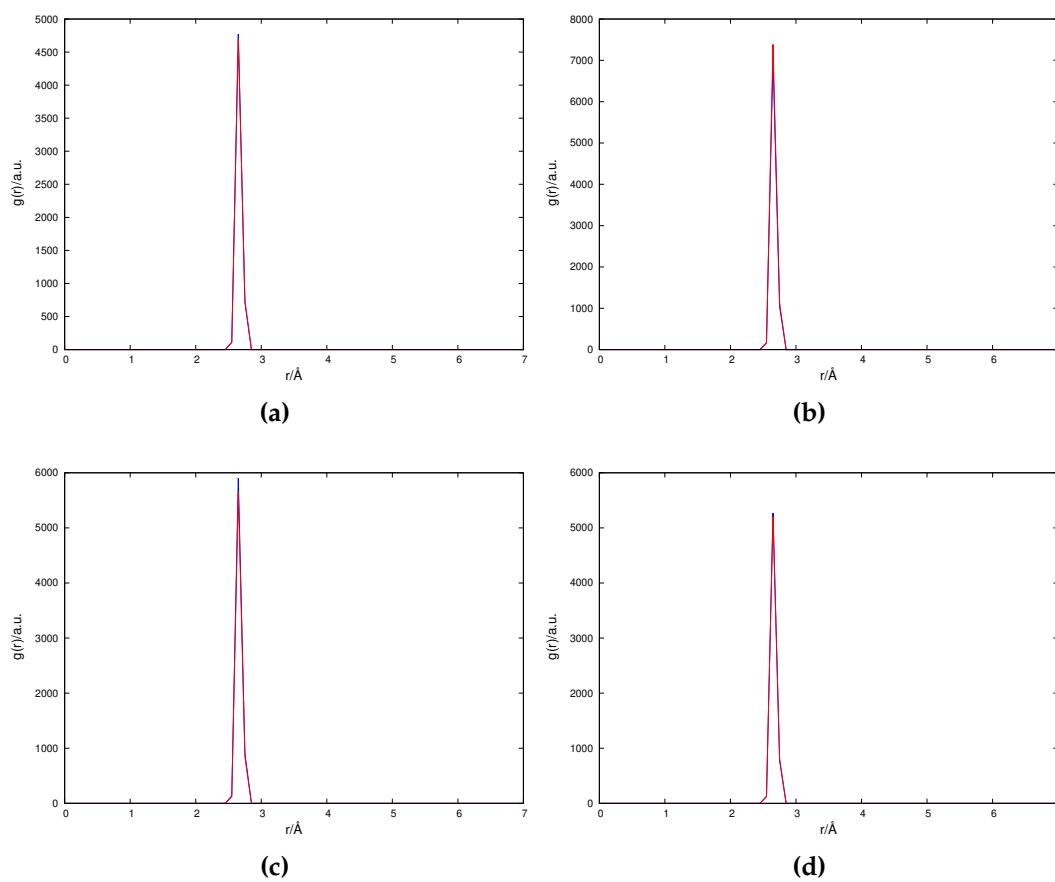


Figure 6.3.8: $g(r)$ contributions of the I-I solute atoms at ground temperature (298.15K) from OPLS-AA (blue) and QUBE (red), a) acetonitrile b) chloroform c) dichloromethane and d) ethanol

6.4 Discussion and Conclusions

The solute-solvent scattering intensity is considerably smaller than that derived from solvent RDFs, and therefore are reflective of small changes in radial distribution function. Given the large scattering amplitude of the solute, and of some solvent atom species (particularly Cl), small RDF variation between large scatterers can have profound impact on the obtained solute-solvent profile. Again the impact of atoms with low-amplitude scatterers (i.e. hydrogen) are effectively masked throughout all the systems considered. The importance of accurate RDFs for larger scatterers, along with the sensitivity of the cross scattering to small changes, reinforces the conclusion from the previous chapter. Indeed, the relative size of the cross term and the lack of experimental reference compared with the ready comparisons possible for solvent terms [1, 72, 92, 93] signifies the importance of minimising all sources of error in the force-field parameterisations. It is observed that

there are disparities in the scattering profiles of OPLS-AA and QUBE observed in all of the solutions considered herein. This indicates that the force-field choice is significant when scattering change is calculated, and is directly linked to the change in radial distribution functions predicted by the chosen force fields [72, 143]. Without an experimental alternative for cross-term extraction, the established force-field dependence of the resultant profiles is even more significant than for solvent-term extraction. Here the profile difference is driven by RDF divergence incurred for atom species combinations with large scattering factors. These RDF differences are attributable to the non-bonded characteristic of the solvent atoms, which alters the interaction with the solute. The analysis of the solute term illustrates that the temperature-dependent change in solute and solute-solvent scattering have similar intensities. This significance means that the observed force-field dependence of the scattering has the ability to distort observed solute changes if not extracted accurately, placing increased importance on cross-term accuracy. It is also illustrated that the solute-solvent interaction has the ability to change solute terms, and that there is a force-field dependence to these terms also. This ties not only the cross-term extraction to the solvent non-bonded parameters, but also that of the solute itself, irrespective of the method used for the solute parameterisation. This is particularly visible in the case of solvatochromatic solutes such as I₂, wherein polar solvents can influence equilibrium bond length. Albeit the classical force field methods herein are not able to demonstrate the polarisation effect created by the solvents within solvatochromatic solvents which drives this influence.

Overall, chapters 5 and 6 illustrate that force-field choice matters in determining solvent and cross-scattering terms, and provides a clear direction for seeking improvements in theoretical prediction. Solvent terms differences are small between force-field methods, but are limited compared with the predicted scattered intensities of experiment. Given the use of force-field methods that show strong agreement with other experimental metrics [5, 188, 207], it casts concern on the limitations of the molecular dynamics trajectories in predicting non-equilibrium experimental events, which will possess a greater degree of disorder and noise. Indeed, recent studies have cast concern on the utilisation of MD radial distributions for cross terms in favour of the "hard-sphere" simulations [208]. Solute-solvent terms also have a force-field dependency, and do not have an experimental benchmark with which to compare. It is also clear in this particular case of a solvatochromatic solute, that the solute-solvent interaction also alters the solute

structure, such that solute scattering change is also dependent on the choice force-field method for solvent, irrespective of the solute parameterisation. Given the comparable temperature-dependent scattering for cross and solute terms, cross-term extraction is necessary for quality solute data. Experimental benchmarks provide a means of further investigation of the accuracy of solvent force fields, and an ability to assess the accuracy of MD trajectories relative to alternative theoretical techniques. In turn this would assist in improving non-bonded interaction of solvents and solutes. However, the induction of partial charges [192] cannot be recreated using fixed force-field parameters alone. Given the success of time-dependent DFT (TDDFT) in elucidating the interaction of I₂ and polar solvents, QM/MM simulation would provide a logical future route to improve the accuracy of solvent-solute terms, with the QM centered on the solute or alternatively solute and first solvation shell. From chapters 3 and 4, providing a high-rung DFT functional for QM regions should be able to recreate accurately the valence electron density. Comparison with other techniques, such as hard-sphere calculations, would assist further in ascertaining more accurate solvent-solute interaction, in particular those with solvatochromatic solutes.

Chapter 7

Analysis of Cu(I)-Phenanthroline Excited-State Properties using QM-Derived Forcefield Parameters

7.1 Introduction

Recently many XFEL scattering studies have exploited the ultrafast visualisation provided to observe the excited-state dynamics of transition metal complexes undergoing metal-to-ligand charge transfer (MLCT) [82, 83, 94]. Transition metal complexes have been subject of great research interest for the potential yielded by their luminescence properties, not least in the development of organic light-emitting diodes (OLEDs) [3]. Such complexes provide excellent emission through the presence of low-lying excited states, which can be reached via photonic or electronic excitation. In many of these metal-organic complexes, excitation leads to the formation of MLCT states which often exhibit a rich photochemistry. While many of the pathways, e.g. internal conversion and fluorescence are similar to organic complexes, other pathways such as intersystem crossing (ISC) [3, 102, 209–211] are more common in transition metal complexes. The triplet states in these complexes can be populated on the ultrafast timescales. Several candidate complexes have been proposed, utilising various combinations of d-block transition metal ions and organic ligands, attempting to balance the abundance and cost of the former with the properties of the candidate complex. Originally research focused on second-/third-row transition metals with bipyridine ligands, including Ru(II) [212–214], Re(I) [215–218], Os(II) [219, 220], Ir(III) [221–223] and Pt(II) [224, 225], though high cost of such elements makes them unviable as options, despite strong performance as emitters. Thereon research has centered around d^{10} transition metal ions, with a particular focus upon

Cu(I) ions complexed with phenanthroline ligands, $[\text{Cu}(\text{phen})_2]^+$ [95–97].

Elucidating the photophysics of copper phenanthroline complexes has led to significant experimental [98–104] and theoretical investigation [3, 101, 104–109] of the complex. For $[\text{Cu}(\text{phen})_2]^+$, the simplest copper phenanthroline, excitation to the lowest singlet excited states (S_1) leads to ISC into the T_1 spin state, accompanied by a significant structural distortion. This distortion is associated with the pseudo Jahn-Teller Effect [99], whereby the charge transfer to the ligand leads to a d^9 configuration (Cu(II)) in the metal centre [102, 105, 106]. This electron degeneracy begets distortion to reduce resultant internal electrostatic potentials, resulting in ligands aligning along a principal axis to maximise interaction between the charge depletion on the copper and charge concentrations [226]. Ergo the ligand-ligand dihedral angle reduces significantly. The relaxation of the excited triplet state back to the ground state is dependent not only on the internal structural distortion but also the surrounding solvent [110]. Emission lifetime is reduced in donating solvents, as opposed to non-donating solvents [227]. The mechanism for emission lifetime reduction has been hypothesised to be an exciplex stabilising the Cu(II) ion triplet state, however there are conflicting results in this regard [228]. The interaction with the solvent therefore requires further investigation [3].

Theoretical chemistry presents an opportunity to further elucidate the internal and external drivers of the structural distortion undergone by copper phenanthroline in its excited state and emission lifetimes. An extensive theoretical study was carried out by Capano *et al* [3], utilising QM/MM (Car-Parinello method [229]) [230, 231] and purely classical molecular dynamics trajectories. Assisted Model Building with Energy Refinement (AMBER) force field parameters were used, but were supplemented for the Cu using parameterisations calculated from DFT. These DFT-enhanced force fields were then compared with the QM/MM trajectories, which utilised DFT in the region defined by the copper phenanthroline complex with a surrounding classical solvent region. The study confirmed that exciplex formation was unlikely to account for the influence of the solvent on emission lifetime. It also indicated the ligand-ligand dihedral angle (figure 7.2.1) as indicative of the length of the duration of the excited state, with larger flattening effects associated with shorted emission lifetimes. The success of the AMBER force fields in improving the understanding the internal dynamics of the copper phenanthroline in ground and excited state is noteworthy, particularly one enhanced with DFT-derived parameters.

The QUantum BEspoke kit (QUBE) force-field offers software that utilises higher-rung DFT (ω B97X-D [25]) derivations of force-field parameters, both the internal bonded parameters and external non-bonded parameters [5]. Previous work herein has indicated the success of high Hartree-Fock exchange fractions in improving the accuracy of electronic structure calculations, particularly with regard to transition metals complexes with organic ligands (chapters 3 and 4). Donating and non-donating solvents have also been parameterised using QUBE in chapter 5. Herein QUBE-derived MD simulations present an opportunity to build on the current theoretical understanding of $[\text{Cu}(\text{phen})_2]^+$ in ground and triplet state, and further assess QUBE as a parameterisation method relative to classical AMBER force field and QM/MM simulation data. It represents a starting point for understanding longer time dynamics of excited transition metal complexes using high accuracy quantum chemically derived force-fields.

7.2 Theoretical and Computational Details

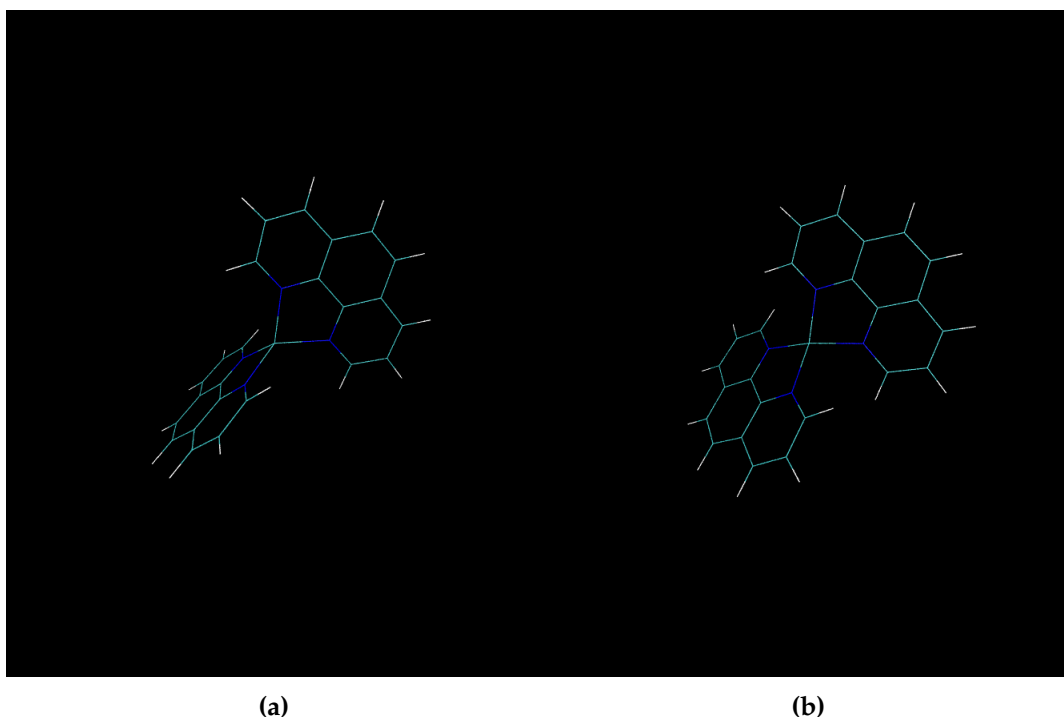


Figure 7.2.1: $[\text{Cu}(\text{phen})_2]^+$ structure in a) ground S_0 and b) excited T_1 states. This illustrates the change in dihedral angle (DHA) between the planes of the phenanthroline ligands due to the pseudo Jahn-Teller effect

[Cu(phen)₂]⁺ optimised structures for ground and triplet state (as shown in figure 7.2.1) are calculated using ground-state ORCA quantum calculations [164] utilising DFT (B3LYP). Force-field parameters are extracted using QUBEKit (Quantum BEspoke Kit) software [5], which utilises DFT (ω B97X-D) to assign parameters, a summary of which is outlined below in table 7.2.1. Included therein are Cu non-bonded parameters that were supplemented with Lennard-Jones parameters used in recent Cu(II) models which account for the Jahn-Teller effect [2]. MeCN and DCM parameters use the same QUBE parameters used in chapters 5 and 6. Molecular dynamical trajectories are calculated using OpenMM software [189], with an identical reporting regime to that used in section 5.2, at room temperature and atmospheric pressure (298.15K and 1.0bar respectively). Due to [Cu(phen)₂]⁺'s positive charge, it was important to take steps to ensure box neutrality and thereby avoid unrealistic electrostatic potentials within the system, particularly given the use of periodic boundary conditions. To that end, a negative ion (Cl⁻) was included to neutralise the box and placed at distance from the solute to avoid interference with studying the solute-solvent interaction.

Atom	Ground State			³ MLCT		
	q (e.c.)	ϵ (KJ mol ⁻¹)	σ (KJ mol ⁻¹)	q (e.c.)	ϵ (KJ mol ⁻¹)	σ (KJ mol ⁻¹)
Cu	0.22	17.51*	0.20*	0.70	17.51*	0.20*
N	-0.26	0.42	0.32	-0.38/- 0.31**	0.42	0.33/0.32**

Table 7.2.1: Non-bonded parameters of the Cu and N atoms, partial charge (q) and the Lennard-Jones (L-J) parameters (ϵ and σ). See section 7.3 for data concerning the internal structure of the Cu-N bonds. *L-J parameters taken from previous model of Jahn-Teller effect [2]. ** There is an asymmetry in the triplet state partial charge of the nitrogen atoms between the two ligands, with corresponding adjustments made in QUBE for the L-J parameters

7.3 Results

Method	Ground State			³ MLCT		
	Cu-N (Å)	$\angle\text{NCuN}_{intra}$ (deg)	$\angle\text{DHA}$ (deg)	Cu-N (Å)	$\angle\text{NCuN}_{intra}$ (deg)	$\angle\text{DHA}$ (deg)
QUBE (CMD)	2.00 (0.077)	86 (3.0)	80 (7)	2.04 (0.063)/1.96 (0.054)	81 (2.4)/85 (2.2)	47 (7) [in MeCN] 49 (6) [in DCM]
AMBER (CMD)	2.00 (0.066)	83 (2.6)	90 (9)	1.98 (0.035)	85 (1.4)	48 (7)
AMBER (QM/MM)	2.03 (0.075)	83 (2.5)	82 (20)	2.01 (0.073)	83 (3.4)	41 (9)

Table 7.3.1: Mean Cu-N bond length, NCuN_{intra} angle formed between copper and nitrogens of the same phenanthroline ligand and dihedral angle (DHA) formed by the two ligand planes (figure 7.2.1), along with standard deviations (σ) for ground and ³MLCT states. Classical MD (CMD)-simulation-derived geometries utilising the QUBE parameters herein are compared with CMD and QM/MM AMBER calculations from Capano *et al* [3]

Table 7.3.1 shows the structural parameters of $[\text{Cu}(\text{phen})_2]^+$ in both the ground and lowest ³MLCT state. In the ground state the structural parameters obtained from QUBE are in close agreement with previous classical AMBER force field, QM/MM MD [3] and compare well to structural fits obtained from EXAFS analysis [228]. The standard deviation is slightly larger than that of the classical AMBER trajectory and in line with that of the QM/MM trajectory, indicative of a slightly lower bond spring constant suggesting QUBE describes the bond strengths slightly better than the AMBER classical force fields. The $\angle\text{NCuN}$ is slightly larger than that from previous simulations but within the standard deviation. It is, as expected, equal for both ligands.

Importantly, the largest different between previous classical AMBER force field and QUBE is observed for the average dihedral angle of 80° which is clearly far closer to the QM-derived angle than the classical analogue.

This dihedral shift represents an important structural parameter in the photophysics of these complexes and therefore the good agreement between QUBE and the computationally more expensive QM/MM MD is very attractive. The ground-state geometry alignment between QUBE and QM/MM appears to vindicate both the findings of the latter and the use of the former to give QM-accurate data without the computational expense in this specific state, while suggesting an advantage over the classical AMBER field.

While all methods are in agreement for the ground state, in the $^3\text{MLCT}$ state, we begin to observe significant divergence between previous theory and QUBE parameterisation, particularly on Cu-N bonds and NCuN angles. Firstly, QUBE predicts a distinct asymmetry emerging between the Cu-N bond lengths between the two phenanthroline ligands. This is expected as although initially equivalent, structural changes and interactions with the environment lead to symmetry breaking and a localisation of the MLCT state onto one of the ligands [108]. This also causes a divergence in the $\angle\text{NCuN}$ bond angles. This asymmetry is not present in the other theoretical systems, which predict a continuation of bond equidistance [104].

QUBE predicts Cu-N bond distances of 2.04 and 1.96 Å. The latter, for which a contraction is observed, is the ligand upon which the MLCT localises and is associated with the attractive Coulomb interaction between the positive charge on the Cu and the electron density localised on the ligand. This contraction of 0.04 Å is in good agreement with previous experimental observations [228]. The other ligand slightly expands and this is associated with the occupation of anti-bonding orbitals in the excited state. The change in the Cu-N bond lengths changes the $\angle\text{NCuN}$ bond angles and these changes are also consistent with previous experiments [228].

The original flattening of the ligand dihedral angle to form the pseudo Jan-Teller geometry is derived from the components of the positive polarisation caused by the metal-to-ligand charge transfer. The ground state structure utilises degenerate valence Cu $3d_{yz}$ and $3d_{xz}$ orbitals to form near perpendicular bonds with the two ligands, in particular with the N 2p orbitals most closely aligned with these respective orientations, particularly N $2p_z$. The original S_0 to S_1 transition induces charge transfer into degenerate anti-bonding orbitals on the ligands [108] and leaves Cu with a positive polarisation in the principal axis with degenerate components. However these orbitals are in the π -conjugated aromatic ring, oriented in y or x respectively. Therefore intersystem crossing to the triplet geometry, whereby the negative polarisation on the ligand reorients towards the principal axis to compensate

for this positive polarisation on the Cu [226]. This also breaks the electron degeneracy and increased localisation of charge on one ligand, leading to the aforementioned imbalance in occupancy of anti-bonding orbitals, such that equilibrium bond lengths change [108]. The closer the ground and excited state energies, the greater the MLCT, and the larger distortion required to offset the potential increase. In turn this shortens emission lifetime. Hence dihedral angle is inextricably linked to emission, and is a product of the charge transfer. The difference between HOMO contributions from Cu $3d_{yz}$ and $3d_{xz}$ orbitals predicted by high-rung DFT leads to imbalanced charge transfer to the ligands depending on their orientation. The average dihedral angle across both solvents is comparable to classical AMBER force fields, whereas that with QM/MM predicts a smaller energy gap as predicted by the dihedral angle change.

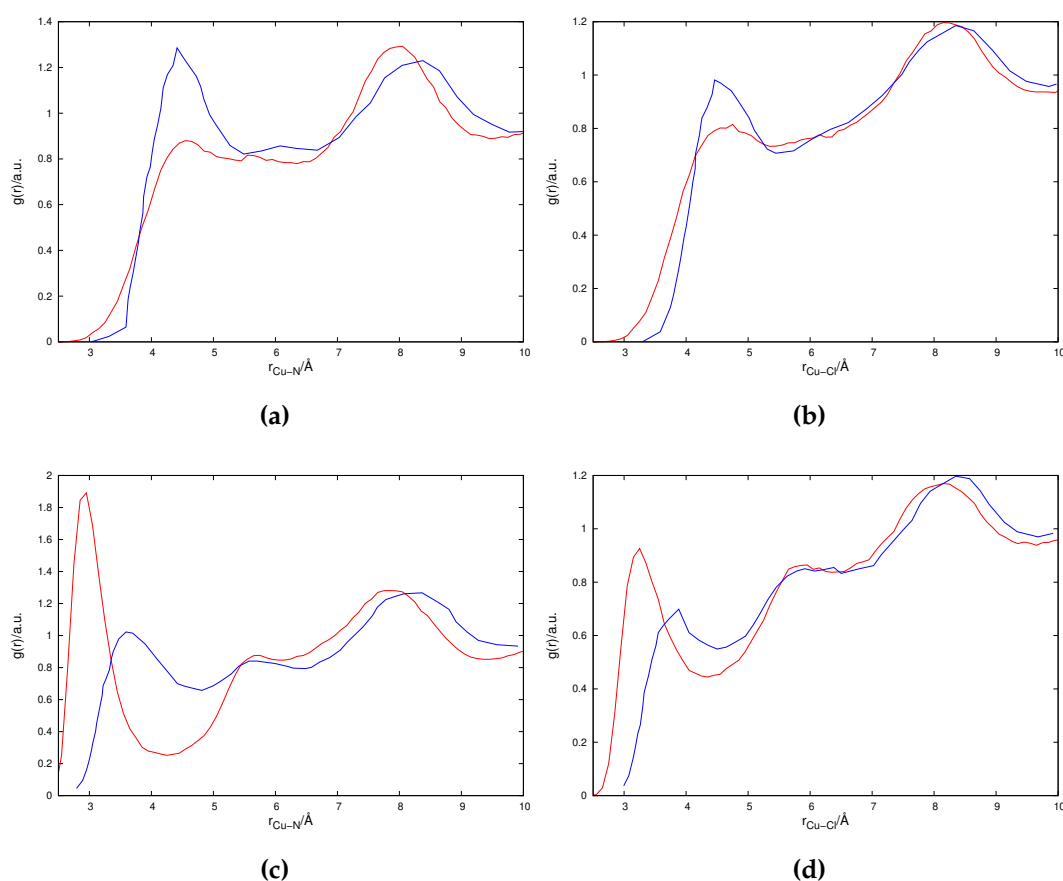


Figure 7.3.1: Radial distribution function $g(r)$ of Cu-solvent atom combinations of solvated $[\text{Cu}(\text{phen})_2]^+$ in ground and excited states (GS and ES respectively). Combinations illustrated are a) GS Cu- N_{MeCN} b) GS Cu- Cl_{DCM} c) ES Cu- N_{MeCN} d) ES Cu- Cl_{DCM} . QUBE and AMBER denoted in red and blue respectively.

The average dihedral angle solvated in MeCN is lower than that in DCM, with a slightly lower dihedral angle, associated with a reduced viscosity of the solvent and with a lowering of the ground-excited energy gap and shorter emission lifetime, which corresponds to previous experimental studies involving donating solvents such as MeCN, relative to DCM. This effect is associated with stabilising the Cu(II) ion while in the triplet state through electron donation. Previous studies [3] attempted to study the effect of the solvent through using MD simulation and understanding of structure of the solvent shell immediately solvent surrounding the copper ion, utilising a radial distribution function to give a representation of the solute-solvent interface. These plots can also be used to understand the possibility of the formation of the exciplex which has been debated in the literature [3]. This work, which used both classical and QM/MM MD, found that RDFs calculated from both simulations exhibited little difference, suggesting that the classical force fields are sufficiently accurate.

Figure 7.3.1 shows the Cu-N and Cu-Cl RDFs for both the ground and excited $^3\text{MLCT}$ state extracted from the classical MD simulations using the QUBE force-field (red). For comparison the RDF extracted from previous classical MD simulations [3] are shown in blue. For both solvents in the electronic ground state, the first solvation shell of the QUBE simulations is more disordered, as the height of the peak in the first solvation shell is decreased. This effect is smaller for DCM, and reduces in both cases as long range ($r > 6 \text{ \AA}$). Importantly, while differences are observed, the general trends remain the same.

However, in contrast there is a definitive shift between QUBE and AMBER force fields in the excited state. For QUBE, the first solvation shell become stronger and moves to short distances from the Cu in both cases. The peak of the first solvation shell occurs just below 3 \AA and is similar for both MeCN and DCM. The shifts in relative position of the solvation shells in the excited state after ground state agreement is indicative of the difference between their respective Cu(II) partial charge. QUBE's high positive charge yields stronger attraction with negative partial charges present in the solvent, leading to a reduction in radius of the first solvent shell relative to the AMBER field. This reduction in distance in combination with the small reduction of angle yields suggests a strong interaction between the solvent and the Cu(II) ion consistent with the exciplex, but the distance is still too large to be considered an actual bond.

7.4 Discussion and Conclusions

This investigation provides strong evidence for the utility of QUBE as a parameterisation method, particularly in regard to transition metal complexes. Herein its ground-state internal geometries compare favourably with QM/MM-established benchmarks and represent an improvement on the previous AMBER force field. It also identifies an asymmetry in the bond lengths and angles between the copper ion and the phenanthroline ligands within the $^3\text{MLCT}$ state that is not identified by both the AMBER field and the QM/MM study and is in strong agreement with recent work [104,226]. Taken in combination with the previous investigations in this work, QUBE's advantages over other parameterisation methods are more pronounced than those observed in chapters 5 and 6. This is perhaps unsurprising when the nature of the molecule considered in this study. It was established in previous chapters (see chapters 3 and 4) that the fraction of Hartree-Fock exchange is significant in simple transition metal complexes and in the relative electronegativity of aromatic systems with extensive conjugated π -bonding with heavily delocalised valence electrons. HF exchange reduces the self-interaction error (SIE), though cannot completely remove it due to the theoretical nature of Kohn-Sham orbitals. The rate of SIE reduction was found to be different for transition metals, halogens and ligands, leading to changes in relative electronegativity and thereby bond polarity as one ascends Jacob's Ladder. QUBE utilises $\omega\text{B97X-D}$ range-separated hybrid orbitals to generate its bonded and non-bonded parameters in a system centered on a transition metal with organic ligands comprised of aromatic compounds. Hence its generated parameters predict significantly more charge transfer to the phenanthroline ligands than AMBER (augmented using B3LYP), and gives a more complete description of the valence degeneracy breakdown of the triplet state, leading to the aforementioned asymmetry. This illustrates that more complex metal-organic complexes represent a domain in which QUBE has potential to be a useful tool for future MD studies, owing to its use of high-rung DFT in the parameterisation process.

QUBE also provides a potential means of elucidating more information around the mechanisms of the solute-solvent interaction. It records a small decrease in triplet state dihedral angle when in the donating solvent MeCN, relative to DCM. The parameterisation of Cu also supports the formation of the first solvation cell closer to Cu than that of the AMBER force field. However, there is also a shift of solvation cell present in non-donating DCM, and

the dihedral angle change is within a standard deviation of the averaged values, so these results providing any form of support of proposed solute-solvent exciplex formation [96, 104, 232] must be met with skepticism, especially given the lack of contradictory evidence in previous studies into the solvent role [3] and the solvation cell radius still exceeding the proximity necessary for meaningful bonding events. However it is clear that there is some solvent influence in the internal structure of the $[\text{Cu}(\text{phen})_2]^+$, particularly in the excited state, and this solvent shell shift is reported in other theoretical studies [107, 233], though these theories solely focused on the S_1 state prior to ISC. QUBE's elucidation of such an effect suggests it offers a useful means not only of providing accurate force fields for the internal structure of the copper phenanthroline complex, but also of studying further the dynamics of its interaction with donating solvents, which are of great research interest into the emission lifetimes of potential OLED candidate metal-organic complexes.

There remains for further study the behaviour of other OLED candidate molecules, particularly other copper phenanthroline complexes, to ascertain the general utility of QUBE in studying such complexes. Also, it must be noted that QUBE excited-state dihedral angle is still higher than that of the QM/MM simulation, which suggests the parameterisation may still struggle to recreate the dynamical processes required to exact the triplet-ground energy gap elucidated by the inclusion of QM TDDFT regions, in particular spin-orbit coupling. Such future investigation will establish the current viability of QUBE as a method of studying OLEDs and direct the future direction for development of QUBEKit software to account for any limitations in accounting for the internal structures or interaction with solvent molecules. The potential shown so far by QUBE suggests that it be a strong tool in future investigation of systems upon which QM-level accuracy of internal structure and solvent interaction is required, without the computational expense of QM/MM, and therefore represents a tool worthy of extensive future research.

Chapter 8

Conclusion

This investigation has underscored the value of DFT, both in providing detailed QM calculations for molecules that require further research and for improving the accuracy of MD trajectories via improved force-field accuracy, and therefore how imperative improvements in DFT are to all branches of theoretical chemistry. Utilising the EFG as a direct measure of valence electron density that could be directly related to both *ab initio* theory and experimental [58–62] results, it was illustrated that DFT can provide extensive insight into the bonding of molecules, even "challenging cases" [33] in regard to transition metal complexes and diatomics, even for *ab initio* theory [234, 235]. Furthermore, DFT can provide calculations with valuable insight into compounds simply beyond the scope of *ab initio* theory within the feasible time frames of most theoretical research [10]. Many of the halogenated aromatic compounds' CCSD(T) calculations remain unfinished at time of writing, owing to the extensive computational expense their calculations require. DFT is able to produce readily available research on the same systems, even high-rung functional groups such as rshGGA, within hours of starting calculations. In order to facilitate improved understanding of molecules of particular research interest within realistic time frames, it is imperative that DFT accuracy be improved for all systems. The EFG is useful for providing a versatile metric of electronic structure accuracy across a variety of different environments, and is shown to reveal significant differences between functional groups in performance relative to theoretical and experimental benchmarks. Improvements in DFT EFG agreement with benchmarks are correlated to the Hartree-Fock exchange fraction used in the respective functionals, which is used to reduce self-interaction error (SIE). This dependence on exchange is in agreement with previous work into DFT accuracy [33, 34, 178, 179]. From study of these systems, it is apparent that the relative electronegativities of transition metals, halogens and aromatic rings change as one ascends Jacob's Ladder, which in turn change

bond polarities and partial charge distribution across the molecule. This reflects recent work attributing error in heteronuclear molecule charge distributions and subsequent dipoles to the self-interaction error [29, 34] which has been related to errors in electronegativity and the first ionisation potential [185–187]. Attempts at tuning ω B97X functionals also confirm this change in relative electronegativity. Using inspection of atomic first ionisation potential as a measure of Mulliken electronegativity, this levelling off of ionisation potential increase is seen most obviously in the transition metals. The logical extrapolation is that the threshold HF exchange fraction at which the maximum amount of SIE possible is cancelled is lower for transition metals than halogens, or that crucial aspects of more local DFT exchange are lost as HF fraction increases, such that increased long-range exchange error reduction comes at the expense of increasing local short-range exchange error. Indeed, Medvedev *et al*'s recent paper analysing normalised electron density error suggested that pure HF exchange had higher error than quarter to half fractions [27]. Imperfect SIE cancellation is a consequence of using theoretical non-interacting Kohn-Sham orbitals, and the work herein suggests that larger atoms with a greater number of orbitals are those which become less electronegative relative to others as HF fraction increases. Such large atoms would have a greater amount of cumulative SIE. Likewise, the amount of Fermi repulsion in these atoms is very high, such that loss of local exchange would have implications on the overall potential associated with the orbitals. Overall, SIE is associated with decreasing the ionisation potential of valence orbitals through excessive electron self-repulsion [33]. This aligns with the findings in this investigation, but requires further investigation.

The impact of such changes in electronegativity as observed in chapters 3 and 4 extend beyond the domain of DFT and have consequences for the accuracy of force-fields, and in turn the accuracy of the MD trajectories calculated therefrom. QUBE utilises DFT to ascertain its bonded parameters and partial charge [4, 5]. The changes in relative electronegativity reported in chapters 3 and 4 lead to changes in the polarity in bonds, thus changing the strength of the bonds and their consequent equilibrium lengths and force constants. Furthermore, it changes the electron density distribution within the molecule, thus affecting all non-bonded parameters as per QUBE's method of atom-in-molecule charge partitioning [151, 152], which in turn is used to scale Lennard-Jones parameters [153]. This influences both internal dynamics of simulated molecules and their interaction with other molecules in the MD trajectory. Chapters 5 and 6 investigated the use of

QUBE relative to experimentally-derived force-field parameterisations from OPLS-AA in order to predict temperature-dependent solvent and solute-solvent scattering in a range of commonly-used solvents, and found that there were small differences in the low Q scattering range, associated with larger distances between atom species driven by non-bonded interaction. The radial distribution functions (RDFs) generated by the time-averaged MD trajectory were used to calculate scattering change per unit temperature using the independent-atom model (IAM) [143]. The significance of the RDF's contribution to the scattering was contingent on the scattering amplitude of the atomic species involved. Hence small differences in the QUBE and OPLS-AA radial distributions for pairings of atomic species with large scattering amplitudes yielded larger changes in the subsequent scattering profiles, while larger changes associated with atoms barely visible to scattering (i.e. hydrogen) were insignificant. Hence the largest visible differences in the scattering profiles of the two force-field methods were those for solvents containing chlorine atoms (DCM and chloroform), the atom species with the largest scattering cross section of all solvent atom species considered. Evaluation of the significance of the cross and solute terms revealed that the force-field dependence was significant enough to change the solute profiles. The non-bonded interaction between solvent species and the solute-solvent was dominated by the solvent partial charge. The ability of QUBE to theoretically predict solvent and solute-solvent scattering terms and represent an advantage over experimental force-field derivations is therefore dependent on high accuracy of its partial charge, particularly in systems with large scatterers. The accuracy of QUBE MD trajectories and its predicted solvent and cross-term scattering therefore depends on the ability of ω B97X-D functionals to produce accurate partial charges. Therefore the accuracy of QUBE MD trajectories and theoretical scattering is intrinsically linked with DFT accuracy and reduction of SIE. Given the divergence between both force fields' solvent terms and experimental equivalents, there are further questions to explore about the use of MD trajectories to predict non-equilibrium events. Given the recent studies by Kim *et al* (2015) [192], it is worth evaluating the predicted solvent-solute interactions relative to QM/MM calculation to ascertain whether theoretical prediction can be further improved via TDDFT elucidating the exact nature of its interaction.

The potential of QUBE's use of high-rung DFT to improve MD simulation is best illustrated through study of copper phenanthroline. Here the complex contains a transition metal and π -conjugated aromatic ligands, reflecting the

systems with Jacob's Ladder electronegativity dependence from chapters 3 and 4. QUBE compared favourably relative to QM/MM $[\text{Cu}(\text{phen})_2]^+$ in the ground state pseudo tetrahedral geometry, and in triplet state captured the Cu-N bond length asymmetry between the two phenanthroline ligands, which was not picked up by the AMBER classical force field or QM/MM. It also provided evidence supporting the possibility of exciplex formation in donating solvents (MeCN) [96, 232], placing it in strong alignment with the latest research into its ground- and excited-state structures and interaction with solvents [104, 226]. Its use of high-rung DFT relative to that used for the AMBER force field parameters (B3LYP) and the QM/MM simulation (BLYP) [3] illustrates the vital use of high-rung range-separated hybrid DFT functionals for molecules similar to those of chapters 3 and 4 that cannot be reproduced with mid-rung hybrid functional, providing potential evidence of an area in which QUBE could provide QM-derived parameters for study of such systems without the computational cost of QM/MM, as well as providing further evidence to support the functional-dependence of transition-metal-complex electronic structure found in the aforementioned previous chapters. Establishing QUBE's accuracy in parameterising metal organic complexes will require an expansion of the current work to consider other complexes, but its agreement with the findings of previous work herein, and the clear improvement relative to previous theoretical study merits further study.

This study provides evidence of the current challenges facing DFT functional development in capturing the electronic structure of challenging case systems, but also of the potential to improving functional accuracy, not only within quantum chemistry but in molecular dynamics and theoretical scattering via the QUBE force field. It has also provided the electric field gradient as a versatile metric that can be used to compare the DFT electron density directly with both *ab initio* theory and experiment, and supports the recent calls [27–29, 34] that consideration of electron density be a larger component of functional development. Using this metric further investigation can be made of the role of HF exchange fraction and self-interaction error cancellation in performance disparities between lower and higher rungs of DFT. The elucidation of potentially different relative electronegativities between transition metals, halogens and organic ligands at different fractions of HF exchange represents a finding of significant interest for future work. Understanding the origins of such disparities, whether it be related

to self-interaction error cancellation limitations alone or possibly the competing nature of SIE cancellation with retaining the useful short-range DFT exchange, has the potential to assist in the development of more versatile, accurate DFT functionals in future that can better capture these molecules and other challenging environments. QUBE's performance in reproducing accurate $[\text{Cu}(\text{phen})_2]^+$ structures indicates the potential such future developments could have in other branches of theoretical chemistry. Theoretical scattering suggests that QUBE has potential in the longer term, but further investigation is required to assess whether the report rate from the trajectory is sufficient to obtain the converged RDF, or if the RDF-sensitivity of combinations of atoms with large scattering cross sections outweigh what it is possible with trajectory error and parameterisation. Though it is clear that the parameters upon which the RDFs depend are also tied to improvements in DFT accuracy, particularly partial charge. Overall, given direction of science to study increasing complex and large molecules beyond the feasible means of *ab initio* methods, both in quantum chemistry and molecular dynamical simulations, it is imperative that DFT continue to improve to improve theoretical chemical study of such systems in order to facilitate advances in medicine, OLEDs and other future technologies, which represent many of the uses and potential uses of the molecules studied herein. This study has provided a method of assessing DFT and identifying underlying potential causes of DFT error, in the hope that future study can take forward the work started here, to improve DFT electronic structure calculations and thereby potentially improve all areas of theoretical chemistry as it faces increasing challenges in the future.

Appendix A

Assessing Functional Errors using Atomisation Energies and Electric Field Gradients

A.1 Atomisation - EFG Characteristic by Functional Group

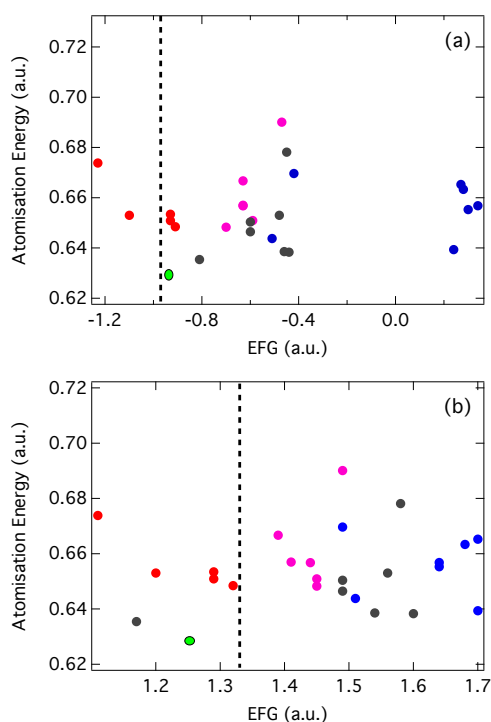


Figure A.1.1: Plot of the $\text{H}_2\text{O} \cdots \text{CuCl}$ atomisation energy as a function of Cu (a) and Cl (b) electric field gradient in the complex by functional group. GGA, hGGA, dhGGA and rshGGA are represented in blue, grey, red and light purple respectively. CCSD(T) is denoted in green, while the dashed line represents experimental EFG.

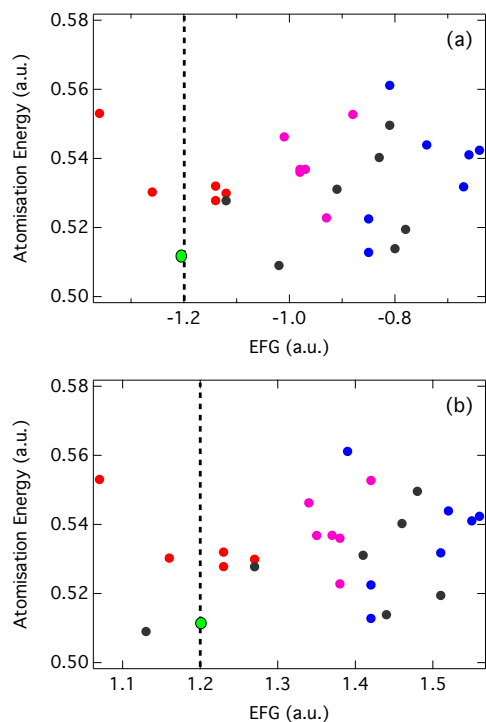


Figure A.1.2: Plot of the $\text{H}_2\text{S} \cdots \text{CuCl}$ atomisation energy as a function of Cu (a) and Cl (b) electric field gradient in the complex by functional group. GGA, hGGA, dhGGA and rshGGA are represented in blue, grey, red and light purple respectively. CCSD(T) is denoted in green, while the dashed line represents experimental EFG.

A.2 ω B97X Tuning via Koopmans' Theorem

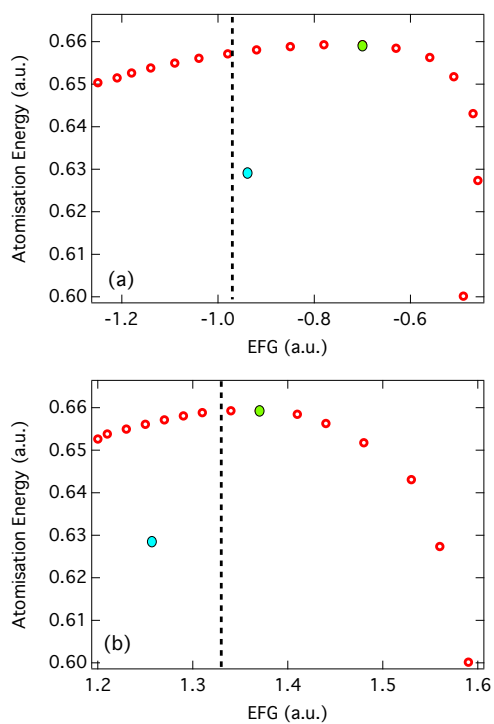


Figure A.2.1: Plot of the change in atomisation and Cu (a) and Cl (b) EFG of ω B97X for $\text{H}_2\text{O} \cdots \text{CuCl}$ as ω is adjusted from 0.05 to 0.8. Optimal ω (green) and CCSD(T) (blue) are also indicated

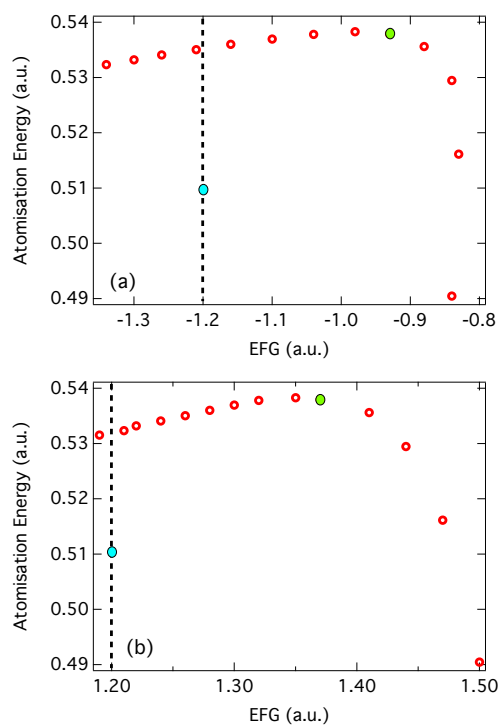


Figure A.2.2: Plot of the change in atomisation and Cu (a) and Cl (b) EFG of ω B97X for $\text{H}_2\text{S} \cdots \text{CuCl}$ as ω is adjusted from 0.05 to 0.8. Optimal ω (green) and CCSD(T) (blue) are also indicated

A.3 Core Polarisation Contribution to Cu Electric Field Gradient

Method	Cu Core Pol. EFG/a.u.
CCSD(T)	-0.374
B2GP-PLYP	-0.170
B2PLYP-D3	-0.090
B2PLYP	-0.090
B3LYP	0.157
B97-D3	0.287
B97	0.129
BLYP	0.317
BP86	0.306
CAM-B3LYP	0.135
DSD-BLYP-D3	-0.201
LC-BLYP	0.272
M062X	-0.022
M06L	0.028
M06	0.133
mPW2PLYP	-0.102
O3LYP	0.189
PBE0	0.087
PBE	0.285
PWPB95	-0.081
PW6B95	0.068
TPSS0	0.011
TPSSh	0.114
TPSS	0.186
ω B97	0.186
ω B97X-D3	0.117
ω B97X	0.121

Table A.3.1: Core polarisation contribution to copper electric field gradient of CuCl of default functionals and CCSD(T)

ω	Cu Core Pol. EFG/a.u.
0.05	0.166
0.10	0.166
0.15	0.162
0.20	0.153
0.25	0.139
0.30	0.121
0.35	0.100
0.40	0.077
0.45	0.054
0.50	0.030
0.55	0.007
0.60	-0.016
0.65	-0.037
0.70	-0.056
0.75	-0.075
0.80	-0.091
0.85	-0.106
0.90	-0.120
0.95	-0.133
1.00	-0.145
1.05	-0.155
1.10	-0.165
1.15	-0.174
1.20	-0.182
1.25	-0.190
1.30	-0.197
1.35	-0.204
1.40	-0.210
1.45	-0.216
1.50	-0.222

Table A.3.2: Core polarisation contribution to copper electric field gradient of CuCl of ω B97X functionals with ω altered from 0.05 through 1.5

Method	Cu Core Pol. EFG/a.u.
CCSD(T)	-0.488
B2GP-PLYP	-0.210
B2PLYP-D3	-0.109
B2PLYP	-0.109
B3LYP	0.188
B97-D3	0.323
B97	0.153
BLYP	0.367
BP86	0.345
CAM-B3LYP	0.171
DSD-BLYP-D3	-0.257
LC-BLYP	0.340
M062X	-0.058
M06L	0.025
M06	0.139
mPW2PLYP	-0.124
O3LYP	0.223
PBE0	0.100
PBE	0.323
PWPB95	-0.112
PW6B95	0.065
TPSS0	0.006
TPSSh	0.122
TPSS	0.202
ω B97	0.230
ω B97X-D3	0.138
ω B97X	0.147

Table A.3.3: Core polarisation contribution to copper electric field gradient of Ar \cdots CuCl of default functionals and CCSD(T)

ω	Cu Core Pol. EFG/a.u.
0.05	0.167
0.10	0.174
0.15	0.176
0.20	0.172
0.25	0.162
0.30	0.147
0.35	0.128
0.40	0.106
0.45	0.081
0.50	0.055
0.60	0.002
0.65	-0.024
0.70	-0.048
0.75	-0.071
0.80	-0.092
0.85	-0.112
0.90	-0.130
0.95	-0.147
1.00	-0.163
1.05	-0.177
1.10	-0.190
1.15	-0.202
1.20	-0.213
1.25	-0.224
1.30	-0.234
1.35	-0.243
1.40	-0.251
1.45	-0.259
1.50	-0.267

Table A.3.4: Core polarisation contribution to copper electric field gradient of Ar···CuCl of ω B97X functionals with ω altered from 0.05 through 1.5

Method	Cu Core Pol. EFG/a.u.
CCSD(T)	-0.585
B2GP-PLYP	-0.250
B2PLYP-D3	-0.135
B2PLYP	-0.135
B3LYP	0.189
B97-D3	0.347
B97	0.149
BLYP	0.376
BP86	0.358
CAM-B3LYP	0.185
DSD-BLYP-D3	-0.340
LC-BLYP	0.384
M062X	-0.063
M06L	-0.026
M06	0.087
mPW2PLYP	-0.151
O3LYP	0.236
PBE0	0.097
PBE	0.332
PWPB95	-0.144
PW6B95	0.043
TPSS0	-0.021
TPSSh	0.100
TPSS	0.182
ω B97	0.266
ω B97X-D3	0.146
ω B97X	0.160

Table A.3.5: Core polarisation contribution to copper electric field gradient of OC...CuCl of default functionals and CCSD(T)

ω	Cu Core Pol. EFG/a.u.
0.05	0.154
0.10	0.166
0.15	0.173
0.20	0.174
0.25	0.170
0.30	0.160
0.35	0.144
0.40	0.124
0.45	0.102
0.50	0.077
0.55	0.050
0.60	0.023
0.65	-0.004
0.70	-0.030
0.75	-0.055
0.80	-0.080
0.85	-0.102
0.90	-0.124
0.95	-0.144
1.00	-0.162
1.05	-0.180
1.10	-0.196
1.15	-0.211
1.20	-0.225
1.25	-0.238
1.30	-0.251
1.35	-0.262
1.40	-0.273
1.45	-0.284
1.50	-0.294

Table A.3.6: Core polarisation contribution to copper electric field gradient of OC...CuCl of ω B97X functionals with ω altered from 0.05 through 1.5

Method	Cu Core Pol. EFG/a.u.
CCSD(T)	-0.731
B2GP-PLYP	-0.387
B2PLYP-D3	-0.263
B2PLYP	-0.263
B3LYP	0.094
B97-D3	-0.126
B97	0.057
BLYP	-0.145
BP86	-0.137
CAM-B3LYP	0.076
DSD-BLYP-D3	-0.448
LC-BLYP	0.275
M062X	-0.208
M06L	-0.093
M06	0.043
mPW2PLYP	-0.281
O3LYP	0.147
PBE0	-0.002
PBE	-0.126
PWPB95	-0.260
PW6B95	-0.046
TPSS0	-0.110
TPSSh	0.030
TPSS	-0.054
ω B97	0.149
ω B97X-D3	0.041
ω B97X	0.051

Table A.3.7: Core polarisation contribution to copper electric field gradient of $\text{H}_2\text{O}\cdots\text{CuCl}$ of default functionals and CCSD(T)

ω	Cu Core Pol. EFG/a.u.
0.05	0.076
0.10	0.083
0.15	0.085
0.20	0.080
0.25	0.069
0.30	0.051
0.35	0.028
0.40	0.001
0.45	-0.029
0.50	-0.061
0.55	-0.093
0.60	-0.126
0.65	-0.157
0.70	-0.188
0.75	-0.216
0.80	-0.243
0.85	-0.268
0.90	-0.291
0.95	-0.312
1.00	-0.332
1.05	-0.350
1.10	-0.367
1.15	-0.382
1.20	-0.397
1.25	-0.410
1.30	-0.422
1.35	-0.434
1.40	-0.445
1.45	-0.455
1.50	-0.465

Table A.3.8: Core polarisation contribution to copper electric field gradient of $\text{H}_2\text{O} \cdots \text{CuCl}$ of ωB97X functionals with ω altered from 0.05 through 1.5

Method	Cu Core Pol. EFG/a.u.
CCSD(T)	-0.549
B2GP-PLYP	-0.260
B2PLYP-D3	-0.157
B2PLYP	-0.157
B3LYP	0.135
B97-D3	0.267
B97	0.099
BLYP	0.299
BP86	0.280
CAM-B3LYP	0.121
DSD-BLYP-D3	-0.314
LC-BLYP	0.289
M062X	-0.122
M06L	-0.036
M06	0.072
mPW2PLYP	-0.172
O3LYP	0.166
PBE0	0.047
PBE	0.256
PWPB95	-0.164
PW6B95	0.008
TPSS0	-0.043
TPSSh	0.070
TPSS	0.144
ω B97	0.177
ω B97X-D3	0.086
ω B97X	0.094

Table A.3.9: Core polarisation contribution to copper electric field gradient of $\text{H}_2\text{S}\cdots\text{CuCl}$ of default functionals and CCSD(T)

ω	Cu Core Pol. EFG/a.u.
0.05	0.111
0.10	0.117
0.15	0.119
0.20	0.116
0.25	0.107
0.30	0.094
0.35	0.077
0.40	0.056
0.45	0.033
0.50	0.008
0.55	-0.018
0.60	-0.043
0.65	-0.068
0.70	-0.092
0.75	-0.115
0.80	-0.137
0.85	-0.157
0.90	-0.175
0.95	-0.193
1.00	-0.209
1.05	-0.224
1.10	-0.237
1.15	-0.250
1.20	-0.262
1.25	-0.273
1.30	-0.283
1.35	-0.293
1.40	-0.302
1.45	-0.311
1.50	-0.319

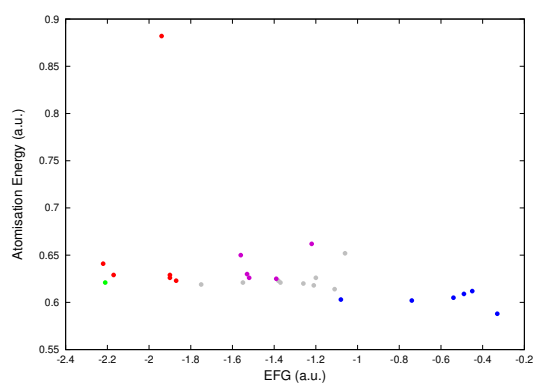
Table A.3.10: Core polarisation contribution to copper electric field gradient of $\text{H}_2\text{S} \cdots \text{CuCl}$ of ωB97X functionals with ω altered from 0.05 through 1.5

Appendix B

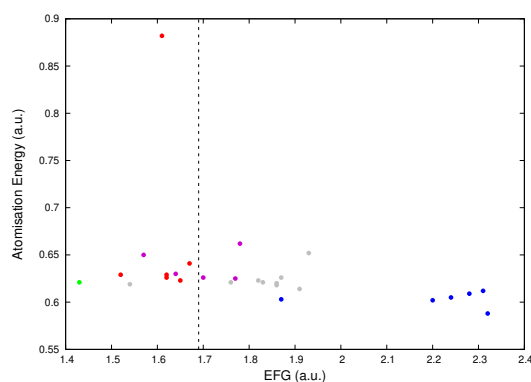
Extending the Understanding of Density and Energetic Error for Silver Complexes and Halogenated Aromatic Compounds

B.1 Silver Complexes

B.1.1 Atomisation - EFG Characteristic by Functional Group

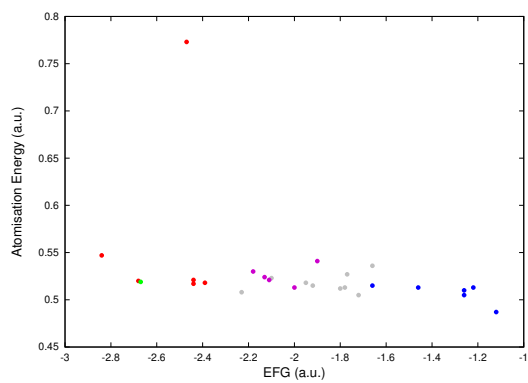


(a)

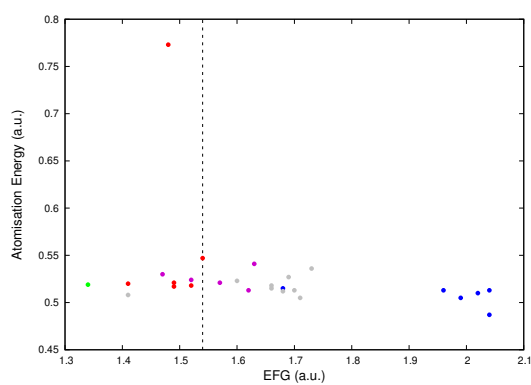


(b)

Figure B.1.1: $\text{H}_2\text{O} \cdots \text{AgCl}$ Atomisation-EFG characteristic for a) silver and b) chlorine. GGA, hGGA, dhGGA and rshGGA are represented in blue, grey, red and light purple respectively. CCSD(T) is denoted in green, while the dashed line represents experimental EFG.

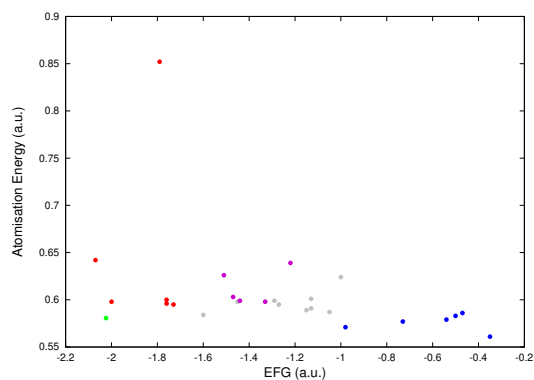


(a)

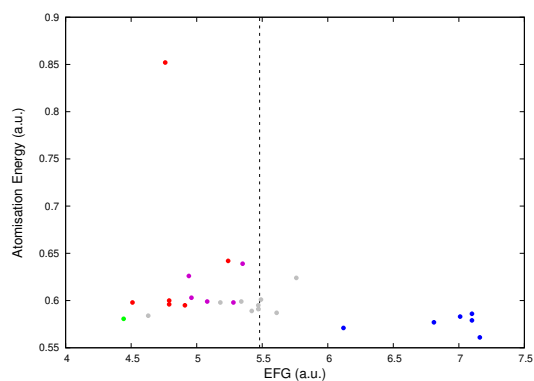


(b)

Figure B.1.2: $\text{H}_2\text{S} \cdots \text{AgCl}$ Atomisation-EFG characteristic for a) silver and b) chlorine. GGA, hGGA, dhGGA and rshGGA are represented in blue, grey, red and light purple respectively. CCSD(T) is denoted in green, while the dashed line represents experimental EFG.

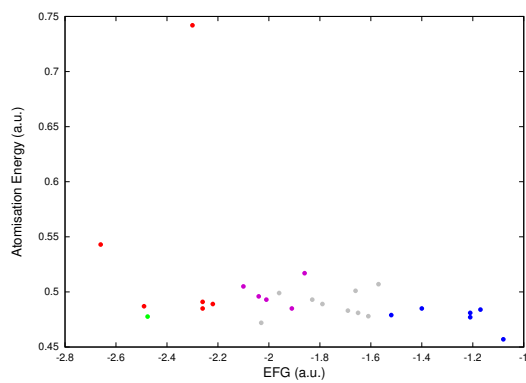


(a)

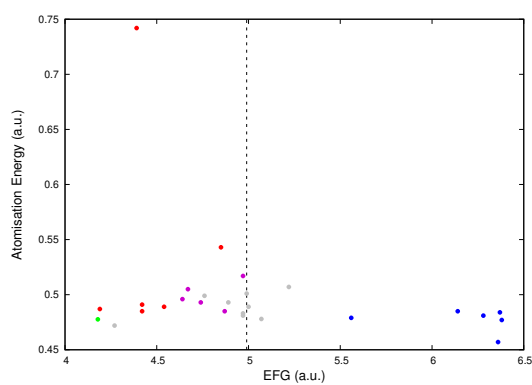


(b)

Figure B.1.3: $\text{H}_2\text{O} \cdots \text{AgI}$ Atomisation-EFG characteristic for a) silver and b) iodine. GGA, hGGA, dhGGA and rshGGA are represented in blue, grey, red and light purple respectively. CCSD(T) is denoted in green, while the dashed line represents experimental EFG.

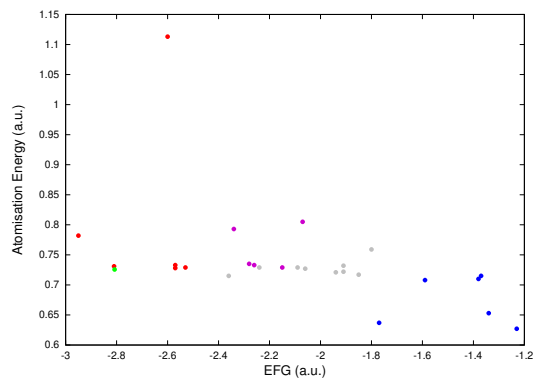


(a)

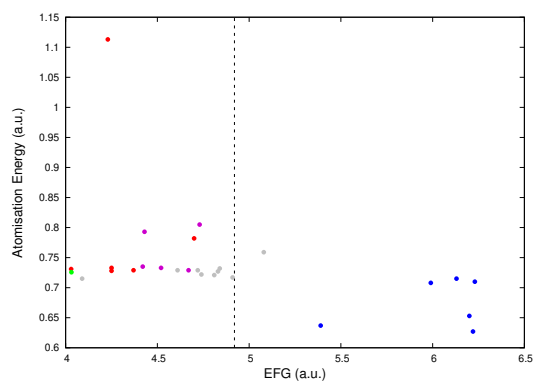


(b)

Figure B.1.4: $\text{H}_2\text{S} \cdots \text{AgI}$ Atomisation-EFG characteristic for a) silver and b) iodine. GGA, hGGA, dhGGA and rshGGA are represented in blue, grey, red and light purple respectively. CCSD(T) is denoted in green, while the dashed line represents experimental EFG.

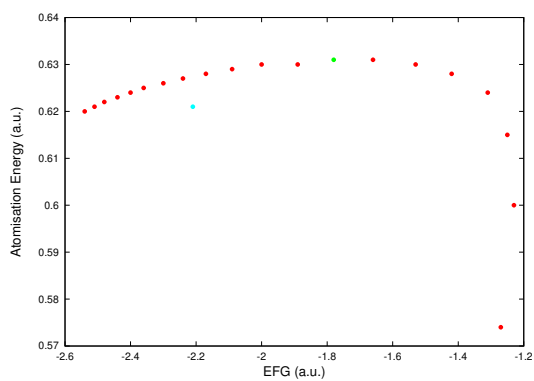


(a)

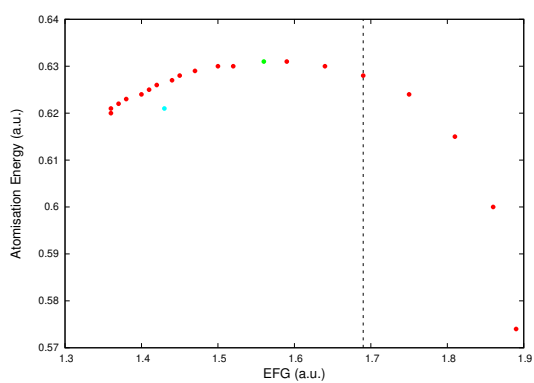


(b)

Figure B.1.5: $\text{H}_3\text{N}\cdots\text{AgI}$ Atomisation-EFG characteristic for a) silver and b) iodine. GGA, hGGA, dhGGA and rshGGA are represented in blue, grey, red and light purple respectively. CCSD(T) is denoted in green, while the dashed line represents experimental EFG.

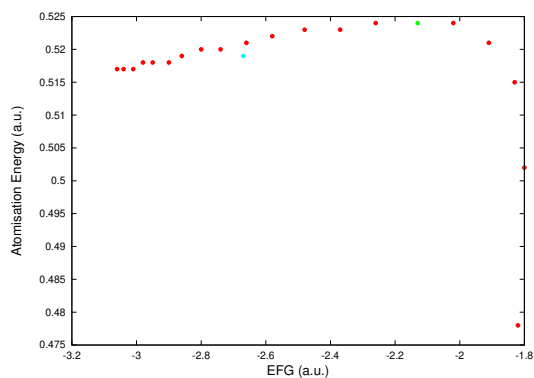
B.1.2 ω B97X Tuning via Koopmans' Theorem

(a)

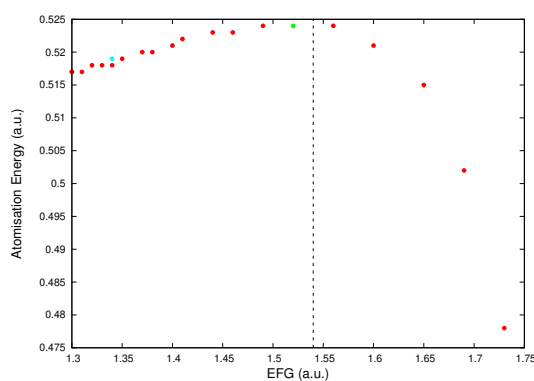


(b)

Figure B.1.6: $\text{H}_2\text{O} \cdots \text{AgCl}$ ω B97X change in atomisation and EFG for a) silver and b) chlorine for $\omega=0.05-1$. Optimal $\omega=0.4$ is denoted in green, with CCSD(T) in cyan

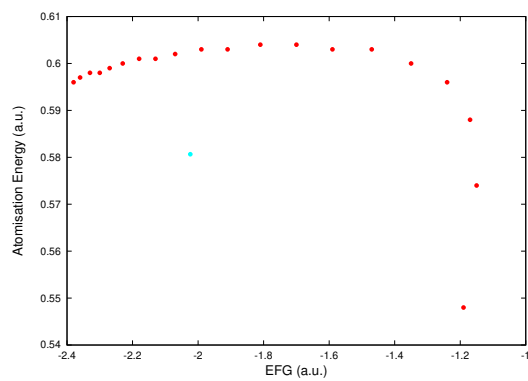


(a)

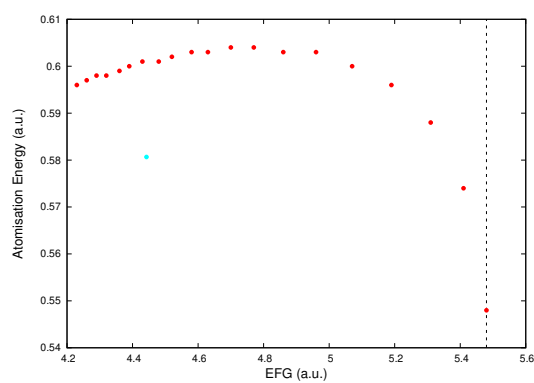


(b)

Figure B.1.7: $\text{H}_2\text{S} \cdots \text{AgCl}$ ωB97X change in atomisation and EFG for a) silver and b) chlorine for $\omega=0.05-1$. Optimal $\omega=0.3$ is denoted in green, with CCSD(T) in cyan

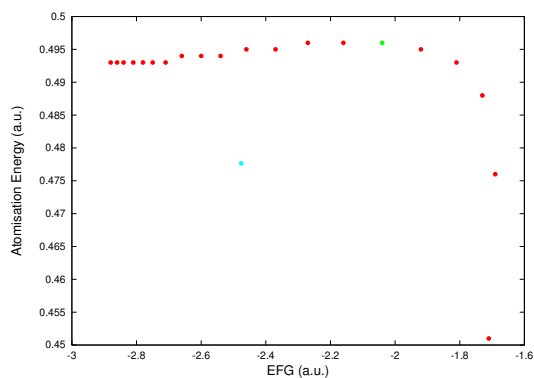


(a)

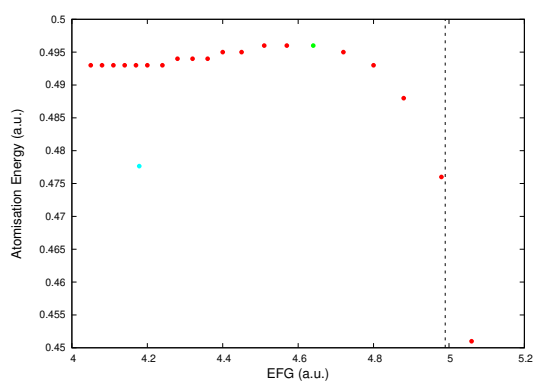


(b)

Figure B.1.8: $\text{H}_2\text{O} \cdots \text{AgI}$ ωB97X change in atomisation and EFG for a) silver and b) iodine for $\omega=0.05-1$. Optimal $\omega > 1$ and therefore beyond the current range, with CCSD(T) in cyan

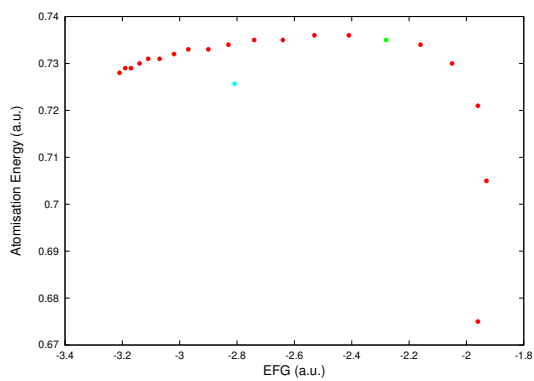


(a)

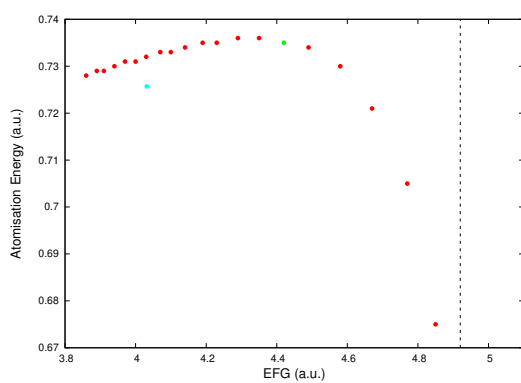


(b)

Figure B.1.9: $\text{H}_2\text{S} \cdots \text{AgI}$ ωB97X change in atomisation and EFG for a) silver and b) iodine for $\omega=0.05-1$. Optimal $\omega=0.3$ is denoted in green, with CCSD(T) in cyan



(a)



(b)

Figure B.1.10: $\text{H}_3\text{N}\cdots\text{AgI}$ ωB97X change in atomisation and EFG for a) silver and b) iodine for $\omega=0.05-1$. Optimal $\omega=0.3$ is denoted in green, with CCSD(T) in cyan

B.2 Halogenated Aromatic Compounds

B.2.1 Atomisation - EFG Characteristic by Functional Group

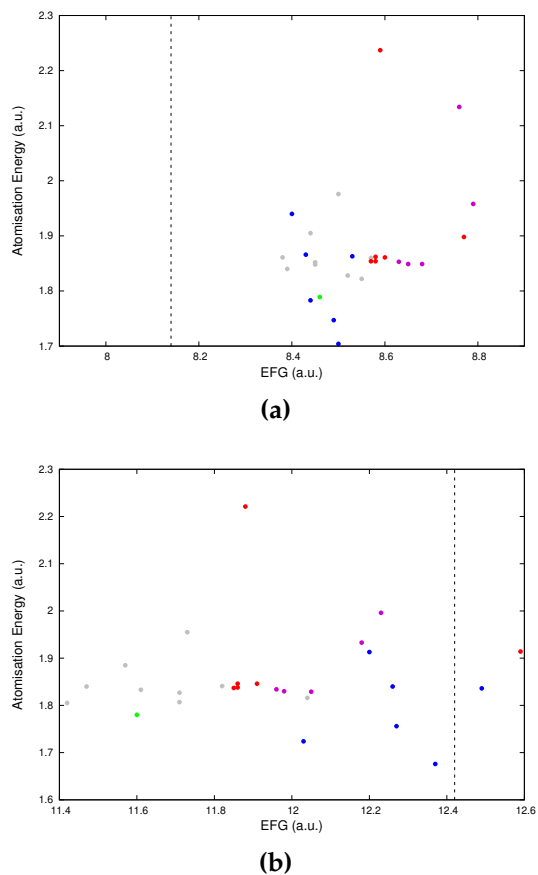
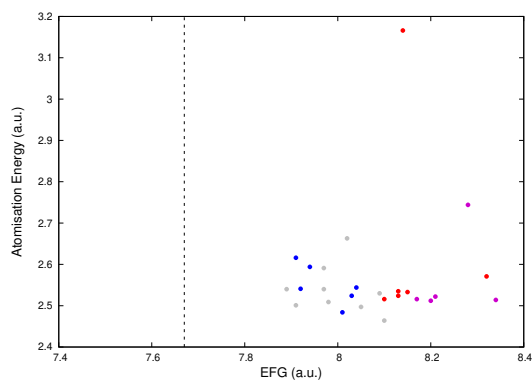
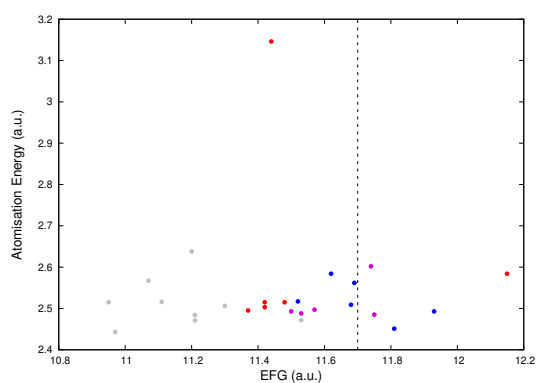


Figure B.2.1: Atomisation-halogen EFG characteristic for a) bromopyrazole and b) iodopyrazole. GGA, hGGA, dhGGA and rshGGA are represented in blue, grey, red and light purple respectively. CCSD(T) is denoted in green, while the dashed line represents experimental EFG.

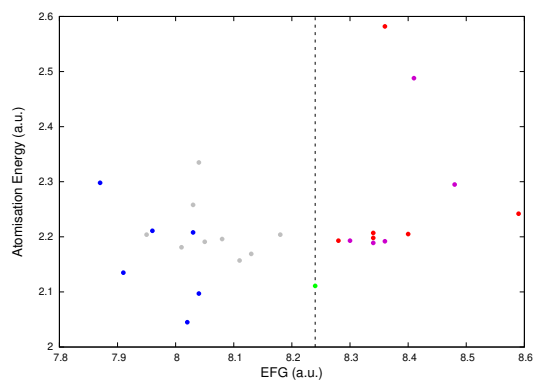


(a)

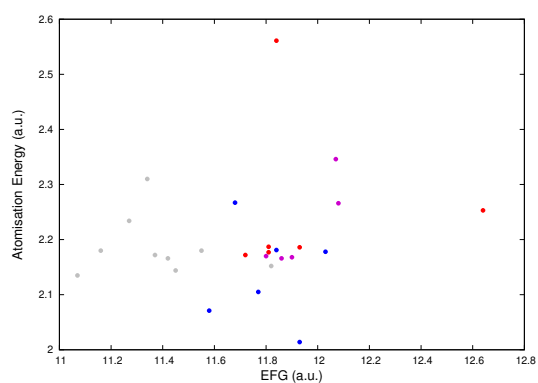


(b)

Figure B.2.2: Atomisation-halogen EFG characteristic for a) bromobenzene and b) iodobenzene. GGA, hGGA, dhGGA and rshGGA are represented in blue, grey, red and light purple respectively. The dashed line denotes experimental EFG.

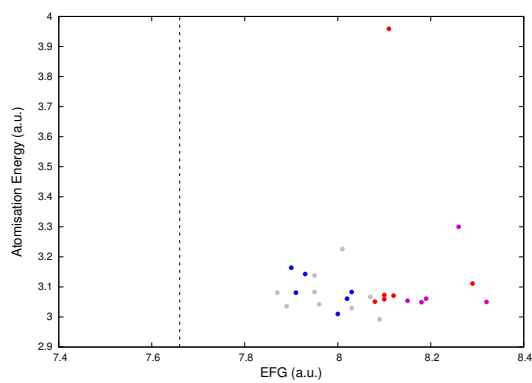


(a)

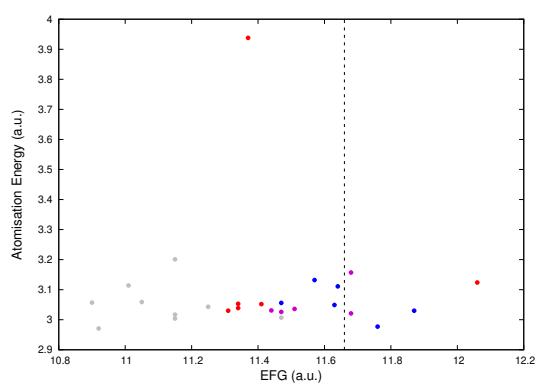


(b)

Figure B.2.3: Atomisation-halogen EFG characteristic for a) 2-bromopyrimidine and b) 2-iodopyrimidine. GGA, hGGA, dhGGA and rshGGA are represented in blue, grey, red and light purple respectively. CCSD(T) is denoted in green (2-bromopyrimidine only), while the dashed line represents experimental EFG (2-bromopyrimidine only).



(a)



(b)

Figure B.2.4: Atomisation-halogen EFG characteristic for a) p-bromotoluene and b) p-iodotoluene. GGA, hGGA, dhGGA and rshGGA are represented in blue, grey, red and light purple respectively. The dashed line denotes experimental EFG.

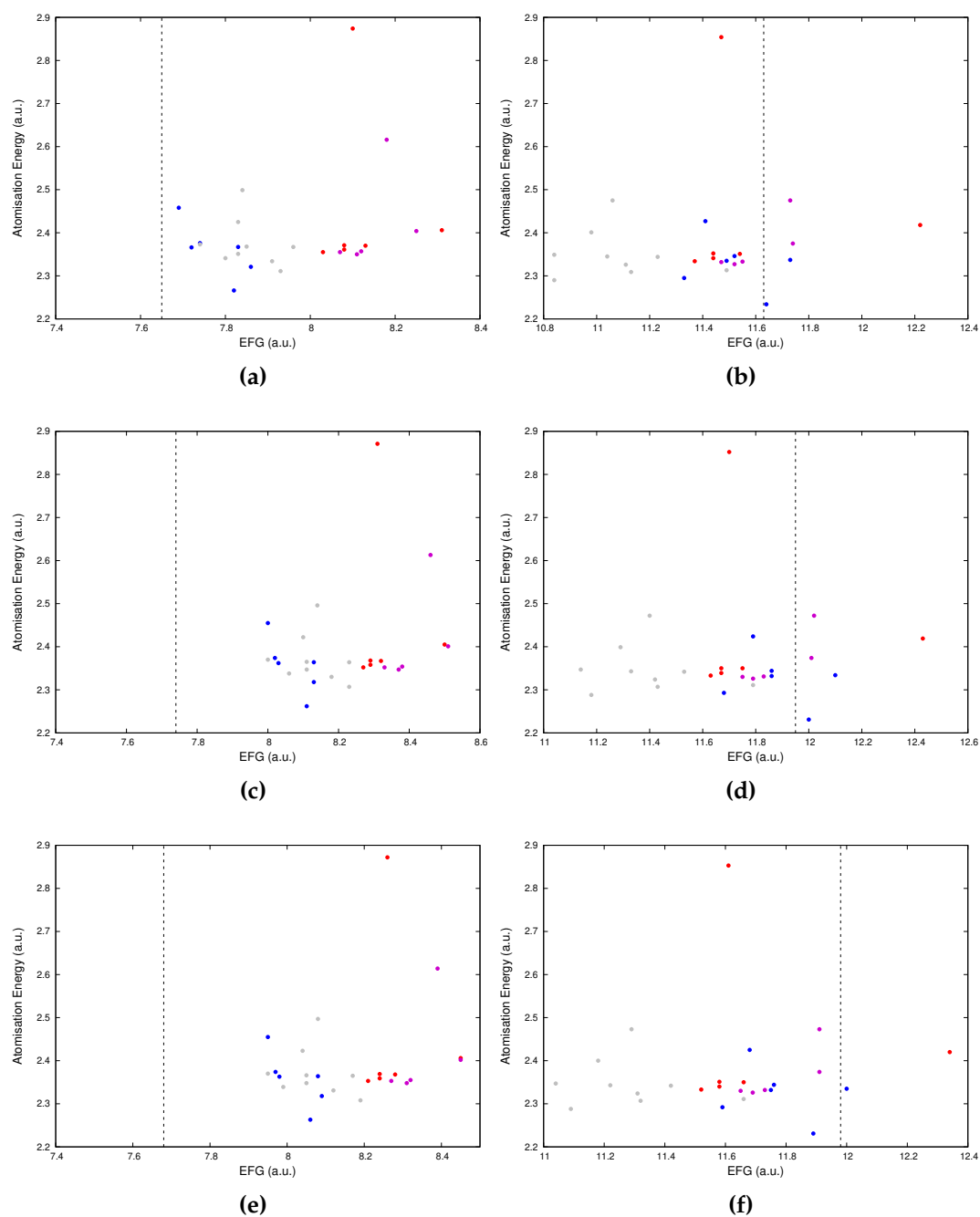
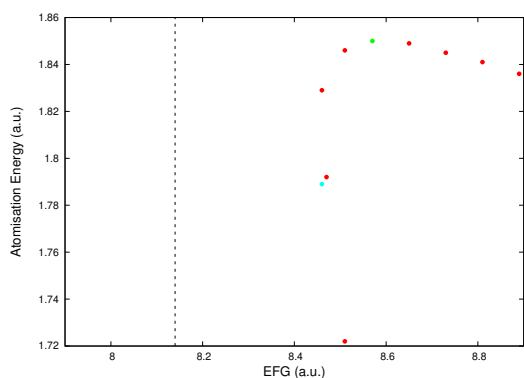
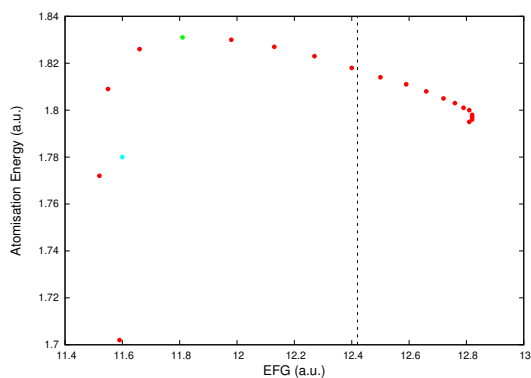


Figure B.2.5: Atomisation-halogen EFG characteristic for a) 2-bromopyridine b) 2-iodopyridine c) 3-bromopyridine d) 3-iodopyridine e) 4-bromopyridine f) 4-iodopyridine . GGA, hGGA, dhGGA and rshGGA are represented in blue, grey, red and light purple respectively. The dashed line denotes experimental EFG..

B.2.2 ω B97X Tuning via Koopmans' Theorem

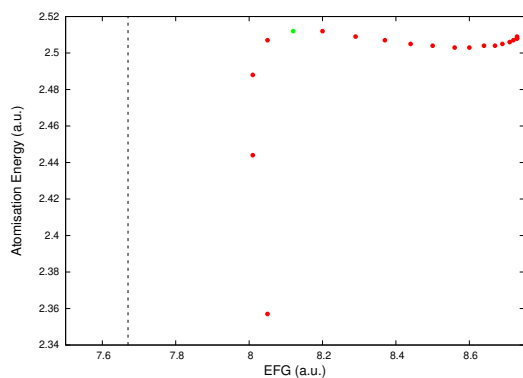


(a)

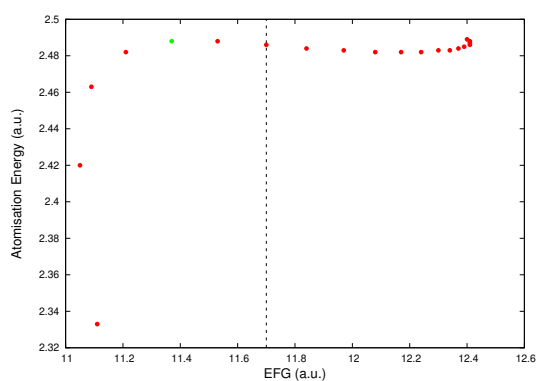


(b)

Figure B.2.6: ω B97X change in atomisation and EFG for a) bromopyrazole and b) iodopyrazole over range $\omega=0.05-1$. Optimal $\omega=0.25$ and is denoted in green, with CCSD(T) in cyan. Experimental EFG is denoted by the dashed line

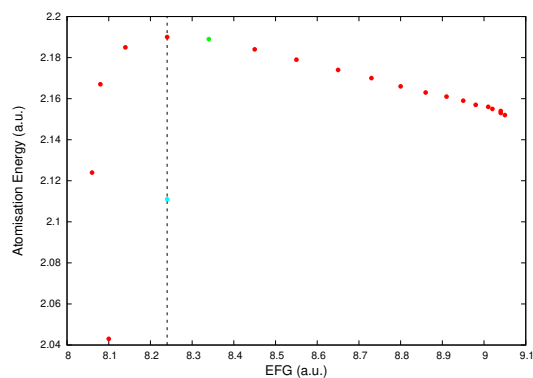


(a)

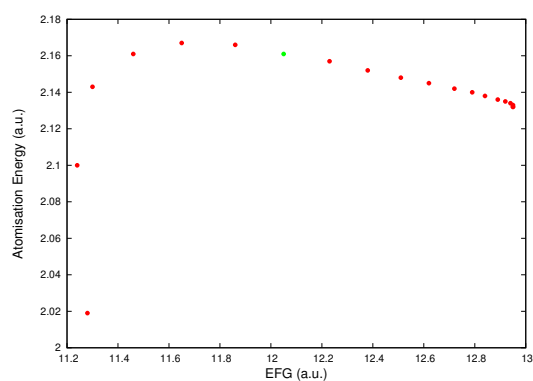


(b)

Figure B.2.7: ω B97X change in atomisation and EFG for a) bromobenzene and b) iodobenzene over range $\omega=0.05-1$. Optimal $\omega=0.25$ and is denoted in green. Experimental EFG is denoted by the dashed line

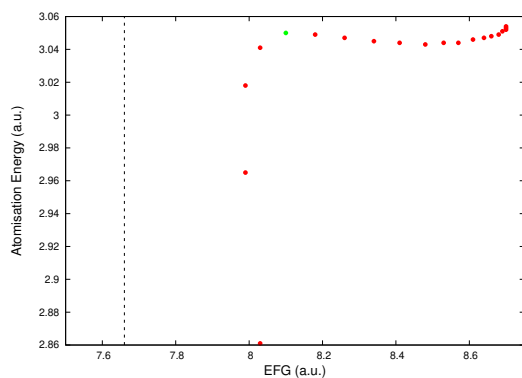


(a)

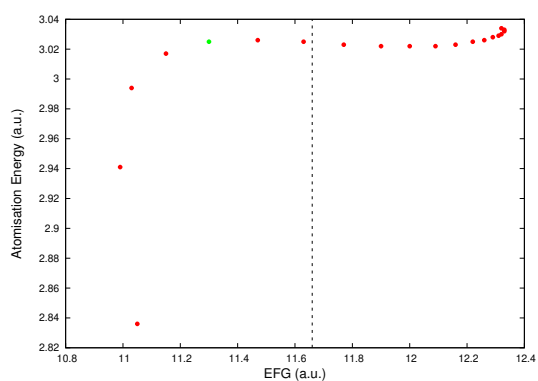


(b)

Figure B.2.8: ω B97X change in atomisation and EFG for a) 2-bromopyrimidine and b) 2-iodopyrimidine over range $\omega=0.05$ -1. Optimal $\omega=0.3$ and 0.35 respectively and is denoted in green, with CCSD(T) in cyan (2-bromopyrimidine only). Experimental EFG is denoted by the dashed line (2-bromopyrimidine only)



(a)



(b)

Figure B.2.9: ω B97X change in atomisation and EFG for a) p-bromotoluene and b) p-iodotoluene over range $\omega=0.05-1$. Optimal $\omega=0.25$ and is denoted in green. Experimental EFG is denoted by the dashed line

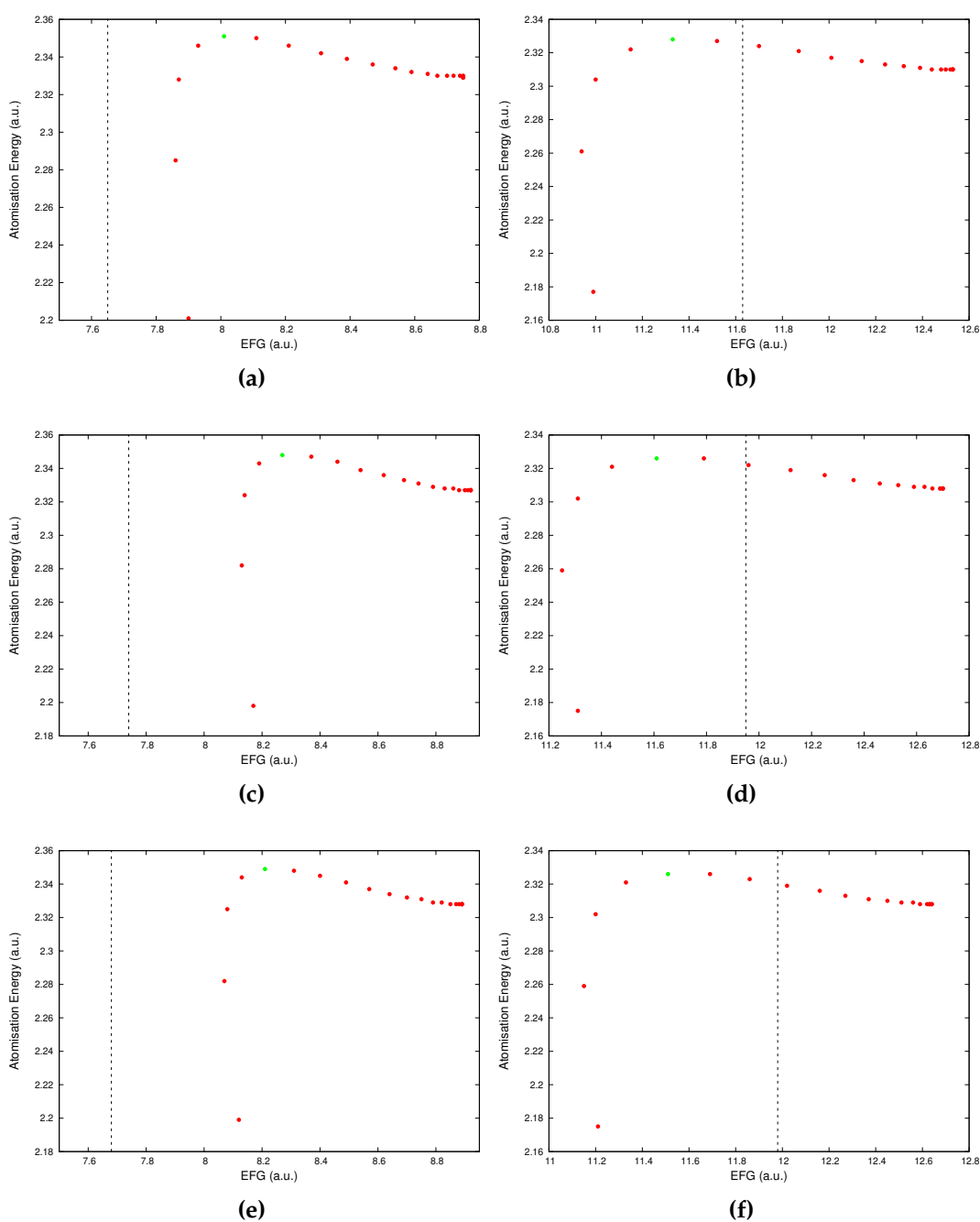


Figure B.2.10: ω B97X change in atomisation and EFG for a) 2-bromopyridine b) 2-iodopyridine c) 3-bromopyridine d) 3-iodopyridine e) 4-bromopyridine f) 4-iodopyridine over range $\omega=0.05-1$. Optimal $\omega=0.25$ and is denoted in green. Experimental EFG is denoted by the dashed line

B.3 Core Polarisation Contribution to Ag Electric Field Gradient

Method	Ag Core Pol. EFG/a.u.
CCSD(T)	-0.683
B2GP-PLYP	-0.333
B2PLYP-D3	-0.203
B2PLYP	-0.203
B3LYP	0.181
B97-D3	0.471
B97	0.144
BLYP	0.546
BP86	0.506
CAM-B3LYP	0.117
DSD-BLYP-D3	-0.391
LC-BLYP	0.288
M062X	-0.116
M06L	0.012
M06	0.065
mPW2PLYP	-0.221
O3LYP	0.223
PBE0	0.063
PBE	0.474
PWPB95	-0.194
PW6B95	0.040
TPSS0	-0.052
TPSSh	0.104
TPSS	0.300
wB97	0.109
wB97X-D3	0.065
wB97X	0.059

Table B.3.1: Core polarisation contribution to silver electric field gradient of AgCl of default functionals and CCSD(T)

ω	Ag Core Pol. EFG/a.u.
0.05	0.137
0.10	0.146
0.15	0.143
0.20	0.125
0.25	0.096
0.30	0.059
0.35	0.018
0.40	-0.025
0.45	-0.068
0.50	-0.110
0.55	-0.150
0.60	-0.188
0.65	-0.222
0.70	-0.254
0.75	-0.283
0.80	-0.309
0.85	-0.333
0.90	-0.355
0.95	-0.375
1.00	-0.392

Table B.3.2: Core polarisation contribution to silver electric field gradient of AgCl of ω B97X functionals with ω altered from 0.05 through 1.00

Method	Ag Core Pol. EFG/a.u.
CCSD(T)	-0.350
B2GP-PLYP	-0.052
B2PLYP-D3	0.057
B2PLYP	0.057
B3LYP	0.392
B97-D3	0.613
B97	0.351
BLYP	0.679
BP86	0.639
CAM-B3LYP	0.335
DSD-BLYP-D3	-0.102
LC-BLYP	0.471
M062X	0.147
M06L	0.272
M06	0.297
mPW2PLYP	0.043
O3LYP	0.414
PBE0	0.286
PBE	0.612
PWPB95	0.059
PW6B95	0.270
TPSS0	0.192
TPSSh	0.321
TPSS	0.470
wB97	0.332
wB97X-D3	0.290
wB97X	0.287

Table B.3.3: Core polarisation contribution to silver electric field gradient of AgI of default functionals and CCSD(T)

ω	Ag Core Pol. EFG/a.u.
0.05	0.137
0.10	0.146
0.15	0.143
0.20	0.125
0.25	0.096
0.30	0.059
0.35	0.018
0.40	-0.025
0.45	-0.068
0.50	-0.110
0.55	-0.150
0.60	-0.188
0.65	-0.222
0.70	-0.254
0.75	-0.283
0.80	-0.309
0.85	-0.333
0.90	-0.355
0.95	-0.375
1.00	-0.392

Table B.3.4: Core polarisation contribution to silver electric field gradient of AgI of ω B97X functionals with ω altered from 0.05 through 1.00

Appendix C

Analysis of Forcefield Methods to Predict Solvent-Term Ultrafast X-ray Scattering Relative to Experimental Metrics

C.1 Temperature-Dependent and Density-Dependent Solvent Scattering Term

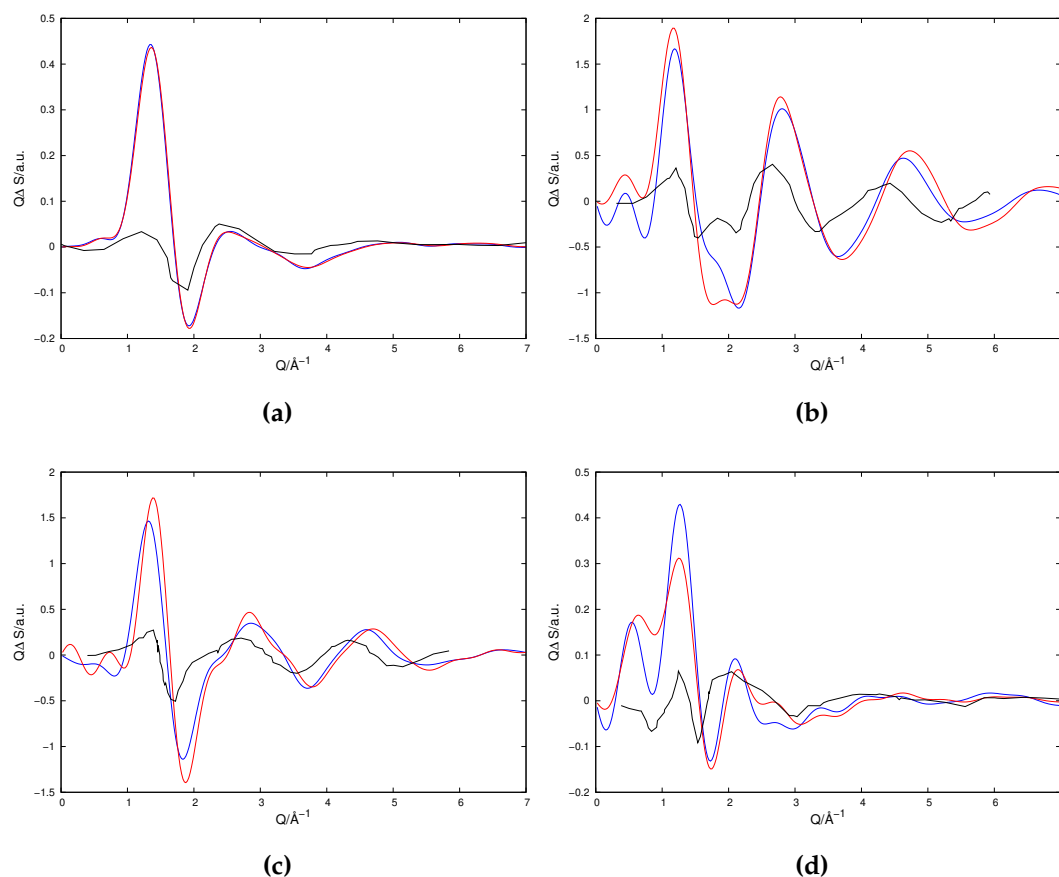
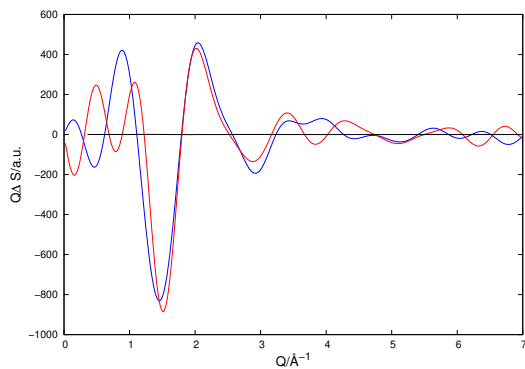
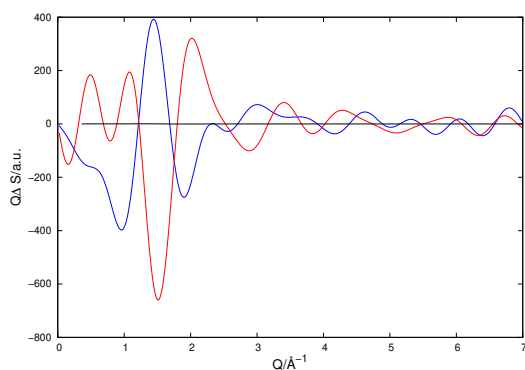


Figure C.1.1: $\frac{\partial S}{\partial T}$ per solvent molecule characteristic calculated from 5K solvent differences from OPLS-AA (blue) and QUBE (red), compared with experimental calculations (black) [1] for a) acetonitrile b) chloroform c) dichloromethane and d) ethanol



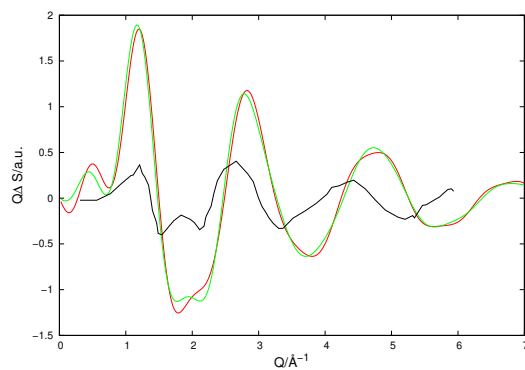
(a)



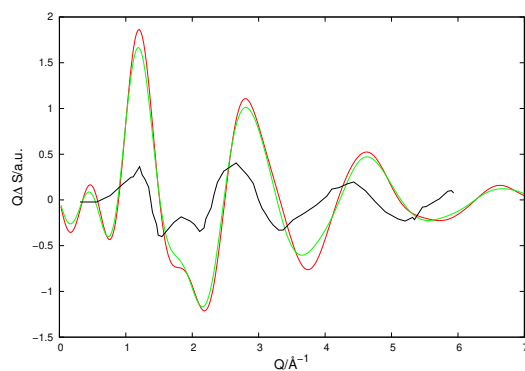
(b)

Figure C.1.2: $\frac{\partial S}{\partial \rho}$ per solvent molecule characteristic calculated from 0.05 bar and 0.20bar solvent pressure differences from OPLS-AA (blue) and QUBE (red), compared with experimental calculations (black) [1] for acetonitrile. Density change for this change in pressure is simply too low to yield meaningful accurate results, hence the predicted scattering change is simply too large. This exact rationale for this erroneous prediction requires further investigation.

C.2 Comparison of Temperature-Dependent Solvent Scattering Terms

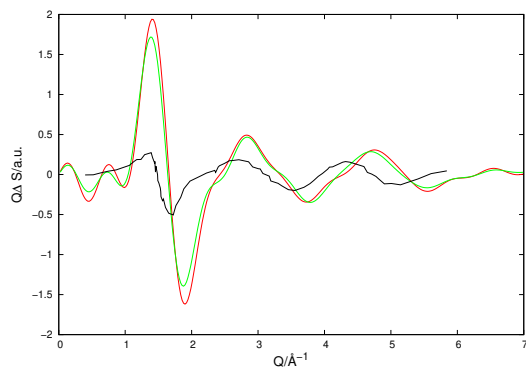


(a)

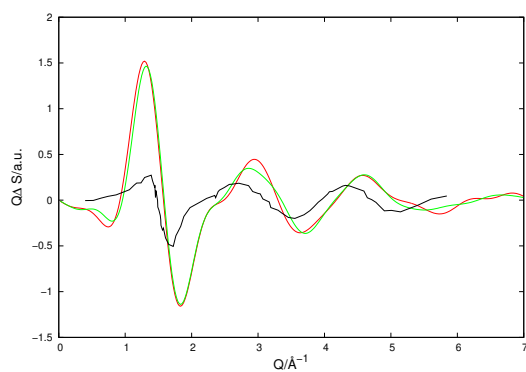


(b)

Figure C.2.1: $\frac{\partial S}{\partial T}$ per solvent molecule characteristic of chloroform calculated from 1K (red) and 5K (green) solvent differences for a) QUBE and b) OPLS-AA, compared with experimental calculations (black) [1]

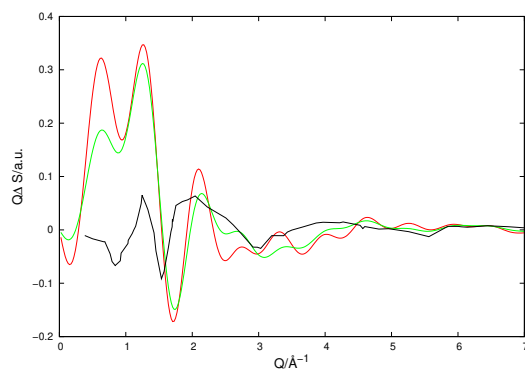


(a)

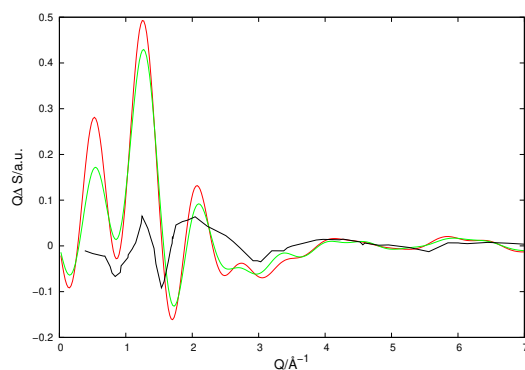


(b)

Figure C.2.2: $\frac{\partial S}{\partial T}$ per solvent molecule characteristic of dichloromethane calculated from 1K (red) and 5K (green) solvent differences for a) QUBE and b) OPLS-AA, compared with experimental calculations (black) [1]



(a)



(b)

Figure C.2.3: $\frac{\partial S}{\partial T}$ per solvent molecule characteristic of ethanol calculated from 1K (red) and 5K (green) solvent differences for a) QUBE and b) OPLS-AA, compared with experimental calculations (black) [1]

C.3 Radial Distribution Functions of Atom Combinations with Large Contributions to scattering

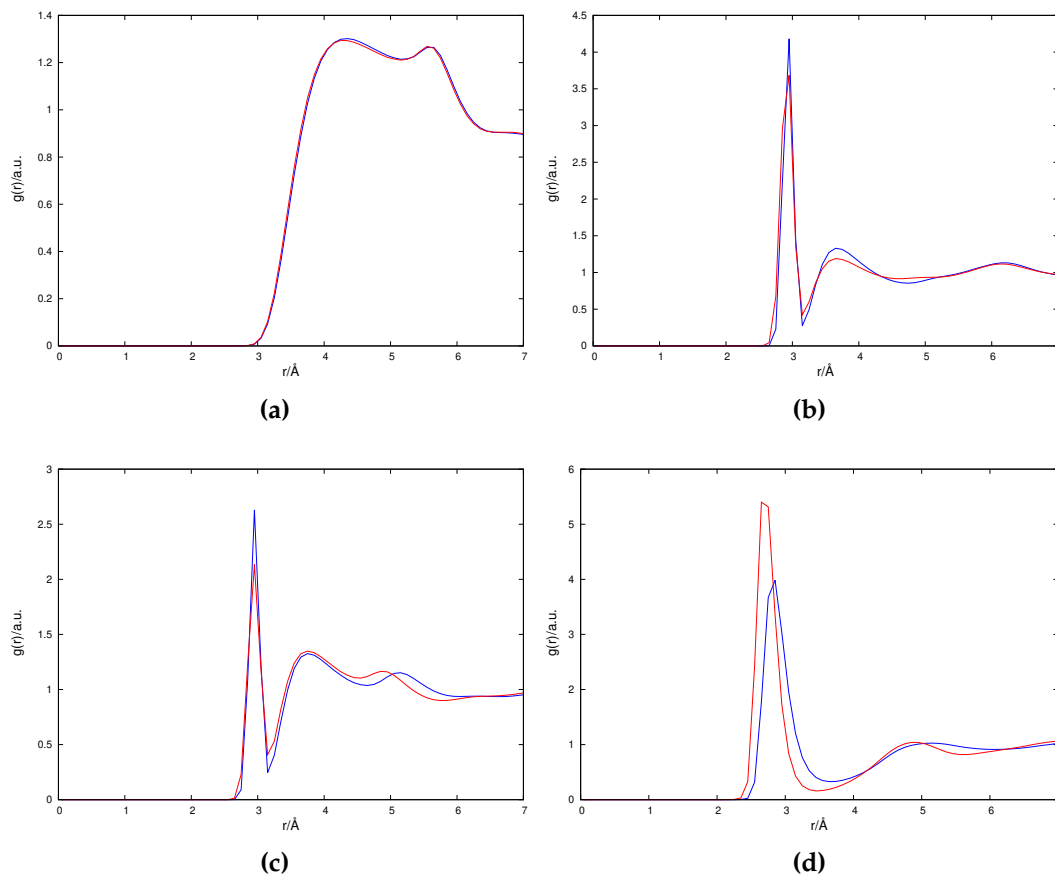


Figure C.3.1: $g(r)$ contributions of dominant scattering atom combinations at 299.15K (1K above ground temperature) from OPLS-AA (blue) and QUBE (red), a) acetonitrile (N-N) b) chloroform (Cl-Cl) c) dichloromethane (Cl-Cl) and d) ethanol (O-O)

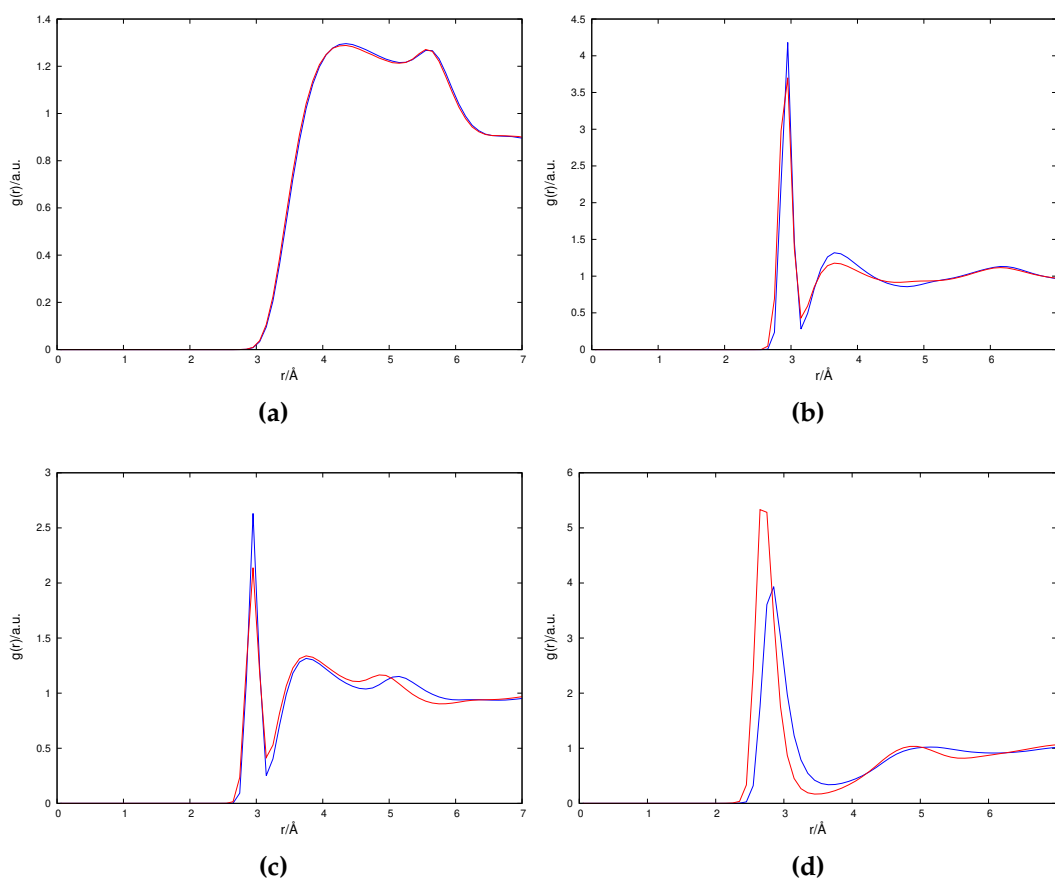


Figure C.3.2: $g(r)$ contributions of dominant scattering atom combinations at 303.15K (5K above ground temperature) from OPLS-AA (blue) and QUBE (red), a) acetonitrile (N-N) b) chloroform (Cl-Cl) c) dichloromethane (Cl-Cl) and d) ethanol (O-O)

Appendix D

Analysis of Forcefield Methods to Predict Solute-Solvent Ultrafast X-ray Scattering

D.1 Temperature-Dependent Solute-Solvent Scattering Term

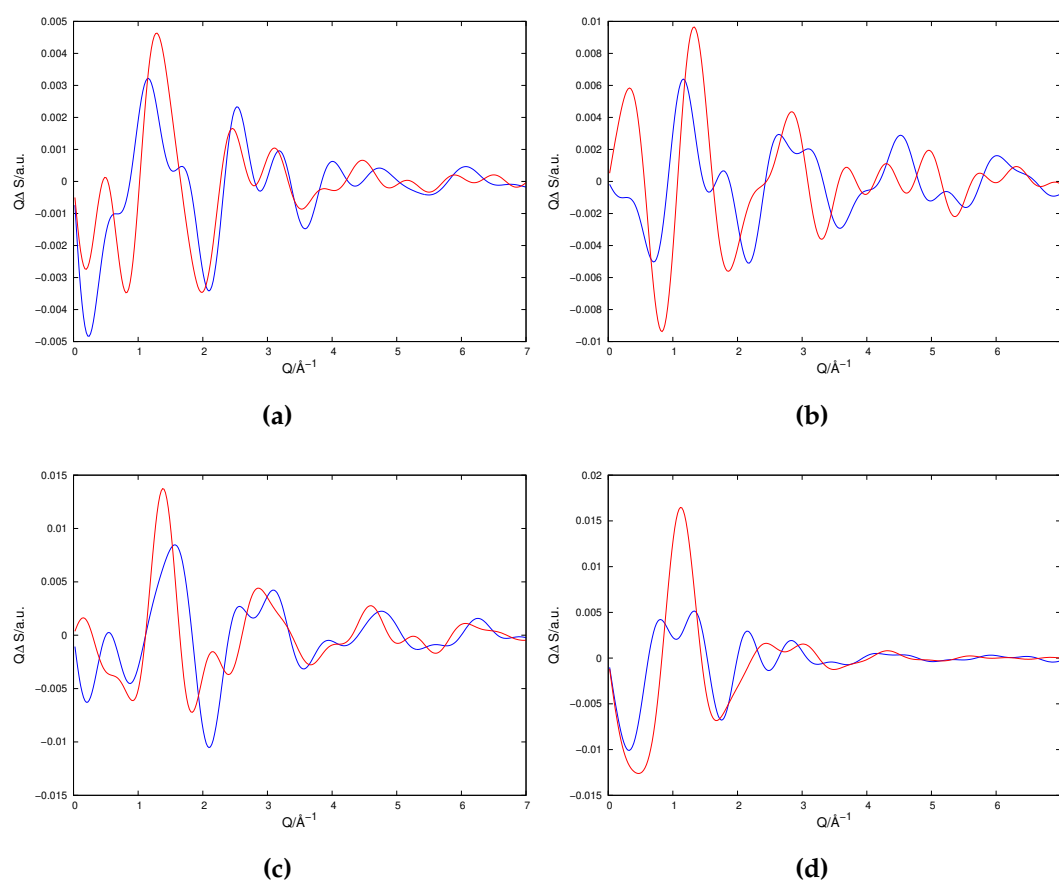
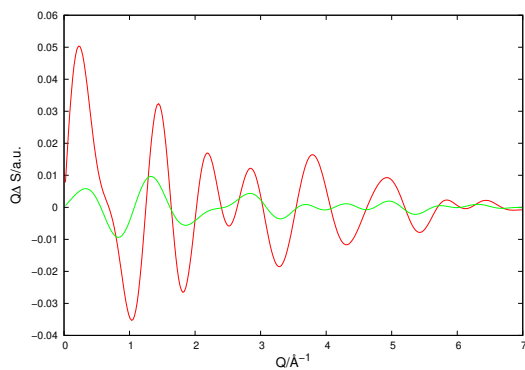
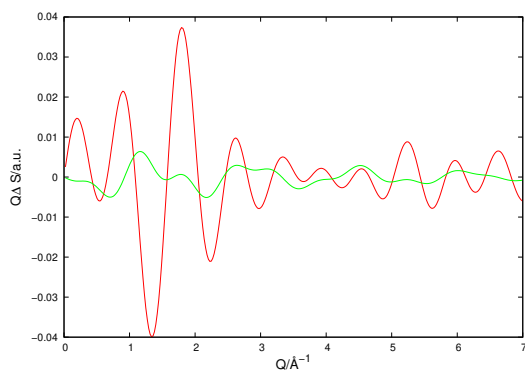


Figure D.1.1: $\frac{\partial S}{\partial T}$ per solvent molecule characteristic calculated from 5K solution differences from OPLS-AA (blue) and QUBE (red) for a) acetonitrile b) chloroform c) dichloromethane and d) ethanol

D.2 Comparison of Temperature-Dependent Solute-Solvent Scattering Terms

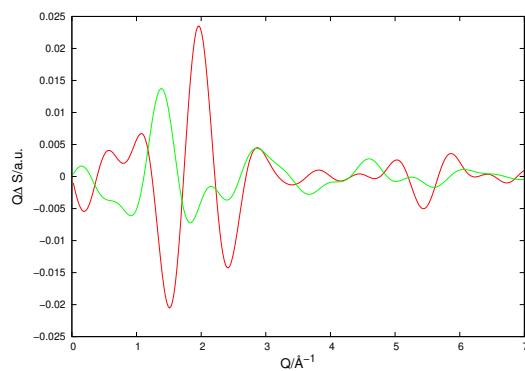


(a)

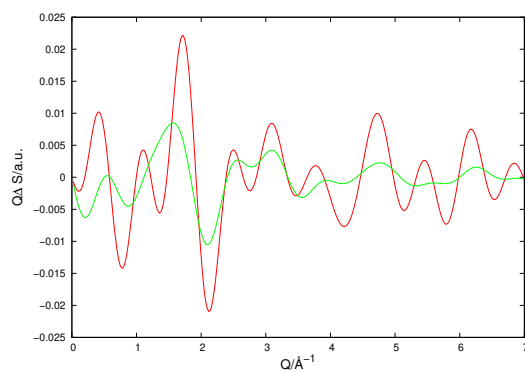


(b)

Figure D.2.1: $\frac{\partial S}{\partial T}$ per solvent molecule characteristic for the cross-term contribution of chlorine calculated from 1K (red) and 5K (green) solvent differences for a) QUBE and b) OPLS-AA

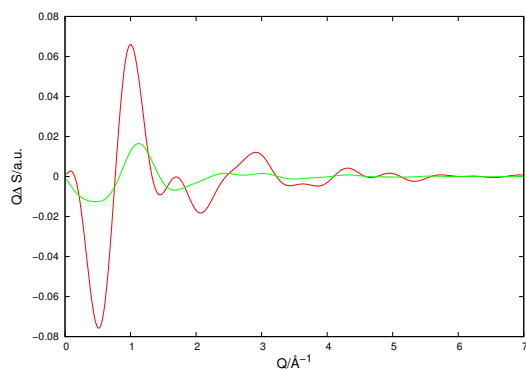


(a)

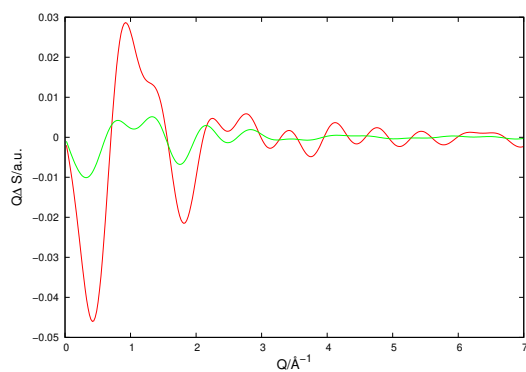


(b)

Figure D.2.2: $\frac{\partial S}{\partial T}$ per solvent molecule characteristic for the cross-term contribution of dichloromethane calculated from 1K (red) and 5K (green) solvent differences for a) QUBE and b) OPLS-AA



(a)



(b)

Figure D.2.3: $\frac{\partial S}{\partial T}$ per solvent molecule characteristic for the cross-term contribution of ethanol calculated from 1K (red) and 5K (green) solvent differences for a) QUBE and b) OPLS-AA

D.3 Radial Distribution Functions with Large Contributions to Solute-Solvent Scattering

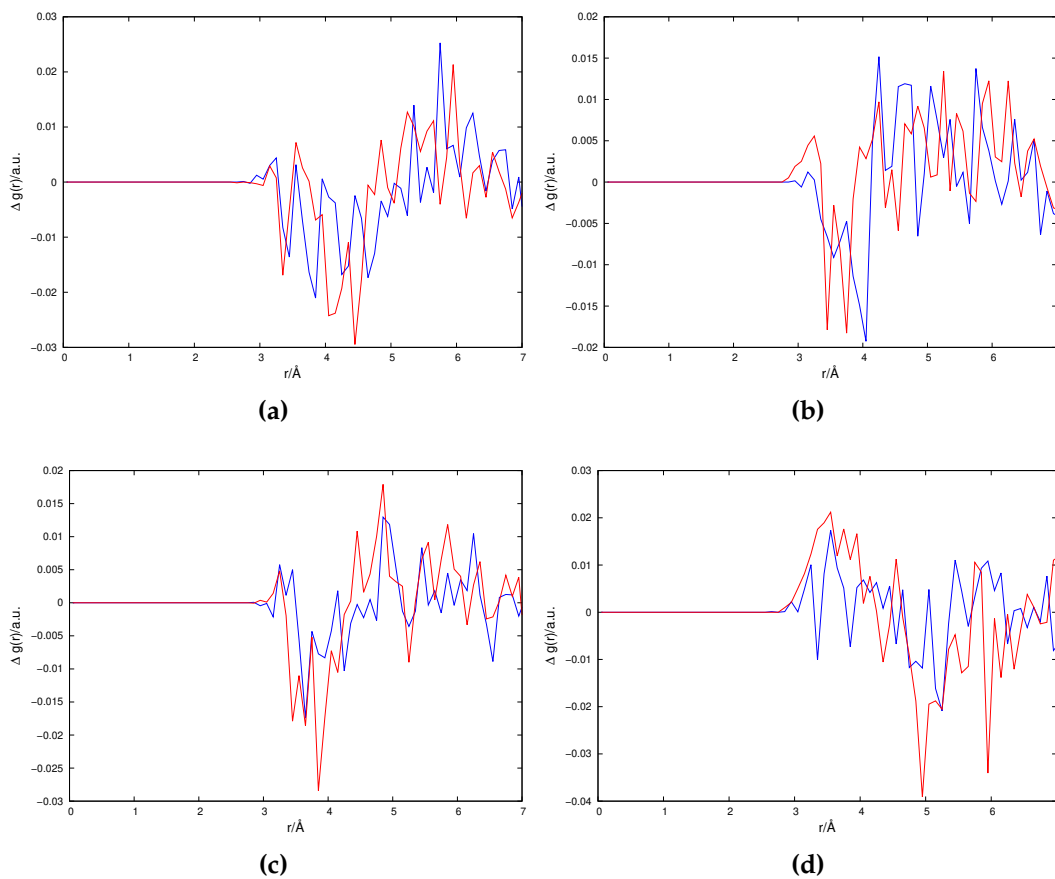


Figure D.3.1: $\Delta g(r)$ contributions of dominant scattering atom combinations calculated from 5K solvent differences from OPLS-AA (blue) and QUBE (red), a) acetonitrile (I-N) b) chloroform (I-Cl) c) dichloromethane (I-Cl) and d) ethanol (I-O)

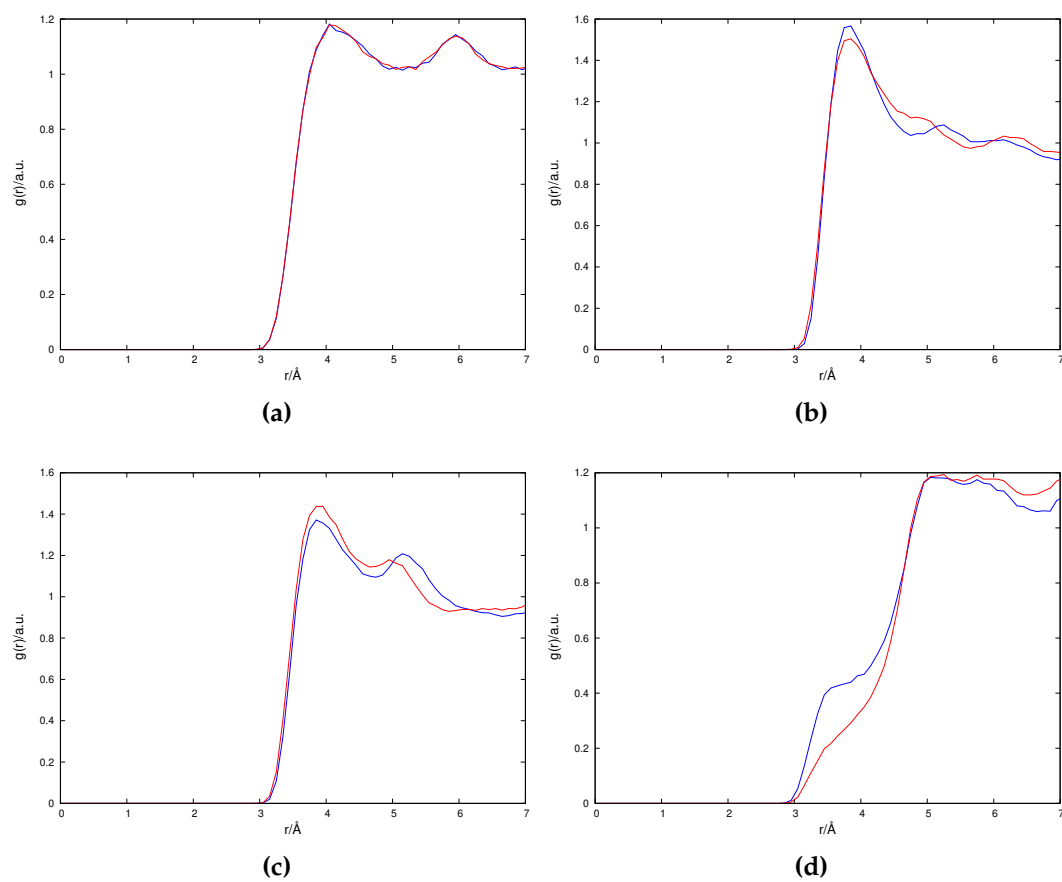


Figure D.3.2: $g(r)$ contributions of dominant scattering atom combinations at 299.15K (1K above ground temperature) from OPLS-AA (blue) and QUBE (red), a) acetonitrile (I-N) b) chloroform (I-Cl) c) dichloromethane (I-Cl) and d) ethanol (I-O)

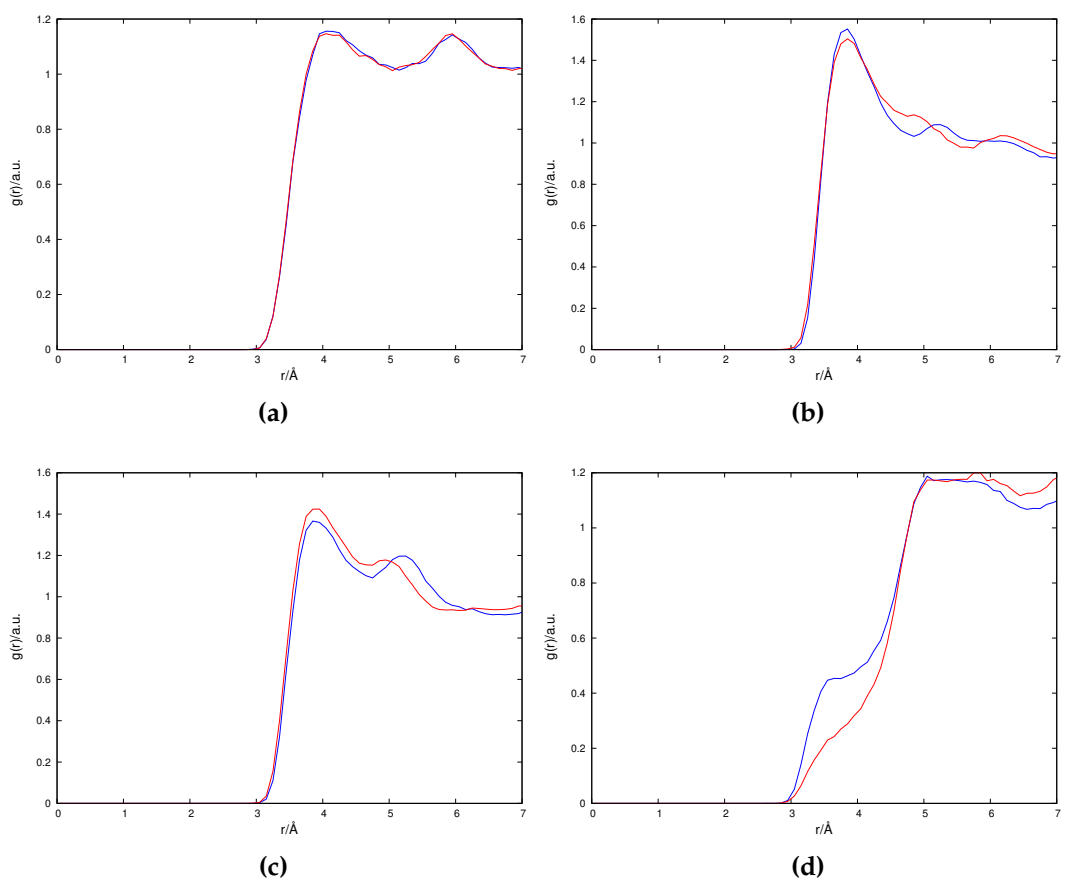


Figure D.3.3: $g(r)$ contributions of dominant scattering atom combinations at 303.15K (5K above ground temperature) from OPLS-AA (blue) and QUBE (red), a) acetonitrile (I-N) b) chloroform (I-Cl) c) dichloromethane (I-Cl) and d) ethanol (I-O)

D.4 Temperature-Dependent Solute Scattering Terms

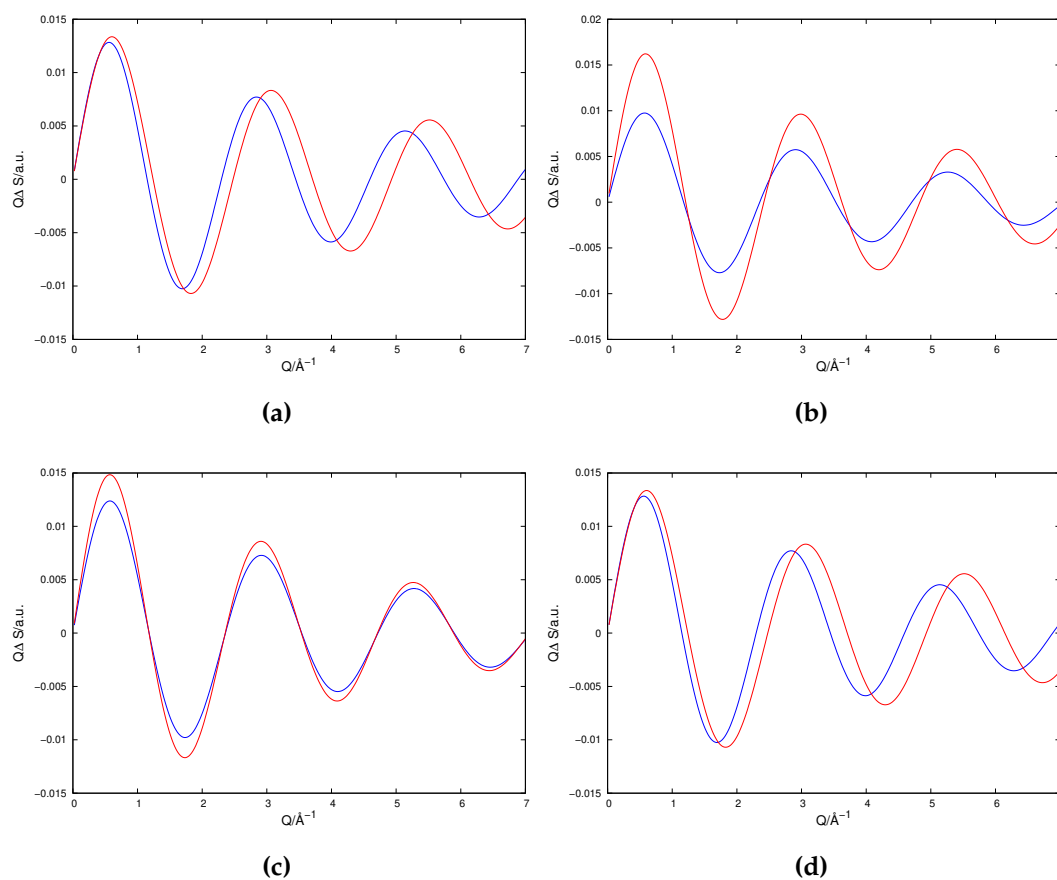
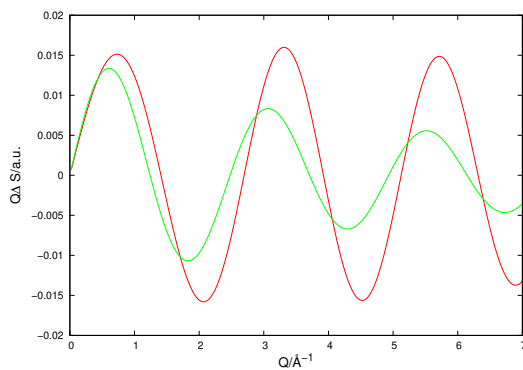
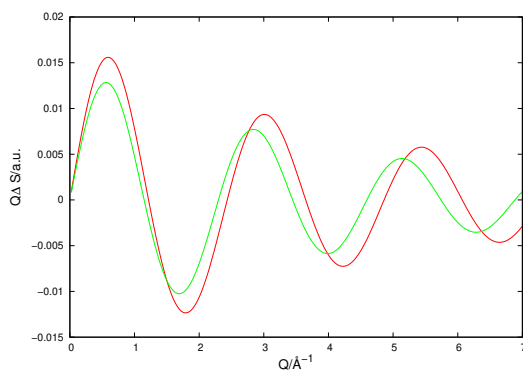


Figure D.4.1: $\frac{\partial S}{\partial T}$ per solvent molecule characteristic if the I_2 solute calculated from 5K solution differences from OPLS-AA (blue) and QUBE (red) for a) acetonitrile b) chloroform c) dichloromethane and d) ethanol

D.5 Comparison of Temperature-Dependent Solute Scattering Terms

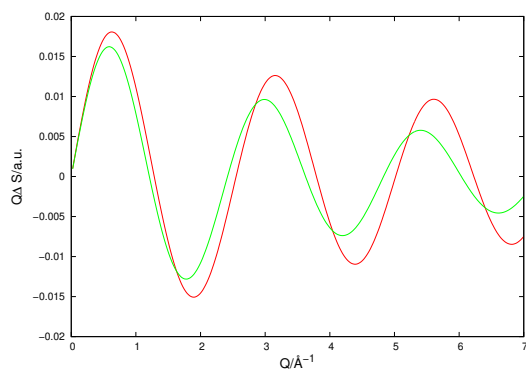


(a)

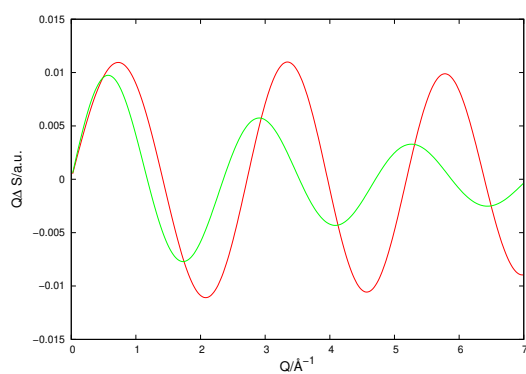


(b)

Figure D.5.1: $\frac{\partial S}{\partial T}$ per solvent molecule characteristic for the solute-term contribution of molecular iodine solvated in acetonitrile calculated from 1K (red) and 5K (green) solvent differences for a) QUBE and b) OPLS-AA

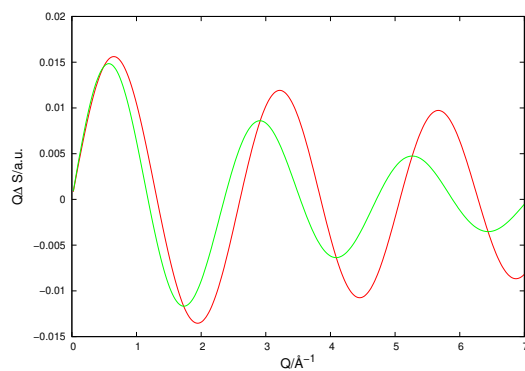


(a)

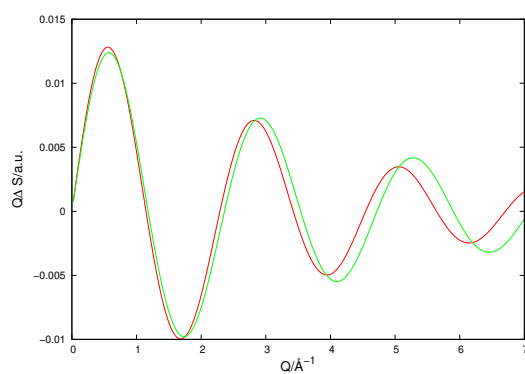


(b)

Figure D.5.2: $\frac{\partial S}{\partial T}$ per solvent molecule characteristic for the solute-term contribution of molecular iodine solvated in chloroform calculated from 1K (red) and 5K (green) solvent differences for a) QUBE and b) OPLS-AA

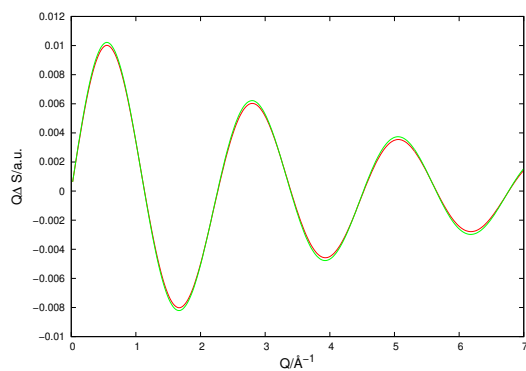


(a)

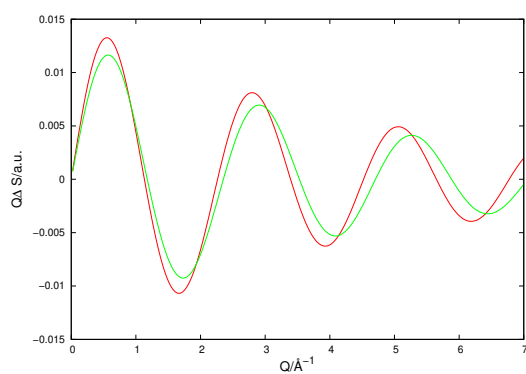


(b)

Figure D.5.3: $\frac{\partial S}{\partial T}$ per solvent molecule characteristic for the solute-term contribution of molecular iodine solvated in dichloromethane calculated from 1K (red) and 5K (green) solvent differences for a) QUBE and b) OPLS-AA



(a)



(b)

Figure D.5.4: $\frac{\partial S}{\partial T}$ per solvent molecule characteristic for the solute-term contribution of molecular iodine solvated in ethanol calculated from 1K (red) and 5K (green) solvent differences for a) QUBE and b) OPLS-AA

D.6 I-I Radial Distribution Functions for Solute Scattering

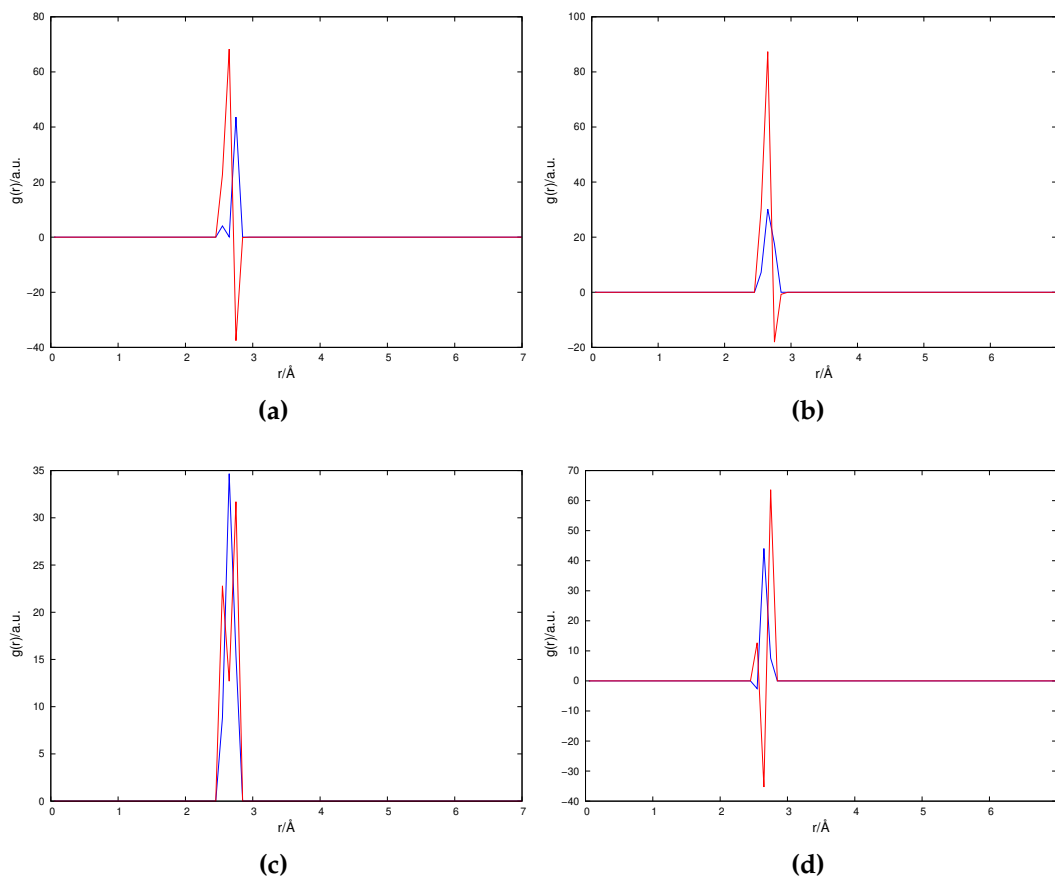


Figure D.6.1: $\Delta g(r)$ contributions of the I-I solute atoms calculated from 5K solvent differences from OPLS-AA (blue) and QUBE (red), a) acetonitrile b) chloroform c) dichloromethane and d) ethanol

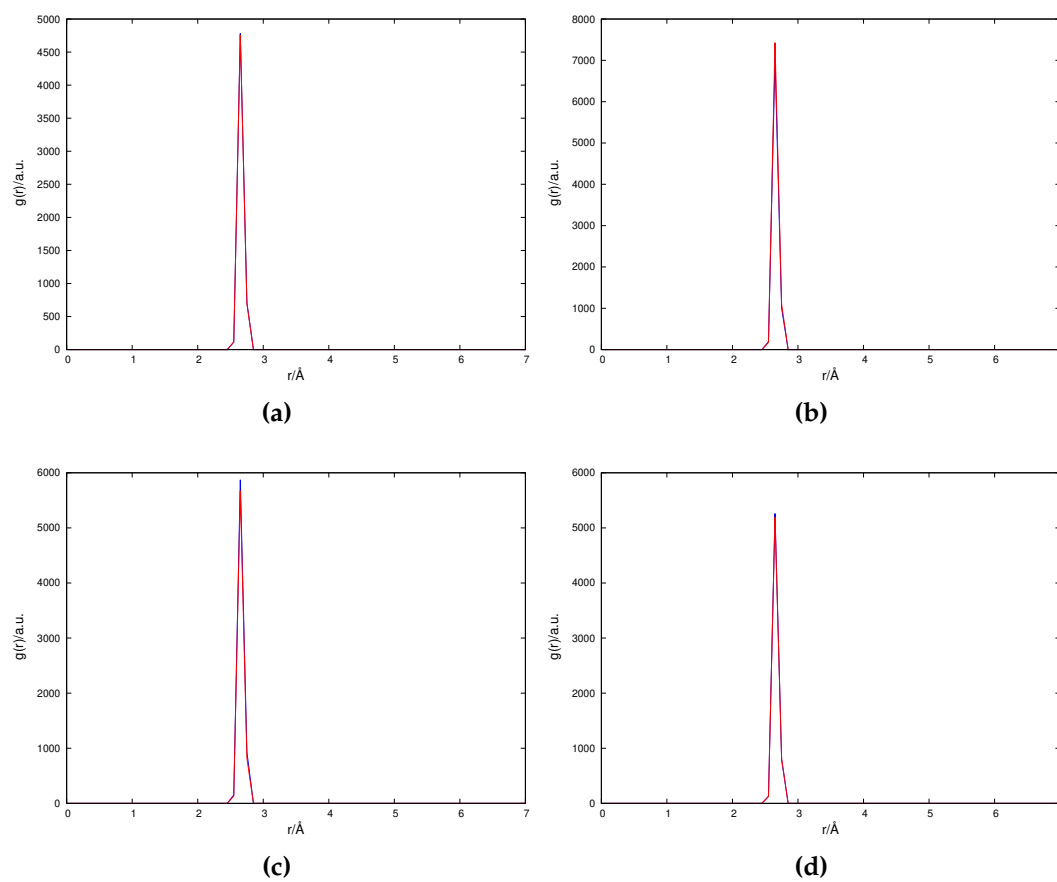


Figure D.6.2: $g(r)$ contributions of the I-I solute atoms at 1K above ground temperature (299.15K) from OPLS-AA (blue) and QUBE (red), a) acetonitrile b) chloroform c) dichloromethane and d) ethanol

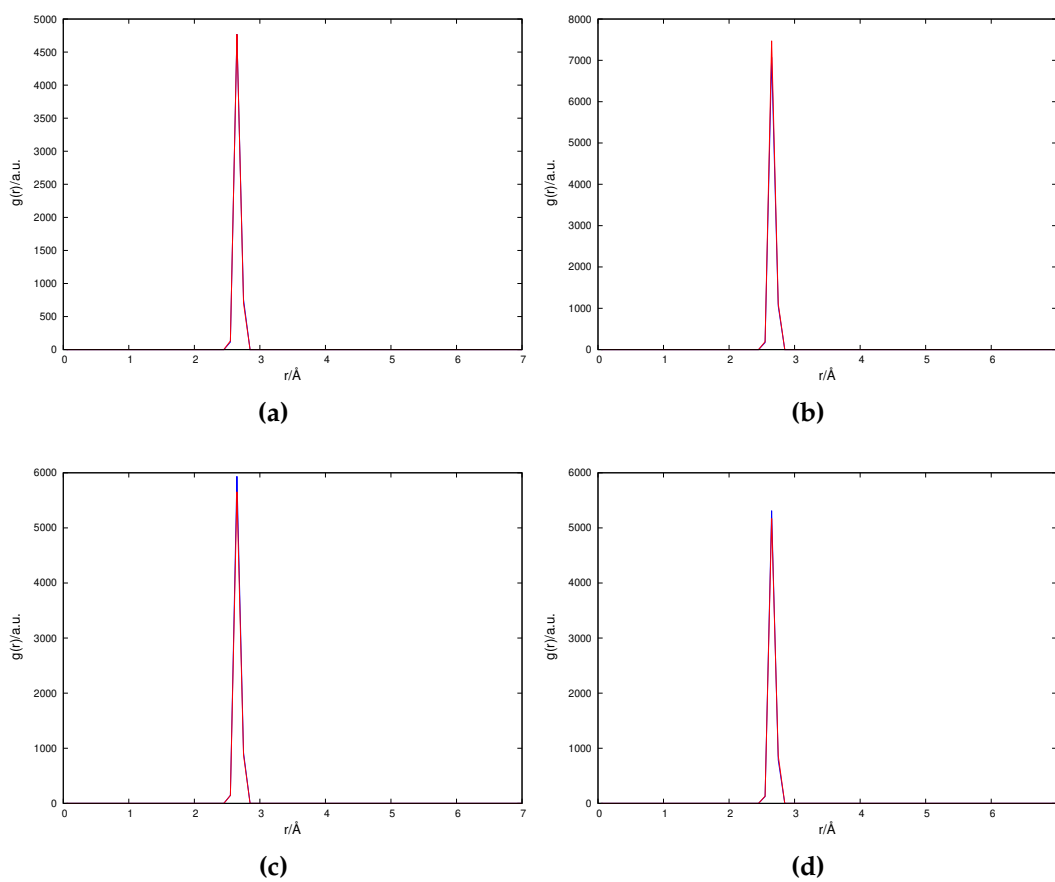


Figure D.6.3: $g(r)$ contributions of the I-I solute atoms at 5K above ground temperature (303.15K) from OPLS-AA (blue) and QUBE (red), a) acetonitrile b) chloroform c) dichloromethane and d) ethanol

Bibliography

- [1] Kjær K.S., van Driel T.B., Kehres J., Haldrup K., Khakhulin D., Bechgaard K., Cammarata M., Wulff M., Sørensen T.J., Nielsen M.M., "Introducing a standard method for experimental determination of the solvent response in laser pump, X-ray probe time-resolved wide-angle X-ray scattering experiments on systems in solution," *Physical Chemistry Chemical Physics*, vol. 15, no. 36, pp. 15003–15016, 2013.
- [2] Liao Q., Kamerlin S.C.L., Strodel B., "Development and application of a nonbonded Cu²⁺ model that includes the Jahn–Teller effect," *The Journal of Physical Chemistry Letters*, vol. 6, no. 13, pp. 2657–2662, 2015.
- [3] Capano G., Rothlisberger, U., Tavernelli, I., Penfold, T.J., "Theoretical rationalization of the emission properties of prototypical Cu(I)–phenanthroline complexes," *The Journal of Physical Chemistry A*, vol. 119, no. 27, pp. 7026–7037, 2015.
- [4] Cole D.J., Vilseck J.Z., Tirado-Rives J., Payne M.C., Jorgensen W.L., "Biomolecular Force Field Parameterization via Atoms-in-Molecule Electron Density Partitioning," *Journal of Chemical Theory and Computation*, vol. 12, pp. 2312–2323, 2016.
- [5] Horton J.T., Allen A.E.A., Dodda L.S., Cole D.J., "Qubekit: automating the derivation of force field parameters from quantum mechanics," *Journal of Chemical Information and Modeling*, vol. 59, no. 4, pp. 1366–1381, 2019.
- [6] Pribram-Jones A., Gross D.A., Burke K., "DFT: A theory full of holes?," *Annual Review of Physical Chemistry*, vol. 66, pp. 283–304, 2015.
- [7] Hohenburg P., Kohn W., "Inhomogenous Electron Gas," *Physical Review*, no. 3B, p. B864, 1964.
- [8] Rezac J., Hobza P., "Describing noncovalent interactions beyond the common approximations: How accurate is the "gold standard," CCSD

- (T) at the complete basis set limit?," *Journal of Chemical Theory and Computation*, vol. 9, no. 5, pp. 2151–2155, 2013.
- [9] Ramabhadran R.O., Raghavachari K., "Extrapolation to the gold-standard in quantum chemistry: Computationally efficient and accurate CCSD (T) energies for large molecules using an automated thermochemical hierarchy," *Journal of Chemical Theory and Computation*, vol. 9, no. 9, pp. 3986–3994, 2013.
- [10] Perdew J.P., Schmidt K., "Jacob's ladder of density functional approximations for the exchange-correlation energy," *AIP Conference Proceedings*, vol. 577, no. 1, pp. 1–20, 2001.
- [11] Kohn W., Sham L.J., "Self-consistent equations including exchange and correlation effects," *Physical Review*, vol. 140, no. 4A, p. A1133, 1965.
- [12] Thomas L.H., "The calculation of atomic fields," in *Mathematical Proceedings of the Cambridge Philosophical Society*, vol. 23, pp. 542–548, Cambridge University Press, 1927.
- [13] Fermi E., "Un metodo statistico per la determinazione di alcune prioriet  dell'atome," *Rend. Accad. Naz. Lincei*, vol. 6, no. 602-607, p. 32, 1927.
- [14] Jensen F., *Introduction to Computational Chemistry*. Wiley, 2017.
- [15] Becke A.D., "Perspective: Fifty years of density-functional theory in chemical physics," *The Journal of Chemical Physics*, vol. 140, no. 18, p. 18A301, 2014.
- [16] Perdew J.P., Ruzsinszky A., Tao J., Staroverov V.N., Scuseria G.E., Csonka G.I., "Prescription for the design and selection of density functional approximations: More constraint satisfaction with fewer fits," *The Journal of Chemical Physics*, vol. 123, no. 6, p. 062201, 2005.
- [17] Langreth D.C., Mehl M.J., "Beyond the local-density approximation in calculations of ground-state electronic properties," *Physical Review B*, vol. 28, no. 4, p. 1809, 1983.
- [18] Perdew J.P., Burke K., Ernzerhof M., "Perdew, Burke, and Ernzerhof reply," *Physical Review Letters*, vol. 78, p. 1396, 1996.

- [19] Kim M-C., Sim E., Burke K., "Understanding and reducing errors in density functional calculations," *Physical Review Letters*, vol. 111, no. 7, p. 073003, 2013.
- [20] Gritsenko O.V., Mentel Ł.M., Baerends E.J., "On the errors of local density (LDA) and generalized gradient (GGA) approximations to the Kohn-Sham potential and orbital energies," *The Journal of Chemical Physics*, vol. 144, no. 20, p. 204114, 2016.
- [21] Becke A.D., "A new mixing of hartree-fock and local density-functional theories," *The Journal of Chemical Physics*, vol. 98, no. 2, pp. 1372–1377, 1993.
- [22] Goerigk L., Grimme S., "Efficient and Accurate Double-Hybrid-Meta-GGA Density Functionals Evaluation with the Extended GMTKN30 Database for General Main Group Thermochemistry, Kinetics, and Noncovalent Interactions," *Journal of Chemical Theory and Computation*, vol. 7, no. 2, pp. 291–309, 2010.
- [23] Goerigk L., Grimme S., "Double-hybrid density functionals," *Wiley Interdisciplinary Reviews: Computational Molecular Science*, vol. 4, no. 6, pp. 576–600, 2014.
- [24] Chan B., Goerigk L., Radom L., "On the inclusion of post-MP2 contributions to double-Hybrid density functionals," *Journal of Computational Chemistry*, vol. 37, no. 2, pp. 183–193, 2016.
- [25] Chai J-D., Head-Gordon M., "Long-range corrected hybrid density functionals with damped atom-atom dispersion corrections," *Physical Chemistry Chemical Physics*, vol. 10, no. 44, pp. 6615–6620, 2008.
- [26] Tsuneda T., Hirao K., "Long-range correction for density functional theory," *Wiley Interdisciplinary Reviews: Computational Molecular Science*, vol. 4, no. 4, pp. 375–390, 2014.
- [27] Medvedev M.G., Bushmarinov I.S., Sun J., Perdew J.P., Lyssenko K.A., "Density functional theory is straying from the path to the exact functional," *Science*, vol. 355, pp. 49–52, 2017.
- [28] Brorsen K.R., Yang Y., Pak M.V., Hammes-Schiffer S., "Is the Accuracy of Density Functional Theory for Atomization Energies and Densities in Bonding Regions Correlated?," *The Journal of Physical Chemistry Letters*, vol. 8, pp. 2076–2081, 2017.

- [29] Hait D., Head-Gordon M., "How accurate is density functional theory at predicting dipole moments? An assessment using a new database of 200 benchmark values," *Journal of chemical theory and computation*, vol. 14, no. 4, pp. 1969–1981, 2018.
- [30] Kepp K.P., "Comment on 'Density functional theory is straying from the path toward the exact functional'," *Science*, vol. 356, no. 6337, pp. 496–496, 2017.
- [31] Kepp K.P., "Energy vs. density on paths toward more exact density functionals," *Physical Chemistry Chemical Physics*, vol. 20, no. 11, pp. 7538–7548, 2018.
- [32] Sim E., Song S., Burke K., "Quantifying density errors in DFT," *The Journal of Physical Chemistry Letters*, vol. 9, no. 22, pp. 6385–6392, 2018.
- [33] Srebro M., Autschbach J., "Does a molecule-specific density functional give an accurate electron density? The challenging case of the CuCl electric field gradient," *The Journal of Physical Chemistry Letters*, vol. 3, no. 5, pp. 576–581, 2012.
- [34] Johnson A.I., Withanage K.P.K., Sharkas K., Yamamoto Y., Baruah T., Zope R.R., Peralta J.E., Jackson K.A., "The effect of self-interaction error on electrostatic dipoles calculated using density functional theory," *The Journal of Chemical Physics*, vol. 151, no. 17, p. 174106, 2019.
- [35] Neese F., Wolf A., Fleig T., Reiher M., Hess B.A., "Calculation of electric-field gradients based on higher-order generalized Douglas–Kroll transformations," *The Journal of Chemical Physics*, vol. 122, no. 20, p. 204107, 2005.
- [36] Karton A., Tarnopolsky A., Lamère J-F, Schatz G.C, Martin J.M.L., "Highly accurate first-principles benchmark data sets for the parametrization and validation of density functional and other approximate methods. derivation of a robust, generally applicable, double-hybrid functional for thermochemistry and thermochemical kinetics," *The Journal of Physical Chemistry A*, vol. 112, no. 50, pp. 12868–12886, 2008.

- [37] Grimme S., Antony J., Ehrlich S., Krieg H., "A consistent and accurate *ab initio* parametrization of density functional dispersion correction (DFT-D) for the 94 elements H-Pu," *The Journal of Chemical Physics*, vol. 132, no. 15, p. 154104, 2010.
- [38] Grimme S., "Semiempirical hybrid density functional with perturbative second-order correlation," *The Journal of Chemical Physics*, vol. 124, no. 3, p. 034108, 2006.
- [39] Stephens P.J., Devlin F.J., Chabalowski C.F., Frisch M.J., "Ab initio calculation of vibrational absorption and circular dichroism spectra using density functional force fields," *The Journal of Physical Chemistry*, vol. 98, no. 45, pp. 11623–11627, 1994.
- [40] Becke A.D., "Density-functional thermochemistry. v. systematic optimization of exchange-correlation functionals," *The Journal of Chemical Physics*, vol. 107, no. 20, pp. 8554–8560, 1997.
- [41] Lee C., Yang W., Parr R.G., "Development of the Colle-Salvetti correlation-energy formula into a functional of the electron density," *Physical Review B*, vol. 37, no. 2, p. 785, 1988.
- [42] Perdew J.P., "Density-functional approximation for the correlation energy of the inhomogeneous electron gas," *Physical Review B*, vol. 33, no. 12, p. 8822, 1986.
- [43] Yanai T., Tew D.P., Handy N.C., "A new hybrid exchange–correlation functional using the Coulomb-attenuating method (CAM-B3LYP)," *Chemical Physics Letters*, vol. 393, no. 1-3, pp. 51–57, 2004.
- [44] Kozuch S., Gruzman D., Martin J.M.L., "Dsd-blyp: A general purpose double hybrid density functional including spin component scaling and dispersion correction," *The Journal of Physical Chemistry C*, vol. 114, no. 48, pp. 20801–20808, 2010.
- [45] Goerigk L., Grimme S., "A thorough benchmark of density functional methods for general main group thermochemistry, kinetics, and non-covalent interactions," *Physical Chemistry Chemical Physics*, vol. 13, no. 14, pp. 6670–6688, 2011.
- [46] Tawada Y., Tsuneda T., Yanagisawa S., Yanai T., Hirao K., "A long-range-corrected time-dependent density functional theory," *The Journal of Chemical Physics*, vol. 120, no. 18, pp. 8425–8433, 2004.

- [47] Zhao Y., Truhlar D.G., "A new local density functional for main-group thermochemistry, transition metal bonding, thermochemical kinetics, and noncovalent interactions," *The Journal of Chemical Physics*, vol. 125, no. 19, p. 194101, 2006.
- [48] Zhao Y., Truhlar, D.G., "The M06 suite of density functionals for main group thermochemistry, thermochemical kinetics, noncovalent interactions, excited states, and transition elements: two new functionals and systematic testing of four M06-class functionals and 12 other functionals," *Theoretical Chemistry Accounts*, vol. 120, no. 1-3, pp. 215–241, 2008.
- [49] Zhao Y., Truhlar D.G., "Density functionals with broad applicability in chemistry," *Accounts of chemical research*, vol. 41, no. 2, pp. 157–167, 2008.
- [50] Schwabe T., Grimme S., "Towards chemical accuracy for the thermodynamics of large molecules: new hybrid density functionals including non-local correlation effects," *Physical Chemistry Chemical Physics*, vol. 8, no. 38, pp. 4398–4401, 2006.
- [51] Handy N.C., Cohen A.J., "Dynamic correlation," *Molecular Physics*, vol. 99, pp. 607–615, 2001.
- [52] "Toward reliable density functional methods without adjustable parameters: The PBE0 model, author="
- [53] Perdew J.P., Burke K., Ernzerhof M., "Generalized gradient approximation made simple," *Physical Review Letters*, vol. 77, no. 18, p. 3865, 1996.
- [54] Zhao Y., Truhlar D.G., "Design of density functionals that are broadly accurate for thermochemistry, thermochemical kinetics, and non-bonded interactions," *The Journal of Physical Chemistry A*, vol. 109, no. 25, pp. 5656–5667, 2005.
- [55] Tao J., Perdew J.P., Staroverov V.N., Scuseria G.E., "Climbing the density functional ladder: Nonempirical meta-generalized gradient approximation designed for molecules and solids," *Physical Review Letters*, vol. 91, no. 14, p. 146401, 2003.

- [56] Lin Y-S., Li G-D., Mao S-P., Chai J-D., "Long-range corrected hybrid density functionals with improved dispersion corrections," *Journal of Chemical Theory and Computation*, vol. 9, no. 1, pp. 263–272, 2012.
- [57] Evans C.J., Gerry M.C.L., "Noble gas–metal chemical bonding? The microwave spectra, structures, and hyperfine constants of Ar–CuX (X= F, Cl, Br)," *The Journal of Chemical Physics*, vol. 112, no. 21, pp. 9363–9374, 2000.
- [58] Mikhailov V.A., Roberts F.J., Stephens S.L., Harris S.J., Tew, D.P., Harvey J.N., Walker N.R., Legon A.C., "Monohydrates of cuprous chloride and argentous chloride: H₂O CuCl and H₂O AgCl characterized by rotational spectroscopy and ab initio calculations," *The Journal of Chemical Physics*, vol. 134, no. 13, p. 134305, 2011.
- [59] Walker N.R., Tew D.P., Harris S.J., Wheatley D.E., Legon A.C., "Characterisation of H₂S CuCl and H₂S AgCl isolated in the gas phase: A rigidly pyramidal geometry at sulphur revealed by rotational spectroscopy and ab initio calculations," *The Journal of Chemical Physics*, vol. 135, no. 1, p. 014307, 2011.
- [60] Stephens S.L., Tew, D.P., Mikhailov, V.A., Walker, N.R., Legon, A.C., "A prototype transition-metal olefin complex C₂H₄AgCl synthesised by laser ablation and characterised by rotational spectroscopy and ab initio methods," *The Journal of Chemical Physics*, vol. 135, no. 2, p. 024315, 2011.
- [61] Medcraft C., Bittner D.M., Tew D.P., Walker N.R., Legon A.C., "Geometries of H₂S MI (M= Cu, Ag, Au) complexes studied by rotational spectroscopy: The effect of the metal atom," *The Journal of Chemical Physics*, vol. 145, no. 19, p. 194306, 2016.
- [62] Medcraft C., Gougoula E., Bittner D.M., Mullaney J.C., Blanco S., Tew D.P., Walker N.R., Legon A.C., "Molecular geometries and other properties of H₂O AgI and H₃N AgI as characterised by rotational spectroscopy and ab initio calculations," *The Journal of Chemical Physics*, vol. 147, no. 23, p. 234308, 2017.
- [63] Cooper G.A., Medcraft C., Littlefair J.D., Penfold T.J., Walker N.R., "Halogen bonding properties of 4-iodopyrazole and 4-bromopyrazole explored by rotational spectroscopy and ab initio calculations," *The Journal of Chemical Physics*, vol. 147, no. 21, p. 214303, 2017.

- [64] Caminati W., Forti P., "Quadrupole hyperfine structure in the rotational spectrum of 2-and 4-bromo-pyridine," *Chemical Physics Letters*, vol. 15, no. 3, pp. 343–349, 1972.
- [65] Caminati W., Forti P., "Quadrupole coupling constants of 2-and 4-iodopyridine by microwave spectroscopy," *Chemical Physics Letters*, vol. 29, no. 2, pp. 239–241, 1974.
- [66] Doraiswamy S., Sharma S.D., "Quadrupole coupling constants and centrifugal distortion constants of 3-bromopyridine from its microwave spectrum," *Journal of Molecular Spectroscopy*, vol. 88, no. 1, pp. 95–108, 1981.
- [67] Gaster S.A. Brown G.G., Arnold S., Hall T.M., "The 70th international symposium on molecular spectroscopy," 2015.
- [68] Chen J., Paulse C.D., Davis R.W., "The microwave spectrum, electric dipole moment, and bromine nuclear quadrupole coupling constants of 2-bromopyrimidine," *Journal of Molecular Spectroscopy*, vol. 145, no. 1, pp. 18–28, 1991.
- [69] Dorosh O., Białkowska-Jaworska E., Kisiel Z., Pszczółkowski L., "New measurements and global analysis of rotational spectra of Cl-, Br-, and I-benzene: Spectroscopic constants and electric dipole moments," *Journal of Molecular Spectroscopy*, vol. 246, no. 2, pp. 228–232, 2007.
- [70] Neill J.L., Shipman S.T., Alvarez-Valtierra L., Lesarri A., Kisiel Z., Pate B.H., "Rotational spectroscopy of iodobenzene and iodobenzene–neon with a direct digital 2–8 GHz chirped-pulse Fourier transform microwave spectrometer," *Journal of Molecular Spectroscopy*, vol. 269, no. 1, pp. 21–29, 2011.
- [71] Alvin Shubert V., Schmitz D., Schnell M., "Communication through the phenyl ring: internal rotation and nuclear quadrupole splitting in p-halotoluenes," *Molecular Physics*, vol. 111, no. 14-15, pp. 2189–2197, 2013.
- [72] Ihee H., Wulff M., Kim J., Adachi S., "Ultrafast X-ray scattering: structural dynamics from diatomic to protein molecules," *International Reviews in Physical Chemistry*, vol. 29, no. 3, pp. 453–520, 2010.
- [73] Kelly A., Knowles K.M., *Crystallography and crystal defects*. John Wiley & Sons, 2020.

- [74] Ahn S., Kim K.H., Kim Y., Kim J., Ihee H., "Protein tertiary structural changes visualized by time-resolved X-ray solution scattering," *The Journal of Physical Chemistry B*, vol. 113, no. 40, pp. 13131–13133, 2009.
- [75] Oang K.Y., Kim J.G., Yang C., Kim T.W., Kim Y., Kim K.H., Kim J., Ihee H., "Conformational substates of myoglobin intermediate resolved by picosecond X-ray solution scattering," *The journal of Physical Chemistry Letters*, vol. 5, no. 5, pp. 804–808, 2014.
- [76] Kern J., Yachandra V.K., Yano J., "Metalloprotein structures at ambient conditions and in real-time: biological crystallography and spectroscopy using X-ray free electron lasers," *Current Opinion in Structural Biology*, vol. 34, pp. 87–98, 2015.
- [77] Northey T., Zotev N., Kirrander A., "Ab initio calculation of molecular diffraction," *Journal of Chemical Theory and Computation*, vol. 10, no. 11, pp. 4911–4920, 2014.
- [78] Kirrander A., Saita K., Shalashilin D.V., "Ultrafast X-ray scattering from molecules," *Journal of Chemical Theory and Computation*, vol. 12, no. 3, pp. 957–967, 2016.
- [79] Lee J.H., Wulff M., Bratos S., Petersen J., Guerin L., Leicknam J.-C., Cammarata M., Kong Q., Kim J., Møller K.B., *et al*, "Filming the birth of molecules and accompanying solvent rearrangement," *Journal of the American Chemical Society*, vol. 135, no. 8, pp. 3255–3261, 2013.
- [80] Song, L., Yang, L., Meng, J., Yang, S., "Thermodynamics of hydrophobic amino acids in solution: A combined experimental–computational study," *The Journal of Physical Chemistry Letters*, vol. 8, no. 2, pp. 347–351, 2017.
- [81] Ponseca Jr C.S., Chabera P., Uhlig J., Persson P., Sundstrom V., "Ultrafast electron dynamics in solar energy conversion," *Chemical Reviews*, vol. 117, no. 16, pp. 10940–11024, 2017.
- [82] Haldrup K., Gawelda W., Abela R., Alonso-Mori R., Bergmann U., Bوردage A., Cammarata M., Canton S.E., Dohn A.O., Van Driel T.B. *et al*, "Observing solvation dynamics with simultaneous femtosecond X-ray emission spectroscopy and X-ray scattering," *The Journal of Physical Chemistry B*, vol. 120, no. 6, pp. 1158–1168, 2016.

- [83] Canton S.E., Kjær K.S., Vankó G., Van Driel T.B., Adachi S-i., Bordage A., Bressler C., Chabera P., Christensen M., Dohn A.O. *et al*, "Visualizing the non-equilibrium dynamics of photoinduced intramolecular electron transfer with femtosecond x-ray pulses," *Nature Communications*, vol. 6, no. 1, pp. 1–10, 2015.
- [84] Christensen M., Haldrup K., Bechgaard K., Feidenhans'l R., Kong Q., Cammarata M., Russo M.L., Wulff M., Harrit N., Nielsen M.M., "Time-resolved X-ray scattering of an electronically excited state in solution. Structure of the 3A_{2u} state of tetrakis- μ -pyrophosphitodiplatinate (II)," *Journal of the American Chemical Society*, vol. 131, no. 2, pp. 502–508, 2009.
- [85] Haldrup K., Harlang T., Christensen M., Dohn A., van Driel T.B., Kjær K.S., Harrit N., Vibenholt J., Guerin L., Wulff M. *et al*, "Bond shortening (1.4 Å) in the singlet and triplet excited states of [Ir² (dimen)₄] 2+ in solution determined by time-resolved X-ray scattering," *Inorganic Chemistry*, vol. 50, no. 19, pp. 9329–9336, 2011.
- [86] Haldrup K., Christensen M., Cammarata M., Kong Q., Wulff M., Mariager S.O., Bechgaard K., Feidenhans'l R., Harrit N., Nielsen M.M., "Structural Tracking of a Bimolecular Reaction in Solution by Time-Resolved X-Ray Scattering," *Angewandte Chemie International Edition*, vol. 48, no. 23, pp. 4180–4184, 2009.
- [87] Christensen M., Haldrup K., Kjær K.S., Cammarata M., Wulff M., Bechgaard K., Weihe H., Harrit N.H., Nielsen M.M., "Structure of a short-lived excited state trinuclear Ag–Pt–Pt complex in aqueous solution by time resolved X-ray scattering," *Physical Chemistry Chemical Physics*, vol. 12, no. 26, pp. 6921–6923, 2010.
- [88] Bratos S., Mirloup F., Vuilleumier R., Wulff M., "Time-resolved x-ray diffraction: Statistical theory and its application to the photo-physics of molecular iodine," *The Journal of Chemical Physics*, vol. 116, no. 24, pp. 10615–10625, 2002.
- [89] Bratos S., Mirloup F., Vuilleumier R., Wulff M., Plech A., "X-ray "filming" of atomic motions in chemical reactions," *Chemical Physics*, vol. 304, no. 3, pp. 245–251, 2004.

- [90] Kong Q., Wulff M., Lee J.H., Bratos S., Ihee H., "Photochemical reaction pathways of carbon tetrabromide in solution probed by picosecond X-ray diffraction," *Journal of the American Chemical Society*, vol. 129, no. 44, pp. 13584–13591, 2007.
- [91] Vincent J., Andersson M., Eklund M., Wöhri A.B., Odelius M., Malmerberg E., Kong Q., Wulff M., Neutze R., Davidsson J., "Solvent dependent structural perturbations of chemical reaction intermediates visualized by time-resolved x-ray diffraction," *The Journal of Chemical Physics*, vol. 130, no. 15, p. 154502, 2009.
- [92] Ihee H., "Visualizing solution-phase reaction dynamics with time-resolved x-ray liquidography," *Accounts of Chemical Research*, vol. 42, no. 2, pp. 356–366, 2009.
- [93] Haldrup K., Vankó G., Gawelda W., Galler A., Doumy G., March A.M., Kanter E.P., Bordage A., Dohn A., van Driel T.B. *et al*, "Guest–host Interactions investigated by time-resolved X-ray spectroscopies and scattering at MHz rates: solvation dynamics and photoinduced spin transition in aqueous $\text{Fe}(\text{bipy})_3^{2+}$," *The Journal of Physical Chemistry A*, vol. 116, no. 40, pp. 9878–9887, 2012.
- [94] Haldrup K., Levi G., Biasin E., Vester P., Laursen M.G., Beyer F., Kjær K.S., Van Driel T.B., Harlang T., Dohn A.O. *et al*, "Ultrafast X-ray scattering measurements of coherent structural dynamics on the ground-state potential energy surface of a diplatinum molecule," *Physical Review Letters*, vol. 122, no. 6, p. 063001, 2019.
- [95] Barbieri A., Accorsi G., Armaroli N., "Luminescent complexes beyond the platinum group: the d10 avenue," *Chemical Communications*, no. 19, pp. 2185–2193, 2008.
- [96] Armaroli N., "Photoactive mono-and polynuclear Cu (I)–phenanthrolines. A viable alternative to Ru (II)–polypyridines?," *Chemical Society Reviews*, vol. 30, no. 2, pp. 113–124, 2001.
- [97] Lazorski M.S., Castellano F.N., "Advances in the light conversion properties of Cu (I)-based photosensitizers," *Polyhedron*, vol. 82, pp. 57–70, 2014.
- [98] Shaw G.B., Grant C.D., Shirota H., Castner E.W., Meyer G.J., Chen L.X., "Ultrafast structural rearrangements in the MLCT excited state

- for copper (I) bis-phenanthrolines in solution," *Journal of the American Chemical Society*, vol. 129, no. 7, pp. 2147–2160, 2007.
- [99] Iwamura M., Takeuchi S., Tahara T., "Real-time observation of the photoinduced structural change of bis (2, 9-dimethyl-1, 10-phenanthroline) copper (I) by femtosecond fluorescence spectroscopy: a realistic potential curve of the Jahn- Teller distortion," *Journal of the American Chemical Society*, vol. 129, no. 16, pp. 5248–5256, 2007.
- [100] Chen L.X., Zhang X., Lockard J.V., Stickrath A.B., Attenkofer K., Jennings G., Liu D-J., "Excited-state molecular structures captured by X-ray transient absorption spectroscopy: a decade and beyond," *Acta Crystallographica Section A: Foundations of Crystallography*, vol. 66, no. 2, pp. 240–251, 2010.
- [101] Iwamura M., Watanabe H., Ishii K., Takeuchi S., Tahara T., "Coherent nuclear dynamics in ultrafast photoinduced structural change of bis (diimine) copper (i) complex," *Journal of the American Chemical Society*, vol. 133, no. 20, pp. 7728–7736, 2011.
- [102] Iwamura M., Takeuchi S., Tahara T., "Substituent effect on the photoinduced structural change of Cu (I) complexes observed by femtosecond emission spectroscopy," *Physical Chemistry Chemical Physics*, vol. 16, no. 9, pp. 4143–4154, 2014.
- [103] Hua L., Iwamura M., Takeuchi S., Tahara T., "The substituent effect on the MLCT excited state dynamics of Cu (I) complexes studied by femtosecond time-resolved absorption and observation of coherent nuclear wavepacket motion," *Physical Chemistry Chemical Physics*, vol. 17, no. 3, pp. 2067–2077, 2015.
- [104] Gimeno L., Blart E. *et al*, "Non symmetrical sterically challenged phenanthroline ligands and their homoleptic copper (i) complexes with improved excited state properties," *Chemistry–A European Journal*, 2020.
- [105] Capano G., Penfold T.J., Röthlisberger U., Tavernelli I., "A vibronic coupling Hamiltonian to describe the ultrafast excited state dynamics of a Cu (I)-phenanthroline complex," *CHIMIA International Journal for Chemistry*, vol. 68, no. 4, pp. 227–230, 2014.

- [106] Capano G., Chergui M., Röthlisberger U., Tavernelli, I., Penfold T.J., "A quantum dynamics study of the ultrafast relaxation in a prototypical Cu (I)-phenanthroline," *The Journal of Physical Chemistry A*, vol. 118, no. 42, pp. 9861–9869, 2014.
- [107] Agena A., Iuchi S., Higashi M., "Theoretical study on photoexcitation dynamics of a bis-diimine Cu (I) complex in solutions," *Chemical Physics Letters*, vol. 679, pp. 60–65, 2017.
- [108] Capano G., Penfold T.J., Chergui M., Tavernelli I., "Photophysics of a copper phenanthroline elucidated by trajectory and wavepacket-based quantum dynamics: a synergetic approach," *Physical Chemistry Chemical Physics*, vol. 19, no. 30, pp. 19590–19600, 2017.
- [109] Czerwieniec R., Leitl M.J., Homeier H.H.H., Yersin H., "Cu (i) complexes—thermally activated delayed fluorescence. photophysical approach and material design," *Coordination Chemistry Reviews*, vol. 325, pp. 2–28, 2016.
- [110] McMillin D.R., Kirchoff J.R., Goodwin K.V., "Exciplex quenching of photo-excited copper complexes," *Coordination Chemistry Reviews*, vol. 64, pp. 83–92, 1985.
- [111] Schrödinger E., "An undulatory theory of the mechanics of atoms and molecules," *Physical Review*, vol. 28, no. 6, p. 1049, 1926.
- [112] Griffiths D.J., *Introduction to Quantum Mechanics, Second Edition*. Pearson International, 2013.
- [113] Holzner S., *Quantum Physics for Dummies*. Wiley, 2013.
- [114] Born M., Huang K., *Dynamical Theory of Crystal Lattices*. Clarendon press, 1954.
- [115] De Carvalho F.F., Bouduban M.E.F., Curchod B.F.E., Tavernelli I., "Nonadiabatic Molecular Dynamics Based on Trajectories," *Entropy*, vol. 16, no. 1, pp. 62–85, 2014.
- [116] Handy N.C., Lee A.M., "The adiabatic approximation," *Chemical Physics Letters*, vol. 252, no. 5-6, pp. 425–430, 1996.
- [117] Born M., Oppenheimer R., "Zur quantentheorie der molekeln," *Annalen der physik*, vol. 389, no. 20, pp. 457–484, 1927.

- [118] Kolos W., Wolniewicz L., "Accurate adiabatic treatment of the ground state of the hydrogen molecule," *The Journal of Chemical Physics*, vol. 41, no. 12, pp. 3663–3673, 1964.
- [119] Ballhausen C.J., Hansen A.E., "Electronic spectra," *Annual Review of Physical Chemistry*, vol. 23, no. 1, pp. 15–38, 1972.
- [120] Pauli W., "Über den zusammenhang des abschlusses der elektronengruppen im atom mit der komplexstruktur der spektren," *Zeitschrift für Physik A Hadrons and Nuclei*, vol. 31, no. 1, pp. 765–783, 1925.
- [121] Sherrill C.D., "An introduction to Hartree-Fock molecular orbital theory," *School of Chemistry and Biochemistry Georgia Institute of Technology*, 2000.
- [122] Hartree D.R., "The wave mechanics of an atom with a non-coulomb central field. part iii. term values and intensities in series in optical spectra," in *Mathematical Proceedings of the Cambridge Philosophical Society*, vol. 24, pp. 426–437, Cambridge University Press, 1928.
- [123] Slater J.C., "Note on Hartree's method," *Physical Review*, vol. 35, no. 2, p. 210, 1930.
- [124] Fock V., "Näherungsmethode zur lösung des quantenmechanischen mehrkörperproblems," *Zeitschrift für Physik*, vol. 61, no. 1-2, pp. 126–148, 1930.
- [125] Paulsen H., Trautwein A.X., "Density functional theory calculations for spin crossover complexes," in *Spin Crossover in Transition Metal Compounds III*, pp. 197–219, Springer, 2004.
- [126] Hund F., "Zur deutung einiger erscheinungen in den molekelspektren," *Zeitschrift für Physik*, vol. 36, no. 9-10, pp. 657–674, 1926.
- [127] Mulliken R.S., "Electronic states and band spectrum structure in diatomic molecules. IV. Hund's theory; second positive nitrogen and swan bands; alternating intensities," *Physical Review*, vol. 29, no. 5, p. 637, 1927.
- [128] Mulliken R.S., "The assignment of quantum numbers for electrons in molecules. i," *Physical Review*, vol. 32, no. 2, p. 186, 1928.
- [129] P. M. Møller C., "Note on an approximation treatment for many-electron systems," *Physical Review*, vol. 46, no. 7, p. 618, 1934.

- [130] Vosko S.H., Wilk L., Nusair M., "Accurate spin-dependent electron liquid correlation energies for local spin density calculations: a critical analysis," *Canadian Journal of Physics*, vol. 58, no. 8, pp. 1200–1211, 1980.
- [131] Perdew J.P., Wang Y., "Accurate and simple analytic representation of the electron-gas correlation energy," *Physical Review B*, vol. 45, no. 23, p. 13244, 1992.
- [132] Becke A.D., "Density-functional exchange-energy approximation with correct asymptotic behavior," *Physical Review A*, vol. 38, no. 6, p. 3098, 1988.
- [133] Rienstra-Kiracofe J.C., Tschumper G.S., Schaefer H.F., Nandi S., Ellison G.B., "Atomic and molecular electron affinities: photoelectron experiments and theoretical computations," *Chemical Reviews*, vol. 102, no. 1, pp. 231–282, 2002.
- [134] Jakobsen S., Kristensen K., Jensen F., "Electrostatic potential of insulin: exploring the limitations of density functional theory and force field methods," *Journal of Chemical Theory and Computation*, vol. 9, no. 9, pp. 3978–3985, 2013.
- [135] Forni A., Pieraccini S., Franchini D., Sironi M., "Assessment of DFT Functionals for QTAIM Topological Analysis of Halogen Bonds with Benzene," *The Journal of Physical Chemistry A*, vol. 120, pp. 9071–9080, 2016.
- [136] Collins R.L., Travis J.C., "The electric field gradient tensor," in *Mössbauer effect methodology*, pp. 123–161, Springer, 1967.
- [137] Pyykkö P., "Year-2017 nuclear quadrupole moments," *Molecular Physics*, vol. 116, no. 10, pp. 1328–1338, 2018.
- [138] Walker N.R., Gerry M.C.L., "Microwave spectra, geometries, and hyperfine constants of OCAgX (X= F, Cl, Br)," *Inorganic Chemistry*, vol. 41, no. 5, pp. 1236–1244, 2002.
- [139] Stephens S.L., Bittner D.M., Mikhailov V.A., Mizukami W., Tew D.P., Walker N.R., Legon A.C., "Changes in the Geometries of C₂H₂ and C₂H₄ on Coordination to CuCl Revealed by Broadband Rotational Spectroscopy and ab-Initio Calculations," *Inorganic Chemistry*, vol. 53, no. 19, pp. 10722–10730, 2014.

- [140] Zaleski D.P., Stephens S.L., Walker N.R., "A perspective on chemistry in transient plasma from broadband rotational spectroscopy," *Physical Chemistry Chemical Physics*, vol. 16, no. 46, pp. 25221–25228, 2014.
- [141] Grubb M.P., Coulter P.M., Marroux H.J.B., Hornung B., McMullen R.S., Orr-Ewing A.J., Ashfold M.N.R., "Translational, rotational and vibrational relaxation dynamics of a solute molecule in a non-interacting solvent," *Nature Chemistry*, vol. 8, pp. 1042–1046, 2016.
- [142] Sivia D.S., *Elementary scattering theory: for X-ray and neutron users*. Oxford University Press, 2011.
- [143] Dohn A.O., Biasin E., Haldrup K., Nielsen M.M., Henriksen N.E., Møller K.B., "On the calculation of x-ray scattering signals from pairwise radial distribution functions," *Journal of Physics B: Atomic, Molecular and Optical Physics*, vol. 48, no. 24, p. 244010, 2015.
- [144] Tschumper G.S., "2 reliable electronic structure computations for weak noncovalent interactions in clusters," *Reviews in Computational Chemistry*, vol. 26, p. 39, 2009.
- [145] Lennard-Jones J.E., "On the determination of molecular fields.—ii. from the equation of state of a gas," *Proceedings of the Royal Society of London. Series A, Containing Papers of a Mathematical and Physical Character*, vol. 106, no. 738, pp. 463–477, 1924.
- [146] Jorgensen W.L., Tirado-Rives J., "The OPLS [optimized potentials for liquid simulations] potential functions for proteins, energy minimizations for crystals of cyclic peptides and crambin," *Journal of the American Chemical Society*, vol. 110, no. 6, pp. 1657–1666, 1988.
- [147] Paulechka E., Kroenlein K., Kazakov A., Frenkel M., "A systematic approach for development of an OPLS-like force field and its application to hydrofluorocarbons," *The Journal of Physical Chemistry B*, vol. 116, no. 49, pp. 14389–14397, 2012.
- [148] Jorgensen W.L., Maxwell D.S., Tirado-Rives J., "Development and testing of the OPLS all-atom force field on conformational energetics and properties of organic liquids," *Journal of the American Chemical Society*, vol. 118, no. 45, pp. 11225–11236, 1996.

- [149] Seminario, J.M., "Calculation of intramolecular force fields from second-derivative tensors," *International Journal of Quantum Chemistry*, vol. 60, no. 7, pp. 1271–1277, 1996.
- [150] Allen A.E.A., Payne M.C., Cole D.J., "Harmonic force constants for molecular mechanics force fields via hessian matrix projection," *Journal of Chemical Theory and Computation*, vol. 14, no. 1, pp. 274–281, 2018.
- [151] Manz T.A., Sholl D.S., "Chemically meaningful atomic charges that reproduce the electrostatic potential in periodic and nonperiodic materials," *Journal of Chemical Theory and Computation*, vol. 6, no. 8, pp. 2455–2468, 2010.
- [152] Manz T.A., Sholl D.S., "Improved atoms-in-molecule charge partitioning functional for simultaneously reproducing the electrostatic potential and chemical states in periodic and nonperiodic materials," *Journal of Chemical Theory and Computation*, vol. 8, no. 8, pp. 2844–2867, 2012.
- [153] Tkatchenko A., Scheffler M., "Accurate molecular van der Waals interactions from ground-state electron density and free-atom reference data," *Physical Review Letters*, vol. 102, no. 7, p. 073005, 2009.
- [154] Chu X., Dalgarno A., "Linear response time-dependent density functional theory for van der waals coefficients," *The Journal of Chemical Physics*, vol. 121, no. 9, pp. 4083–4088, 2004.
- [155] Verlet L., "Computer "experiments" on classical fluids. I. Thermodynamical properties of Lennard-Jones molecules," *Physical Review*, vol. 159, no. 1, p. 98, 1967.
- [156] Andersen H.C., "Molecular dynamics simulations at constant pressure and/or temperature," *The Journal of Chemical Physics*, vol. 72, no. 4, pp. 2384–2393, 1980.
- [157] Berendsen H.J.C., Postma J.P.M., van Gunsteren W.F., DiNola A.R.H.J., Haak J.R., "Molecular dynamics with coupling to an external bath," *The Journal of Chemical Physics*, vol. 81, no. 8, pp. 3684–3690, 1984.
- [158] Nosé S., "A molecular dynamics method for simulations in the canonical ensemble," *Molecular Physics*, vol. 52, no. 2, pp. 255–268, 1984.
- [159] Hoover W.G., "Canonical dynamics: Equilibrium phase-space distributions," *Physical Review A*, vol. 31, no. 3, p. 1695, 1985.

- [160] Van Meer R., Gritsenko O.V., Baerends E.J., "Physical meaning of virtual kohn–sham orbitals and orbital energies: an ideal basis for the description of molecular excitations," *Journal of Chemical Theory and Computation*, vol. 10, no. 10, pp. 4432–4441, 2014.
- [161] Hamprecht F.A., Cohen A.J., Tozer D.J., Handy N.C., "Development and assessment of new exchange–correlation functionals," *The Journal of Chemical Physics*, vol. 109, no. 15, pp. 6264–6271, 1998.
- [162] Boese A.D., Doltsinis N.L., Handy N.C., Sprik M., "New generalized gradient approximation functionals," *The Journal of Chemical Physics*, vol. 112, no. 4, pp. 1670–1678, 2000.
- [163] Boese A.D., Handy N.C., "A new parametrization of exchange–correlation generalized gradient approximation functionals," *The Journal of Chemical Physics*, vol. 114, no. 13, pp. 5497–5503, 2001.
- [164] Neese F., "The ORCA program system," *Wiley Interdisciplinary Reviews: Computational Molecular Science*, vol. 2, no. 1, pp. 73–78, 2012.
- [165] Dunning Jr. T.H., "Gaussian basis sets for use in correlated molecular calculations. i. the atoms boron through neon and hydrogen," *The Journal of Chemical Physics*, vol. 90, no. 2, pp. 1007–1023, 1989.
- [166] Kendall R.A., Dunning Jr. T.H., Harrison R.J., "Electron affinities of the first-row atoms revisited. systematic basis sets and wave functions," *The Journal of Chemical Physics*, vol. 96, no. 9, pp. 6796–6806, 1992.
- [167] Woon D.E., Dunning Jr. T.H., "Gaussian basis sets for use in correlated molecular calculations. iii. the atoms aluminum through argon," *The Journal of Chemical Physics*, vol. 98, no. 2, pp. 1358–1371, 1993.
- [168] Balabanov N.B., Peterson K.A., "Systematically convergent basis sets for transition metals. I. All-electron correlation consistent basis sets for the 3d elements Sc–Zn," *The Journal of Chemical Physics*, vol. 123, no. 6, p. 064107, 2005.
- [169] Balabanov N.B., Peterson K.A., "Basis set limit electronic excitation energies, ionization potentials, and electron affinities for the 3 d transition metal atoms: Coupled cluster and multireference methods," *The Journal of Chemical Physics*, vol. 125, no. 7, p. 074110, 2006.

- [170] Baer R., Livshits E., Salzner U., "Tuned range-separated hybrids in density functional theory," *Annual Review of Physical Chemistry*, vol. 61, pp. 85–109, 2010.
- [171] Tawada Y., Tsuneda T., Yanagisawa S., Yanai T., Hirao K., "A long-range-corrected time-dependent density functional theory," *The Journal of Chemical Physics*, vol. 120, no. 18, pp. 8425–8433, 2004.
- [172] Yanagisawa S., Tsuneda T., Hirao K., "An investigation of density functionals: The first-row transition metal dimer calculations," *The Journal of Chemical Physics*, vol. 112, no. 2, pp. 545–553, 2000.
- [173] Iikura H., Tsuneda T., Yanai T., Hirao K., "A long-range correction scheme for generalized-gradient-approximation exchange functionals," *The Journal of Chemical Physics*, vol. 115, no. 8, pp. 3540–3544, 2001.
- [174] Furche F., Perdew J.P., "The performance of semilocal and hybrid density functionals in 3 d transition-metal chemistry," *The Journal of Chemical Physics*, vol. 124, no. 4, p. 044103, 2006.
- [175] Zhang W., Truhlar D.G., Tang M., "Tests of exchange-correlation functional approximations against reliable experimental data for average bond energies of 3d transition metal compounds," *Journal of Chemical Theory and Computation*, vol. 9, no. 9, pp. 3965–3977, 2013.
- [176] Wasserman A., Nafziger J., Jiang K., Kim M-C., Sim E., Burke K., "The importance of being inconsistent," *Annual Review of Physical Chemistry*, vol. 68, pp. 555–581, 2017.
- [177] Antes I., Dapprich S., Frenking G., Schwerdtfeger P., "Stability of Group 11 Carbonyl Complexes Cl-M-CO (M= Cu, Ag, Au)," *Inorganic Chemistry*, vol. 35, no. 7, pp. 2089–2096, 1996.
- [178] Schwerdtfeger P., Pernpointner M., Laerdahl J.K., "The accuracy of current density functionals for the calculation of electric field gradients: A comparison with ab initio methods for HCl and CuCl," *The Journal of Chemical Physics*, vol. 111, no. 8, pp. 3357–3364, 1999.
- [179] Thierfelder C., Schwerdtfeger P., Saue T., "Cu 63 and au 197 nuclear quadrupole moments from four-component relativistic density-functional calculations using correct long-range exchange," *Physical Review A*, vol. 76, no. 3, p. 034502, 2007.

- [180] Hait D., Head-Gordon M., "How accurate are static polarizability predictions from density functional theory? An assessment over 132 species at equilibrium geometry," *Physical Chemistry Chemical Physics*, vol. 20, no. 30, pp. 19800–19810, 2018.
- [181] Fraley A.E., Sherman D.H., "Halogenase engineering and its utility in medicinal chemistry," *Bioorganic & medicinal chemistry letters*, vol. 28, no. 11, pp. 1992–1999, 2018.
- [182] Dunning Jr, T.H., "Gaussian basis functions for use in molecular calculations. iii. contraction of (10s6p) atomic basis sets for the first-row atoms," *The Journal of Chemical Physics*, vol. 55, no. 2, pp. 716–723, 1971.
- [183] Visscher L., Dyall K.G., "Dirac–Fock atomic electronic structure calculations using different nuclear charge distributions," *Atomic Data and Nuclear Data Tables*, vol. 67, no. 2, pp. 207–224, 1997.
- [184] Fleming I., *Molecular orbitals and organic chemical reactions*. John Wiley & Sons, 2011.
- [185] Ruzsinszky A., Perdew J.P., Csonka G.I., Vydrov O.A., Scuseria G.E., "Spurious fractional charge on dissociated atoms: Pervasive and resilient self-interaction error of common density functionals," *The Journal of Chemical Physics*, vol. 125, no. 19, p. 194112, 2006.
- [186] Dutoi A.D., Head-Gordon M., "Self-interaction error of local density functionals for alkali–halide dissociation," *Chemical Physics Letters*, vol. 422, no. 1-3, pp. 230–233, 2006.
- [187] Adhikari S., Santra B., Ruan S., Bhattarai P., Nepal N.K., Jackson K.A., Ruzsinszky A., "The Fermi–Löwdin self-interaction correction for ionization energies of organic molecules," *The Journal of Chemical Physics*, vol. 153, no. 18, p. 184303, 2020.
- [188] Caleman C., van Maaren P.J., Hong M., Hub J.S., Costa L.T., van der Spoel D., "Force field benchmark of organic liquids: density, enthalpy of vaporization, heat capacities, surface tension, isothermal compressibility, volumetric expansion coefficient, and dielectric constant," *Journal of Chemical Theory and Computation*, vol. 8, no. 1, pp. 61–74, 2012.
- [189] Eastman P., Swails J., Chodera J.D., McGibbon R.T., Zhao Y., Beauchamp K.A., Wang L-P., Simmonett A.C., Harrigan M.P., Stern

- C.D., *et al.*, "OpenMM 7: Rapid development of high performance algorithms for molecular dynamics," *PLoS Computational Biology*, vol. 13, no. 7, p. e1005659, 2017.
- [190] Dodda L.S., Vilseck J.Z., Tirado-Rives J., Jorgensen W.L., "1.14* CM1A-LBCC: localized bond-charge corrected CM1A charges for condensed-phase simulations," *The Journal of Physical Chemistry B*, vol. 121, no. 15, pp. 3864–3870, 2017.
- [191] Wulff M., Bratos S., Plech A., Vuilleumier R., Mirloup F., Lorenc M., Kong Q., Ihee H., "Recombination of photodissociated iodine: A time-resolved x-ray-diffraction study," *The Journal of Chemical Physics*, vol. 124, no. 3, p. 034501, 2006.
- [192] Kim K.H., Ki H., Lee J.H., Park S., Kong Q., Kim J., Kim J., Wulff M., Ihee H., "Solvent-dependent structure of molecular iodine probed by picosecond X-ray solution scattering," *Physical Chemistry Chemical Physics*, vol. 17, no. 14, pp. 8633–8637, 2015.
- [193] Rosen H., Shen Y.R., Stenman F., "Raman study of iodine complexes in solutions," *Molecular Physics*, vol. 22, no. 1, pp. 33–47, 1971.
- [194] Yarwood J., Catlow B., "Far-infrared interaction-induced spectra of the halogens," *Journal of the Chemical Society, Faraday Transactions 2: Molecular and Chemical Physics*, vol. 83, no. 10, pp. 1801–1814, 1987.
- [195] Danten Y., Guillot B., Guissani Y., "Investigation of charge-transfer complexes by computer simulation. i. iodine in benzene solution," *The Journal of Chemical Physics*, vol. 96, no. 5, pp. 3782–3794, 1992.
- [196] Danten Y., Guillot B., Guissani Y., "Investigation of charge-transfer complexes by computer simulation. ii. iodine in pyridine solution," *The Journal of Chemical Physics*, vol. 96, no. 5, pp. 3795–3810, 1992.
- [197] Buontempo U., Di Cicco A., Filipponi A., Nardone M., Postorino P., "Determination of the I₂ bond-length distribution in liquid, solid and solution, by extended x-ray absorption fine structure spectroscopy," *The Journal of chemical physics*, vol. 107, no. 15, pp. 5720–5726, 1997.
- [198] Barreto R.C., Coutinho K., Georg H.C., Canuto S., "Combined Monte Carlo and quantum mechanics study of the solvatochromism of phenol in water. The origin of the blue shift of the lowest π - π^* transition," *Physical Chemistry Chemical Physics*, vol. 11, no. 9, pp. 1388–1396, 2009.

- [199] Marini A., Muñoz-Losa A., Biancardi A., Mennucci B., "What is solvatochromism?," *The Journal of Physical Chemistry B*, vol. 114, no. 51, pp. 17128–17135, 2010.
- [200] Ponnuchamy V., "A theoretical investigation of different point charges combined with GAFF and OPLS-AA for acetic anhydride," *Chemical Physics Letters*, p. 137707, 2020.
- [201] Storer J.W., Giesen D.J., Cramer C.J., Truhlar D.G., "Class IV charge models: A new semiempirical approach in quantum chemistry," *Journal of Computer-Aided Molecular Design*, vol. 9, no. 1, pp. 87–110, 1995.
- [202] Udier-Blagović M., Morales De Tirado P., Pearlman S.A., Jorgensen W.L., "Accuracy of free energies of hydration using CM1 and CM3 atomic charges," *Journal of Computational Chemistry*, vol. 25, no. 11, pp. 1322–1332, 2004.
- [203] Jakalian A., Jack D.B., Bayly C.I., "Fast, efficient generation of high-quality atomic charges. AM1-BCC model: II. Parameterization and validation," *Journal of Computational Chemistry*, vol. 23, no. 16, pp. 1623–1641, 2002.
- [204] Jakalian A., Bush B.L., Jack D.B., Bayly C.I., "Fast, efficient generation of high-quality atomic charges. AM1-BCC model: I. Method," *Journal of Computational Chemistry*, vol. 21, no. 2, pp. 132–146, 2000.
- [205] Dewar M.J.S., Zoebisch E.G., Healy E.F., Stewart J.J.P., "Development and use of quantum mechanical molecular models. 76. AM1: a new general purpose quantum mechanical molecular model," *Journal of the American Chemical Society*, vol. 107, no. 13, pp. 3902–3909, 1985.
- [206] Marenich A.V., Jerome S.V., Cramer C.J., Truhlar D.G., "Charge model 5: An extension of Hirshfeld population analysis for the accurate description of molecular interactions in gaseous and condensed phases," *Journal of Chemical Theory and Computation*, vol. 8, no. 2, pp. 527–541, 2012.
- [207] Horton J.T, Allen A.E.A, Cole D.J., "Modelling flexible protein–ligand binding in p38 α MAP kinase using the QUBE force field," *Chemical Communications*, vol. 56, no. 6, pp. 932–935, 2020.

- [208] Kim J., Kim J.G., Ki H., Ahn C.W., Ihee H., "Estimating signal and noise of time-resolved x-ray solution scattering data at synchrotrons and xfel," *Journal of Synchrotron Radiation*, vol. 27, no. 3, 2020.
- [209] Cannizzo A., van Mourik F., Gawelda W., Zgrablic G., Bressler C., Chergui M., "Broadband femtosecond fluorescence spectroscopy of $[\text{Ru}(\text{bpy})_3]^{2+}$," *Angewandte Chemie*, vol. 118, no. 19, pp. 3246–3248, 2006.
- [210] Tavernelli I., Curchod B., Rothlisberger U., "Nonadiabatic molecular dynamics with solvent effects: A LR-TDDFT QM/MM study of ruthenium (II) tris (bipyridine) in water," *Chemical Physics*, vol. 391, no. 1, pp. 101–109, 2011.
- [211] Penfold T.J., Gindensperger E., Daniel C., Marian C.M., "Spin-vibronic mechanism for intersystem crossing," *Chemical Reviews*, vol. 118, no. 15, pp. 6975–7025, 2018.
- [212] Damrauer N.H., Cerullo G., Yeh A.T., Boussie T.R., Shank C.V., McCusker J.K., "Femtosecond dynamics of excited-state evolution in $[\text{Ru}(\text{bpy})_3]^{2+}$," *Science*, vol. 275, no. 5296, pp. 54–57, 1997.
- [213] Yeh A.T., Shank C.V., McCusker J.K., "Ultrafast electron localization dynamics following photo-induced charge transfer," *Science*, vol. 289, no. 5481, pp. 935–938, 2000.
- [214] Bhasikuttan A.C., Suzuki M., Nakashima S., Okada T., "Ultrafast fluorescence detection in Tris (2, 2'-bipyridine) ruthenium (II) complex in solution: relaxation dynamics involving higher excited states," *Journal of the American Chemical Society*, vol. 124, no. 28, pp. 8398–8405, 2002.
- [215] Cannizzo A., Blanco-Rodriguez A.M., el Nahhas A., Sebera J., Zalis S., Vlcek A.J.; Chergui M., "Femtosecond Fluorescence and Intersystem Crossing in Ruthenium (I) Carbonyl- Bipyridine Complexes," *Journal of the American Chemical Society*, vol. 130, no. 28, pp. 8967–8974, 2008.
- [216] el Nahhas A., Cannizzo A., van Mourik F., Blanco-Rodriguez A. M., Zalis S., Vlcek A. J., Chergui M., "Ultrafast excited-state dynamics of $[\text{Re}(\text{L})(\text{CO})_3(\text{bpy})]_n$ complexes: involvement of the solvent," *The Journal of Physical Chemistry A*, vol. 114, no. 22, pp. 6361–6369, 2010.

- [217] el Nahhas A., Consani C., Blanco-Rodriguez A.M., Lancaster K.M., Braem O., Cannizzo A., Towrie M., Clark I.P. *et al.*, "Ultrafast excited-state dynamics of rhenium (I) photosensitizers [Re (Cl)(CO)₃ (N, N)] and [Re (imidazole)(CO)₃ (N, N)]⁺: diimine effects," *Inorganic Chemistry*, vol. 50, no. 7, pp. 2932–2943, 2011.
- [218] el Nahhas A., Van Der Veen R.M., Penfold T.J., Pham V.T., Lima F.A., Abela R., Blanco-Rodriguez, A.M. *et al.*, "X-ray absorption spectroscopy of ground and excited rhenium–carbonyl–diimine complexes: Evidence for a two-center electron transfer," *The Journal of Physical Chemistry A*, vol. 117, no. 2, pp. 361–369, 2013.
- [219] Braem O., Messina F., Baranoff E., Cannizzo A., Nazeeruddin M.K., Chergui M., "Ultrafast relaxation dynamics of osmium–polypyridine complexes in solution," *The Journal of Physical Chemistry C*, vol. 117, no. 31, pp. 15958–15966, 2013.
- [220] Zhang X., Canton S.E., Smolentsev G., Wallentin C-J., Liu Y., Kong Q., Attenkofer K., Stickrath A.B., Mara M.W., Chen L.X. *et al.*, "Highly accurate excited-state structure of [Os (bpy)₂dcbpy]²⁺ determined by X-ray transient absorption spectroscopy," *Journal of the American Chemical Society*, vol. 136, no. 24, pp. 8804–8809, 2014.
- [221] Yang C-H., Li S-W., Chi Y., Cheng Y-M., Yeh Y-S., Chou P-T., Lee G-H., Wang C-H., Shu C-F., "Heteroleptic cyclometalated iridium (iii) complexes displaying blue phosphorescence in solution and solid state at room temperature," *Inorganic Chemistry*, vol. 44, no. 22, pp. 7770–7780, 2005.
- [222] Li J., Djurovich P.I., Alleyne B.D., Yousufuddin M., Ho N.N., Thomas J.C., Peters J.C., Bau R., Thompson M.E., "Synthetic control of excited-state properties in cyclometalated Ir (III) complexes using ancillary ligands," *Inorganic Chemistry*, vol. 44, no. 6, pp. 1713–1727, 2005.
- [223] Zhao N., Wu Y-H., Wen H-M., Zhang X., Chen Z-N., "Conversion from ILCT to LLCT/MLCT excited state by heavy metal ion binding in iridium (III) complexes with functionalized 2, 2'-bipyridyl ligands," *Organometallics*, vol. 28, no. 19, pp. 5603–5611, 2009.

- [224] Castellano, F.N., Pomestchenko, I.E., Shikhova, E., Hua, F., Muro, M.L., Rajapakse, N., "Photophysics in bipyridyl and terpyridyl platinum (ii) acetylides," *Coordination Chemistry Reviews*, vol. 250, no. 13-14, pp. 1819–1828, 2006.
- [225] Rachford A.A., Goeb S., Ziessel R., Castellano F.N., "Ligand localized triplet excited states in platinum (ii) bipyridyl and terpyridyl peryleneacetylides," *Inorganic Chemistry*, vol. 47, no. 10, pp. 4348–4355, 2008.
- [226] Gutiérrez-Arzaluz L., Ramírez-Palma D.I., Ramírez-Palma L.G., Barquera-Lozada J.E., Peon J., Cortés-Guzmán F., "Origin of the Photoinduced Geometrical Change of Copper (I) Complexes from the Quantum Chemical Topology View," *Chemistry—A European Journal*, vol. 25, no. 3, pp. 775–784, 2019.
- [227] Eggleston M.K., McMillin D.R., Koenig K.S., Pallenberg A.J., "Steric effects in the ground and excited states of Cu (NN)²⁺ systems," *Inorganic Chemistry*, vol. 36, no. 2, pp. 172–176, 1997.
- [228] Penfold T.J., Karlsson S., Capano G. *et al*, "Solvent-induced luminescence quenching: Static and time-resolved x-ray absorption spectroscopy of a copper (i) phenanthroline complex," *The Journal of Physical Chemistry A*, vol. 117, no. 22, pp. 4591–4601, 2013.
- [229] Car R., Parrinell M., "Unified approach for molecular dynamics and density-functional theory," *Physical Review Letters*, vol. 55, no. 22, p. 2471, 1985.
- [230] Laio A., VandeVondele J., Röthlisberger U., "A Hamiltonian electrostatic coupling scheme for hybrid Car–Parrinello molecular dynamics simulations," *The Journal of Chemical Physics*, vol. 116, no. 16, pp. 6941–6947, 2002.
- [231] Laio A., VandeVondele J., Röthlisberger U., "D-RESP: Dynamically generated electrostatic potential derived charges from quantum mechanics/molecular mechanics simulations," *The Journal of Physical Chemistry B*, vol. 106, no. 29, pp. 7300–7307, 2002.
- [232] Mara M.W., Fransted K.A., Chen L.X., "Interplays of excited state structures and dynamics in copper (i) diimine complexes: Implications and perspectives," *Coordination Chemistry Reviews*, vol. 282, pp. 2–18, 2015.

- [233] Levi G., Biasin E., Dohn A.O., Jónsson H., "On the interplay of solvent and conformational effects in simulated excited-state dynamics of a copper phenanthroline photosensitizer," *Physical Chemistry Chemical Physics*, vol. 22, no. 2, pp. 748–757, 2020.
- [234] Hait D., Tubman N.M., Levine D.S., Whaley K.B., Head-Gordon M., "What Levels of Coupled Cluster Theory Are Appropriate for Transition Metal Systems? A Study Using Near-Exact Quantum Chemical Values for 3d Transition Metal Binary Compounds," *Journal of Chemical Theory and Computation*, vol. 15, no. 10, pp. 5370–5385, 2019.
- [235] Aoto Y.A., de Lima Batista A.P., Koehn A., de Oliveira-Filho A.G.S., "How to arrive at accurate benchmark values for transition metal compounds: computation or experiment?," *Journal of Chemical Theory and Computation*, vol. 13, no. 11, pp. 5291–5316, 2017.